UNICAMP

UNIVERSIDADE ESTADUAL DE CAMPINAS
Instituto de Física "Gleb Wataghin"

RICARDO JAVIER PEÑA ROMAN

Investigating the electronic and optical properties of atomically thin materials with a scanning tunneling microscope

Investigando as propriedades eletrônicas e ópticas de materiais atomicamente finos com um microscópico de tunelamento com varredura

CAMPINAS
2022

RICARDO JAVIER PEÑA ROMAN

Investigating the electronic and optical properties of atomically thin materials with a scanning tunneling microscope

Investigando as propriedades eletrônicas e ópticas
de materiais atomicamente finos
com um microscópico de tunelamento com varredura

Thesis presented to the Institute of Physics "Gleb Wataghin" of the University of Campinas in partial fulfillment of the requirements for the degree of Doctor in Science, in the field of Physics.

Tese de doutorado apresentada ao Instituto de Física "Gleb Wataghin" da Universidade Estadual de Campinas como parte dos requisitos exigidos para a obtenção do título de Doutor em Ciências, na Área de Física.

Advisor/Orientador: Prof. Dr. Luiz Fernando Zagonel

Este exemplar corresponde à versão final da tese defendida pelo aluno Ricardo Javier Peña Roman, e orientada pelo Prof. Dr. Luiz Fernando Zagonel.

CAMPINAS
2022

Ficha catalográfica
Universidade Estadual de Campinas
Biblioteca do Instituto de Física Gleb Wataghin
Lucimeire de Oliveira Silva da Rocha - CRB 8/9174

P37i
Peña Roman, Ricardo Javier, 1990-
Investigating the electronic and optical properties of atomically thin materials with a scanning tunneling microscope / Ricardo Javier Peña Roman. – Campinas, SP : [s.n.], 2022.

Orientador: Luiz Fernando Zagonel.
Tese (doutorado) – Universidade Estadual de Campinas, Instituto de Física Gleb Wataghin.

1. Dicalcogenetos de metais de transição. 2. Nitreto de boro hexagonal. 3. Microscopia de tunelamento de elétrons. 4. Microscopia de força atômica. 5. Espectroscopia ótica. I. Zagonel, Luiz Fernando, 1979-. II. Universidade Estadual de Campinas. Instituto de Física Gleb Wataghin. III. Título.

Informações para Biblioteca Digital

Título em outro idioma: Investigando as propriedades eletrônicas e ópticas de materiais atomicamente finos com um microscópio de tunelamento com varredura
Palavras-chave em inglês:
Transition metal dichalcogenides
Hexagonal boron nitride
Scanning tunneling microscopy
Atomic force microscopy
Optical spectroscopy
Área de concentração: Física
Titulação: Doutor em Ciências
Banca examinadora:
Luiz Fernando Zagonel [Orientador]
Daniel Mário Ugarte
Abner de Siervo
Luiz Gustavo de Oliveira Lopes Cançado
Fernando Loureiro Stavale Junior
Data de defesa: 05-07-2022
Programa de Pós-Graduação: Física

Identificação e informações acadêmicas do(a) aluno(a)
- ORCID do autor: https://orcid.org/0000-0003-4673-1127
- Currículo Lattes do autor: http://lattes.cnpq.br/3361655652086132

MEMBROS DA COMISSÃO JULGADORA DA TESE DE DOUTORADO DO ALUNO RICARDO JAVIER PEÑA ROMAN - RA 190934 APRESENTADA E APROVADA AO INSTITUTO DE FÍSICA "GLEB WATAGHIN", DA UNIVERSIDADE ESTADUAL DE CAMPINAS, EM 05/07/2022.

COMISSÃO JULGADORA:

- Prof. Dr. Luiz Fernando Zagonel - Presidente e Orientador (IFGW/UNICAMP)

- Prof. Dr. Daniel Mario Ugarte (IFGW/ UNICAMP)

- Prof. Dr. Abner de Siervo (IFGW/ UNICAMP)

- Dr. Luiz Gustavo de Oliveira Lopes Cançado (Departamento de Física/Universidade Federal de Minas Gerais)

- Dr. Fernando Loureiro Stavale Junior (Centro Brasileiro de Pesquisas Físicas)

OBS.: Ata da defesa com as respectivas assinaturas dos membros encontra-se no SIGA/Sistema de Fluxo de Dissertação/Tese e na Secretaria do Programa da Unidade.

CAMPINAS

2022

A Olga, María, Nataly e Isabella.

Acknowledgments

Em primeiro lugar, quero agradecer ao Prof. Dr. Luiz Fernando Zagonel pela oportunidade de trabalhar na construção de seu laboratório e do seu grupo de pesquisa. Agradeço a liberdade e confiança para eu poder explorar todas as minhas ideias durante a realização desta tese. Obrigado pela sua amizade, pela tolerância e paciência.

Agradeço ao Prof. Dr. Daniel Mario Ugarte por aceitar participar na banca examinadora da tese. Pelas conversas e ajuda para melhorar o manuscrito, e também por tudo o aprendizado adquirido nas aulas de microscopia e materiais. Ao Prof. Dr. Abner de Siervo, pela participação na banca e por acompanhar tudo o meu processo no departamento de física aplicada. Sempre ajudando com ideias e discussões sobre experimentos de fisica de superfícies. Agradeço também aos professores, Dr. Luiz Gustavo de Oliveira Lopes Cançado e Dr. Fernando Loureiro Stavale Júnior pela participação na banca examinadora da tese.

I would like to express my deepest gratitude to Dr. Eric le Moal and Dr. Elizabeth Boer-Duchemin for the opportunity to work in their group at the Institut des Sciences Moléculaires d'Orsay (ISMO) during my P.hD. internship there. Thank you very much for the supervision, discussions, and collaboration. I also want to express my gratitude to Delphine Pommier and Rémi Bretel for sharing their knowledge about STM-LE experiments on 2D semiconductors and for all the discussions we had about the experimental results.

À Dra. Ingrid David Barcelos pelo fornecimento das amostras de WSe_2 e por toda a colaboração, dedicação e discussões ao longo deste projeto. I also want to thank Prof. Alberto Zobelli, Prof. Guillaume Cassabois, Prof. Bernard Gil, Prof. Peter H Beton, and Prof. Sergei V Novikov for providing the sample of monolayer h-BN, for complementary measurements and interesting discussions about the h-BN properties. Thanks to all for the collaboration.

A todas as pessoas que me ajudaram e ofereceram sua amizade desde os meus primeiros dias na Unicamp, e no Brasil: à família Antunes, Vinicius, Diego (Cajuru), Yves, Murilo, Fábio, e ao Professor Fernando Alvarez. Obrigado!

Agradezco a todo mis seres queridos, a mi mamá, a mi hermana Maria y a toda la familia Román. Gracias por hacerme sentir tan querido por todos ustedes. En especial a mi mamá, Olga Maria Román Rodríguez, que ha sido mi ejemplo y motivación para muchas cosas. También doy gracias a Nacaré, Edgar, Nayarit y Edgar Eduardo por haberme recibido en su familia desde muy joven y hacerme sentir uno más de ustedes.

Quiero expresar también mi más profunda gratitud a Nataly Zaribeth Herrera Reinoza. Por todo el amor, por estar a mi lado en mis mejores y peores momentos, por la paciencia, la tolerancia, y por acompañarme en este camino desde mis inicios. Este logro es en grande parte gracias a ti, que siempre me apoyaste, motivaste y me levantaste el ánimo para seguir adelante. Por supuesto, agradezco también a Isabella la Bella. Por ser tan especial, por portarte tan bien, por ser tan inteligente, por dejarme trabajar siempre, por hacerme feliz y ser mi razón para seguir luchando.

Agradeço às professoras do Centro de Convivência Infantil (CECI), do Programa de Desenvolvimento e Integração da Criança e do Adolescente (PRODECAD) e da Escola

Estadual Físico Sérgio Pereira Porto, por cuidar e educar a Isa ao longo de 6 anos. À Unicamp, ao pessoal administrativo do DFA e da secretaria da pós-graduação do IFGW.

Finalmente, agradeço ao Ministério da Ciência, Tecnologia e Inovações e Conselho Nacional de Desenvolvimento Científico e Tecnológico – CNPq, pelos dois primeiros meses de bolsas, processo nº 142531/2018-9. À Fundação de Amparo à Pesquisa do Estado de São Paulo (Fapesp) pelo financiamento do doutorado através dos processos nº 2018/08543-7 e 2020/12480-0.

Abstract

This thesis presents a scanning tunneling microscopy (STM) study of atomically thin materials. We study exfoliated p-doped monolayers of tungsten disulfide (WSe_2) on gold thin film substrates and epitaxial monolayers of hexagonal boron nitride (h-BN) on graphite. We combine STM measurements and related techniques with complementary characterizations employing atomic force microscopy and optical spectroscopy for investigating aspects such as point defects, sample doping, sample-substrate coupling, and their impact on the electronic and optical properties of the material.

Firstly, we present the design and implementation of a new light collection device based on an off-axis parabolic mirror with 72% of collection efficiency to perform luminescence experiments in STM. The optical device can be used as an optical accessory of an adapted Pan STM, able to operate at low temperature and ultra-high vacuum (UHV) conditions without affecting the performance of the microscope. The potential of the device is demonstrated by performing STM-luminescence as well as *in-situ* Photoluminescence (PL)/Raman measurements on several systems.

Secondly, we report the observation of excitons electrically generated on monolayers of TMD onto metallic substrates by using tunneling electrons in an STM. The as-transferred samples of WSe_2 monolayers are optically active due to an interfacial water layer that decouples the material from the underlying substrate. The intrinsic sample-substrate decoupling allows exciting the local electroluminescence of the sample via STM-induced light emission (STM-LE) in ambient conditions. The presence of the interfacial water layer is due to air moisture, and it is a consequence of the sample preparation method. The STM-LE and PL spectra are similar, indicating that the luminescence is due to the recombination of neutral and charged (trions) excitons. The trion to exciton ratio is controlled with the tunneling current setpoint. Excitons can only be generated at sample bias voltage above 2.0 V, i.e., with tunneling electrons at energies equal to or above the electronic band gap of monolayer WSe_2. STM images and scanning tunneling spectroscopy (STS) measurements under UHV conditions demonstrated the presence of intrinsic point defects and confirmed the p-type doping of the sample. The proposed STM-LE excitation mechanism is the elastic tunneling of electrons and the direct injection of carriers on the conduction band of the semiconductor.

Finally, we present the measurement of the electronic band gap and the exciton binding energy of monolayer h-BN. The sharp interface in the van der Waals heterostructure of h-BN on graphite enables the employ of low-temperature STS measurements to determine the electronic band gap. We demonstrate that defect-free monolayer h-BN on graphite has an electronic band gap of 6.8 ± 0.2 eV and an exciton binding energy of 0.7 ± 0.2 eV. These values are about 1 eV lower than predicted for a free-standing monolayer. In addition, in some regions of the monolayer h-BN, we identified point defects by STM imaging, which have intragap electronic levels around 2.0 eV below the Fermi level. Moreover, STM-Cathodoluminescence (STM-CL) and PL show complex spectra typically associated with intragap states related to carbon point defects.

Resumo

Esta tese apresenta um estudo via microscopía de tunelamento com varredura (STM) em materiais atomicamente finos. Estudamos monocamadas exfoliadas de dissulfeto de tungstênio (WSe_2) dopado tipo-p depositadas em substratos de filmes finos de ouro, e monocamadas epitaxiais de nitruro de boro hexagonal (h-BN) em grafite. Combinamos medidas de STM e técnicas associadas com caracterizações complementares empregando microscopia de força atômica e espectroscopia óptica, para investigar aspectos como defeitos pontuais, dopagem da amostra, acoplamento amostra-substrato e seu impacto nas propriedades eletrônica e óptica do material.

Em primeiro lugar, apresentamos o desenho e a implementação de um novo dispositivo óptico baseado em um espelho parabólico fora do eixo com 72% de eficiência de coleção de luz, para realizar experimentos de luminescência em STM. O dispositivo pode ser usado como acessório óptico de um microscópio STM adaptado que opera em condições de baixa temperatura e em ultra alto vácuo (UHV), sem afetar o desempenho do microscópio. O potencial do dispositivo é demonstrado através da realização de medidas de luminescência em STM e fotoluminescência (PL)/Raman in situ em vários sistemas.

Em segundo lugar, reportamos a observação de excitons gerados eletricamente em monocamadas de TMDs sobre substratos metálicos, usando elétrons de tunelamento em um STM. As amostras transferidas de monocamadas WSe_2 são opticamente ativas devido a uma camada interfacial de água que desacopla o material do substrato subjacente. O desacoplamento intrínseco amostra-substrato permite excitar a eletroluminescência local da amostra via emissão de luz induzida por STM (STM-LE) em condições normais de temperatura e pressão. A presença da camada de água interfacial se deve à umidade do ar e é uma consequência do método de preparo da amostra. Os espectros STM-LE assemelha-se aos espectros PL, indicando que a luminescência é devido à recombinação de excitons neutros e carregados (tríons). A razão de trion para exciton é controlada com a corrente de tunelamento. Os excitons só podem ser gerados com tensão de tunelamento acima de 2.0 V, ou seja, com elétrons de tunelamento em energias iguais ou acima do band gap eletrônico da monocamada WSe_2. Imagens de STM e medidas de espectroscopia de tunelamento de elétrons (STS) em condições de UHV demonstraram a presença de defeitos pontuais intrínsecos e confirmaram a dopagem tipo-p da amostra. O mecanismo de excitação via STM-LE proposto é o tunelamento elástico de elétrons e a injeção direta de portadores na banda de condução do semicondutor.

Finalmente, apresentamos a medida do band gap eletrônico e da energia de ligação do éxciton em uma monocamada de h-BN. A interface abrupta, na heteroestrutura de van der Waals de h-BN em grafite permite utilizar medidas de STS a baixa temperaturas para determinar o band gap eletrônico. Demonstramos que monocamadas de h-BN livre de defeitos tem um gap eletrônico de 6,8±0,2 eV e uma energia de ligação de éxciton de 0,7±0,2 eV. Esses valores são cerca de 1 eV mais baixos do que o previsto para uma monocamada isolada (sem substrato). Além disso, identificamos defeitos pontuais por imagens de STM, que possuem níveis eletrônicos intragap em torno de 2,0 eV abaixo do nível de Fermi. Medidas de catodoluminescência em STM (STM-CL) e PL mostram espectros complexos tipicamente associados a estados intragap relacionados a defeitos pontuais de carbono no h-BN.

Contents

Chapter 1

Introduction and motivation

Materials with a crystal structure conformed by the stacking of van der Waals (vdW) bounded layers can be separated into stable units of atomically thin layers. These atomically thin layers are considered two-dimensional (2D) materials. Graphene (Gr), a single layer of carbon atoms in a hexagonal lattice, is likely the most explored 2D material in the last years. The demonstration of the Gr isolation in 2004, and the observation of its promising electronic and mechanical properties [1–3], for instance, gave rise to a growing interest in exploring other 2D materials like transition metal dichalcogenides (TMDs), hexagonal boron nitride (h-BN), black phosphorus (BP), among others [4].

In particular, 2H-TMDs, like molybdenum disulfide (MoS_2) or tungsten diselenide (WSe_2), are materials that in the monolayer limit are direct band gap semiconductors with a strong luminescence dominated by excitonic effects [5, 6]. The optical properties of these kinds of materials are understood in terms of a complex exciton dynamic involving different exciton species such as neutral excitons, trions (charged excitons), bi-excitons, localized/defect-bond excitons, and dark excitons [7, 8]. Such characteristics of TMDs are interesting for investigating many fundamental phenomena related to the physic of excitons in 2D semiconductors [9], besides the considerable interest for applications in optoelectronics and nano-photonics [10, 11]. Another attractive 2D material, from the optical point of view, is h-BN. In contrast to TMDs, h-BN is a wide band gap material with a luminescence characterized by the exciton recombination around 6 eV, which makes it a potential candidate for technological applications in deep ultraviolet (DUV) light sources [12].

The atomically thin character of 2D materials makes them extremely sensitive to different factors such as variation of the sample dielectric environment and local spatial variation of such environment due to the sample-substrate coupling [13–16], strain/stress gradients [17–20], or Moiré potentials [21–23]. For instance, the electronic and optical properties of TMDs and h-BN monolayers can drastically change in systems in which the monolayers are in direct contact with metallic substrates. The strong sample-substrate interaction at the interface leads to a renormalization of the electronic structure and to a total quenching of the intrinsic luminescence. This effect is observed typically in samples grown by epitaxial methods [13, 24]. However, in samples mechanically transferred onto metallic supports, the impact of the substrate is not clear since metallic substrates can produce quenching [25] or not [15] on the luminescence of the 2D material. Moreover, the electroluminescence emission observed in some devices based on transferred monolayers of TMDs, shows a spatial variation of the luminescence with most of the light emission localized at one of the device's electrodes [26]. Therefore, the heterogeneity of the sample environment impacts the sample's optical properties and the performance of 2D materials-based devices.

In the case of monolayer h-BN, its successful application in the design of light-emitting devices, for instance, depends on the understanding of its electronic and optical properties. Therefore, it is relevant to know the values of fundamental constants such as the electronic band gap and the exciton binding energy. However, due to its wide band gap and the technical challenge regarding accomplishing experiments of DUV optical spectroscopy, many of these properties of h-BN remain unresolved. Mainly, the direct or indirect character of the electronic band gap has been under discussion for several years, and the value of the electronic band gap is still an open question.

Angle-Resolved Photoemission Spectroscopy (ARPES) has been used to investigate the band structure of bulk, and monolayer h-BN [27, 28]. However, ARPES provides information only about the electronic structure of the valence band (filled states). Consequently, the description of the whole band structure of h-BN is missing. Scanning tunneling spectroscopy (STS) can be employed to probe both filled and empty states in h-BN and measure the electronic band gap. Nonetheless, STS had not provided a precise measurement of the h-BN electronic band gap. Most of the h-BN samples explored by STS consisted of h-BN monolayers grown on metallic surfaces as Ru(0001) or Rh(111) [29, 30]. Hence, the strong interaction at the sample-substrate interface in those systems represents a relevant issue for employing the STS technique to determine the electronic band gap. Usually, the monolayers under investigation presented metallic characteristics, and the STS results provided reduced values of the electronic band gap.

Atomically thin materials also have the property that their surface is naturally passivated without dangling bonds. Hence, it is easy integrating different 2D materials to construct vertical heterostructures where the vdW interactions bond layers with different lattice constants [31, 32]. Vertical vdW heterostructures combing different TMD monolayers have been used for generating interlayer excitons with emissions in the infrared range [33, 34]. The weak sample-substrate interaction in vdW heterostructures allows the sample to preserve most of its electronic and optical properties, in contrast to samples on metals. The vdW interaction between a single monolayer h-BN epitaxially grown on graphite allowed Elias *et al.* [35] to demonstrate in 2019 that a monolayer h-BN is a direct band gap material, with an optical band gap of 6.1 eV. This finding suggests that monolayer h-BN on graphite might be ideal for measuring the h-BN electronic band gap employing STS.

Additionally, the luminescence properties, in both monolayers of TMD a h-BN, are modified by the presence of impurities [36], adsorbates [37], and defects [38–40]. Several recent works have demonstrated that point defects can help to enhance the light emission in the monolayers of TMDs [41, 42], but also the emission of defect-bound excitons at low temperatures results in single-photon emission in the visible spectral range [43, 44]. In the case of h-BN samples, point defects introduce intragap states, and optical transitions between the defect's electronic levels lead to single-photon emission in the visible and ultraviolet range at room temperature [39, 45, 46]. Single-photon emission sources are essential elements for application in quantum optics and quantum computing [47].

Although the chemical composition of TMDs and h-BN is relatively simple, the optical spectra involving emissions related to point defects give no information or a definitive answer about which specific defects are responsible for enhancing the luminescence and which ones participate in single-photon emission processes. Then, we can see that if it were possible to identify the nature of a specific point defect and control its density, we might think about designing and tailoring the properties of 2D materials via defects control to enhance them for new functionalities useful for some applications. The investigation of individual point defects in atomically thin materials is a challenge because it requires the implementation of experimental techniques with the sensitivity and selectivity necessary for measuring their structure together with their electronic and optical properties at the relevant spatial scale; this means at the atomic or nanometer scale.

Scanning tunneling microscopy (STM) is an experimental technique able to probe the atomic structure and electronic properties of sample surfaces with a high spatial resolution (atomic resolution under some conditions) and in real space. Furthermore, the tunneling electrons in STM can be used as a nanoscale excitation source to investigate the optical properties of the system under study. In STM-induced light emission (STM-LE), the sample is locally and electrically excited at the STM tip position [48]. Studying the optical properties of atomically thin materials at the nanometer scale employing STM-LE can provide fundamental insights into their complex excitonic emissions and how these emissions can be affected by nanoscale variation of the surrounding sample environment, such as sample-substrate interface interaction, point defects, moiré potentials, among others. Moreover, in STM-LE, we investigate the electroluminescence response of the sample, meaning that we have the opportunity of exploring and combining electrical and optical properties of the 2D materials, leading to optoelectronic applications for practical devices.

In contrast to photoluminescence (PL), the investigation of excitons by STM-LE has the following challenges: i) for the exciton formation, both electrons and holes need to be present in the sample at the same time, which means that if one charge is injected locally by the STM tip, the opposite charge must come from the substrate or be present in the sample (doped sample). ii) The charge carrier lifetime needs to be long enough to meet the oppositely charged partner. iii) Samples in direct contact with metallic substrates can present hybridized electronic states at the interface, leading to fast charge transfer to the metal. Then, direct contact or proximity of the sample to the metallic tip or substrate must be avoided. Otherwise, the intrinsic excitonic luminescence will be quenched. In many cases, an insulating decoupling layer between the emitter and the metallic electrode is necessary to preserve the luminescence of the sample [48].

STM-LE applied to the study of TMD monolayers was reported for the first time by N. Krane *et al.* in 2016 [24]. They used the tunneling current in an STM operated at 4 K to excite the electroluminescence of monolayer MoS_2 epitaxially grown on Au(111) surface. Nonetheless, the direct contact between the TMD and the metallic substrate produces a quenching of the excitonic luminescence. Then, what is observed is the photon emission generated by the radiative decaying of plasmonic modes localized in the tunneling junction between the gold tip and the metallic substrate. The first observation of the excitonic emission by STM-LE was reported by Pommier, *et al.* in 2019 [49]. In this publication, excitonic luminescence resulting from the electrical generation of excitons using an STM under ambient conditions is demonstrated in a monolayer of $MoSe_2$ deposited on transparent conducting substrates (indium-thin-oxide, ITO). However, a direct correlation between the sample doping induced by intrinsic point defects and the excitonic electroluminescence response is missing.

In h-BN, STM and high-resolution transmission electron microscopy [50, 51] have been employed for investigating individual point defects. Despite these efforts, a clear correlation between the point defect electronic levels inside the wide band gap and the light emission related to defects has not been established yet. Few-layer h-BN samples have been investigated optically through Cathodoluminescence (CL) measurements. However, CL only resolves DUV emissions in samples with six layers of thickness [52]. Consequently, besides the electronic band gap value and the exciton binding energy remaining unaddressed experimentally, the CL emission in monolayer has not been detected so far, which is essential for understanding how the DUV optical response in h-BN changes with the number of layers.

In this thesis, we present the investigation of the morphological, electronic, and optical properties of the atomically thin materials WSe_2 and h-BN. This work aims to probe the properties of 2D materials at the nanometer scale by using the imaging and spectroscopic capabilities of STM and the possibility of performing local electroluminescence using tunneling electrons and CL. Part of the Ph.D. project involved designing and implementing a new light injection/collection system based on an off-axis parabolic mirror to perform luminescence experiments inside a commercial scanning tunneling microscope.

The main objectives of this thesis are:

- To develop a high-performance light collecting device able to record the luminescence signals we are interested in (exciton and defect-related emissions), and at the same time compatible with a low temperature and ultra-high vacuum STM.
- To investigate point defects properties and their role on the electronic and optical properties of the 2D materials.
- To investigate the sample-substrate coupling between a monolayer of a 2D material and its underlying support and how this coupling can affect the electronic and optical properties of the material.

Organization of the manuscript.

This manuscript contains the following chapters:

Chapter 1 corresponds to the present introduction.

Chapter 2 introduces the morphological, electronic, and optical properties of semiconducting TMDs and h-BN.

Chapter 3 describes the fundamentals of STM and Luminescence spectroscopy in STM. The chapter discusses the working principle and operation modes of an STM for acquiring images and spectroscopic data and also the excitation and light emission mechanisms in STM luminescence experiments. Additionally, in this chapter, we describe the experimental setup, sample preparation and methods.

Chapter 4 presents our published work on designing and implementing a new optical accessory for performing different luminescence experiments in a commercial STM that operates under ultra-high vacuum conditions and at low temperatures.

Chapter 5 contains our published work investigating the morphological electronic and optical properties of exfoliated WSe_2 monolayers on gold support using tunneling electrons in STM.

Chapter 6 presents the published work investigating the morphological and fundamental electronic and optical properties of a single layer of epitaxial h-BN on graphite.

In **Chapter 7**, we present the general conclusions of this work and some perspectives.

Chapter 2

2D materials: semiconducting transition metal dichalcogenides and hexagonal boron nitride

2.1 Semiconducting transition metal dichalcogenides

2.1.1 Introduction

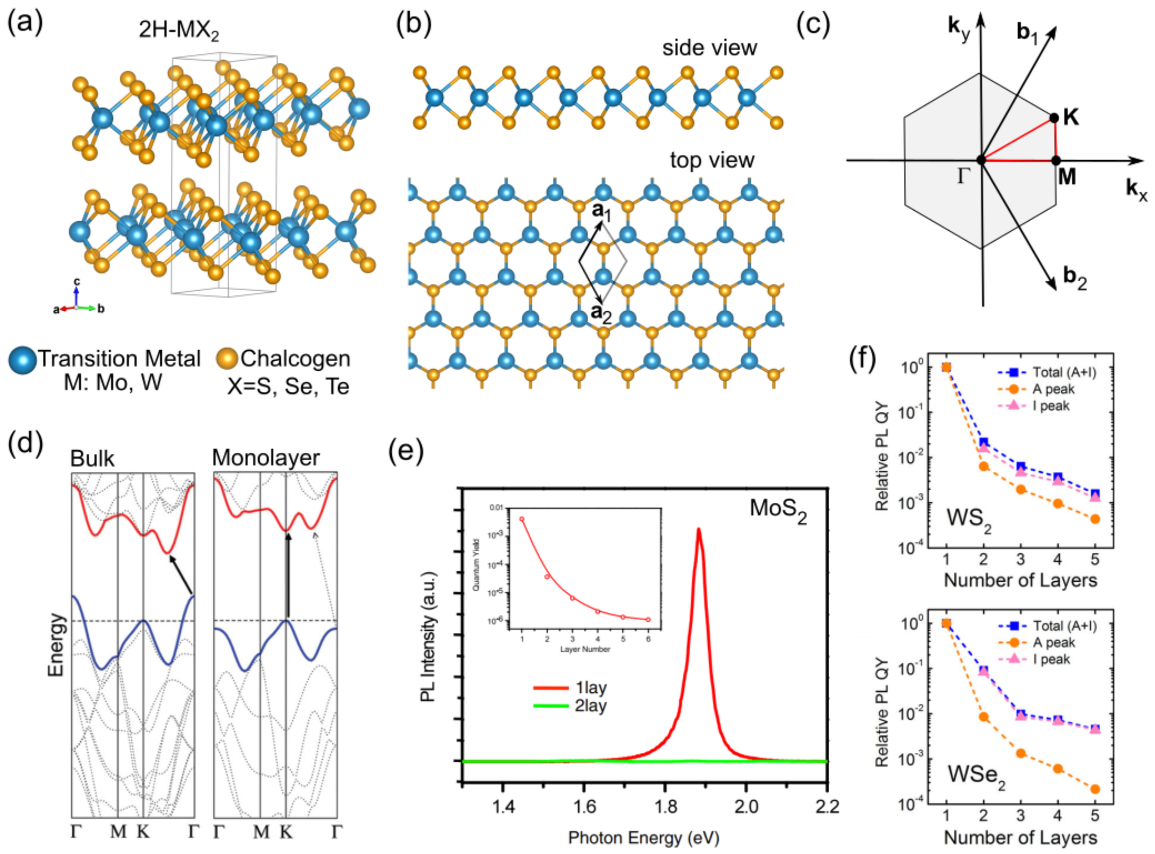

Figure 2.1: (a) 2H-MX$_2$ structure of semiconducting TMDs. The number of atoms in the unit cell was increased for the best visualization of the layered structure. (b) Side view and top view of a single monolayer of TMD. The unit cell is indicated by the vectors $\mathbf{a}_1$ and $\mathbf{a}_2$ in the top view. (c) Representation in two dimensions of the first Brillouin zone. (d) Electronic band gap crossover in the transition from bulk to monolayer. The black arrow indicates the electronic band gap. Adapted from [53]. (e) Room temperature photoluminescence (PL) and quantum yield (QY) of monolayer MoS$_2$. Taken from [5]. (f) Room temperature PL QY of WS$_2$ and WSe$_2$ monolayers. Adapted from [54].

Transition metal dichalcogenides (TMDs) are layered materials with chemical composition MX$_2$, where M corresponds to a transition metal element and X to a chalcogen (like sulfur (S), selenium (Se), and tellurium (Te)). There are many different TMD materials, and depending on the combination between the transition metal and the chalcogen elements, these can behave as semiconductors, conductors, superconductors, or insulators [6, 55]. We are interested in the study of semiconducting TMDs like MoSe$_2$, WSe$_2$, and WS$_2$. These are known as Group-6 TMDs because they contain transition metal elements from group 6 in the periodic table [56]. The most stable crystal structure of semiconducting TMDs is depicted in Figure 2.1(a), which is called the 2H-MX$_2$ structure since it contains two MX$_2$ layers per hexagonal unit cell. From Figures 2.1(a) and 2.1(b), we can note that every single layer of MX$_2$ is constituted of three atomic layers covalently bonded in the sequence X-M-X. The top view of the monolayer shows a honeycomb structure similar to the graphene structure but with the difference that here M and X atoms are not in the same atomic plane. Inside the unit

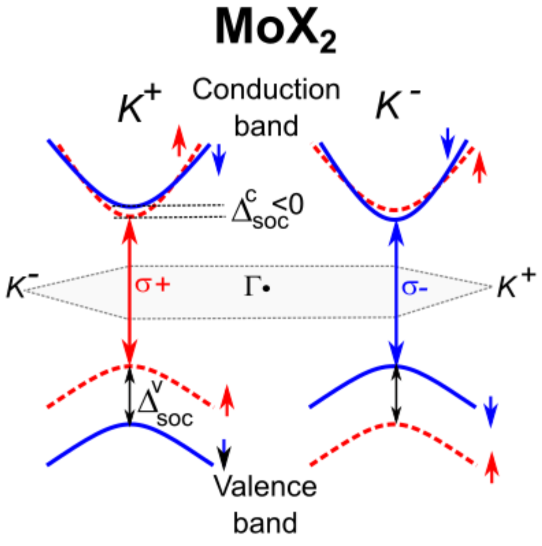

Figure 2.2: K-valleys of Mo-based (MoX_2) and W-based (WX_2) TMDs. The valence band and conduction band splitting due to the spin-orbit interaction are illustrated in the figure.

cell, the layers interact through van der Waals forces, which is a weak interaction that makes possible the exfoliation of a single crystal of TMD to reduce the number of layers until it reaches the monolayer limit. The hexagonal unit cell in the reciprocal space that define the first Brillouin zone in two dimensions is shown in Figure 2.1(c).

In their bulk form, all 2H-MX_2 TMDs have an indirect electronic band gap, with a valence band maximum (VBM) at the Γ point of the first Brillouin zone and a conduction band minimum (CBM) in the middle point between the Γ and K points, see Figure 2.1(d). In monolayers, the electronic band gap becomes direct at the K point. The band gap crossover from the indirect-to-direct in the K point is put in evidence by a strong luminescence observed in monolayers [5, 53, 54]. In Figure 2.1(e), we can see how strong is the photoluminescence (PL) emission in monolayer MoS_2 when compared with the emission of a bilayer. The inset figure shows that the quantum yield (QY) of MoS_2 increases by four orders of magnitude when the thickness of the material goes from bulk to a single monolayer. The same is observed in other TMDs, like WS_2 and WSe_2. In this case, the evolution of the QY with the number of layers is shown in Figure 2.1(f). Note that at room temperature (RT), the QY in W-based monolayers is two orders of magnitude higher than in Mo-based monolayers.

2.1.2 Direct band gap and spin-orbit coupling

Besides the band gap crossover described above, effects due to spin-orbit coupling (SOC) produce a splitting in the valence band (VB), and the conduction band (CB) [8, 57, 58]. Figure 2.2 summarizes some of the results found in the literature for the electronic band structure in monolayers of TMDs considering the SOC. The figure illustrates that the splitting in the CB band has different signs for MoX_2 and WX_2 monolayers. The energy values of the band splitting are shown in Table 2.1. On the other hand, it is important to point out that in monolayers, the K points in the Brillouin zone are divided into two non-equivalent groups known as the K^+ and K^- points (this is a consequence of the lack of inversion symmetry in monolayers). The band edges at these points are usually referred to as K^+ and K^- valleys. Additionally, we can note that direct optical transitions at the K points can be valley selective because it is possible to use circularly polarized light, σ^+ and σ^-, to excite optical transitions only at the K^+ and K^- valleys, respectively [8, 56].

Table 2.1: Values of some electronic and optical properties of semiconducting TMDs. Taken from [59].

Property	**Symbol**	**MoSe$_2$**	**MoS$_2$**	**WSe$_2$**	**WS$_2$**
Electronic band-gap (eV)	E_g (bulk)	1.09	1.29	1.20	1.35
	Eg (monolayer)	2.2	2.5	2.1	2.7
Exciton binding energy (eV)	E_b (monolayer)	0.6	0.6	0.5	0.7
CB spin-orbit splitting (eV)	Δ^C_{SOC}	-0.021	-0.003	0.036	0.029
VB spin-orbit splitting (eV)	Δ^V_{SOC}	0.180	0.160	0.430	0.380
Monolayer, PL peak position (eV)	A exciton	1.58	1.92	1.65	2.02
Monolayer, absorption peak position (eV)	B exciton	1.75	2.03	2.09	2.36

2.1.3 Excitons

From the experimental point of view, one way of obtaining information about the electronic structure of materials is by exciting them with light and analyzing their optical response. In the case of semiconducting TMD monolayers, the optical properties are dominated by exciton transitions. Thus, for understanding the light emission properties of these materials, it is convenient to start with the definition of what an exciton is and how it behaves in atomically thin materials. Figure 2.3(a) illustrates the process of optical absorption by free carries, in which an electron initially in the VB absorbs the energy of an incident photon. After that, this electron is promoted to the CB, leaving an empty electron state in the VB called "hole". Note that this optical absorption process is possible only if the incident photon's energy is equal to or larger than the electronic band gap, E_g. This last is defined as the energy difference between the VBM and CBM. The electron-hole pair at the band edges can recombine via direct band-to-band transition with the emission of a photon at the energy of the electronic band gap. The attractive electrostatic interaction between electron and hole pairs created by optical absorption leads to the formation of *excitons*. An exciton is a bound electron-hole pair that can recombine radiatively [60, 61].

As the exciton is a two-particle state, it should be represented in the k-space in a two-particle picture, such as shown in Figure 2.3(b). The exciton momentum is given by $\mathbf{K} = \mathbf{k}_e + \mathbf{k}_h$ and it transnational mass is $M = m_e + m_h$, with $\mathbf{k}_e$ ($\mathbf{k}_h$) and m_e (m_h) the electron (hole) momentum and mass, respectively. An exciton can be treated as a hydrogen-like system with discrete energy levels E_n, with $n = 1, 2, 3...$, and the dispersion relation for any excitonic state can be expressed as $E_n = E_g - E_b(n) + \hbar^2 K^2/2M$, where $E_b(n)$ is the binding energy of the nth excitonic state. The energy states of an exciton are represented in Figure 2.3(b) for bound states with $n = 1$ and 2 and the continuum. An exciton transition from the ground state to the continuum is equivalent to an optical transition by free carriers. In direct band gap semiconductors, we observe direct exciton transitions at $\mathbf{K}$=0, and the exciton energy is given by:

$$E_n = E_g - E_b(n), \tag{2.1}$$

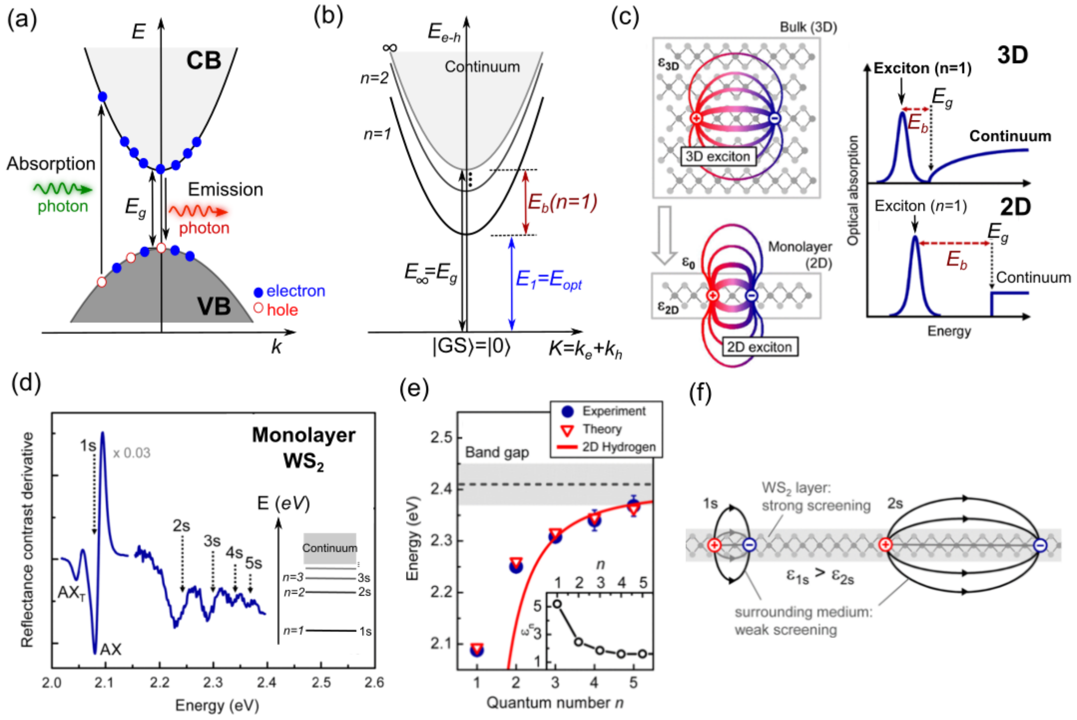

Figure 2.3: (a) Free carrier optical absorption and band-to-band radiative recombination. (b) Two-particle picture for the exciton representation. The excitonic states are shown as discrete parabolic states. E_{opt} is the optical band gap defined as the energy of the fundamental exciton state at $\mathbf{K}=0$ measured from the ground-state ($|GS\rangle$), and E_b corresponds to it exciton binding energy. The electronic band gap, E_g, is defined as the energy difference between $|GS\rangle$ and the continuum. (c) Left side: illustration of excitons in real space for bulk (3D) and monolayer (2D) TMDs. Right side: expected optical absorption spectrum in each system. (d) Reflectance spectrum of monolayer WS_2, the excitonic levels are labeled by their respective quantum numbers; these are illustrated in the energy diagram in the inset. (e) Energies of exciton levels are experimentally and theoretically obtained. The red curve corresponds to the fitting using the 2D hydrogen-like model for Wannier excitons. The inset plot corresponds to the effective dielectric constant calculated for the nth exciton. (f) Illustration of $1s$ and $2s$ excitonic states in the presence of a non-uniform environment. Figures (c)-(f) are adapted from [62].

Hence, any photon with energy equal to or larger than E_n can create an electron-hole pair, and an exciton can be formed. The minimum energy required to create an electron-hole pair corresponds to the lowest exciton energy, $E_1 = E_{opt}$, which is called optical gap or optical band gap. In practice, we expect to observe a set of absorption lines at energies E_n below the energy E_g, in optical absorption spectra of samples with excitonic transitions. Moreover, the electron-hole pair forming an exciton can recombine radiatively. Then, PL measurements show spectra with a strong emission peak centered at the energy position of the exciton ground-state ($n = 1$), i. e., at $E_1 = E_{opt}$.

An important parameter to be considered in the measurements of excitonic transitions in semiconducting samples is the exciton binding energy, because this quantity defines the exciton stability at a given temperature. By solving the Schrödinger equation for an electron-hole pair interacting through a potential $V(r) = e^2/\varepsilon r$, with e being the fundamental electron charge, ε the effective dielectric constant of the medium and $r = |\mathbf{r}_e - \mathbf{r}_h|$ the relative electron-hole distance, we can find that the exciton binding energy for bulk semiconductors (three-dimensional, 3D, systems) is given by:

$$E_b^{3D}(n) = 13.6\left(\frac{\mu}{m_e\varepsilon^2}\right)\frac{1}{n^2}\ eV, \tag{2.2}$$

where $n = 1.2, 3...$ is the principal quantum number for the excitonic states, and $\mu = m_e m_h/(m_e + m_h)$ is the reduced mass of the exciton. In two-dimensional (2D) systems, like semiconducting quantum wells, the hydrogen-like model for an electron-hole pair in the potential $V(r) = e^2/\varepsilon r + V_{\text{conf}}$ where V_{conf} is the confinement potential, gives an exciton binding energy of:

$$E_b^{2D}(n) = 13.6\left(\frac{\mu}{m_e\varepsilon^2}\right)\frac{1}{(n-1/2)^2}\ eV, \tag{2.3}$$

note that in this case, the exciton binding energy varies as $1/(n-1/2)^2$ instead of $1/n^2$. Therefore if we take the fundamental exciton state ($n = 1$), we can see that $E_b^{2D} = 4E_b^{3D}$. In general, $E_b^{3D} < 30$ meV, thus at RT it is hard to observe excitonic effects because the thermal energy, $k_BT \approx 25$ meV, is enough to dissociate the formed excitons. Then, excitons are only measured at cryogenic temperatures in bulk semiconductors. The fact that the binding energy of the exciton ground-state is four times larger in 2D than in 3D systems makes possible the detection of exciton transitions even at RT in systems like quantum wells where the E_b^{2D} may be of some tens of meV [8, 60, 61].

In atomically thin materials, excitonic effects are enhanced due to the reduced dimensionality and changes in the dielectric environment. Figure 2.3(c) illustrates that in the transition from bulk to monolayer, the exciton is confined in the monolayer plane, and the dielectric screening is reduced. In monolayer, we can see that the electric field lines that keep together the electron-hole pair in an exciton begin to extend outside the sample. This effect enhances the electrostatic interaction, and the exciton binding energy increases. The binding energy of excitons in monolayers of TMDs may be of some hundreds of meV, meaning that excitons in these kinds of materials are very stable and dominate their optical properties at room and low temperatures [8, 62]. On the right side of Figure 2.3(c), the expected optical absorption spectra for 3D and 2D materials are schematically represented. The absorption is dominated by the fundamental excitonic peak ($n = 1$), observed below the absorption to the continuum. The optical absorption to the continuum is proportional to the density of states of the system. In 3D, it varies as a function of the root-square of the energy, and in 2D, it is constant (flat). The figure also clarifies the difference between the optical gap and the electronic band gap. The optical band gap is given by the energy position of the excitonic peak, and this can be related to the electronic band gap (E_g) through the exciton binding energy (E_b) using the expression:

$$E_{opt} = E_g - E_b, \tag{2.4}$$

which, in essence, is the same equation (2.1) for the specific cases of $n = 1$. In the transition from bulk to monolayer it is expected that both E_g and E_b increase.

The energy of the ground state and some excited excitonic states can be measured by reflectance spectroscopy. This was done by Chernikov, *et al.* [62] in monolayer WS_2. Some of the results are presented in Figures 2.3(d) and 2.3(e). The exciton ground-state and the first four excited excitonic states, labeled as $1s, 2s, 3s, 4s$, and $5s$ in a Rydberg series for values of n from 1 to 5, are shown in the spectrum of Figure 2.3(d). We can observe the strong $1s$ transition at 2.09 eV. The excited states are at higher energies with a progressive reduction of the peak intensity, meaning that the coupling to the light of the excited states is weak compared with the fundamental exciton transition. The energy position for each excitonic state is plotted in Figure 2.3(e). We can note that only the $n = 3 - 5$ states follow the 2D hydrogen-like model for the excitonic states (given by equation (2.3)). The non-hydrogenic behavior of the excitonic levels with $n = 1, 2$ is due to the fact that the dielectric environment around the exciton is nonuniform, as shown in Figure 2.3(f). The strength and the form of the effective electrostatic (Coulomb) interaction between the electron-hole pair forming an exciton are modified by the dielectric properties of the environment, i. e., by the dielectric constant of the monolayer and the surrounding environment. The effective dielectric constant felt by the nth exciton is shown in the inset of Figue 2.3(e). Note that it decreases when increasing n. For $n \geq 3$, the effective dielectric constant is roughly uniform, and the hydrogen model becomes applicable. In general, the excitonic levels in a monolayer can be determined by solving the Schrödinger equation for the electron-hole pair in a potential:

$$V(r) = -\frac{\pi e}{2r_0}\left[H_0\left(\frac{r}{r_0}\right) + Y_0\left(\frac{r}{r_0}\right)\right], \tag{2.5}$$

with H_0 and Y_0 being the Struve and Bessel functions, respectively. Equation (2.5) describes the interaction of the electron hole-pair within a 2D thin dielectric continuum, where r is the relative electron-hole distance and r_0 is a crossover term that represents the screening length, which for the large electron-hole distance it behaves like a Coulomb interaction, $1/r$, and for small separation, this is modeled as $\log(r)$. The theoretical exciton states calculated by this nonhydrigenic model are plotted in Figure 2.3(e) as red triangles, which are in agreement with the experimental data (blue points). It is worth noting that it is possible to determine a value for the ground-state exciton binding energy from the data. From the fitting of the hydrogenic states, an electronic band gap of $(2.41 \pm 0,04)$ eV is obtained. Combining this value with the energy transition for the $1s$ exciton, we will find using the equation (2.4), that the exciton binding energy is of (0.320 ± 0.040) eV.

Absorption and emission of light

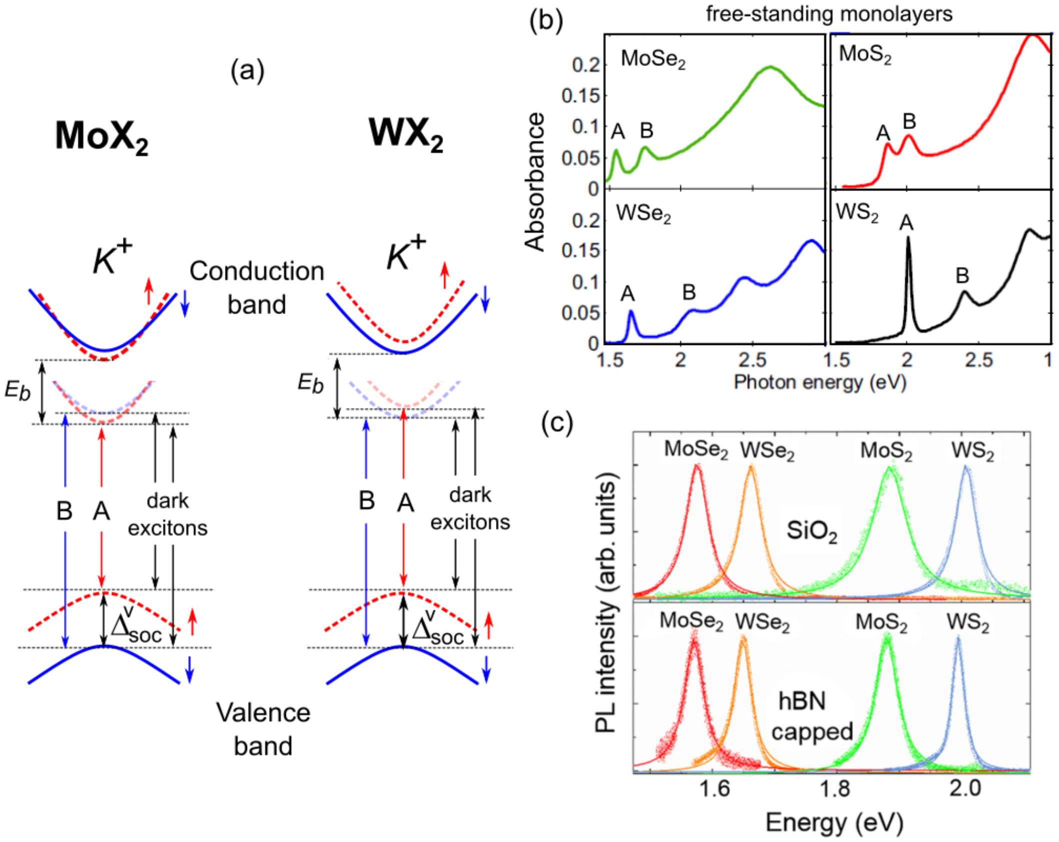

Figure 2.4: (a) K^+ valley illustrating the spin-orbit splitting in the CB, VB, and the exciton ground-states in MoX_2 and WX_2 monolayers. The bright A and B excitons conserve the spin state while in dark excitons there is not spin conservation. (b) Room temperature absorbance spectra of some free-standing monolayers of TMDs, Adapted from [63]. (c) room temperature photoluminescence (PL) spectra of monolayer of TMDs on SiO_2 substrates and h-BN (hexagonal boron nitride) capped monolayers. Adapted from [64]

The light absorption and emission spectra observed at RT in monolayers of TMDs can be interpreted in terms of the optical transitions shown in the band diagrams in Figure 2.4(a). Here we consider the K^+ valley for MoX_2 and WX_2 monolayers. However, the same description can be done for the K^- valley. Although we know that it only makes sense to represent the excitonic states in a two-particle picture, it is convenient to show the excitonic levels in a one-particle picture to clarify the effect of the spin-orbit splitting on the energy levels. The exciton ground-state splits into two spin-states similar to the spin-orbit splitting in the CB. This effect gives rise to different excitonic transitions for the exciton ground-state. Excitonic transitions with conservation of the spin are called "bright excitons", and these are divided into A-excitons and B-excitons, depending on the spin orientation of the states involved in the transition. Excitons with nonconservation of the spin state are known as "dark excitons" [8, 56, 65]. The possible bright and dark excitonic transitions in the K^+ valley are illustrated in the figure. The light emission efficiency of a monolayer of TMDs is determined by its dark or bright character at a given temperature. For instance, at RT, WX_2 TMDs are more efficient for light emission than MoX_2 monolayers. The reason is that at RT, MoX_2 monolayers are considered to be essentially dark because the thermal energy of the electrons in the lowest level of the exciton ground-state is enough for populating the second level, and the dark exciton configuration is favored. This may explain the results in Figures 2.1(e) and 2.1(f), where the QY in monolayers of MoS_2 is lower than in monolayer WS_2.

Figure 2.4(b) shows the absorbance spectra for some free-standing monolayers of TMDs at RT. All the spectra present two well-resolved peaks that correspond to optical absorptions by bright A and B excitons. The spectral shape of the absorbance is preserved in monolayers transferred on fused silica substrates. However, the supported monolayer absorbs 1/3 less than the suspended ones [63]. In contrast to absorption, the PL spectra in Figure 2.4(c) show a single emission peak mainly attributed to the recombination of spin-allowed A excitons. The figure compares the spectra for monolayers supported by silicon dioxide (SiO_2) substrate and monolayers capped with hexagonal boron nitride (h-BN). In both cases, the emission peak's energy position is the same for a given TMD. However, the peak width is reduced in h-BN capped monolayers because the quality of the sample is preserved. The capping with h-BN not only protects the monolayers from their surrounding environment and contaminants but also allows the decoupling of the monolayers from the substrate, avoiding the roughness of the SiO_2 surface being transferred to the material [64]. The energy position for the excitonic transitions observed by optical absorption and PL in some monolayers of TMDs are listed in Table 2.1.

Electronic band gap and exciton binding energy

The ground-state exciton binding energy (E_b) can be obtained from the expression: $E_b = E_g - E_{opt}$. Therefore, if we want to determine E_b experimentally, we should be able to measure both the electronic band gap (E_g) and the optical band gap (E_{opt}). The value of E_{opt} can be obtained directly from the energy transitions of spin-allowed A excitons observed by optical absorption, PL, or reflectance measurements, such as discussed above. However, the direct measurement of E_g by optical spectroscopy is more complicated because the strong coupling to the light of the exciton states may mask the band-to-band transition, which would give us information about E_g. Thus, methods like the explained above for monolayer WS_2 are necessary, where it was mandatory to measure several excited excitonic states by reflectance to determine the electronic band gap from a fitting of the experimental data. Another way of measuring the electronic band gap is by using Scanning tunneling Spectroscopy (STS). STS is a technique used in this work, and it will be explained in detail in chapter 3. In STS, we have a direct measure of the local density of states of the sample and therefore also of E_g, meaning that we could combine STS with optical spectroscopy measurements for the study and characterization of the electronic and excitonic properties of monolayer TMDs. As an example, we show the results in Figure 2.5, reported by Ugeda, *et al.* [66] in the case of monolayer $MoSe_2$ grown on a bilayer of graphene (BLG).

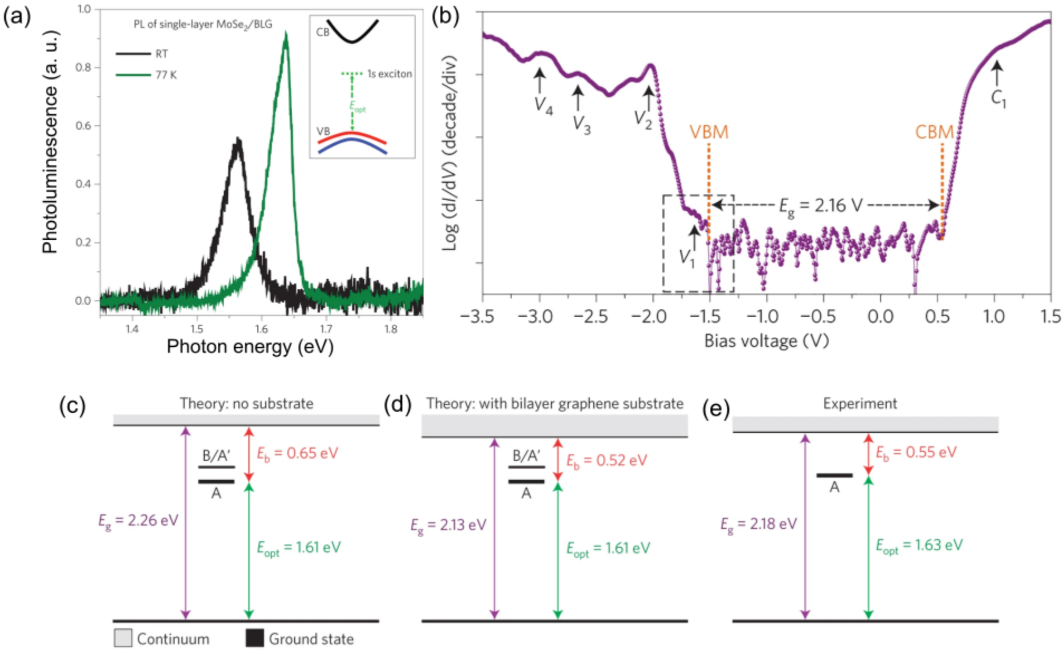

Figure 2.5: (a) PL spectra of monolayer $MoSe_2$ on a BLG substrate and at two different temperatures. The PL peak positions are 1.55 eV and 1.63 eV, for the spectrum at RT and 77 K respectively. (b) STS curve measured at 5 K. The electronic band gap E_g is determined by the VBM and CBM onset. Electronic band gap and optical transition determined theoretically for (c) free-standing monolayer MoS_2 and for (b) monolayer $MoSe_2$ supported by 2L of Gr. (d) Energy levels determined from the experimental data. Adapted from [66].

Figure 2.5(a) shows that E_{opt} is determined by PL spectroscopy. The PL peak at RT is at the energy of (1.55 ± 0.01) eV, which is shifted to (1.63 ± 0.01) eV at the temperature of 77 K. The energy shift is attributed to the thermal reduction of the electronic band gap, which is not expected to change significantly for temperatures bellow 77 K. Then the optical band gap is taken as being of $E_{opt} = (1.63 \pm 0.01)$ eV. Additionally, the electronic structure of the sample was investigated by STS. Figure 2.5(b) shows the STS curve for monolayer $MoSe_2$. The result indicates a VBM and CBM located at (-1.55 ± 0.03) and (0.63 ± 0.02) eV, respectively, these band edge positions are measured concerning the position of the Fermi Level, E_F, $(V_{bias} = 0)$V. Therefore, the value for the electronic band gap is $E_g = E_{CBM} - E_{VBM} = (2.18 \pm 0.04)$ eV. Therefore, the exciton binding energy is of (0.550 ± 0.040) eV, which is of the same order of magnitude as the value determined above for monolayer WS_2.

The calculated and measured values for the electronic band gap, optical band gap, and exciton binding energies are compared in the diagrams for energy levels in Figure 2.5(c)-(e). From Figure 2.5(c)-(d) we can see that the calculated values of 2.26 eV for the electronic band gap and 0.65 eV for the exciton binding energy in free-standing monolayer $MoSe_2$ are reduced to 2.13 eV and 0.52 eV, respectively, when screening effect due to the substrate are taken into account in the monolayer $MoSe_2$ supported by the BLG substrate. In contrast, no change is observed in the value for the optical band gap (1.61 eV). The theoretical values for monolayer $MoSe_2$/BLG are in agreement with the measured values shown in Figure 2.5(e). These results demonstrate that the substrate screening reduces the electronic band gap and the exciton binding energy in supported monolayers without changing the optical band gap. In Table 2.1 are shown values for E_g, and E_b in monolayers of TMDs.

2.1.4 Excitonic species

Up to now, we have discussed the optical properties of monolayer TMDs related to *neutral spin-allowed A and B excitons* and *spin-forbidden excitons.* These transitions have been represented in Figure 2.4. However, there are other exciton complexes, as can be seen in Figure 2.6. For instance, excitons formed by electrons and holes living at different valleys in the k-space with the same spin state define what is called *momentum-forbidden dark excitons*, as illustrated in Figure 2.6(a). Additionally, the presence of defects, impurities, or strain can induce potentials where excitons can be trapped. In this case, excitons are referred to as *localized excitons.* Furthermore, excitons involving the electrostatic interaction between several particles are also possibles, which is the case of *trions* (charged excitons) or *biexcitons* [8, 9, 67–69].

Figure 2.6(b) shows that at RT, the light emission properties of monolayers are dominated by the recombination of spin-allowed bright A excitons (indicated as X^0 in the figure) with a second contribution at lower energy coming from the recombination of trions, X^* [70]. Trions can be positive (X^+) or negative (X^-). However, in the data shown in Figure 2.6(b), the electric charge of trions is unknown, then the symbol * is used to label them. The trion binding energy is given by the energy difference between X^0 and X^*, and in most of the TMDs, it is between 30-40 meV [69–71]. In some cases, it is also possible to observe the recombination of B excitons in the PL spectrum, as in the spectrum for MoS_2. At low temperature (LT), MoX_2 monolayers present the simplest luminescence spectra where in general, the X^0 and X^* peaks are resolved [64, 70, 71]. Nevertheless, the situation is competently different in samples of WX_2 monolayers, in which are observed complex spectra with different excitonic emissions [69]. In Figure 2.6(c) are displayed the LT electroluminescence (EL) spectra for WSe_2 and WS_2 monolayers. Similar spectra are observed by PL [64, 70, 71]. In both spectra, emission peaks related to different excitonic species are measured. We can see emissions associated with neutral excitons X^0, but also luminescence due to the recombination of biexcitons (XX), localized excitons L_{1-3}, and dark excitons (X^D). Additionally, charged excitons are observed, like trions (X^-_{1-2}), charge biexctions (XX^{-1}), and dark trions ($\mathrm{X}^{D\pm}$) [69].

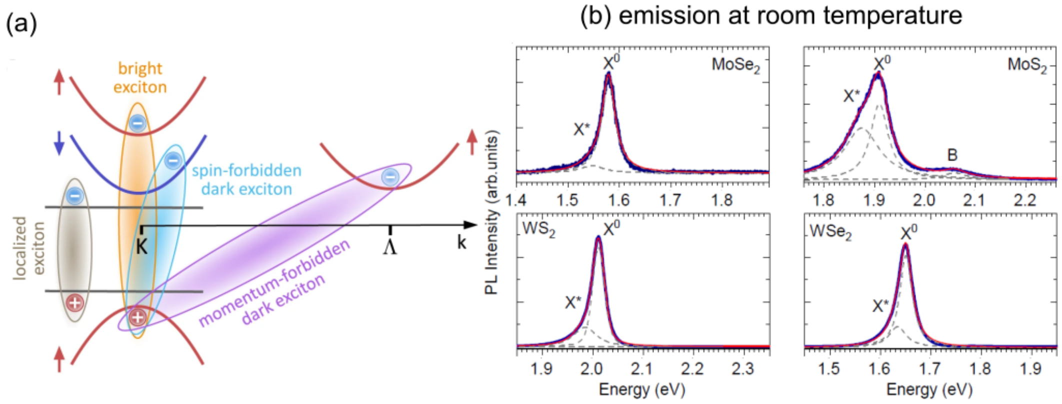

(c) complex emission at low temperature (5K)

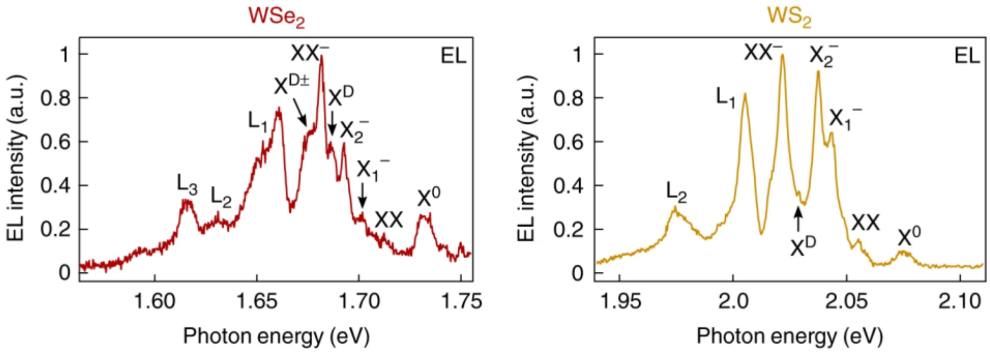

Figure 2.6: (a) Some exciton types in monolayer TMDs. The exciton can be bright due to direct transition at the K point with spin conservation. Electrons and holes with different spin states lead to spin-forbidden dark excitons, similarly, excitons formed by electrons and holes with the same spin states but with the valley at different points of the Brillouin zone are considered momentum-forbidden dark excitons. Localized excitons consist of neutral excitons trapped in defects/impurities- or strain-induced potentials. Adapted from [9]. (b) Luminescence (PL) spectra at RT in some monolayers TMDs. The emission peak is a convolution of the luminescence emitted by the recombination of neutral excitons (X^0) and trions X^*. In particular, the spectrum in monolayer MoS_2 also shows the emission coming from B excitons. Adapted from [70]. (c) Complex low temperature (5K) electroluminescence spectra in WSe_2 and WS_2 monolayers. Adapted from [69].

2.1.5 Point defects and sample doping

Individual point defects in atomically thin materials can be identified by using scanning tunneling microscopy/spectroscopy (STM/STS) [72–74]. In Figure 2.7(a)-(d) are displayed STM images of defective TMD samples. Point defects are observed as bright and dark spots, and the defect density can vary from one scanned region to another. The type of doping introduced by a specific kind of defect can be proved using STS. In Figures 2.7(e)-(i) are shown results reported by Rivera, *et al.* [75] for intrinsic point defects in WSe_2. The STM image in Figure 2.7(e) indicates the presence of both bright and dark point defects, which are individually imaged in Figure 2.7(f) and (g), respectively. The STS curves in Figures 2.7(h) and (i) reveal donor (D) and acceptor (A) midgap states, demonstrating that bright and dark defects induce p-type and n-type samples doping, respectively. Similar results have been reported by Edelberg, *et al.* [76] in $MoSe_2$, some of the results are presented in Figures 2.7(j)-(n). Once again, bright and dark defects are found in STM images, as shown in Figure 2.7(j). Atomically resolved STM images of individual defects are depicted in Figures 2.7(k) and (l). In this case, the bright defect is denoted as -X, indicating this defect is related to Se sites. In contrast,

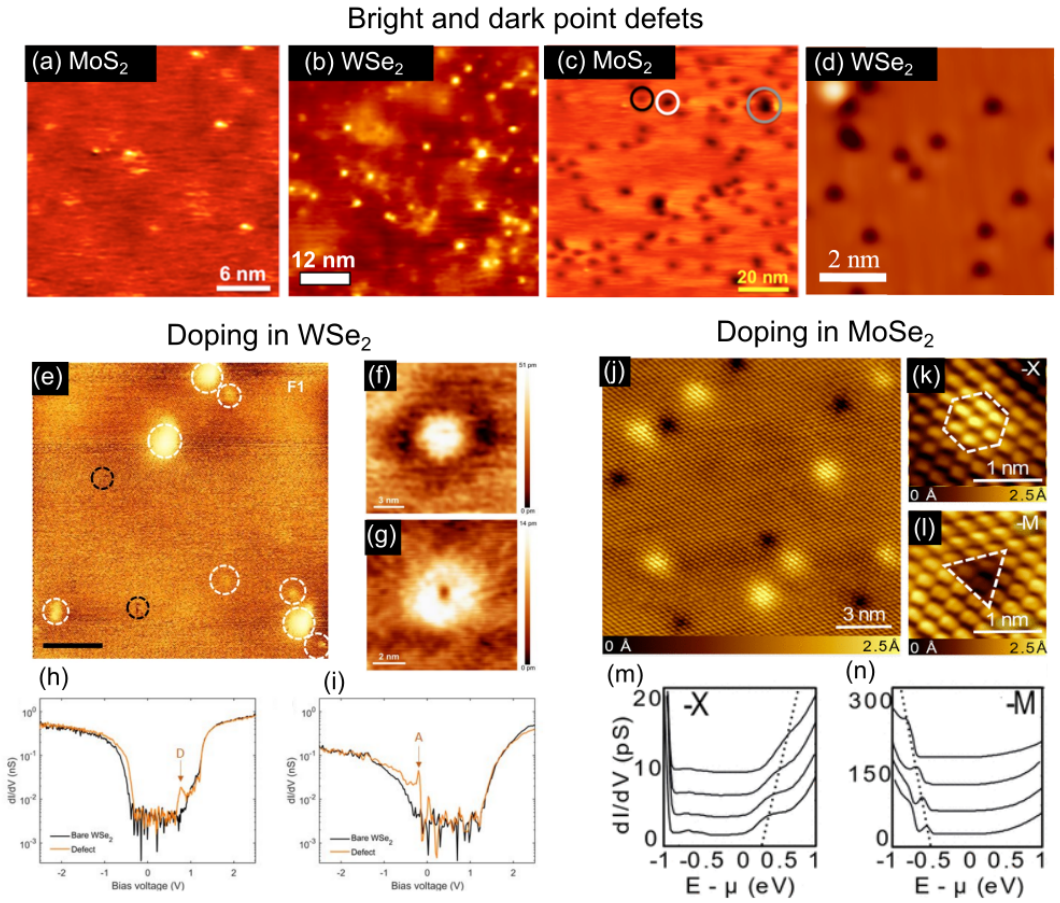

Figure 2.7: STM images revealing bright point defects in (a) MoS$_2$ (adapted from [72]) and (b) WSe$_2$ (adapted from [73]) and dark point defects in (c) MoS$_2$ (adapted from [72]) and (d) WSe$_2$ (adapted from [74]). Characterization of defects in WSe$_2$. Results adapted from [ref]: (e) STM image of the WSe$_2$ surface. The white and black dotted circles indicate bright and dark defects, respectively. The scale bar is 10 nm. (f) STM images of an individual bright defect, (g) STM images of an individual dark defect. STS curves showing the (h) donor, D, and the (i) acceptor, A, states introduced by the bright and dark defects, respectively. The black STS curve acquired in defect-free regions is shown for comparison. Characterization of defects in MSe$_2$. Results adapted from [75]: (j) STM image of the MoSe$_2$ surface. Both dark and bright defects are observed. Atomically resolved STM images of (k) an individual bright defect, -X, associated with Se sites, and of (l) an individual dark defect, -M, related to Mo sites. STS curves were measured at various distances from the (m) -X defect and (n) -M defect. In both cases, the STS curve recorded over the defect correspond to the first curve from the bottom to the up. Results adapted from [76].

dark defects are associated with Mo sites, and it is denoted as -M defect. In Figure 2.7(m) we can see STS spectra taken as a function of the distance from the center of the -X defect out to a distance of 3.5 nm. The spectrum measured directly over the defect presents a resonance near the CB edge, indicating the n-type doping introduced by -X defects. The resonance in the STS curve is shifted when increasing the tip-defect distance, likely due to band bending effects. Analogously, the STS curves acquired around the -M defect are shown in Figure 2.7(n). Here we observe a resonance close to the VB edges, which demonstrates that -M defects behave as acceptor-like defects.

2.2 Hexagonal boron nitride

2.2.1 Introduction

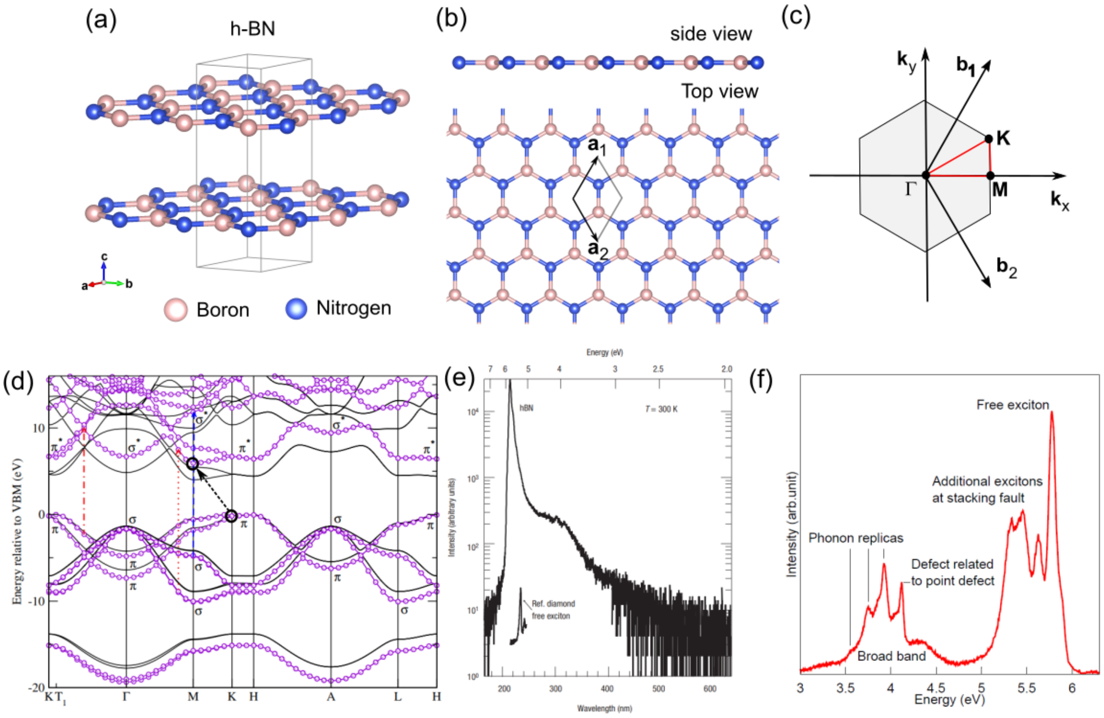

Figure 2.8: (a) Hexagonal boron nitride (h-BN) crystal structure. The number of atoms in the unit cell was increased for the best visualization of the layered structure. (b) Side view and top view of a single monolayer h-BN. The unit cell is indicated by the vectors $\mathbf{a}_1$ and $\mathbf{a}_2$ in the top view. (c) Hexagonal first Brillouin zone in two-dimensions. (d) Electronic band structure of bulk h-BN [77]. Cathodoluminescence spectrum of (e) high a quality h-BN crystal [78] and (f) a thin h-BN flake [79]

Hexagonal boron nitride (h-BN) is another important layered material. Its crystal structure is very similar to the graphite structure, i. e., monolayers of boron and nitrogen atoms covalently bonded in a hexagonal lattice are stacked vertically by van der Waals interactions, as shown in Figure 2.8(a). Analogous to TMDs, h-BN crystal can be exfoliated in several layers until obtaining a single monolayer h-BN. Figure 2.8(b) shows that a monolayer h-BN is atomically thin, with a honeycomb structure as the graphene. The 2D Brillouin zone is shown in Figure 2.8(c). In contrast to TMDs, h-BN is a wide band gap material ($>$6 eV). In Figure 2.8(d) is displayed, the calculated band structure of bulk h-BN, where it can be observed an indirect band gap between the

K and M points of the Brillouin zone [77]. Due to its large band gap, h-BN crystals are characterized by a strong excitonic luminescence in the deep ultraviolet (DUV) spectral range. This can be seen in the cathodoluminescence (CL) spectrum depicted in Figure 2.8(e). High-quality single crystals of h-BN present a strong and narrow emission peak at $\sim$ 6 eV [78]. This emission is attributed to the recombination of Frenkel excitons [61]. Typically, most h-BN samples present undesired structural defects like stacking faults or point defects. These defects introduce electronic levels inside the wide band gap of the material, then different optical transitions involving these defect states can be observed in the luminescence spectra. For instance, Figure 2.8(f) shows the CL spectrum of an h-BN sample with different types of defects. The emission is dominated by the recombination of free exciton close to 6 eV, and additional emission peaks are observed around 5.5 eV and 4.0 eV, which are attributed to defects such as stacking fault and point defects, respectively. Phonon replicas are also detected [79].

2.2.2 Electronic properties of monolayer h-BN

Band gap crossover

In analogy with the observed in semiconducting TMDs, an indirect-to-direct band gap crossover was predicted by Paleari *et al.* in 2018 [80] for h-BN in the transition from bulk to monolayer. Simulations of the electronic band structure of h-BN as a function of the number of layers are shown in Figure 2.9. Interestingly, the electronic band gap for monolayer h-BN is predicted to be a direct band gap at the K point. When the number of layers increases, the electronic band gap becomes indirect between the M and K points. The VBM and CBM are defined by the π and π^* states, respectively. Figure 2.9(b) shows the calculated imaginary part of the dielectric function $\varepsilon_2(\omega)$. The black line at 7.3 eV represents the onsets for the absorption to the continuum, i. e. the value of the electronic band gap. The inset figure illustrates the π and π^* states localized at the nitrogen (gray) and boron (green) atoms, respectively. Below the electronic band gap, we observe a set of peaks that correspond to different excitonic states. The exciton ground state is observed as the strongest peak at around 5.4 eV, meaning that the exciton binding energy is about 1.9 eV. The calculations also predict that the dielectric screening increases when the number of h-BN layers increases, reducing both the electronic band gap and the exciton binding energy. At the same time, the optical band gap defined by the energy of the ground state exciton remains constant. Additionally, the number of excitonic lines increases for h-BN with more than one layer. These are assigned to different bright and dark exciton states.

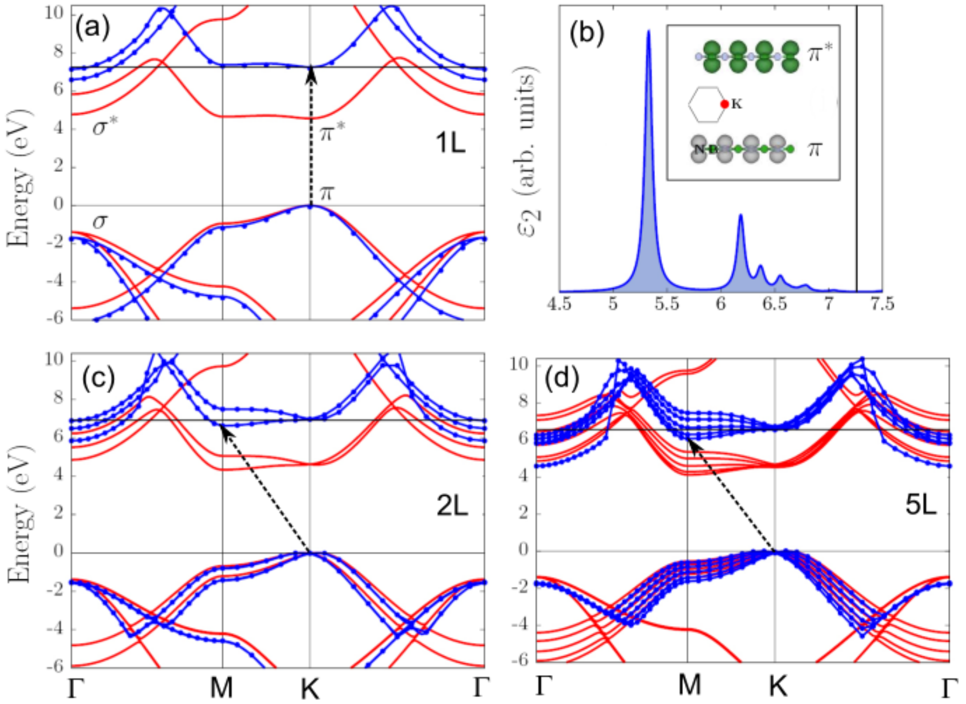

Figure 2.9: (a) Electronic band structured and (b) imaginary part of the dielectric function of monolayer h-BN (1L). The inset shows a representation of the Brillouin zone and the π and π^* states at the K point. The boron and nitrogen atoms are represented in green and gray, respectively. (c) band structure for a bilayer (2L) and (d) a pentalayer (5L) of h-BN. Adapted from [80]

Electronic and optical band gaps

Typically, optical transitions in h-BN samples are investigated by CL spectroscopy. Schué *et al.* [81] reported CL measurements on h-BN samples with different thicknesses. As indicated in Figure 2.10(a), they measured the CL response of bulk h-BN and also of exfoliated samples with thicknesses ranging from 100 layers (100L) to 6 layers (6L) of h-BN. The simplest spectrum is obtained in the sample of 6L, where the narrow emission peak at 5.9 eV is attributed to the recombination of free excitons. This emission peak is slightly shifted to lower energy, reducing the intensity for samples with more layers. Additional emission peaks are observed below 5.9 eV when increasing the sample thickness. All of them are attributed to phonon replicas, observed at the same energy position but with different intensities. Even though Schué *et al.* found some dimensionality effects on the light emission properties of h-BN, no information about the DUV emissions of a single monolayer h-BN resolved by CL has been reported so far.

The DUV luminescence of monolayer h-BN was measured for the first time by Elias *et al.* [35] in 2019. In their work, monolayer h-BN epitaxially grown on graphite (HOPG) was investigated by PL and reflectance measurements, see Figure 2.10(b). The optical spectra measured on monolayer h-BN/HOPG are depicted in Figure 2.10(c). The sharp PL peak observed at 6.1 eV in the spectrum for monolayer h-BN is attributed to the fundamental exciton transition. The reflectance spectrum shows a resonance at the same energy position, meaning that there is no Stoke shift between the PL and reflectance. Hence, the emission at 6.1 eV is interpreted as direct recombination of excitons with both electrons and holes at the same valley in k-space. In addition, the PL spectrum for bulk h-BN is displayed. The band gap is indirect, and the exciton transition is measured at 5.95 eV. The results obtained by Elias *et al.* demonstrated that (as observed in semiconducting TMDs) the transition from bulk to monolayer leads to an indirect-to-direct band gap crossover in h-BN.

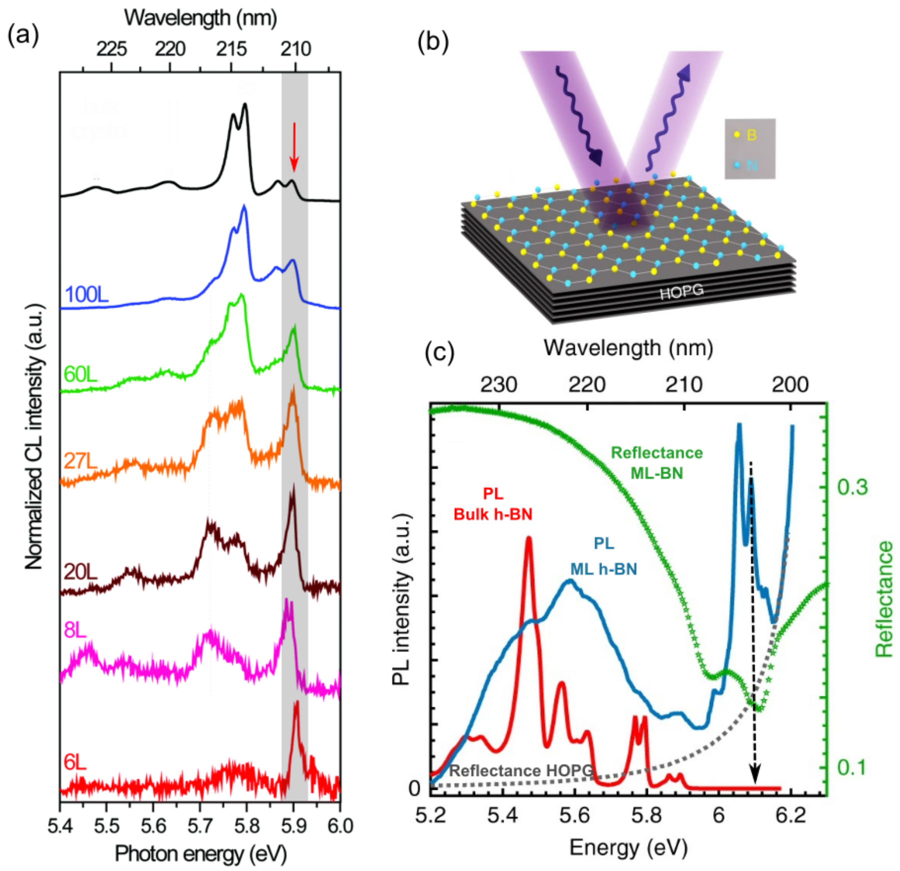

Figure 2.10: (a) Normalized CL spectra of bulk h-BN and exfoliated h-BN with thicknesses going from 100 L to 6 L. The free exciton transition is highlighted by the gray area and the red arrow. Adapted from [81]. (b) Sketch of optical DUV measurement in epitaxial monolayer (ML) h-BN on graphite (HOPG). (c) PL and reflectance spectra of ML h-BN. The PL of bulk h-BN and the reflectance of bare h-BN are shown for comparison. Adapted from [35].

The band gap crossover reported by Elias *et al.* is in agreement with the simulation published by Paleari *et al.* However, the energy position for the exciton ground-state is different. Paleari *et al.* calculated an excitonic transition at 5.4 eV and an electronic band gap of 7.3 eV, which led to an exciton binding energy of 1.9 eV. Elias *et al.* observed the exciton transition at 6.1 eV, then if we take the same exciton binding energy, we have that the electronic band gap of a single monolayer h-BN should be about 8 eV. This huge electronic band gap has not been measured yet. Nevertheless, a recent GW$_0$ calculation of the electronic band structure for a free-standing monolayer has predicted a direct band gap of 8.18 eV at the K point of the Brillouin zone [82], as indicated in Figure 2.11(a). Moreover, the calculated optical absorption spectrum for in-plane optical polarization shows a strong absorption peak at 6.10 eV for the fundamental exciton transition, see Figure 2.11(b), in agreement with the value found by Elias and co-workers. Therefore an exciton binding energy of 8.18 eV$-$6.10 eV$=$2.08 eV is expected for Frenkel excitons in free-standing monolayers. On the other hand, Wirtz, *et al.* obtained, from first-principle calculations, that the exciton binding energy increases from 0.7 eV to 2.1 eV in the transition from bulk to monolayer [83].

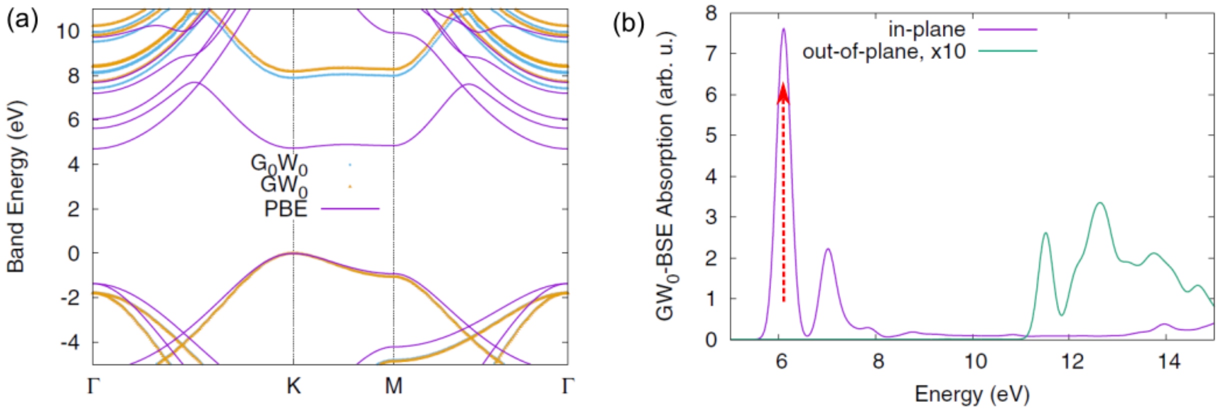

Figure 2.11: (a) Electronic band structure of free-standing monolayer hBN, calculated by DFT-PBE, GW theory at the single-shot (G_0W_0) and partially self-consistent (GW_0). (b) GW0-BSE optical absorption spectrum of monolayer hBN for in-plane and out-of-plane polarization. Taken from [82].

Substrate effect on the electronic band gap and the exciton binding energy

As expected for any 2D material, the electronic and optical properties of a monolayer h-BN can be affected by the presence of the substrate. Figure 2.12 shows some interesting theoretical results about the effects of the substrate on the electronic band gap and the exciton binding energy. In Figure 2.12(a), the electronic band gap for a monolayer is evaluated as a function of the distance L to a graphene layer. The electronic band gap predicted from GW calculation presents a $1/L$ dependence, and the equilibrium distance is about 3.5 Å. The model also predicts that the electronic band gap of the free-standing monolayer is reduced by 1 eV when supported by a single Gr layer [84]. The same renormalization of the electronic band gap is predicted for a monolayer supported by graphite [85], as can be seen in Figure 2.12(b).

More recently, Guo *et al.* [16] reported the effect of the substrate on the exciton binding energy (E_b) and the electronic band gap (E_g). In Figure 2.12(c) are plotted the E_b and E_g values obtained from GW calculations for monolayer h-BN on different substrates. The results present a linear scaling between E_b and E_g, due to substrate screening with a slope close to one. Therefore, any change in E_g will be canceled for a similar change of E_b of the 1s exciton state. Hence, the energy of the exciton ground state peaks remains constant, i.e., the emission peak of the fundamental excitonic transition is insensitive to the environmental screening. This explains the experimental and theoretical results in Figures 2.10(c) and Figures 2.11(b), where the excitonic emission is measured and predicted at 6.1 eV, respectively. The results reported by Guo *et al.* confirm that the values for both E_b and E_g in free-standing monolayer are reduced by about 1 eV when Gr is used as substrate. Note that h-BN presents the same substrate effect observed in monolayer $MoSe_2$ on Gr(see Figures 2.5).

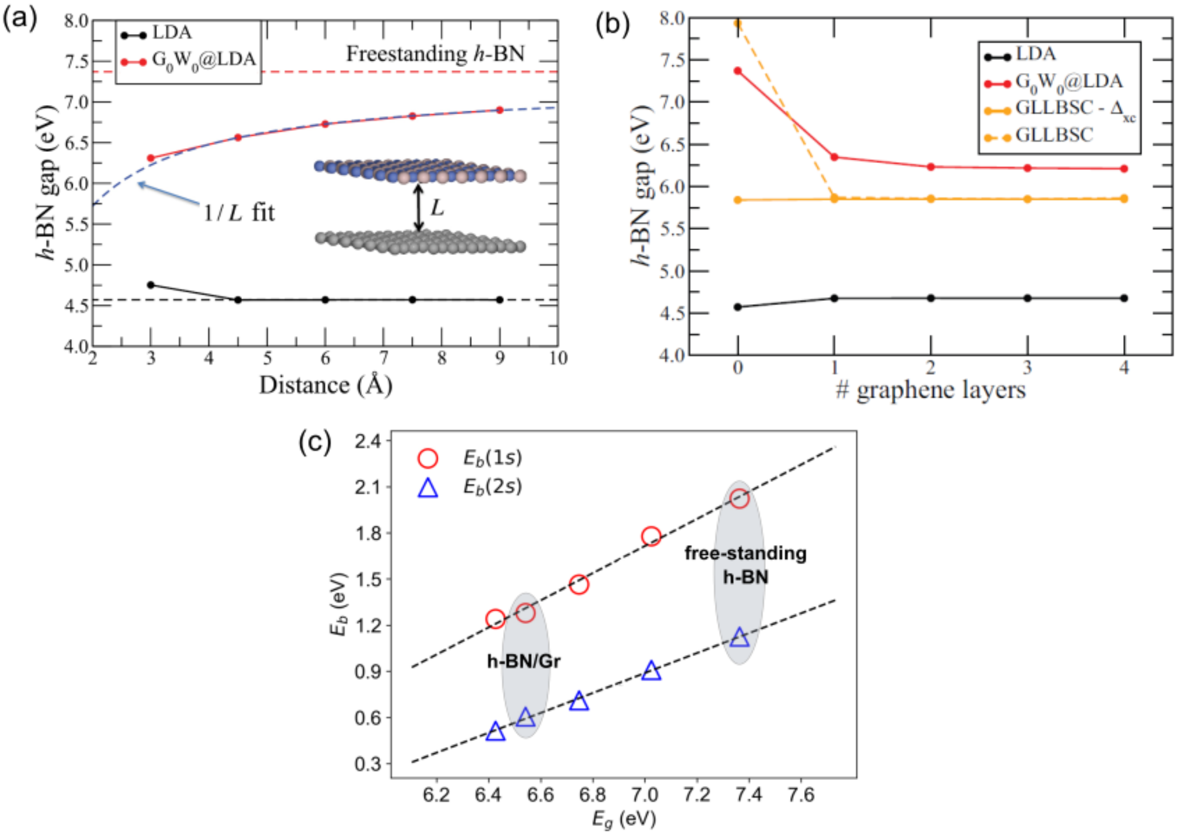

Figure 2.12: (a) Electronic band gap of monolayer h-BN as a function of the distance to a graphene layer. Figure taken from [84]. (b) Electronic band gap of monolayer h-BN supported by graphite (several layers of Gr). Figure Taken from [85]. (c) Linear scaling between the exciton binding energy (E_b) and the electronic band gap of monolayer h-BN calculated from GW approximation and considering different substrates. The data point from right to left corresponds to monolayer h-bn (1) free-standing (2) on h-BN, (3) on SnS_2, (4) on Gr and (5) on $SnSe_2$ substrate. Adapted from [16].

Measurements of the band structure and electronic band gap

We have discussed in this chapter that STS is a technique able to measure locally and directly the DOS of the sample. However, previous STM/STS measurements on h-BN have not given a clear answer for the electronic band gap. The main reason for that is that most of the STM/STS studies have been carried out on h-BN samples grown on metallic substrates. The growth of a 2D material on a metallic substrate leads to a band gap renormalization due to strong interactions with the substrate, which is related to the dielectric screening by the metal and (or) the formation of additional interface electronic states, including hybridization, among others [13, 29, 86, 87].

In Figure 2.13 are displayed some examples. Figure 2.13(a) shows an STM image of a high-quality single layer h-BN grown on the Ru(0001) surface [29]. The STS curve acquired on this sample can be seen in Figure 2.13(b). Note that instead of observing a large band gap as expected for h-BN, the sample presents metallic characteristics. This metallic behavior observed in the h-BN layer is due to the strong sample-substrate interaction which arises from the local charge transfer, as represented in Figure 2.13(c). Interestingly, when h-BN is grown on Gr/Cu(111) [88] as illustrated in Figure 2.13(d), electronic states of the metallic substrate are measured on the h-BN layer. In this case, intragap states due to the copper support are measured by STS, and the h-BN band gap is not observed, as can be noted in the series of STS curves in Figure 2.13(f), which were measured along the dashed red line in the STM images shown in Figure 2.13(e).

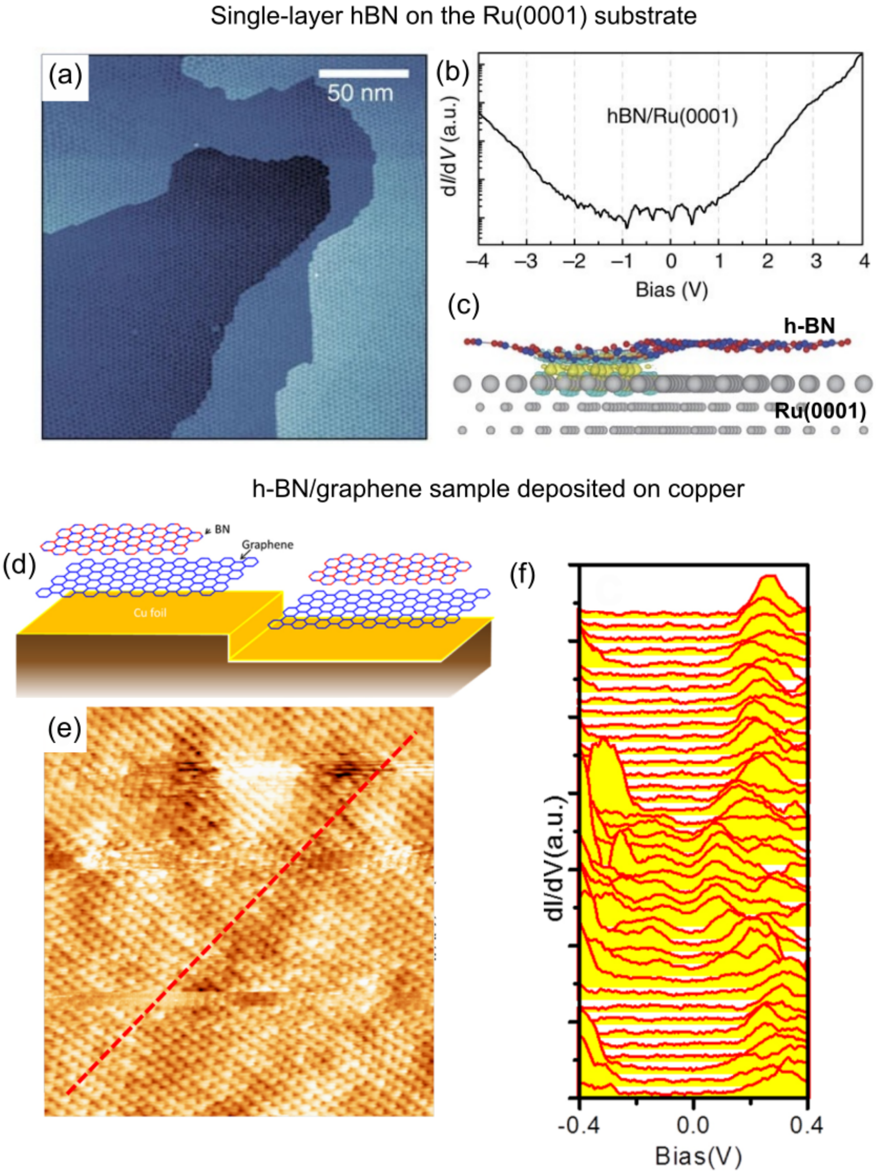

Figure 2.13: (a) STM image of a high-quality monolayer h-BN grown on Ru(0001). (b) STS curve acquired on h-BN/Ru(0001). (c) Atomistic model for the charge density difference induced by the sample-substrate interaction. Figures adapted from [29]. (d) Illustration of the CVD grown of h-BN/Gr on a Cu (Copper) foil. (e) STM image of top h-BN layer with a scan size of 10nm10nm. (f) STS curves acquired along the dashed red line in (e). Figures adapted from [88].

2.2.3 Point defects and Luminescence related to point defects

Even though STM is a tool able to identify atomic defects in 2D materials, as shown in Figure 2.7, a detailed STM/STS investigation of point defects in monolayer h-BN is missing. STM imaged bright point defects related to possible carbon impurities in Gr capped bulk h-BN [50]. However, as can be seen in Figure 2.14(a), using Gr as conducting electrodes affects the STM images, and the identification of the defect is difficult. Although the dI/dV (STS) map in Figure 2.14(b) shows the presence of defects in bulk h-BN. Additionally, defects in h-BN on HOPG were observed by Summerfield *et al.* using conductive atomic force microscopy (cAFM), and STM measurements [89]. Some of the results are shown in Figure 2.14(c)-(f). Figure 2.14(c) shows defects observed as bright points in h-BN/HOPG. The defects are attributed to defects in the HOPG substrate created during the sample preparation process, see Figure 2.14(d). STM measurements also demonstrate the presence of defects with nanometric sizes, as can be observed in the image of Figure 2.14(e) and the profiles in Figure 2.14(f). The authors also suggest using a combination of UHV and LT AFM/STS measurements to fully investigate point defects in h-BN/HOPG samples to correlate and understand the electronic and optical properties of point defects in h-BN. These studies might help to reveal the chemical nature of defects in h-BN and their impact on the sample properties.

From the electronic and optical point of view, point defects introduce electronic levels inside the h-BN band gap, as illustrated in the diagram of Figure 2.15(a). Optical transitions involving intragap states related to point defects can result in the emission of single photons. The luminescence spectra of single-photon emitters in h-BN are characterized by a narrow emission peak called zero-phonon line (ZPL), which corresponds to transitions between two states without phonon participation. Transitions involving phonons are called phonon replicas or phonon sidebands (PSB). These are observed as a broad and weak peak below the energy position of the ZPL. Single-photon emitters are observed at RT in monolayer and multilayer h-BN with a ZPL around 620 nm (2.0 eV) and PSB at 680 nm (1.83 eV) and 693 nm (1.79 eV) [45–47], see Figure 2.15(b). CL measurements obtain similar spectra on bulk h-BN with a ZPL at 4.1 eV [39]. The atomic structure of point defects responsible for emitting single photons in h-BN is still under discussion.

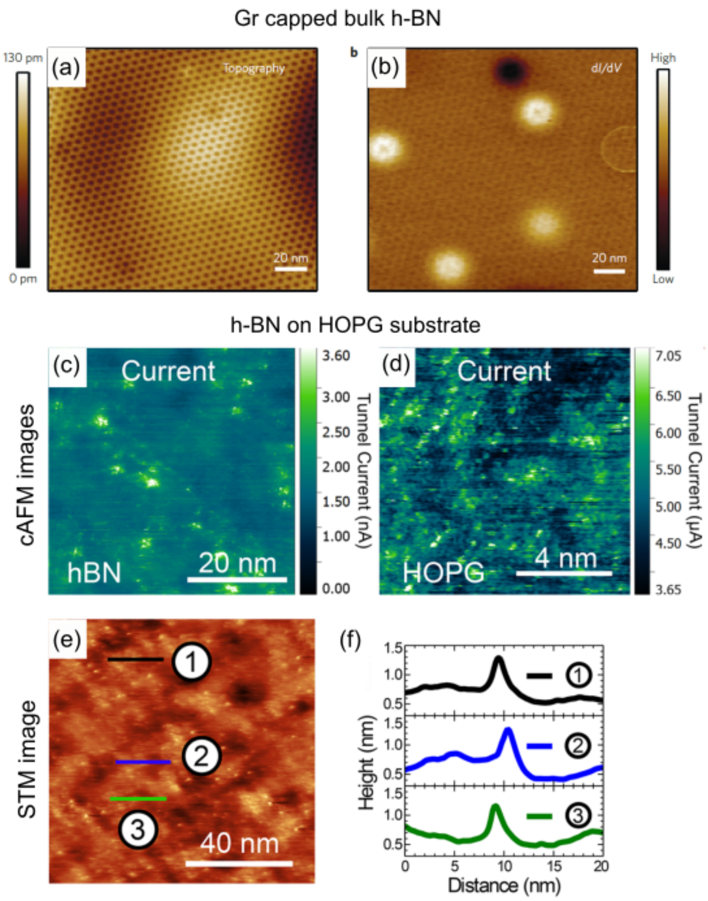

Figure 2.14: (a) Topography and (b) differential conductance map of Gr capped bulk hBN. Taken from [50]. (c) conductive atomic force microscopy (cAFM) of h-BN/HOPG and (d) bare HOPG substrate. (e) STM image of a monolayer hBN/HOPG, the profile indicated by the colored lines are shown (f). Figures adapted from [89].

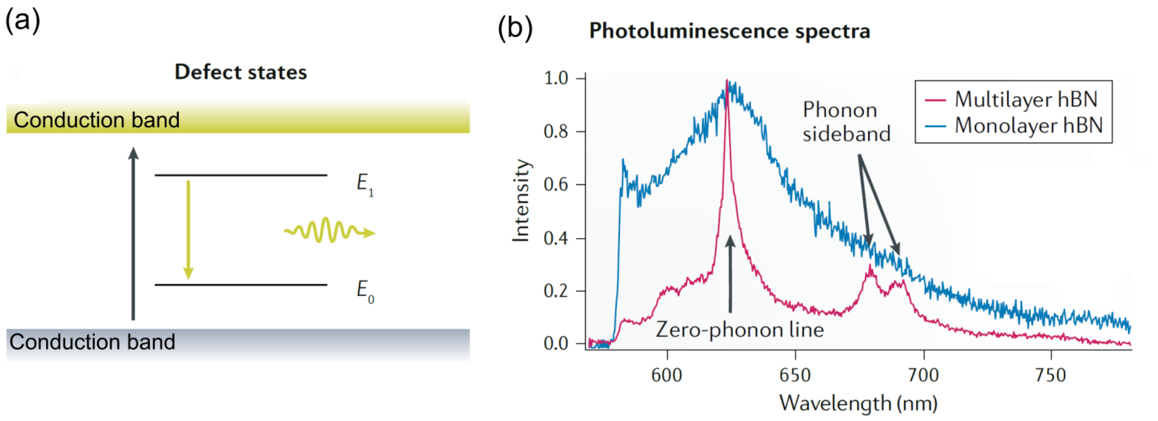

Figure 2.15: (a) Schematic illustration of the intragap states, E_0 and E_1, introduced by point defects in h-BN. A single-photon can be emitted due to an electronic transition from E_1 to E_0. PL spectra of single-photon emission from monolayer and multilayer h-BN at room temperature. Figures adapted from [47].

Chapter 3

Scanning tunneling microscopy, luminescence spectroscopy in STM, experimental setup, samples and methods

3.1 Scanning Tunneling Microscopy

Nowadays, scanning tunneling microscopy (STM) is a well-established experimental technique in nanoscience since this provides unique opportunities for probing and exploring the physical properties of matter with atomic precision and in real space. The instrument used in this type of microscopy is called scanning tunneling microscope (STM), and it was invented in 1981 at the IBM research division in Zurich by the physicists Gerd Binnig and Heinrich Rohrer [90]. The scientific potential of this tool was put in evidence one year after its invention when it was implemented to solve one of the most relevant problems in surface science at that time, the 7×7 reconstruction of the Si(111) surface [91]. Binning and Rohrer were awarded the Nobel prize in physics only five years after the STM invention.

3.1.1 The quantum tunneling phenomenon

Before starting to describe how an STM works, it is convenient to introduce here the concept of *tunneling*. Let us consider the one-dimensional (1D) problem of a particle with energy E and mass m traveling toward a potential barrier like the one shown in Figure 3.1. From the classical point of view, if the particle's energy is lower than the height of the barrier ($E < V_0$), there is no way that the particle can penetrate it to go from one side to the other. However, the same problem has another solution if the particle under study is a quantum particle, for instance, an electron. In this case, the particle is described by a wavefunction $\psi(z)$ that satisfies the Schrödinger equation. By solving the Schrödinger equation (see appendix A), we can find that inside the barrier, the particle is described by:

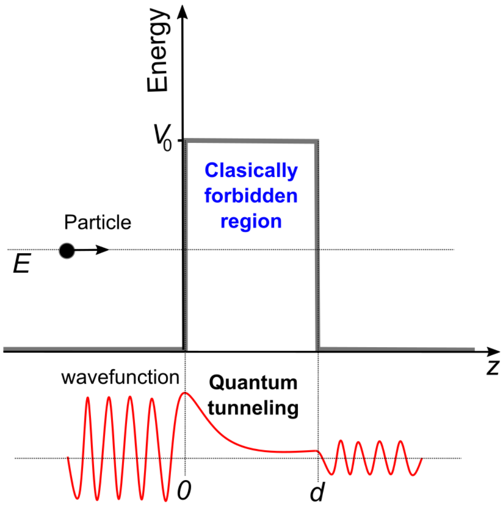

Figure 3.1: One-dimensional model of quantum tunneling through a rectangular potential barrier.

$$\psi(z) \propto e^{-kz}, \quad \text{with} \quad k = \sqrt{2m(V_0 - E)/\hbar^2}, \quad \text{for} \quad E < V_0, \tag{3.1}$$

This is, a real wavefunction that decays exponentially, and $|\psi(z)|^2$ gives the probability of finding the particle at the position z inside the barrier. We can note that this probability is non-zero, which means that the particle can penetrate the barrier, and the phenomenon is known as *quantum tunneling*. The probability of observing the particle in the other side of the barrier is given by the transmission coefficient T:

$$T = \frac{|\psi(z)|^2}{|\psi(0)|^2} \propto e^{-2kd}, \tag{3.2}$$

Where d is the size of the tunneling barrier, the exponential dependence of T on the barrier width d is very characteristic of quantum tunneling for any shape of the tunneling barrier.

3.1.2 The STM working principle

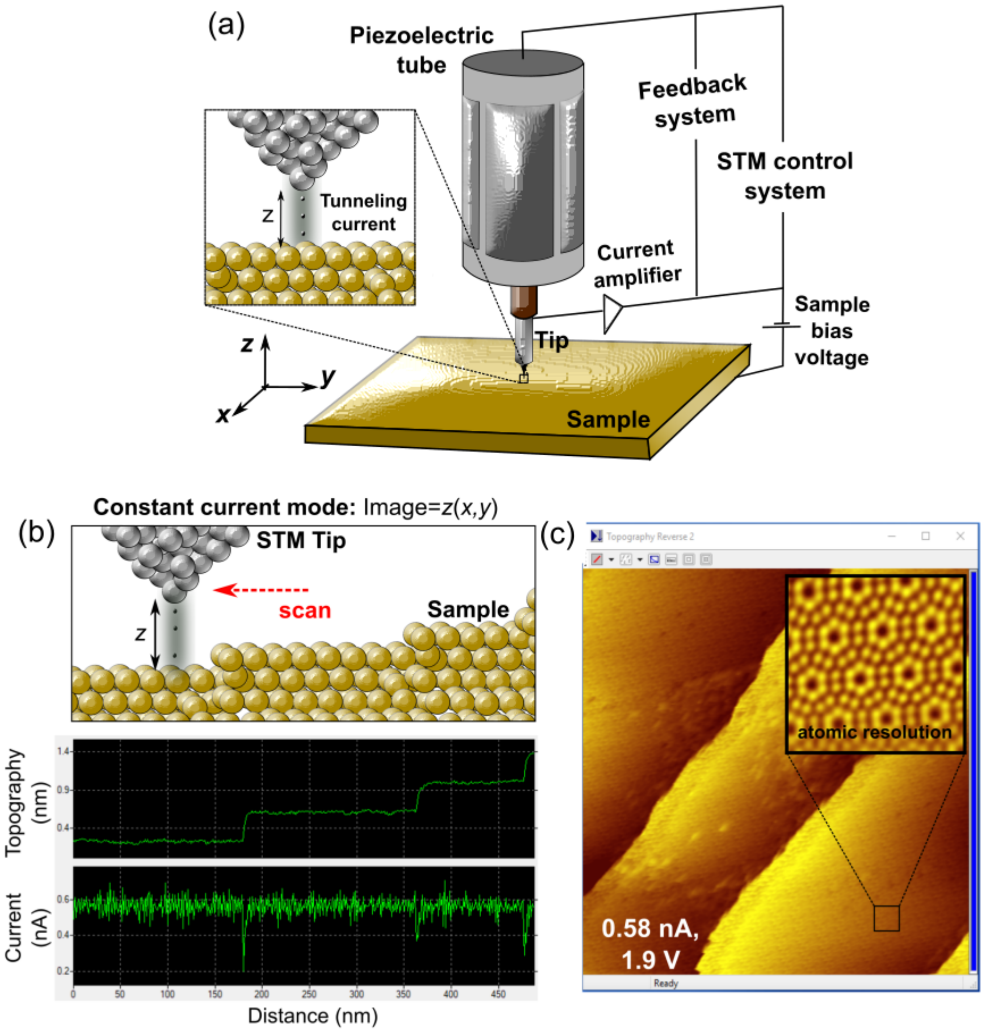

Figure 3.2: (a) Schematic illustration of the STM system. (b) STM imaging acquisition in the constant current operation mode. (c) STM image of the Si(111)-7x7 surface reconstruction.

In STM, an atomically sharp metallic tip, usually made of tungsten (W) or Platinum-Iridium (Pt-Ir), is used as a probe. The tip is attached to a piezoelectric tube that expands or contracts in a controlled way after applying a bias voltage. This allows manipulating the STM tip position with atomic precision. The principle of operation of an STM is illustrated in Figure 3.2. A bias voltage is applied between the metallic tip and a conducting surface. With the help of the piezoelectric tube, the tip is placed very close (< 1 nm) to the sample surface until detecting a flow of electrons between the two electrodes without mechanical contact, such as shown in Figure 3.2(a).

The observed current (in the range of pico-Ampere (pA) to nano-Ampere (nA)) is due to the quantum tunneling of electrons between the tip and the sample. It is used to probe the sample locally and obtain topographic or electronic information on the sample surface. STM images can be acquired by scanning the tip over the surface. The most common scanning mode for imaging acquisition is the constant current mode, which is illustrated in Figure 3.2(b). In this imaging acquisition mode, the tip scans the surface keeping the tunneling current constant, and a feedback system adjusts the tip height by approaching or retracting the tip to a tip-sample distance where the tunneling current remains constant. The image is formed by recording the tip-sample distance for each lateral position of the STM tip. Figure 3.2(c) shows a large area constant current image of the Si(111)-7x7 surface, revealing the surface topography with atomic steps. Reducing the scan size to a few nanometers, atomically resolved images are recorded as in the inset figure.

The tunneling process in an STM junction is illustrated in Figure 3.3. Due to the small tip-sample distance, the wavefunction of electrons in the tip and the sample overlap. Then, when a bias voltage is applied, the Fermi level in the tip is shifted with respect to the Fermi level in the sample, and the tunneling of electrons occurs. The fundamental 1D quantum tunneling model discussed in the previous section can be used to understand some important aspects of the tunneling current in an STM. Assuming the tunneling junction as a metal-vacuum-metal junction, we have that the electron wavefunction at the metallic surface of one of the electrodes will decays exponentially inside the vacuum barrier as a function of the distance z. In a solid, the minimum energy required to remove an electron is given by the material's work function. Thus, the electron will be in the presence of an effective potential barrier defined by the work function Φ. For simplicity, let us assume that the work function is the same for the tip and the sample. Considering small biases, such as that $eV_{bias} \ll \Phi$, we can treat the tunneling barrier as a rectangular potential barrier, and the electron will tunnel from an energy level very close to the Fermi level in one of the electrodes to the Fermi level in the other one. Therefore, we can use equations 3.1 and 3.2 but taking into account that in this case $V_0 - E = E_{\text{vacuum}} - E_F \approx \Phi$, and the tunneling current, I_t, can be described by:

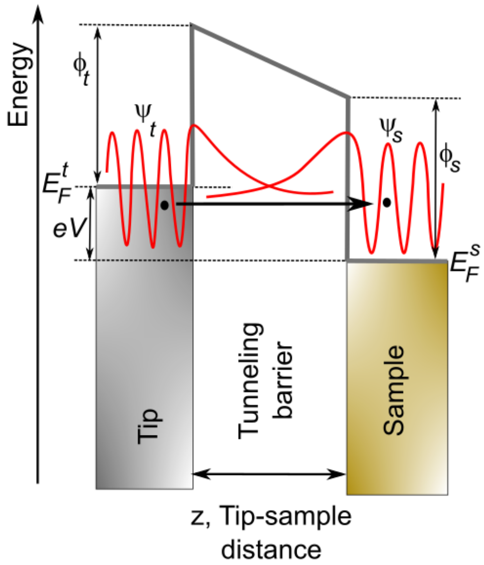

Figure 3.3: Tunneling process in the STM junction. E_F^i, ψ_i, and ϕ_i, correspond to the Fermi energy, wavefunction, and work function, respectively. The index $i = t, s$ denote the tip (t) and the sample (s).

$$I_t \propto e^{-2kz} \quad \text{with} \quad k = \sqrt{2m_e\Phi/\hbar^2}, \tag{3.3}$$

where m_e is the free electron mass.

The high spatial resolution achieved in STM is a consequence of the strong dependence of the tunneling current on the tip-sample distance z. This can be seen easily by evaluating equation 3.3 with some typical values in STM experiments. For example, in a metallic STM junction under vacuum, $\Phi \approx 5 \ eV$ and $2k$ will be about 23 nm^{-1}, which means that a variation of 0.1 nm in the tip-sample distance will induce a change in the tunneling current value of 9.98 times, i. e. in one order of magnitude. This sensitivity of the tunneling current with the tip-sample distance results in an extremely high vertical resolution, which can be in the pm range. Furthermore, comparing the tunneling current originated in the closets atom of the tip to the sample with the current from the second closets atom in the tip to the sample surface. We have more than one order of magnitude of difference. In other words, this means that most of the tunneling current is mainly provided by the last atom in the STM tip apex, which explains the sub-nanometric lateral resolution in the STM [92–94].

3.1.3 STM imaging and spectroscopy

In practice, the tunneling current in an STM junction is described by the expression (see appendix A):

$$I_t(x, y, z, V) \propto \int_0^{eV} d\epsilon\, T(z, \epsilon, V)\rho^{\text{tip}}(\epsilon - eV)\rho^{\text{sample}}(\epsilon, x, y), \tag{3.4}$$

where ρ^{tip} is the density of states (DOS) of the tip and ρ^{sample} is the local density of states (LDOS) of the sample. Taking into account that a single atom constitutes the tip apex, we can consider ρ^{tip} as a constant. Therefore the tunneling current can be written as:

$$I_t(x, y, z, V) \propto \int_0^{eV} d\epsilon\, T(z, \epsilon, V)\rho^{\text{sample}}(\epsilon, x, y), \tag{3.5}$$

It means that an STM image represents the LDOS of the sample, evaluated at the STM tip position, at the energy ϵ around the Fermi's level of the tip. Additionally, $T(z, \epsilon, V)$ corresponds to the transmission coefficient given by:

$$T(z, \epsilon, V) = \exp\left\{ - 2z\sqrt{\frac{2m_e}{\hbar^2}\left(\frac{\phi_{\text{t}} + \phi_{\text{s}}}{2} + \frac{eV}{2} - \epsilon\right)}\right\}, \tag{3.6}$$

this term shows the exponential dependence of the tunneling current on the tip-sample distance z, which is responsible for the high spatial sensitivity in STM, as discussed above. Moreover, the transmission coefficient increase exponentially for higher electron energies, i. e., the tunneling probability is higher for electrons with high energies. The tunneling processes in an STM junction with different bias polarities are illustrated in Figure 3.4, where the horizontal arrows with different lengths represent the tunneling probability for electrons at a given energy. Figure 3.4(a) shows that when a positive bias is applied to the sample, we can probe the empty states of the sample since electrons tunnel from filled tip states to empty sample states. The opposite process is shown in Figure 3.4(b). For negative sample bias, electrons tunnel from filled sample states to empty states of the tip, then filled states of the sample are probed.

Let us now consider the derivative of the tunneling current in equation 3.5 with respect to the sample bias V. In the approximation of small bias ($eV \ll \phi_t, \phi_t$) we have:

$$\frac{dI}{dV} \propto \rho^{\text{sample}}(eV, x, y), \tag{3.7}$$

the quantity dI/dV is called *difference conductance*, and it is proportional to the LDOS of the sample at the energy eV. Therefore, measuring dI/dV means a direct measurement of $\rho^{\text{sample}}(eV, x, y)$. This constitutes the principle of scanning tunneling spectroscopy (STS) as a local probe of the electronic properties of the sample.

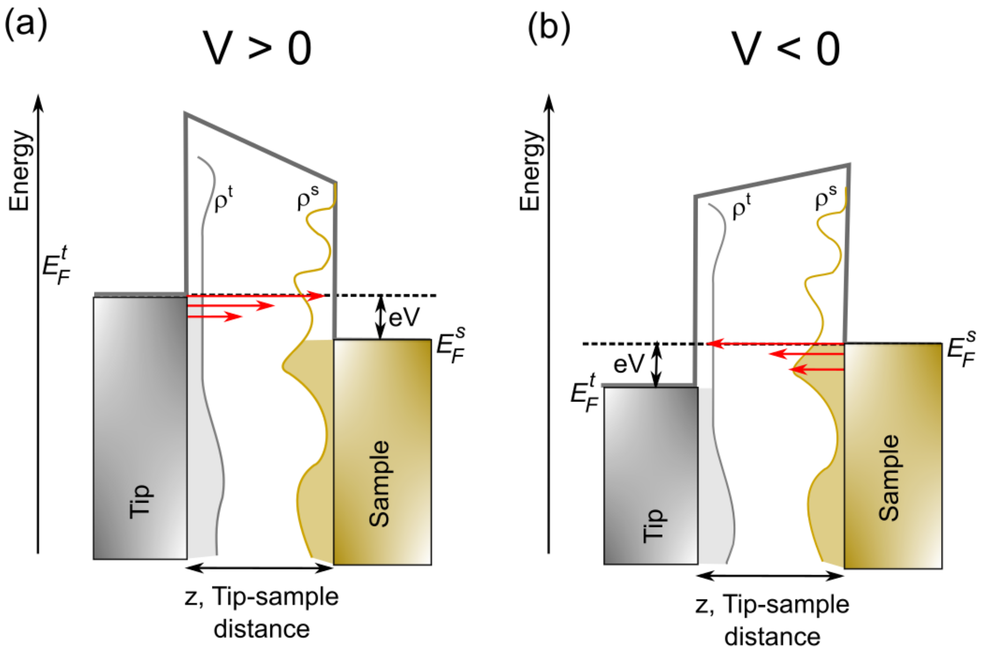

Figure 3.4: Representation of the tunneling process at (a) positive sample bias (V>0), and (b) at negative sample bias (V<0). Empty (filled) sample states are probed when using V>0 (V<0). The density of states of the tip and the sample are indicated as ρ^t and ρ^s, respectively.

3.2 Luminescence spectroscopy with an STM

3.2.1 STM-Induced light emission (STM-LE)

The tunneling current in an STM can induce the emission of photons from the sample under investigation. The experimental technique based on this fact is known as STM-induced light emission (STM-LE) or scanning tunneling luminescence (STL or STML). In STM-LE, the STM tip is used to excite the photon emission locally, allowing the study of the sample's optical properties with the spatial resolution of STM. The first observation of light emission from an STM junction was reported in 1988 by Gimzewski *et al.* who investigated samples of polycrystalline tantalum and Si(111)7×7 [95]. After that, Berndt *et al.* implemented the technique for investigating optical properties of metal and semiconductor surfaces on a subnanometer scale [96, 97].

The light emission mechanisms in STM-LE are related to the excitation of localized surface plasmons in metal surfaces (plasmonic emission) or the electrical generation of excitons in molecules or semiconductor surfaces (excitonic emission). Next, we will describe the excitation processes for the plasmonic and excitonic emissions in STM luminescence experiments.

Plasmonic light emission

The concept of *plasmon* (a quasi-particle) is used to describe the collective oscillation of free electrons in a bulk metal. The oscillations of free electrons at the interface between a metal and a dielectric (or vacuum) are known as *surface plasmons*, which can interact with the electric field produced by the oscillations of charges to form *surface plasmon polaritons* (SPPs). SPPs are electromagnetic waves that propagate along the metal-dielectric interface with a wavevector $\vec{k}_{SPP}$. Figure 3.5(a) illustrates the propagation of a SPP, with $\vec{k}_{SPP}$ parallel to the interface and an in-plane magnetic field $\vec{H}_y$. The electric field perpendicular to the interface is evanescent, as shown in Figure 3.5(b).

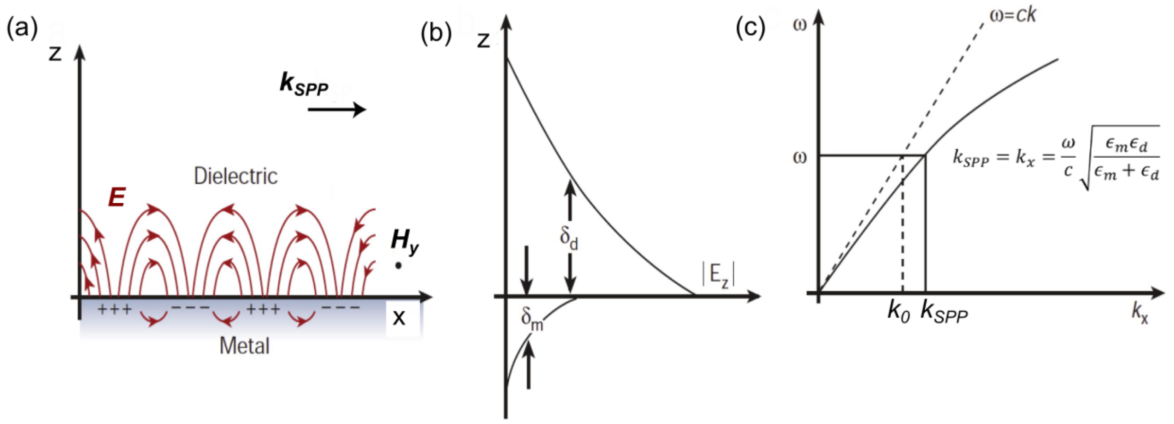

Figure 3.5: a) illustration of a surface plasmon polariton (SPP). (b) Evanescence of the electric field perpendicular to the interface, $\delta_{d,m}$ are the penetration depth of the electric field into the dielectric and metal, respectively. (c) Dispersion relation of SPPs (solid line) and light (dashed line). $\epsilon_{d,m}$ are the dielectric functions of the dielectric and metal, respectively, and c is the speed of light in vacuum. Adapted from [98].

The dispersion relation of SPPs depends on the bulk metal's plasmon frequency and the dielectric functions of the metal and the dielectric. Such dispersion relation can be obtained by solving the Maxwell equation at the metal-dielectric interface [61, 99]. Figure 3.5(c). shows the dispersion curve for SPPs, compared with the curve for propagating light in vacuum. We can see that for a given frequency (energy), the momentum $\vec{k}_{SPP}$ is always larger than the momentum of photons $\hbar\vec{k}_0$. Therefore, SPPs are non-radiative or excited by light unless the momentum mismatch is overcome. One way of overcoming the momentum mismatch and producing the conversion of SPPs in light is to break the translational symmetry of the plane by surface roughness or a sharp tip (STM tip) [98–100].

In STM experiments, we put a sharp metallic tip close (nanometer-close) to the metallic surface. The surface plasmon localized on the tip apex interacts with the SPPs of the sample and produces a plasmonic nano-cavity in the tunneling junction. Thereby are produced what is known as tip-induced plasmons (TIPs) or localized plasmon modes [98, 100], understanding that are plasmons localized or confined in the tip-sample cavity. In contrast to SPPs, localized surface plasmon are radiative by nature and can be coupled to light (i.e., they can be excited by light).

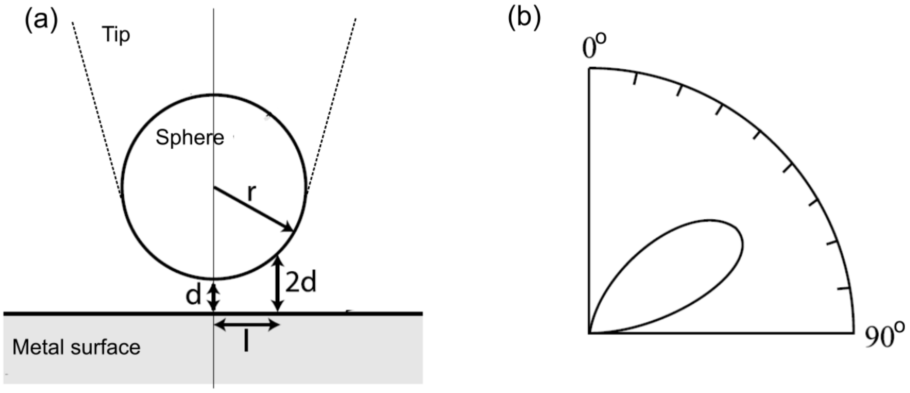

Figure 3.6: (a) Geometry of a spherical metal particle above a metal surface used by Rendell *et al.* to calculate the localized plasmon modes. This geometry is similar to an STM tunneling junction. Adapted from [98]. (b) Calculated angular distribution of the radiation emitted by localized plasmons. Adapted from [101].

Rendell *et al.* [101] calculated the plasmonic modes for localized plasmons in a tunneling junction. The investigated junction was a metallic sphere of ratio r placed at a distance d from a flat metallic surface, as shown in Figure 3.6(a). This tunneling geometry is similar to an STM tunneling junction if we consider an STM tip apex with a spherical shape. The authors showed that a localized plasmon could be described as an oscillating dipole perpendicular to the flat surface and confined to a region of about $l = \sqrt{2dr}$ from the tip apex. The oscillating dipole has a maximum radiation intensity at an angle of approximately 60° from the normal surface, such as shown in Figure 3.6(b). Additionally, Rendell *et al.* obtained that localized plasmons have discrete plasmonic modes with frequencies:

$$\omega_n = \omega_p \sqrt{\frac{\tanh{(n+\frac{1}{2})\beta_0}}{\epsilon_d + \tanh{(n+\frac{1}{2})\beta_0}}}, \quad \text{with} \quad \beta_0 \approx \sqrt{\frac{2d}{r}}, \tag{3.8}$$

where n is the plasmon mode number, ω_p is the plasma frequency of the metal, and ϵ_g is the dielectric constant of the surrounding medium. From this result, we can see that, for a given tip-sample distance, the plasmonic modes will depend on the plasmonic mode of the bulk metals (i.e., on the dielectric properties of the materials forming the plasmonic nano-cavity) and on the tip radius (tip shape).

In STM, localized plasmons are excited by the inelastic tunneling of electrons [96, 102], as can be seen in Figure 3.7. The rate of inelastic tunneling was calculated by Person and Baratoff [103], who estimated that 1% of the electrons tunnels inelastically exciting plasmonic modes during a tunneling process, being the total photon emission efficiency of 10^{-3} photon per electron. Figure 3.7(b) shows an energy diagram for the inelastic tunneling in an STM junction. During the tunneling, electrons in the barrier lose energy. The energy lost is transferred to excite localized plasmon modes in the STM junction. The excited plasmons can decay radiatively. Figure 3.7(c) shows an STM-LE spectrum measured on a gold (111) surface with a gold tip. A broadband emission characterizes the plasmonic spectrum since electrons can tunnel to a continuum of states in the sample. Additionally, the plasmonic emission presents a quantum cutoff defined by $h\nu = |eV|$, where V is the sample bias voltage. This cutoff is independent of the bias polarity, and it is expected for inelastic tunneling processes, where only can be excited plasmonic modes that emit photons with energy equal to or less than the tunneling electrons.

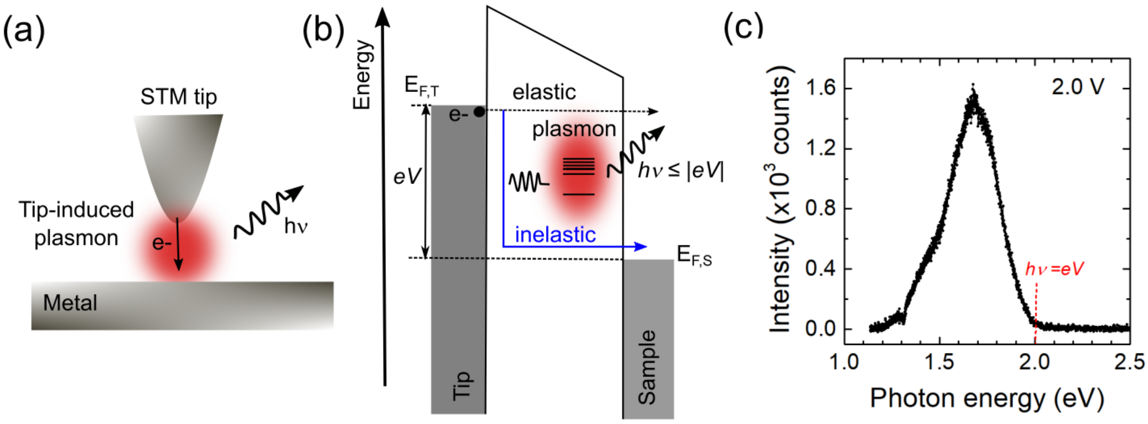

Figure 3.7: (a) Schematic diagram of photon emission due to localized plasmons in STM tunneling junction. (b) Energy diagram for elastic and inelastic tunneling of electrons. The energy lost in inelastic tunneling is transferred to excite plasmonic modes that emit photons with energy $h\nu = |eV|$. V is the bias voltage, and $E_{F,T(s)}$ are the Fermi level in the tip and sample, respectively. (c) STM-LE spectrum measured on a gold(111) surface with a gold STM tip.

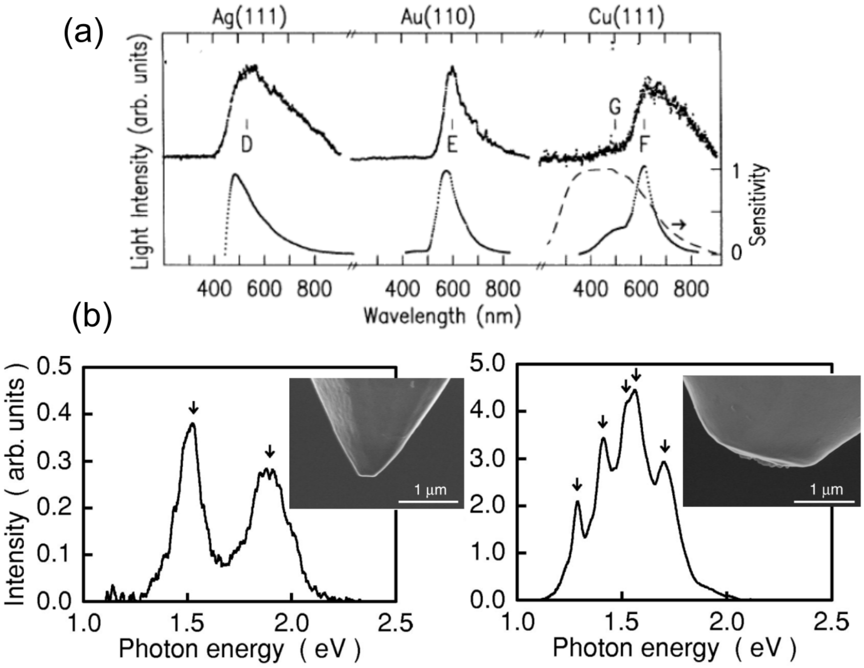

Figure 3.8: (a) STM-LE spectra of the surfaces Ag(111), Au(110), and Cu(111). The top row corresponds to the experimental data and the bottom row to the calculated spectra. The dashed curve corresponds to the sensitivity of the detection system. Adapted from [96].(b) STM-LE spectra of Au(111) surface measured with the tip shown in the SEM images. Adapted from [104].

As discussed above, the shape of the plasmonic STM-LE spectra will depend on the chemical nature of the metals forming the tunneling junction and the structure of the STM tip. Figure 3.8(a) shows results reported by Berndt *et al.*, who measured STM-LE spectra on different metallic surfaces with a tungsten (W) tip [96]. The spectra are compared with the calculated spectra shown in the bottom row. We can see that the maximum intensity of the plasmon emissions is at different energies for different metals, besides the difference in the spectral shape as demonstrated in the calculated curves. The influence of the STM tip on the STM-LE spectra was investigated by Meguro *et al.* [104]. In Figure 3.8(b) are presented STM-LE spectra measured on Au(111) surface using gold STM tips with different shapes. The shape of the tips was explored by scanning electron microscopy (SEM). We can see that truncated tips apex produces STM-LE spectra with multiple peaks whose number and energies depend on the tip shape.

Excitonic light emission

The excitonic light emission from an STM junction depends on the system under investigation. For instance, in inorganic semiconductor surfaces, luminescence is generated due to the recombination of electron-hole pairs through band-to-band transitions. The excitation mechanism is the injection of carriers from the tip to the semiconductor bands [97, 105–107]. As an illustration, in Figure 3.9, we show some results reported by Sakurai *et al.* on STM-LE of GaAs(110) surface *et al.* [105]. Figure 3.9(a) shows the excitation mechanism for the light emission in semiconductor surfaces, where an electron tunnels elastically from the tip to the semiconductor's conduction band. The electron decays until the band edge and then recombines radiatively with a hole in the sample. The quantum emission efficiency is about 10^{-4} photons per electron. STM-LE spectra measured at different sample voltages are presented in Figure 3.9(b). The spectra show a narrow peak at 1.48 eV. The energy of the emission is attributed to band gap transitions in GaAs bulk because the electronic band gap of the surface is larger and indirect [105, 106, 108].

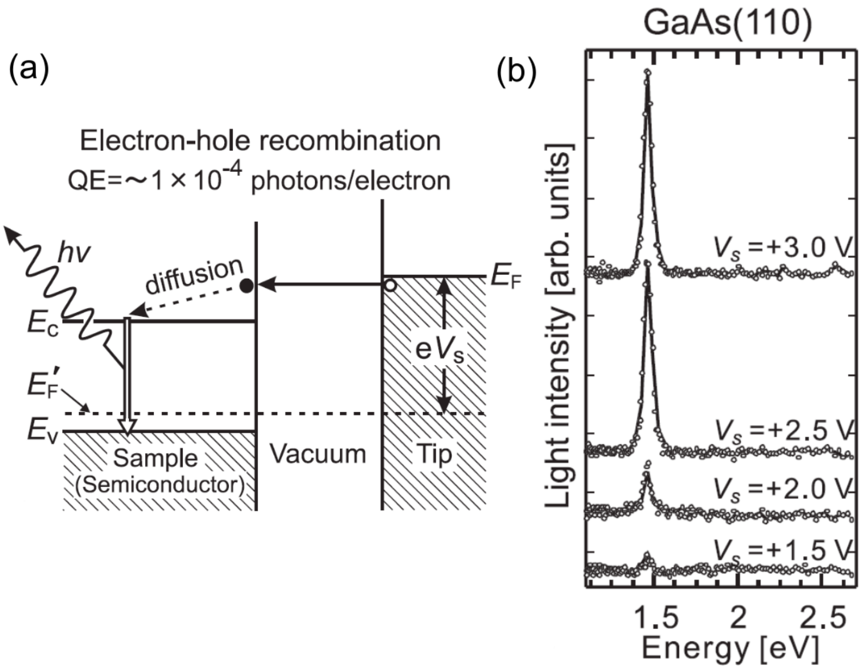

Figure 3.9: (a) Schematic diagram of the STM-LE excitation mechanism in semiconductor surfaces. (b) STM-LE spectra of clean GaAs(110) surface acquired at different bias voltage. Adapted [105].

Molecules deposited on metal surfaces can be investigated with STM. However, observing the molecular excitonic luminescence via STM-LE requires having the molecules decoupled from the substrate. A molecule in direct contact with the metal substrate will exhibit hybridized electronic states, then any charge injected in the molecule will be transferred rapidly to the substrate, avoiding the radiative recombination of charges [109]. Therefore STM-LE spectra of molecules on metals are essentially plasmonic since the hybridized electronic levels offer new channels for the inelastic tunneling of electrons, promoting the excitation of localized plasmons [110–114], as shown in the energy diagram of Figure 3.10(a). Hence, the electronic coupling between the molecule and the metallic support results in a total quenching of the intrinsic excitonic molecular luminescence. It is expected to observe a similar behavior on monolayers of TMDs (three atoms of thickness) on metal surfaces. In Chapter 5 we will describe how it is possible to obtain the intrinsic excitonic emission in a monolayer of TMD on a metal substrate via STM-LE.

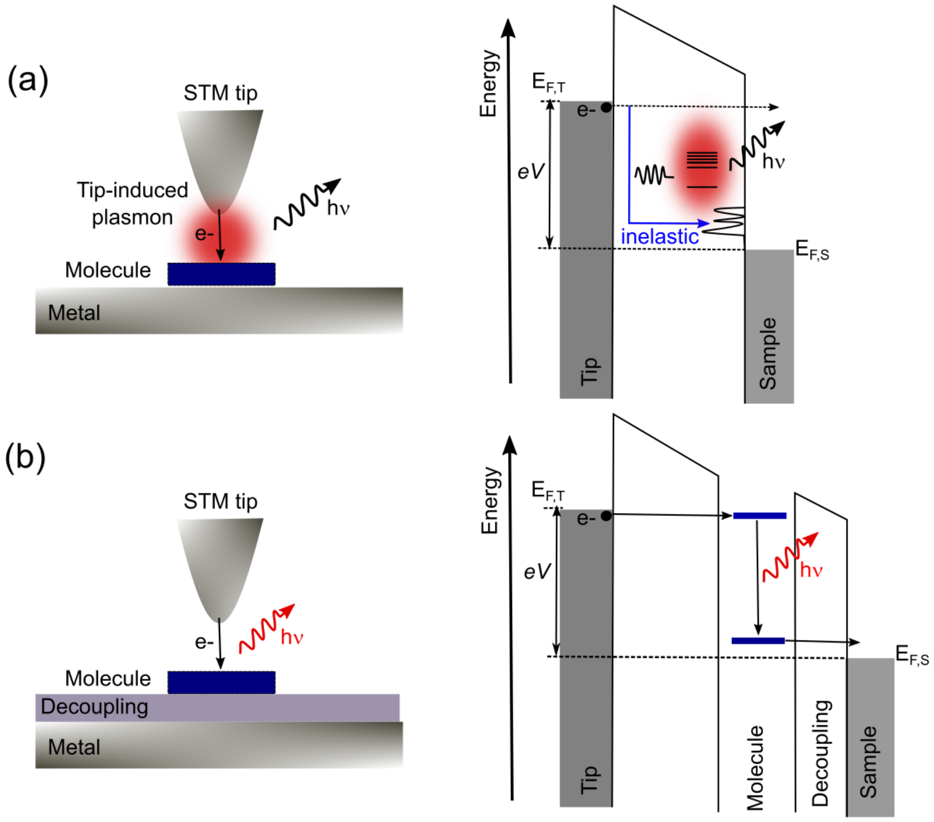

Figure 3.10: (a) Schematic illustration and energy diagram for the photon emission involving localized plasmon in systems with molecules in direct contact with a metal surface. (b) (a) Schematic illustration and energy diagram for the photon emission due to molecular transitions in systems where the molecules are decoupled from the metallic substrate. In the energy diagram, V is the bias voltage, and $E_{F,T(s)}$ are the Fermi level in the tip and sample, respectively.

There are several strategies for observing the excitonic emission of molecules in STM-LE measurements. The main idea is to introduce a barrier able to decouple the emitter from the substrate and, at the same time, allow the tunneling of electrons. As illustrated in Figure 3.10(b), in decoupled molecules, electrons tunneling from the tip induces the radiative recombination of charges due to direct transitions between molecular orbitals. In this case, quantum efficiencies of 10^{-4} and 10^{-5} photon per electron have been reported [105, 115]. The excitonic emission of decoupled molecules can also be excited in tunneling processes mediated by plasmon. In this case, plasmonic modes are excited through the inelastic tunneling of electrons, and then the energy of the plasmon is transferred to the molecule to excite an exciton [116, 117].

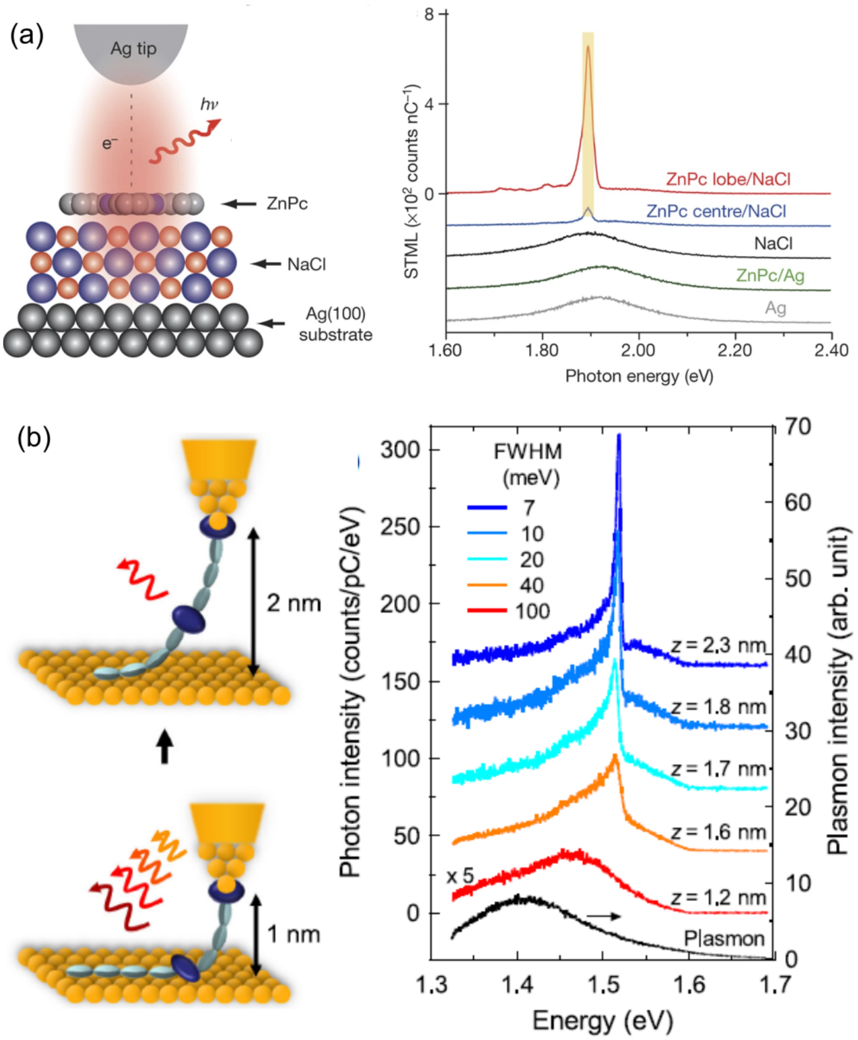

Figure 3.11: (a) STM-LE measurements on a ZnPc molecule decoupled from the Ag(100) surface by a thin layer of NaCl. Adapted form [118]. STM-LE on a suspended molecule. The molecule is suspended using a molecular wire and controlled STM manipulation. Adapted from [119].

For decoupling molecules from the metallic substrate and carrying out STM-LE measurements, methods involving the growth of molecular multilayers [120–122] or ultrathin insulating layers such as Sodium Chloride (NaCl) [118, 123, 124] or Aluminum Oxide (Al_2O_3) [115, 125] have been employed. Another approach consists of suspending the emitter between the tip and the sample using a molecular wire [119, 126]. Figure 3.11 shows some STM-LE results on decoupled single molecules. In Figure 3.11(a), we see the excitation of a single Zinc-phthalocyanine (ZnPc) molecule decoupled from the Ag(100) surface by a thin layer of NaCl. The STM-LE spectra show a plasmonic emission from the molecule in direct contact with the substrate. However, the intrinsic molecular luminescence can be observed in STM-LE spectra recorded on the molecule deposited on NaCl/Ag(100). In addition, Figure 3.11(b) presents the case of suspended molecules. This decoupling method was demonstrated by Chong *et al.* [119] in porphyrin molecules linked to oligothiophene wires on Au(111) surface. The STM-LE spectra show a plasmonic emission of the molecule on the metal surface. Using STM manipulation, the molecule can be suspended above the substrate by attaching the tip to the molecular wire. The intrinsic molecular luminescence appears after suspending the emitter from the metal surface at tip-sample distances above 1.2 nm. The luminescence line width is reduced when the tip-sample distance increases.

3.2.2 Luminescence in TMD monolayers studied by STM-LE

Here we present the state of the art of STM luminescence measurements in monolayers of TMDs. We describe some important aspects in the investigation of TMDs employing STM, such as typical luminescence spectra, mechanics for the excitation and emission of light, the influence of the STM tip, point defects, and the underlying support.

Epitaxial monolayer MoS_2 on Au(111) substrate

The first report showing the optical excitation of a single layer of TMD using tunneling electrons in an STM was published by Krane, et al. in 2016 [24]. In their work, monolayers of MoS_2 epitaxially grown on the Au(111) surface were morphologically characterized by STM images. At the same time, the electronic and optical properties were investigated through STS and STM-LE measurements, respectively, all under ultra-high vacuum conditions and at low temperatures (4 K). Some of the results published by Krane, et al. are shown in Figure 3.12. An illustrative representation of the measurement is presented in Figure 3.12(a), where electrons tunneling from a gold tip to the sample are used to probe its electronic and optical properties locally.

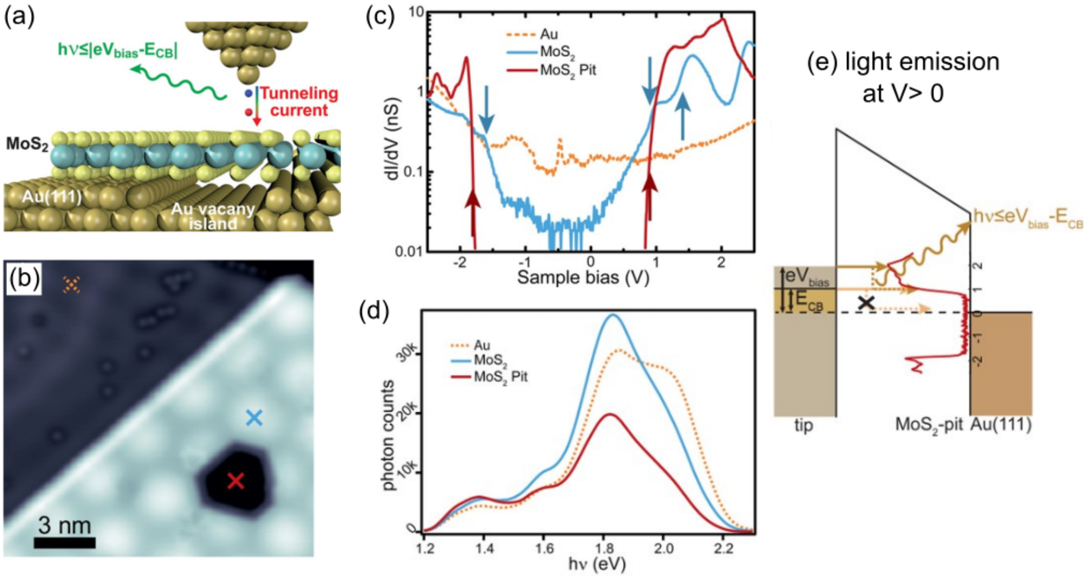

Figure 3.12: (a) Illustration of STM-LE in epitaxial monolayer MoS_2 on Au(111) surface. (b) STM image of MoS_2 and Au(111) with a pit defect, images acquired under UHV conditions and at 4 K. Low temperature (c) STS and (d) STM-LE spectra (3.5 V, 10 nA)measured at the STM tip position indicated by the crosses in (b). (e) STM-LE light emission mechanism for positive sample bias. Figures adapted from [24].

In the STM image shown in Figure 3.12(b), we can see the Au(111) surface and also the MoS_2/Au(111) surface, which is characterized by a hexagonal moiré pattern of about 3.3 nm of periodicity. The image also reveals a nanometer-sized pit in the region where the monolayer MoS_2 is. The pit appears because it is a region of the Au substrate with some atoms missing (Au vacancy island). Thus, the monolayer on the pit is considered quasi-freestanding. The STS and STM-LE spectra acquired on the gold substrate and the supported and quasi-freestanding monolayer MoS_2 are compared in Figures 3.12(c) and 3.12(d), respectively. The spectra were measured at the tip position indicated by the crosses in (b). The STS curve of the MoS_2 pit (red curve) shows an electronic band gap defined by the band onsets at -1.8 V and 0.9 V. However, in the STS on MoS_2 (blue curve), the electronic band gap is difficult to be determined because it is observed tunneling current for small sample bias, which is expected due to hybridization and screening with the metallic states of the Au(111) substrate. Additionally, the STM-LE spectra in Figure 3.12(c) indicate a strong sample-substrate interaction because all the spectra have the same spectra shape, i.e., broad emission peaks related to surface plasmon modes localized in the tunneling junction formed between the gold tip and the gold substrate. The STM-LE light emission mechanism for positive sample bias is explained in Figure 3.12(e). Localized plasmons are excited by the inelastic tunneling of electrons from the tip to the semiconductor's conduction band. Therefore, photons with energy $h\nu \leq eV_{\text{bias}} - 1\ eV$ are detected. These results demonstrated that for probing excitons by STM-LE in monolayer TMDs, the sample must not be in direct contact with metallic substrates to avoid the excitation of localized plasmonic modes.

Exfoliated monolayer $MoSe_2$ on ITO substrate

The excitonic emission in a monolayer of TMD excited by tunneling electrons in STM was first observed by Pommier, *et al.* in 2019 [49]. In this case, a mechanically exfoliated monolayer $MoSe_2$ is transferred onto a nonmetallic transparent conducting substrate (ITO) and excited using a tungsten tip. The STM-LE measurements were carried out in air and at RT. Part of the results published by Pommier, *et al.* are shown in Figure 3.13. The spectra obtained by PL and STM-LE in monolayer $MoSe_2$ are displayed in Figure 3.13(a). Both spectra present the emission expected for the recombination of spin-allowed A excitons, i. e., a narrow peak centered at 1.58 eV. The inset in Figure 3.13(a) corresponds to a real-space optical microscope image of the STM-LE signal from monolayer $MoSe_2$, the intensity profile taken along the white arrow indicates that most of the emitted light is localized below the STM tip position. However, emission from hot spots localized several micrometers away from the STM tip is detected.

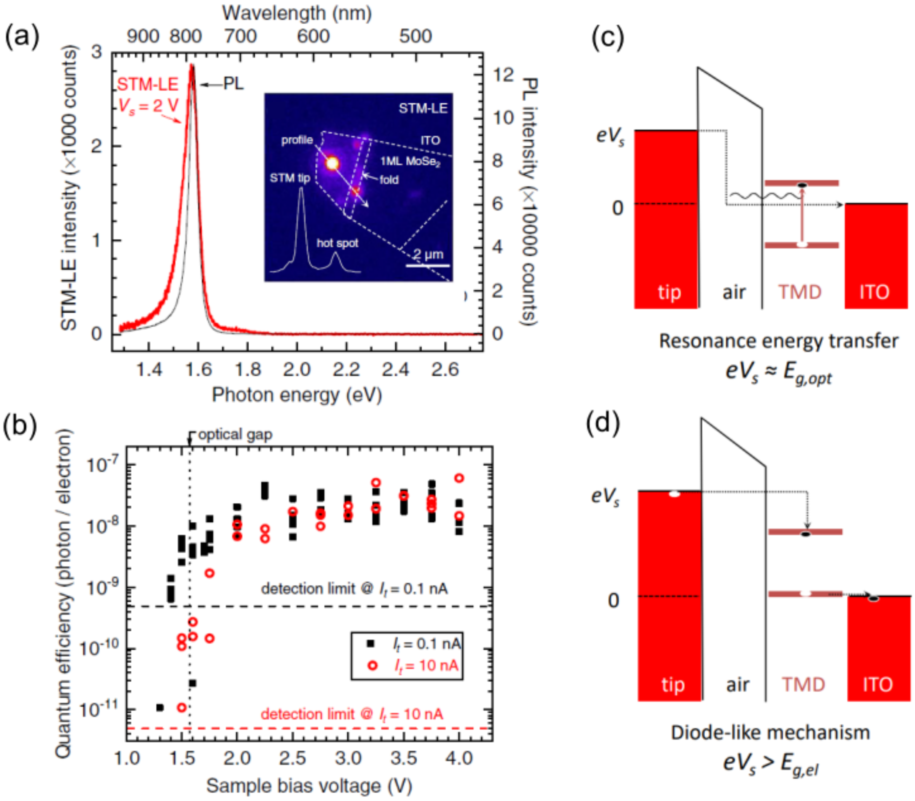

Figure 3.13: (a) RT STM-LE (2V, 10 nA) and PL spectra of monolayer $MoSe_2$. Inset: real space optical microscopy images of the STM-LE signal in monolayer $MoSe_2$ (4 V, 5 nA). (c) Photon emission quantum efficiency of the STM-LE signal. Figures (a)-(b) are adapted from [49]. (c) Energy transfer excitation mechanism. (d) Charge injection excitation (diodo-like) mechanism. Figures (c) and (d) were taken from [127].

The quantum efficiency of the excitonic emission generated electrically with tunneling electrons is evaluated in the plot of Figure 3.13(b), where the number of photons per tunneling electron is plotted as a function of the positive sample bias. We can see that the photon emission quantum efficiency is about 10^{-7} photons per electron. This is observed for low (0.1 nA) and high (10 nA) tunneling current setpoint and for electrons with energies above 1.5 eV (close to the optical band gap for monolayer $MoSe_2$). The possible excitation mechanisms for the excitonic emission observed by STM-LE in monolayer $MoSe_2$ are shown in Figures 3.13(c) and 3.13(d). The energy transfer process is represented in Figure 3.13(c), here electrons with energy below the electronic band gap, $E_g \sim 2.2$ eV, and close the optical band gap, E_{opt}, tunnel inelastically from the tip to the sample, and the energy lost during the tunneling process is transferred to the exciton. For electrons with energy above E_g, the most likely mechanism is the injection of charge, such as shown in Figure 3.13(d). Electrons tunnel from the tip to the CB of the semiconductor, for the excitons formation holes must be present in the sample or coming from the substrate.

Epitaxial monolayer WS_2 on Gr/SiC substrate

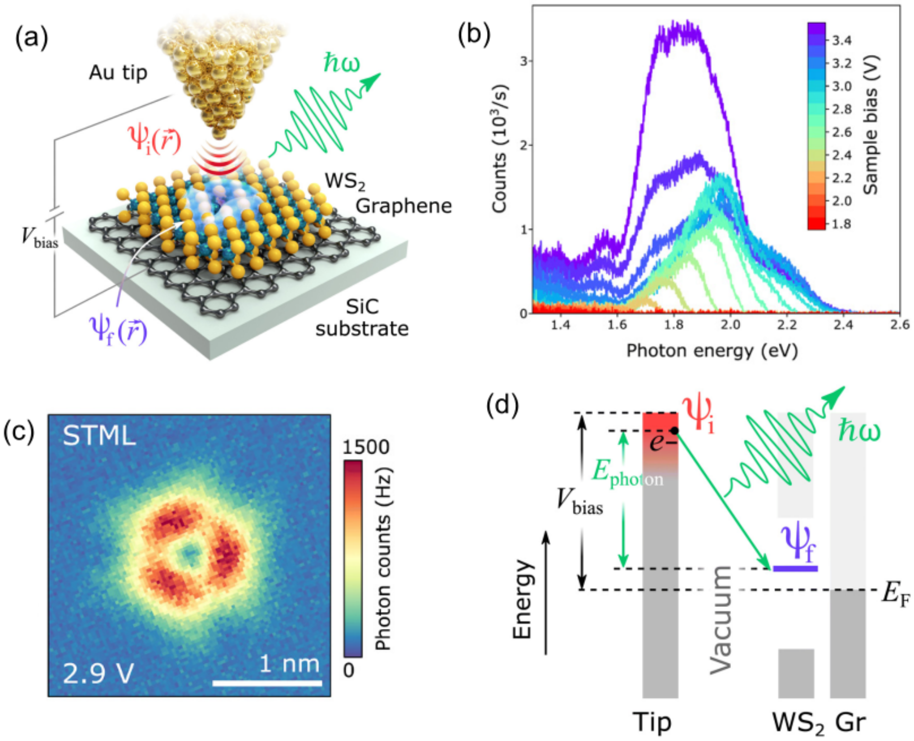

Figure 3.14: (a) STM-LE on a single point defect (sulfur vacancy defect, Vac_s). (b) STM-LE spectra on a Vac_s at different sample bias voltage. (c) STM-LE map of a Vac_s (29 V, 20 nA). (d) Excitation mechanism. Adapted from [128].

Samples of monolayer WS_2 grown on epitaxial graphene on silicon carbide (SiC) substrate were investigated by Schuler, *et al.* [128]. The optical properties of single point defects were investigated with atomic resolution under UHV conditions and at LT. The excitation process of a single defect using tunneling electrons from an Au-coated tip is represented in Figure 3.14(a). The STM-LE spectra measured as a function of the sample bias voltage on a sulfur vacancy defect (Vac_s) are shown in Figure 3.14(b). The broadband emission peaks suggest that localized plasmons mediate the emission due to the presence of the Au-tip. The narrow peaks expected for excitonic transitions of defect-bounded excitons are not observed, meaning that the intrinsic luminescence of monolayers can be strongly affected by both plasmonic tip and substrate. The atomically resolved photon emission map of an individual Vac_s is shown in Figure 3.14(c), and the STM-LE excitation mechanism can be seen in Figure 3.14(d). Photons are emitted due to the inelastic tunneling of the electron from the tip state ψ_i to the defect state ψ_f.

3.2.3 STM-Cathodoluminescence (STM-CL)

The STM can also be employed to perform cathodoluminescence measurements (STM-CL) [48, 129–132], which requires operating the microscope in field emission (FE) mode. For operating in FE, it is necessary to retract the STM tip from the sample surface at distances of 100-150 nm. After that, voltages in the range of 100-200 V are applied between the tip and the sample, producing field emission electron beam (FEEB) currents of few micro-amperes (μA), as can be seen in the current versus voltage curve ($I-V$ curve) in Figure 3.15(a). The $I-V$ curve presented in Figure 3.15(a) was obtained when the STM described in Section 3.3 is operated in FE under UHV conditions (1.3x10^{-10} mbar). We used a W tip and a sample of Si(111). The tip-sample distance is 100 nm. As a voltage source and amperemeter, we used a KEITHLEY electrometer model 6517A. FE currents are described by the Fowler-Nordheim equation [133]: $I = AV^2 \exp(-B/V)$, where A and B are constants that depend on the tip-sample distance and the work function of the tip, I is the measured current, and V is the applied voltage. The inset in in Figure 3.15(a) shows a plot of $\log(I/V^2)$ versus $1/V$. The data presents a linear behavior, in agreement with the Fowler-Nordheim equation, and demonstrates the field emission regime of the microscope.

In STM-CL, electrons field-emitted from the tip apex excite the sample by electron bombardment, generating the emission of photons as illustrated in Figure 3.15(b). The sample volume excited by the FEEB is less than 10 nm in-depth and around d ($\sim$ 100 nm) laterally [130, 131]. This technique has been employed with success to investigate impurities in wide band gap materials, such as Magnesium Oxide (MgO) [134] and Zinc Oxide (ZnS) [135, 136] thin films. For this thesis, we performed STM-CL measurements on monolayers h-BN. In chapter 6 we will show the investigation of the fundamental electronic and optical properties of monolayers h-BN, as well as the characterization of point defects employing STM, STS, and STM-CL.

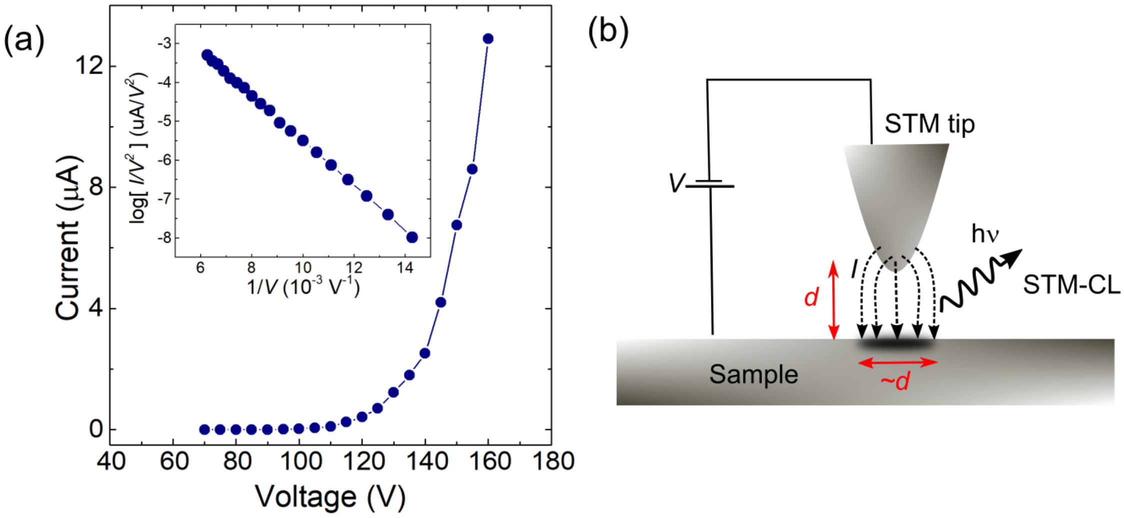

Figure 3.15: (a) Current as a function of the voltage applied between a W tip and Si(111) surface. The inset shows the Fowler-Nordheim plot that demonstrates the field emission regime in the operation of the STM. (b) Schematic diagram of the STM tunneling junction in field emission mode for STM-CL measurements.

3.3 Experimental setup

Figure 3.16(a) shows a description of our UHV-LT STM system. It is a commercial STM from RHK technology, model PanScan flow. The system consists of a tip and sample insertion chamber, which is pumped using a scroll pump and a turbo-molecular pump to reach a base pressure of 1.3×10^{-7} mbar before transferring tips and samples to the main chamber of the STM, which is maintained at UHV (1.3×10^{-10} mbar) employing an ion pump and a titanium sublimation pump. To operate at low temperatures, the system has a cryogenic refrigeration circuit based on a continuous flow of Helium or Nitrogen

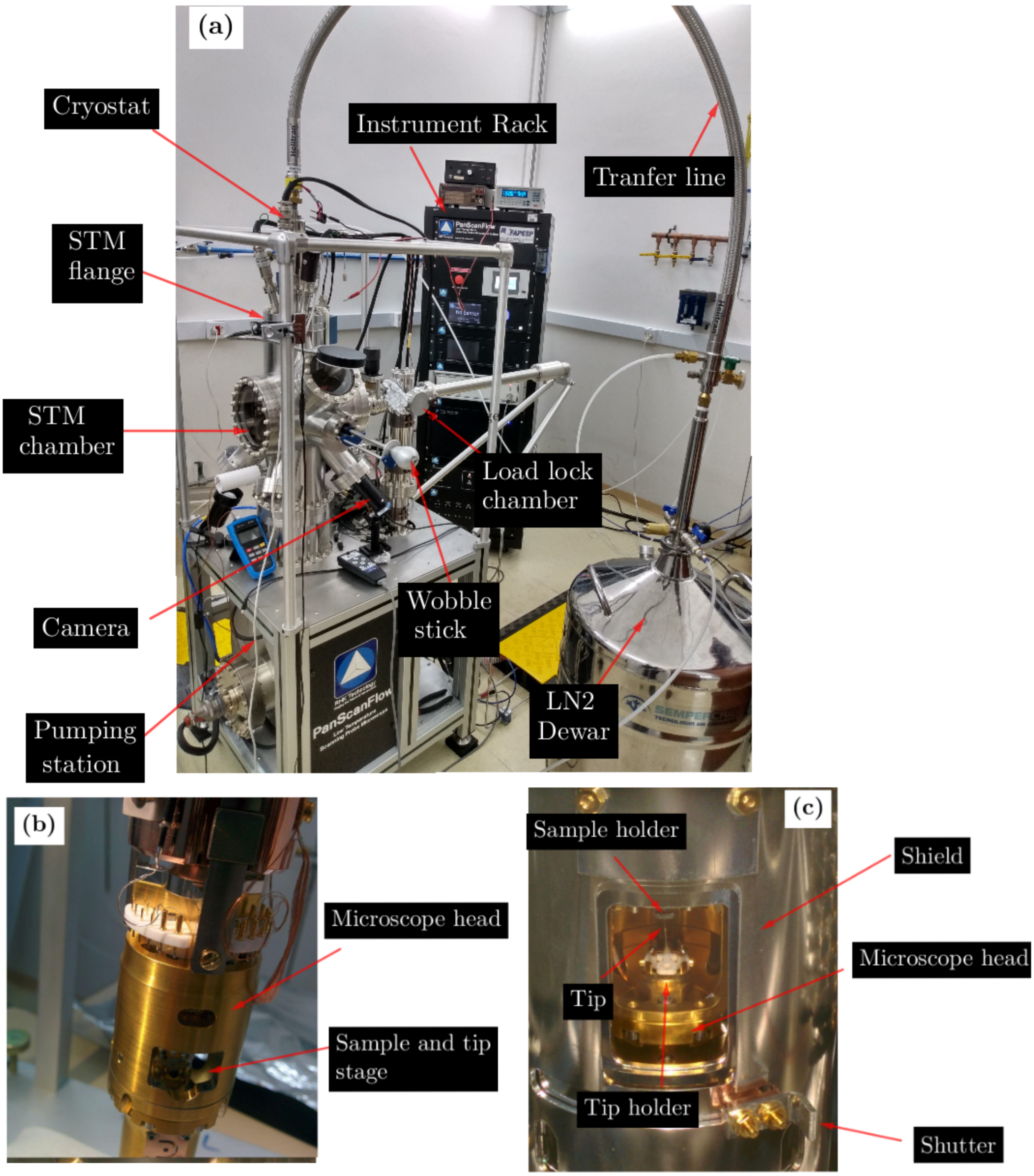

Figure 3.16: (a) Description of the UHV-LT STM system. (b) PanScan STM head. (c) Sample and tip stages.

liquid, reaching 12 K and 80 K, respectively. Figure 3.16(b) shows the PanScan-type STM head.Figure 3.16(c) shows a view of the tunnel junction configuration, which is externally protected by a set of shields and shutters to optimize thermal insulation.

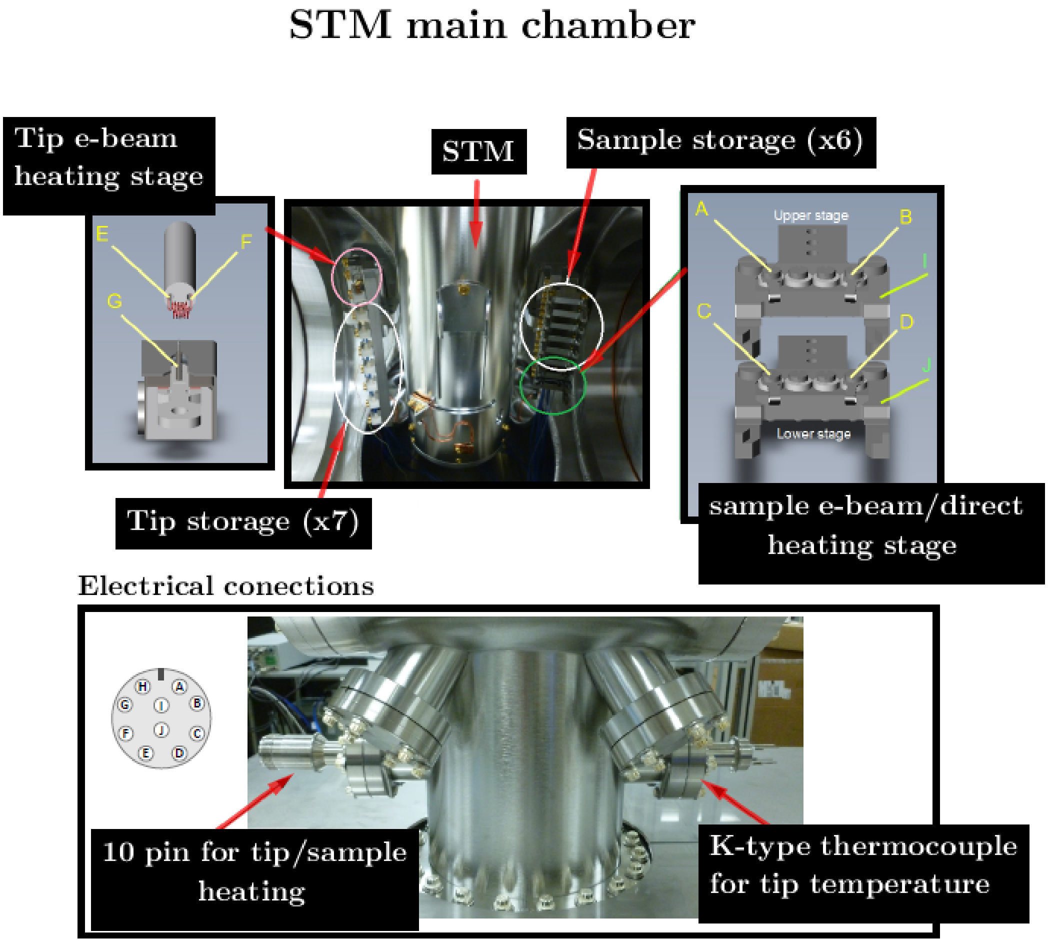

Figure 3.17: Internal view of the main chamber and electrical connections for treatments on tips and samples (images adapted from the STM user manual).

Figure 3.17 shows an internal view of the main chamber of the STM and the external electrical connections for treatments on tips and samples. In this chamber, in addition to the STM head, it is possible to store several samples and tips in a UHV environment. For the cleaning and treatment of samples, it has a heating system by thermal radiation and electron bombardment (e-beam). In some samples, it is possible to perform electrical resistance heating by applying a voltage and passing a DC current through them.

3.3.1 Tip preparation

For all the experiments presented in this thesis, we used platinum-iridium (Pt-Ir, 80:20) and tungsten (W) tips, see Figure 3.18. Pt-Ir tips are prepared by making a diagonal cut in the Pt-Ir wire with scissors or pliers. Figure 3.18(a) shows a Pt-Ir prepared by mechanical cutting. This is a quick and easy method of preparing an STM tip. However, the morphology and shape of the tip apex are random. In the case of W tips, the shape of the tips can be controlled through electrochemical etching processes. For that, a 0.25 mm diameter W wire is introduced in a sodium hydroxide solution (4 g of NaOH in 40 ml of deionized water), as illustrated in Figure 3.18(b), a copper cylinder is used as a counter electrode. When applying a voltage of 3-4 V between the electrodes, the etching process occurs, which causes the wire to thin at the liquid-air interface due to the meniscus formed by the surface tension around the wire. The shape of the tip is defined by the shape of the meniscus. Chemically, what happens in the wire is that W is converted into tungstate anions (WO_4^{-2}, while at the counter electrode, the reduction of water produces the release of hydroxyls (OH-) [15]. When the wire is thin enough, the weight of the part immersed in the solution pulls it down until it fractures. At the instant of wire fracture, the current in the circuit drops drastically to zero, and the voltage source is automatically turned off. The obtained tip is carefully washed with deionized water to eliminate NaOH residues and stored in isopropyl alcohol to be then treated in the UHV chamber of the STM. Figure 3.19 shows a scanning electron microscope (SEM) image of a W tip prepared by electrochemical etching.

(*a*) Pt-Ir tip prepared by mechanical cutting

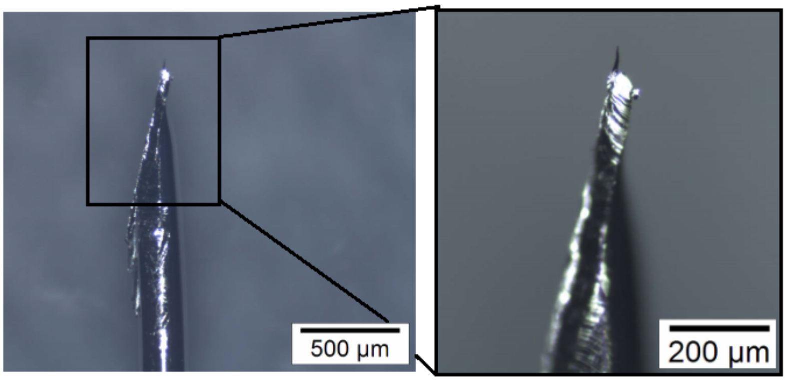

(*b*) W tip prepared by electrochemical etching

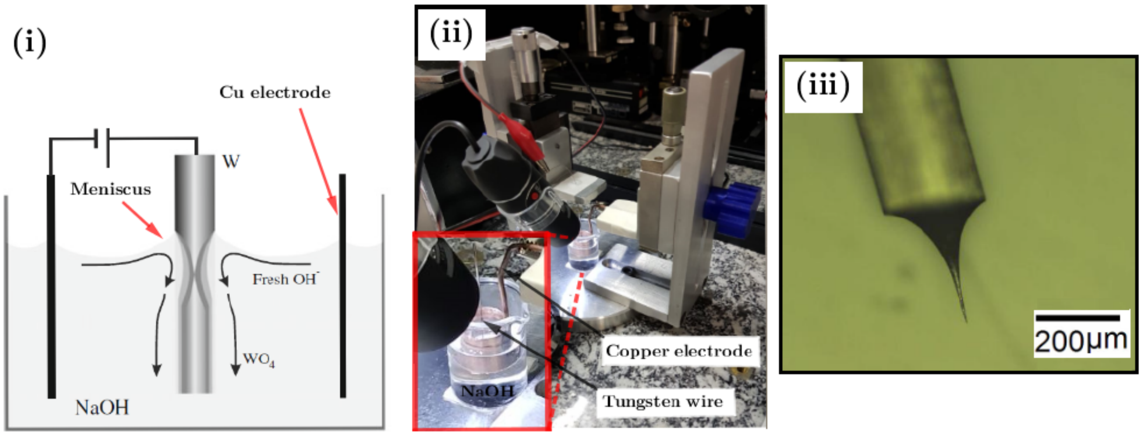

Figure 3.18: Tip preparation for STM. (a) Pt-Ir tip prepared by mechanically cutting the wire with scissors. (b) preparation of W tips: (i) description of the electrochemical etching process (adapted from [15]), (ii) tip preparation system from our laboratory, and (iii) example of a W tip obtained by electrochemical etching.

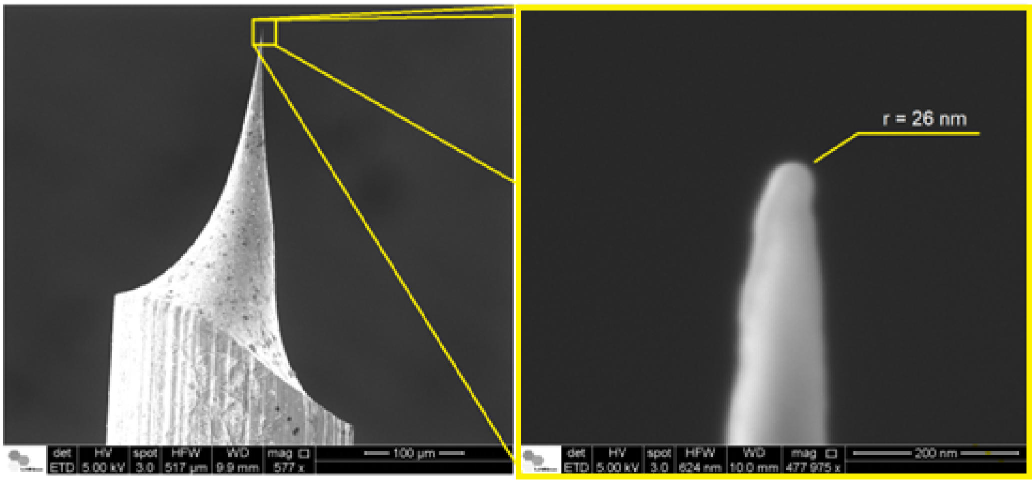

Figure 3.19: SEM images of a typical W tip.

3.3.2 Light collection system

To perform STM-LE and STM-CL measurements, we need to use an optical system to collect the emitted light in the tunneling junction. The next chapter presents a new light collection system developed and implemented during this Ph.D. project.

3.4 Sample preparation and methods

Monolayers of WSe_2 were prepared by the mechanical exfoliation method. We used a p-type WSe_2 single-crystal purchased from HQ Graphene. The monolayers were transferred to gold thin film (~100 nm of thickness) substrates. The samples were prepared and provided by Dr. Ingrid David Barcelos from Brazilian Synchrotron Light Laboratory (LNLS) and the Brazilian Center for Research in Energy and Materials (CNPEM) in Campinas, São Paulo Brazil. In total, we investigated six samples of monolayer WSe_2 on gold. Some samples were studied under UHV conditions (~$5x10^{-10}$ mbar) at room temperature (RT) by STM and STS to explore the properties of point defects and sample doping. Before STM/STS measurements, the samples were cleaned by mild thermal annealing at 400 K for 12 hours under UHV. The sample-substrate coupling was investigated by combining PL/Raman and AFM (tapping mode) measurements in ambient conditions on as-prepared and thermal annealed samples. STM-LE measurements were performed in air and at RT in as-transferred monolayers.

We used a Horiba MicroRaman system for *ex-situ* Raman/PL (outside the STM). The system uses a 532 nm laser with a spot size of 2 μm. The excitation power was 10 μW. We employed both a Nanosurf EasyScan2 Flex AFM and a Bruker/Veeco Innova AFM for the acquisitions of AFM images. The STM-LE experiments were performed using the RHK STM with an optical system based on an off-axis parabolic mirror to collect and inject light inside the STM. In this setup (described in the next chapter), STM-LE and *in situ* PL can be performed. For STM-LE, we used the STM tip as a nanoscale excitation source with tunneling currents between 25-90 nA and a sample bias voltges of 2.0-4.0 V. For PL, we used a 532 nm laser diode operated below 100 μW of power, the spot size of the light focused by the mirror on the sample surface is about 2 μm. Spectra are recorded using an imaging spectrometer coupled to a cooled CCD camera.

In *in situ* PL experiments, the tip is retracted from the sample. STM-LE signal can also be recorded panchromatically using a photomultiplier tube (PMT). More details about the experimental conditions and complementary techniques can be found in chapter 5 and appendix B, respectively.

Monolayer h-BN was grown on highly oriented pyrolytic graphite (HOPG) by the high-temperature plasma-assisted molecular beam epitaxy method [137]. The sample was grown in the following conditions: substrate temperature of about 1390 ^{o}C with a high-temperature effusion Knudsen cell for boron and a standard Veeco radio-frequency plasma source for active nitrogen. The sample was prepared, provided, and characterized through AFM measurements in ambient conditions by the group of Prof. Peter H Beton and Prof. Sergei V Novikov from the School of Physics and Astronomy at the University of Nottingham in the United Kingdom. This sample was also optically characterized using deep ultraviolet PL by the group of Prof. Guillaume Cassabois and Prof. Bernard Gil from the Laboratoire Charles Coulomb at the Université de Montpellier in France. They measured the PL spectrum of the sample at 10 K, using an excitation beam provided by the fourth harmonic of a CW mode-locked Ti: Sa oscillator with a repetition of 82 MHz. The spot size is of the order of 50 μm, with an excitation power of 30 μW .

Our group investigated the sample surface morphology and its electronic properties using STM/STS.. These measurements were performed under UHV conditions at low temperature ($\sim$2x10^{-10} mbar at 80 K). The h-BN sample was annealed at 773 K for 6 hours under UHV conditions before STM/STS measurements. We also performed STM-CL and *in situ* PL/Raman (laser of 532 nm and spot size: 2 μm) under UHV and at 100 K and RT. STM-CL was carried out by operation of the STM in field emission mode. For that, the STM tip was retracted around 150 nm from the h-BN sample surface. After that, a high bias voltage between 150 and 180 V was applied to the sample, which caused field emission currents of 5–10 μA. As a voltage source and amperemeter, we used a KEITHLEY electrometer model 6517A. More details about the experimental conditions can be found in chapter 6.

Chapter 4

Using an off-axis parabolic mirror in an optical device for luminescence experiments in STM

This chapter contains a manuscript reproduced from:

Ricardo Javier Peña Román, Yves Auad, Lucas Grasso, Lázaro Padilha, Fernando Alvarez, Ingrid David Barcelos, Mathieu Kociak, and Luiz Fernando Zagonel

Design and implementation of a device based on an off-axis parabolic mirror to perform luminescence experiments in a Scanning Tunneling Microscope

Review of Scientific Instruments 93, 043704 (2022), with the permission of AIP Publishing.

The light emitted locally around the STM tip position is very weak in STM-LE measurements. The light emission yield is at most 10^{-4} to 10^{-6} photons per tunneling electron [105], depending on the system under investigation. Moreover, due to the low current in STM, usually from 10 pA to 10 nA, we should expect luminescence signals coming from the tunneling junction with 10^{1}-10^{7} photons per second. Therefore, optical characterizations of materials through luminescence spectroscopy in STM require the implementation of optical setups with a high collection and transmission efficiencies.

The integration of light collection devices to STM microscopes is a challenge, mainly because the space around the tunneling junction is minimal, and in some cases, STMs need to be constructed specifically to allow luminescence studies [138]. Recently, K. Edelmann et al. [139], proposed a light collection approach where the STM tip itself was integrated inside a light-collecting mirror in a Low-Temperature and Ultra High Vacuum STM (LT-UHV STM), reaching 75% of collection efficiency. Another high collection efficiency system consists in coupling an STM head to an inverted optical microscope using a high numerical aperture oil immersion objective lens to reach 69% collection efficiently in air [140]. Other approaches have been proposed from which one could point out a few using lenses [100, 141–143], mirrors, [144–146] or optical fibers [105, 147]. Some of these approaches have light collection efficiencies below 10%, and some are below 1%, limiting their practical use. Thus, systems with higher efficiencies operate only in air or are restricted to specially designed STMs.

This chapter presents an alternative approach to a light collection system in luminescence experiments in STM. Our approach consists of an optical device based on an off-axis parabolic mirror designed to have a collection efficiency of 72%. The mirror is placed between the sample surface and the STM tip holder, and it can be introduced or retracted from the STM head when necessary. In addition, the whole light collection, transmission, and detection scheme is designed to have a high collection efficiency with minimum transmission loss while keeping a spectral resolution of about 0.5 nm. We explore the coupling of this optical device to an adapted LT-UHV PanScan STM and its implementation for performing different kinds of luminescence measurements in STM.

In the following, we present the results published in **Review of Scientific Instruments 93, 043704 (2022).**

Reproduced from: Review of Scientific Instruments 93, 043704 (2022); https://doi.org/10.1063/5.0078423

Design and implementation of a device based on an off-axis parabolic mirror to perform luminescence experiments in a Scanning Tunneling Microscope

Ricardo Javier Peña Román,[1] Yves Auad,[1] Lucas Grasso,[1] Lázaro Padilha,[1] Fernando Alvarez,[1] Ingrid David Barcelos,[2] Mathieu Kociak,[3] and Luiz Fernando Zagonel[1, a)]
[1)]*"Gleb Wataghin" Institute of Physics, University of Campinas – UNICAMP, 13083-859, Campinas, SP, Brazil.*
[2)]*Brazilian Synchrotron Light Laboratory (LNLS), Brazilian Center for Research in Energy and Materials (CNPEM), 13083-970, Campinas, SP, Brazil.*
[3)]*Université Paris-Saclay, CNRS, Laboratoire de Physique des Solides, 91405, Orsay, France*

We present the design, the implementation, and illustrative results of a light collection/injection strategy based on an off-axis parabolic mirror collector for a low-temperature Scanning Tunneling Microscope (STM). This device allows to perform STM induced Light Emission (STM-LE) and Cathodoluminescence (STM-CL) experiments as well as *in situ* Photoluminescence (PL) and Raman spectroscopy as complementary techniques. Considering the *Étendue* conservation and using an off-axis parabolic mirror, it is possible to design a light collection and injection system that displays 72% of collection efficiency (considering the hemisphere above the sample surface) while maintaining high spectral resolution and minimizing signal loss. The performance of the STM is tested by atomically resolved images and scanning tunneling spectroscopy results on standard sample surfaces. The capabilities of our system are demonstrated by performing STM-LE on metallic surfaces and 2D semiconducting samples, observing both plasmonic and excitonic emissions. Also, we carried out *in situ* PL measurements on semiconducting monolayers and quantum dots, and *in situ* Raman on graphite and hexagonal boron nitride (h-BN) samples. Additionally, STM-CL and PL were obtained on monolayer h-BN gathering luminescence spectra that are typically associated with intragap states related to carbon defects. The results show that the flexible and efficient light injection and collection device based on an off-axis parabolic mirror is a powerful tool to study several types of nanostructures with multiple spectroscopic techniques in correlation with their morphology at the atomic scale and electronic structure.

I. INTRODUCTION

In the past decades, quantum-confined structures, plasmonic nanostructures, and other optically active systems which rely on nanoscopic details of their morphology or electronic structure have been extensively created, studied, and applied in several fields.[1] This is particularly true for III-V, III-N, II-VI quantum structures which can form Quantum Dots (QDots) and Nanowires (NW) of great interest in nanotechnology.[2–5]. More recently, monolayers of some two-dimensional (2D) materials like the transition metal dichalcogenides (TMDs) are of great technological interest due to their direct band gap.[6–9] Moreover, the quantum efficiency (QE) of some 2D materials has been observed to depend on the defect density.[10–13] In general, objects of interest in nanotechnology are smaller than the optical diffraction limit and so are the relevant details in their structure, including point defects which are in the atomic scale. Widespread spectroscopic investigations by optical absorption or photoluminescence (PL) are hence usually limited to ensembles of these materials and cannot resolve some relevant features of their light emission and morphology.

Therefore, techniques with spatial resolution in the nanometric or atomic scales and spectroscopic capabilities in the meV are thus necessary for many problems in the field. [1,14,15] Two analog but completely different approaches are known to reach atomic resolution and provide spectroscopy data. On the one hand, using fast electrons, (Scanning) Transmission Electron microscopes ((S)TEM) provide atomic resolution imaging with several contrast methods and also spectroscopic techniques like Electron Energy Loss Spectroscopy (EELS). In the IR to UV range, EELS gives access to several physical properties such as dielectric function and band gap, as well as to different physical excitation including plasmons, excitons, and phonons.[15] On the other hand, using a physical probe with low energy electrons, Scanning Tunneling Microscopy (STM) also reaches atomic resolution and provides a spectroscopic technique to measure the local densities of states (LDOS) in the conduction and valence bands by means of Scanning Tunneling Spectroscopy (STS).[16,17] Moreover, beyond electronic spectroscopic techniques, both STEM and STM can be associated with light collection devices to perform cathodoluminescence (STEM-CL) and STM Induced Light Emission (STM-LE), respectively. Recent reviews have been published about these two techniques highlighting, in several physical systems, the great potential and interest of locally and electrically excited luminescence.[18,19] It is important to mention that CL can also be performed similarly in Scanning Electron Microscopes (SEMs) with similar interests as in STEMs and was the subject of a recent review as well.[20] In particular, and within the scope of the present work, STM-LE has already yielded great insights for plasmonics,

---

[a)]Electronic mail: The author to whom correspondence may be addressed: zagonel@ifi.unicamp.br.

oxides, molecules, III-V and II-VI semiconductors among others[21–26] and more recently in the 2D semiconductors $MoSe_2$ and WSe_2.[27–30]

One key issue in STM-LE studies is the light collection strategy since the light emission yield is about 10^{-4} to 10^{-6} photons per electron[31]. Such quantum yield is much smaller than what is achieved by STEM-CL for instance, which can be as high as 1 photon per electron[18,32]. Nevertheless, the collection efficiency is optimized for STEM-CL to provide sufficient spectral signal-to-noise ratio and acquisition speed. In STM-LE, given the tunneling current typically used in STM, typically from 10 pA to 10 nA, one would not expect much more than about 10^7 photons per second (p/s) from a tunneling junction, and as few as 10^1 p/s might be extracted in some cases. Knowing that, it is no surprise if the light collection efficiency and transmission efficiency is even more critical in STM-LE than in STEM-CL.

Integrating efficient light collection devices in an STM is not easy and therefore several strategies have been considered and some STMs were constructed specifically to allow STM-LE studies.[33] In a recent paper by K. Edelmann et al.[34], for instance, the STM tip itself was integrated inside a light collecting mirror in a Low-Temperature and Ultra High Vacuum STM (LT-UHV STM), reaching 75% of collection efficiency. Using another high collection efficiency device, E. Le Moal et al. employed an STM mounted on an inverted optical microscope using a high numerical aperture oil immersion objective lens to reach 69% collection efficiently in air with the added benefit of the ability to perform Fourier imaging.[23] Many other approaches have been proposed from which one could single out a few using lenses[35–38], mirrors,[39–41] or optical fibers[31,42]. Some of these approaches have light collection efficiencies below 10%, some of them below 1%, limiting very much their practical use. Some systems with higher efficiencies operate only in air or are restricted to specially designed STMs. However, despite all efforts, light collection systems compatible with adapted versions of commercially available LT UHV STM and with collection efficiencies above 50 % are still sparse.

In this paper, we present the design criteria, some conception aspects, and representative results from an alternative approach to light collection and injection in an LT-UHV STM reaching a collection efficiency of about 72% of the hemisphere. In our approach, an off-axis parabolic mirror is placed between the sample surface and the STM tip holder. A hole in the mirror allows the tip to reach the sample surface. The tunneling junction is at the focal point of the parabolic mirror and hence the collected light is collimated and sent to the exterior of the UHV chamber through a vacuum viewport. The whole light collection, transmission, and detection scheme is designed to have a high collection efficiency associated with a high spectroscopic resolution with minimum transmission loss. Also, the device is compatible with most commercial Pan STMs after need adaptations. In this work, we show results obtained with the specially modified STM demonstrating its performance at LT and room temperature (RT) on Highly Oriented Pyrolytic Graphite (HOPG), Si(111)-7x7, and WSe_2 surfaces. Also, we have performed luminescence measurements in different conditions and samples. First, we show STM-LE under UHV at LT temperature on a gold (111) surface to observe the plasmonic emission from the tunneling junction. We also show *in situ* PL measurements on WSe_2 monolayers and spherical core-shell quantum dots as well as *in situ* Raman measurements on HOPG substrate under UHV conditions. In an exfoliated WSe_2 monolayers on a gold thin film substrate, we observed excitonic emission and also plasmonic emission from the substrate, both excited by the tunnel current. At RT and 100 K, we observed PL ad STM-CL from defects on a monolayer of h-BN. Finally, with the STM in air, we show STM-LE in exfoliated WSe_2 monolayers on a gold substrate.

II. DEVICE DESIGN FOR LUMINESCENCE IN STM

A. General design guidelines

Among the several possibilities of light collection devices for STMs (mirror, lens, fibers) and also the different STM strategies (Pan design, Beatle design, or others) and operating conditions (LT, RT, UHV, or in Air), some choices and compromises are always made. Detailed discussion about the design of STMs can be found in references[43,44] while a review discussing light collection strategies is given in ref[45]. In this paper, we discuss a solution consisting of the development of a high-performance add-on accessory to suitable Pan STMs. In this sense, for the combined STM and optical device for light collection and injection, we considered the following compromises:

- The device must be compatible with an STM able of being operated at LT (chilled tip and sample), UHV, or in air; STM tips should be readily exchangeable in vacuum; STM modifications to accommodate the device should be minimal;
- The device should have a high solid angle, at least higher than 50% of the hemisphere (collection solid angle > 3 sr), have efficient transmission up to the detector, and display to high spectral resolution (suitable for *in situ* Raman spectroscopy);
- The optical device for light injection and collection must be compatible with several optical experiments, including PL and Raman spectroscopy, for instance;
- Any effects of the light collector on the performance of the STM in regular imaging and spectroscopic measurements should be negligible when not in use;
- The alignment of the light collection system should be sufficiently accurate to assure its performance.

A suitable STM design for such light collection and injection device is the Pan design: the tip has coarse approach motion and all scanning axis while the sample has coarse motion in the plane.[44] It is very rigid, allows easy tip exchange, and is compatible with low-temperature

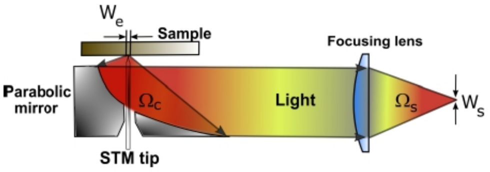

FIG. 1. Illustration of the basic elements (solid angles and widths) to be considered in the Luminance/*Étendue* conservation.

operation. Pan design also allows sufficient clearance for mirrors with high NA. Using a Pan STM, the mirror is aligned with the tunneling junction as defined by the tip position. Moving the sample does not affect the mirror alignment and positioning regions of interest under the tip is possible without affecting the mirror alignment. In this paper, we discuss the performance of this optical device as installed in a adaped UHV PanScan Flow Cryo STM from RHK Technology. From the optical device point of view, the PanScan has the added advantage that only minor modifications were needed to make it compatible with the insertion of the device (see Sec. II E).

B. Optical design considerations

Given the definition of the major general design points regarding the STM and the parabolic mirror, the whole light transmission chain must be evaluated. For that, the starting point is the Luminance (also called Radiance or Brightness) conservation theorem together with the *Étendue* conservation theorem.[46,47] The Luminance is related to the amount of power emitted by a source and its spacial and angular distributions and can be expressed as:

$$L = \frac{d\Phi}{cos(\theta)d\Omega_c dA} = n^2 \frac{d\Phi}{d\acute{E}tendue_c} \tag{1}$$

Where L is the emitted Luminance collected from the source, n is the refraction index, Φ is the emitted power, $d\Omega_c$ is the differential of collection solid angle, dA is the differential emission area and θ is the angle between the normal to the differential area and the centroid of the differential solid angle.[46] Since we will consider only the power that is actually collected by the Parabolic mirror, the solid angle considered is already that of the collection mirror. Hence, eq. (1) refers already to the collected Luminance. The relation of the Luminance (collected from a source) with the *Étendue* of the collection optics is also given in (1).[47] The *Étendue* is related to the light gathering and light transferring power of an optical system and/or each one of its elements, as discussed in ref.[47,48], and describes the trade-offs in terms of angular and spatial distributions when collecting or transferring light. The *Étendue* is defined as

$$\acute{E}tendue = n^2 \int\int cos(\theta)dAd\Omega \tag{2}$$

and can be seen as the weighted solid angle area product, both for collection and transmission.[47] As this quantity is conserved, it shows that when reducing the solid angle, an increase in area is expected. For clipped Lambertian sources, which is the case that we will consider here as a simple representation of the light emitted by the region being scanned by the STM, the *Étendue* can be expressed as:

$$\acute{E}tendue_{Clip.Lamb.} = n^2 \pi W^2 sin^2 \theta^{max} \tag{3}$$

Where θ^{max} is the maximum angle between the normal of the area W^2 and outer points of the optical element collecting or transferring light, and W is the total width of the area emitting or transmitting light (this considers that the system has rotation symmetry which is not the case for the parabolic mirror).[47] From the emission point of view, W_e is the convolution of the used imaging Field of View (region of the sample been scanned by the STM tip), and the carrier spread on the sample (similarly to the beam spread in TEMS or "ionization pears" in SEMs). Therefore, W_e represents the total width from which emitted light should be collected. Note that θ^{max} is related to the solid angles Ω under consideration, as indicated in Fig. 1 and its differentials $d\Omega$ in eqs. (1) and (2).

The notion of *Étendue* and Luminance (or Brightness, as typically called in the Electron Microscopy community) and its conservation is important in the case of STM-luminescence experiments (and for cathodoluminescence in electron microscopes). Indeed, as already mentioned, the total emitted power Φ is typically small. However, this weakness is counterbalanced by the very small emitting area W_e^2 in the definition of Luminance. In other words, an STM excited luminescent source is a bright, but not an intense, emitter. Preserving Luminance (both in terms of power and in terms of coherence) is therefore essential here. At the same time, large collection angles, represented by Ω_c in Fig. 1 and by θ^{max} in eq. (3), are needed to increase the collected power, Φ.

Luminance is conserved in an ideal optical system, but in reality, it can be reduced, for instance, by aberrations, geometrical and chromatic, that induce an increase of spatial and angular distributions. Also, some Luminance is lost in surface reflections and by apertures that reduce Φ, for instance. Therefore, to preserve the collected power (linked to the measured signal intensity) and the Luminance (linked to spectral resolution, see more on this in the following), each optical element up to the spectrometer should be designed carefully.

Given the Luminance of the source and its conservation, one needs to make sure that the *Étendue* (also called Geometrical Extent) of the optical system is preserved so that none of the collected power is lost. To optimize the spectroscopic optical acquisition chain, it is best to isolate angular and spatial distributions in the spectrometer and collection ends using the *Étendue* for a Lambertian source:

$$\frac{\Phi}{\pi L} = W_e^2 sin^2 \theta_c^{max} \leq W_s^2 sin^2 \theta_s^{max} = \frac{\acute{E}tendue_s}{\pi n^2} \tag{4}$$

Where θ_s^{max} is the angular acceptance at the spectrometer entrance and W_s is the light beam width in the spectrometer dispersive direction. The inequality $\le$ means that the product $W_s^2 sin^2\theta_s^{max}$ should be equal or larger than $W_e^2 sin^2\theta_c^{max}$ to accept all collected light. Simply put, eq. (4) means that there is a trade-off between collection efficiency, related to θ_c^{max}, and field of view, given by W_e, on the sample side, with respect to the spectrometer acceptance angle, θ_s^{max}, and slit width, W_s, on the spectrometer side. Also, eq. (4) means therefore that the spectrometer *Étendue* is a limiting factor to the compromise between light collection efficiency and field of view. Fig. 1 illustrates the solid angles and widths in eq. (4). Note that the angles in eq. (4) refer to conical angular ranges in 3 dimensions and, therefore, relate to the solid angles in space.

In practical terms, most light spectrometers use parallel detectors such as CCDs, and their pixel size together with the spectrometer point spread function (PSF) and magnification define the relation between the entrance slit width and the spectrometer resolution (for a given grating). Indeed, the spectral resolution depends on several parameters, including some intrinsic to the spectrometer (NA, aberrations, grating), some extrinsic (especially the size of the beam at the entrance aperture). The latter needs to be optimized for maximum spectral resolution. It is, therefore, a matter of choosing a target resolution (width of peaks on the CCD) and then injecting the light already with the desired light beam width, W_s. Note that eq. (4) shows the link between the Luminance of the source (left-hand side) and the spectrometer entrance slit width, that is its resolution (right-hand side). Typically, for 25 μm wide pixels, a light beam width of about 100 μm entering the spectrometer is already sufficiently narrow to provide a spectral resolution near the maximum attainable (without even using the slits), since a typical spectrometer magnification is near 1 and its point spread function has a full width at half maximum (FWHM) of about two pixels.

In our setup, for a 600 gr/mm grating, the spectrometer resolution is about 0.22 nm for 10 μm entrance slits and 0.5 nm entering with a beam width of 100 μm (and entrance slits fully open). Such spectral resolution is sufficient for most experiments with semiconductors and can be further increased by changing the grating. Closing the slits to reduce W_s is still possible but it would reduce the spectrometer *Étendue*, causing light loss. Considering a spectrometer with NA=0.12, that is with a maximum acceptance angle of 7°, and using $W_s = 100\ \mu$m, and considering a parabolic mirror with a high numeric aperture with θ_c^{max} about 80° (see Sec. II D), one has:

$$W_e \le \frac{W_s sin\theta_s}{sin\theta_c^{max}} \cong 12\ \mu\text{m} \qquad (5)$$

This means that, provided all light emission comes from a region smaller than $W_e^2 = 12^2\ \mu\text{m}^2$, a high proportion of the emitted light (>70%, see Sec. II D) can be collected and transmitted to the spectrometer without loss into a width $W_s = 100\ \mu$m. Note that if the emission width is larger (or the mirror is misaligned, what is equivalent), the Luminance would be reduced accordingly and signal would be lost. Therefore, the mirror alignment must be accurate in the sub-micrometer range and only a region of a few micrometers can be explored on the sample plane. One must note that in some situations, like in some plasmonic applications, keeping a high spectral resolution is not mandatory. In this case, a larger width at the spectrometer entrance could be used which would ultimately give more flexibility on the light collection optics. To reach larger regions, the mirror could be scanned together with the tip as demonstrated in ref.[34] or the sample could be scanned.[49]

It is important to note that this calculation does not depend on the specific microscope holding the light collection optics and therefore it applies to SEMs and TEMs performing cathodoluminescence and STMs performing STM-LE or other. Another relation between collection efficiency, field of view, entrance slits width, and spectrometer numerical aperture was shown in ref.[49] which was derived using a different approach in two dimensions and provided different values but a very similar trend. Finally, these calculations must be considered as an upper limit for an ideal system with rotation symmetry. A given particular optical system may not reach this value and may have a narrower field of view or alignment tolerance. In particular, off-axis parabolic mirrors are known for their low tolerance to misalignment, and simulations (see in sec. II D) indicate that W_e in our system is smaller than predicted in this model.

A general scheme of the STM together with the light collector is presented in Fig. 2(a). Basically, in the Pan design, the coarse motion of the tip base moves the tip upwards until a tunneling current is observed. At this point, the electronics of the STM control the tip-sample distance using the scanner tube to maintain a constant current. A lateral scan can be performed for imaging in constant tunneling current mode in which the current is held constant by adjusting the tip-sample distance along the scan. Luminescence induced by the tunneling current illuminates the parabolic mirror which directs the light beam as parallel rays towards the outside of the thermal shields and also outside of the UHV chamber to a dedicated collection optics. Note that this approach allows one to exploit all advantages of free space optics for different experiments and for light injection as well. Finally, the coupling to the spectrometer entrance can be accomplished by free optics using only mirrors and lens or additionally using optical fibers.[38,50]

C. Light collection/injection possibilities

Considering that the parabolic mirror reflects all gathered light as a parallel beam to the exterior of the UHV chamber, it is a matter of working with this beam in free optics in air. Therefore, outside the vacuum viewport and on top of an optical table, several experiments are possible. Typically, tunneling current induced luminescence (STM-LE) is sent to the entrance of an optical spectrometer with a CCD detector, as shown in Fig. 2(b). In this way, STM-LE spectra can be acquired for a given tip position and tunneling condition. Moreover, spectral images can be

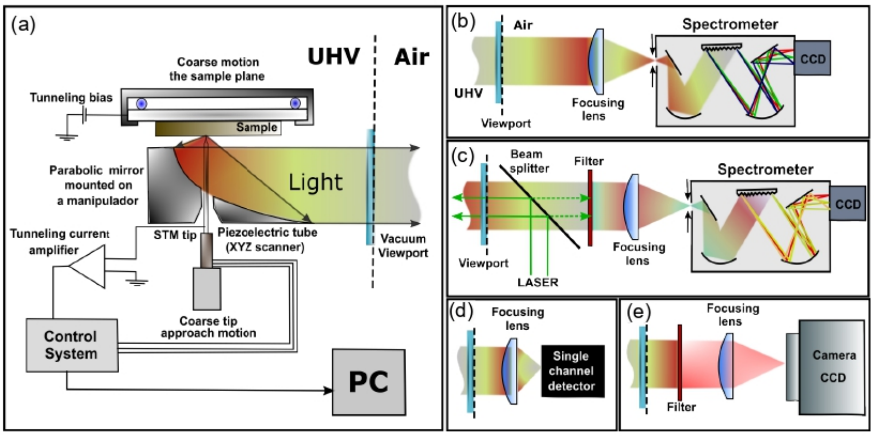

FIG. 2. (a) Scheme of the parabolic mirror inside the STM directing collected rays perpendicularly to the direction of the tip. (b-e) Possible experiments: in (b) all light is directed to the entrance of a spectrometer; in (c) a beam splitter is inserted in the parallel beam path and PL/Raman can be performed; in (d) the light is injected in a large area single channel detector; and in (e) the angular distribution of the emission is recorded by a CCD positioned directly in front of the parallel light beam.

acquired by synchronizing the STM tip scanning with the spectra acquisition. When working under UHV conditions, it is also possible to operate the STM in Field Emission (FE) mode to perform cathodoluminescence experiments (STM-CL). In this case, the STM tip is retracted 100-200 nm from the sample surface and an external voltage source (0-500) V is used to produce an electron beam and excite the sample by electron bombardment.[21,22,51–53]

Alternatively, by adding a laser on the optical table, light can be injected to perform *in situ* PL and Raman experiments (with or without the use of the STM tip), as indicated in Fig. 2(c), similarly to ref[54]. Tip effects can be explored by doing tip-enhanced PL or tip-enhanced Raman spectroscopy (TERS) with appropriate tips, as demonstrated and reviewed in[55–58]. Interestingly, parabolic mirrors are very good in focusing laser beams and hence very suitable for these techniques.[56,59–61] PL can also be useful, for instance, to check that a given sample is optically active *in situ*. The laser spot size is estimated as smaller than 2 μm as observed from sample damage (dark spots observed on samples after PL experiments).

Another possibility, shown in Fig. 2(d), consists in directing the light to the entrance of a large area single channel detector, like a photo-multiplier tube (PMT) or a photodiode, which can be useful to perform luminescence mapping.[27] This mode is also interesting for QE measurements. Indeed, some single channel detectors have well documented QE and it is possible to measure the quantum yield of a given sample in a specific tunneling condition. This is relevant when absolute quantum yield is required and a good mean of comparing data among different setups. Also, in this setup, only the viewport and one lens are placed between and mirror and a large area detector (which minimizes any possible misalignment loss). This ensures low and controlled light loss such that detector counts can be accurately related to emitted photons. This is not exactly the case for the setup in Fig. 2(b) since some elements in the optical path are less accurately known and, most importantly, the CCD QE is not always well-known.[62]

Finally, by placing a CCD camera in front of the mirror, as shown in Fig. 2(e), angle-resolved emission patterns can be recorded, similarly as has been done by Le Moal, et al.[23] and indicated by Romero, et al.[63]. This strategy has been extensively used in SEMs in A. Polman Group.[64,65]. This mode is particularly relevant to assist the understanding of the light emission mechanism.[27] As shown in Fig. 2(e), a filter (and also a polarizer) can be used to distinguish among different light signals.

Another possible experiment is coincidence detection: using a beam splitter and two single channel detectors[66–68]. It must be noted that such experiments are possible with off-axis parabolic mirrors as demonstrated in STEM and SEM[18,20,69] and have also been demonstrated in STM-LE (using lens or mirrors)[20].

D. Optical Simulations

Taking into account all design considerations that defined the key aspects of the light detection device, it is important to determine its efficiency and usability by simulations. Indeed, the model presented in eq. (4) refers to systems with rotation symmetry, considers a clipped Lambertian source, and considers that the optics is in fact aligned. Simulations can evaluate the system for an isotropic source, can consider the actual mirror shape, and consider the misalignment properly, that is: the source is outside of the focal point (and not an extended source). For that, we have performed optical ray trace simulations using homemade software.[70] Here, simulations consider the light source as a dimensionless isotropic emitter. This source model represents an individual

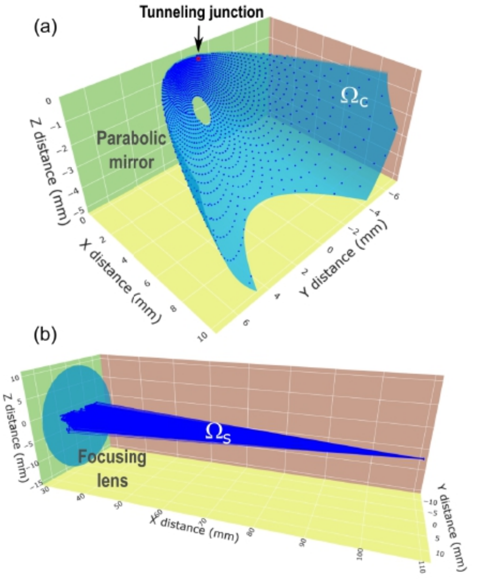

FIG. 3. Typical visualization to inspect the transmission of isotropic light rays emitted by the tunneling junction (red point in (a)) up to the spectrometer entrance. (a) Emission from the isotropic source is collected by the parabolic mirror. Each blue dot indicates where a given ray from the source hit the mirror (semitransparent blue surface). (b) Rays are focused by a lens (semitransparent blue surface) into the spectrometer entrance. Each line indicates the path light ray that was collected by the mirror and send to the lens and is shown to focus into a small region corresponding to the position of the spectrometer entrance.

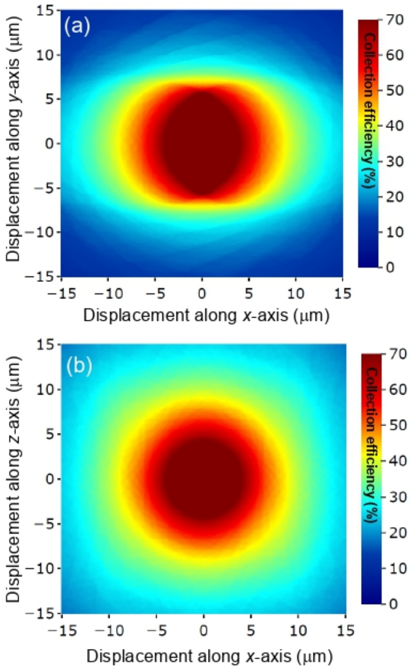

FIG. 4. Heat map that shows the collection efficiency (in %) as a function of the position of a point emitter in the sample plane, x-y, (a) and out of the plane, z-x, (b). The dark red region has maximum collection and corresponds to the W_e region.

emitter for a fixed STM tip position. The source is moved on the surface plane to account for the scanning and charge carrier spread. Diffraction effects are not taken into account.

Optical ray trace simulations follow individual light rays from the isotropic emitter along the optical path (parabolic mirror and focusing lens) up to the spectrometer entrance (or the optical fiber entrance). The code considers a large number of rays for statistical relevance and provides detailed information on the outcome of each light ray emitted from the source. From the simulations, the collection solid angle of the mirror employed was determined to be 72% of 2π, that is, 72% of the hemisphere or 4.5 sr, with an θ_{max} of about 80°. This compares well to recent publications in the field such as 75% in ref.[34] for a similar LT UHV STM or 69% in ref.[23] for an air STM also capable of Fourier imaging. Moreover, as discussed previously, the initial *Étendue* is preserved up to the spectrometer in the proposed design, which gives high spectral resolution (0.5 nm as discussed in Sec. II C) and high transmission efficiency of ($\approx$ 50% as discussed in Sec. II E).

Fig. 3 shows one example of a visualization of such simulations. Fig. 3(a) shows the position where light rays from an isotropic source hit the mirror surface. After hitting the mirror, the light follows as parallel rays to the focusing lens. In Fig. 3(b), the lens focuses the rays in the optical fibers (equivalent to the spectrometer entrance). This kind of visualization can be used to inspect the simulation and understand the light path from the source, for instance.

The result of another relevant simulation is the region on the sample that can be scanned without loss of collection efficiency. Indeed, as observed in eq. (5), the higher the numerical aperture (collection solid angle), the smaller the field of view for a given *Étendue* (and similarly for the depth of focus).[49] As mentioned, given the mirror geometry, calculating the region of emission with maximum *Étendue* also provides information about the misalignment the mirror can sustain without significant collection loss as moving the tip is equivalent to moving the mirror. A typical result of such simulation in the case of our system is shown in Fig. 4.

Figures 4(a) and 4(b) show the area which preserves optimum collection (dark red area) on our system. They indicate that the mirror and the light source can be about 5 μm apart in any direction without loss of efficiency. This indicates both the region that can be scanned by the STM tip and the mirror alignment tolerance. Eq. (5) can not predict this region accurately as it does not take into account some aspects of the actual optical system. The most relevant difference is that eq. (5) considers an extended source with area W_e^2 (Lambertian source) while simulation in Fig. 4 considers a point source (isotropic emitter) that is moved in the same plane (sample

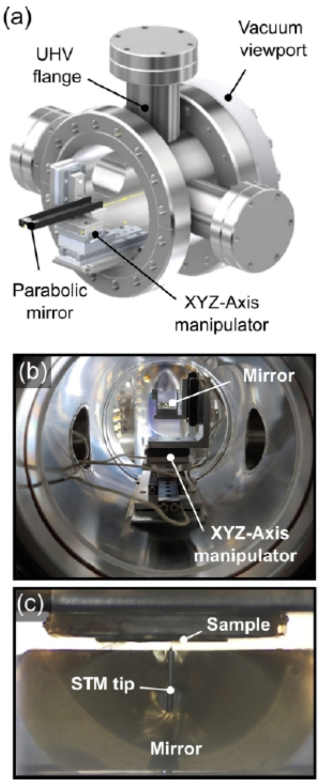

FIG. 5. (a) Optical device chamber with the manipulator and the mirror in a standby position. (b) A picture of the manipulator as observed from the rear. (c) A picture of the mirror showing an STM tip and the sample.

surface plane), which better represents the actual physical system (particularly for charge carrier diffusion length smaller than 1 μm). Another difference between the model and optical system is the absence of rotational symmetry (needed in the model). Also, the simulations consider the exact mirror shape while the simulations use only its angular aperture θ_{max}.

The results in Fig. 4 also recall that, again similarly with STEM-CL, STM-LE is a method that excites very locally but collects globally.[18,32,71] That means that one knows where carriers where injected or where the excitation source is with great precision (possibly in the atomic scale), however the emission can happen more than a micrometer away as already observed in TMDs.[27] In our case, the whole area in Fig. 4 is collected and hence the emission could come from anywhere in that area. This is very different from confocal optical microscopy, for instance, in which both injection and collection are related to a small area.

E. Optical device implementation

Considering the design criteria in Sec. II A and the alignment demands in Sec. II B and II D, we chose to use a piezo-driven manipulator with a long arm that holds the mirror. To implement it, we build a small chamber, as shown in Fig. 5(a). Such manipulator can place the tunneling junction at the focal point of the mirror and also retract the mirror outside the STM thermal shields. When the mirror is retracted, the STM thermal shields can be fully closed as usual. In this design, the manipulator and its mirror never enter in mechanical contact with the STM body or thermal shields. Fig. 5(a) displays a computer-aided design (CAD) drawing of the chamber where the manipulator is installed. Fig. 5(b) shows a picture of the manipulator from the rear of the chamber (viewport side). In Fig. 5(c), it is possible to see a picture of the mirror showing the STM tip passing through the mirror hole and the sample on the top. It is worth mentioning that the tip length has to be a bit longer than usual to pass through the mirror. Therefore, we adapted the tip holder and we could not notice a significant difference in image quality using the standard tip holder with short tips or the adapted tip holder with slightly longer tips (see Sec. III).

Modifications were needed to adapt the RHK PanScan STM body, thermal shields, and chamber to receive the optical device. Openings on the rear of the STM and thermal shields were added or adapted to allow the positioning of the mirror. Fig. 6 shows the optical device chamber attached to the STM main chamber and, in the insert, the mirror in position with the arm of the manipulator passing through the thermal shield and STM body.

The fact that the mirror is mechanically decoupled from the STM has advantages and drawbacks. When not in use, surely, the performance of the STM is not affected by the optical device. However, inserting the mirror in position will drive thermal instabilities. That is basically because the STM has a weak thermal link to the cryostat to avoid strong mechanical coupling. Hence, at the moment, the operation is more stable when the optical device is used with the STM at room temperature. In some physical systems such as WSe_2 monolayers, that is, in fact, the best temperature to operate.[9,72] Nevertheless, using the optical system at LT is feasible depending on the tolerance to thermal drifts one can bear. Also, simple modifications can be done to cool the mirror and allow stable measurements at low-temperature as well.

Outside the viewport indicated in the drawing of Fig. 5(a), several optical experiments can be realized, as discussed in sec. II B and shown in Fig. 2. Most importantly, for spectroscopy, the light collection system to perform STM-LE contains only 3 refractive optical elements (the vacuum viewport, one lens, and the optical fiber), and hence surface reflection loss is kept small. The total collection/transmission efficiency of the system at 750 nm can be estimated as 50% (considering from the collection inside the STM up to reaching the spectrometer CCD but without considering the CCD QE) with a spectral resolution of 0.5 nm (for a 600 gr/mm grating). In this calculation, we considered initial

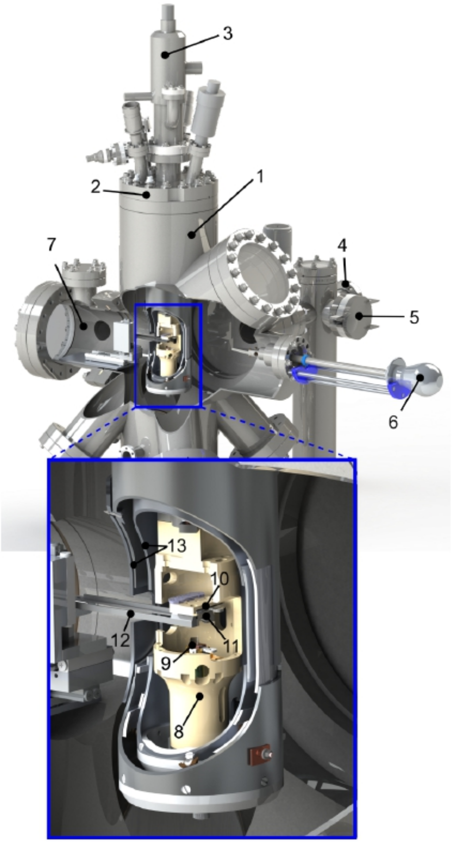

FIG. 6. CAD view of the RHK STM body and thermal shield revealing the opening and showing the manipulator of the optical device holding the mirror in a measurement position. (1) UHV main chamber, (2) STM flange, (3) cryostat, (4) transfer arm, (5) load-lock chamber, (6) wobble stick, (7) optical device chamber, (8) STM head, (9) STM tip, (10) sample, (11) mirror, (12) manipulator arm (mirror support), and (13) thermal shields.

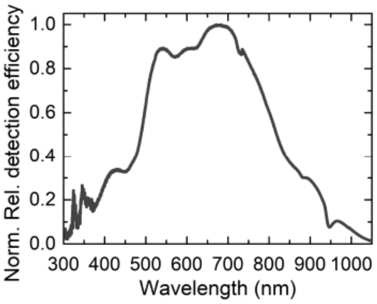

FIG. 7. Instrument response function for a 300 gr/mm diffraction grating blazed at 600 nm.

collection (72%), refractive surface reflections (3% each), and grating efficiency (80%). Other gratings can be used with higher groove density (for Raman spectroscopy, for instance) or lower groove density (for spectroscopy of plasmonic modes, for instance). Note that the careful matching of all optical elements and their correct alignment, as discussed in II B, allowed the reduction of light loss to a minimum and reaching such collection/transmission efficiency with 0.5 nm spectral resolution (at 750 nm). The efficiency from the collection (mirror) up to the light beam that will hit the CCD detector with a given resolution is a meaningful way to evaluate the performance of a spectroscopy light gathering system.

Due to the wavelength dependent efficiency of each optical element, the (relative) spectrometer response as a function of the wavelength has to be determined experimentally. This is particularly important when dealing with large spectra, like those of plasmonic emission, or spectra ranging in spectral regions with significant efficiency variation. Fig. 7 shows a typical instrument response function of our setup in its current configuration. The efficiency increase from 300 nm to 600 nm is mostly due to the grating (with some features due to the CCD) while the fall from 700 nm to 1000 nm is mostly due to the CCD. Some absorption regions are noted at ≈720 nm, ≈ 880 nm, and ≈ 940 nm and are due to absorption in the coupling optical fiber. This curve can be used to correct spectra and compensate for the different efficiencies along the available spectral range. STM-LE spectra in Sec. IV A were corrected using such a curve.

III. STM PERFORMANCE

We evaluated the performance of the STM after the modifications mentioned previously by performing STM images and STS on some samples at hand. These tests were performed after the installation of the light collection/injection device and the usual bake-out of the whole system (including the optical device). The chamber pressure remained near $2\text{x}10^{-11}$ mbar after the installation. The results presented in this section were obtained with the mirror fully retracted and the thermal shields fully closed. That is the usual condition for STM/STS operation. The typical temperatures using LHe and LN$_2$ as coolant were 12 K and 80 K, respectively. These temperatures were fairly easy to reach and stable to maintain using a temperature controller. Fig. 8 shows a set of STM images and STS curves obtained operating the STM at LT. The STM images were acquired in constant-current mode with electrochemically etched tungsten tips, and using the adapted tip holder with slightly longer tips (suitable for luminescence experiments). For image processing, the WSXM [73] and Gwyddion [74] software were used. The STS curves were taken using a lock-in after obtaining stable topographic images.[44]

Fig. 8(a)-(c) show STM/STS results obtained in a HOPG sample and operating the microscope at 12 K. Before the measurements, the HOPG crystal has been cleaved in air using an adhesive tape and promptly introduced into the

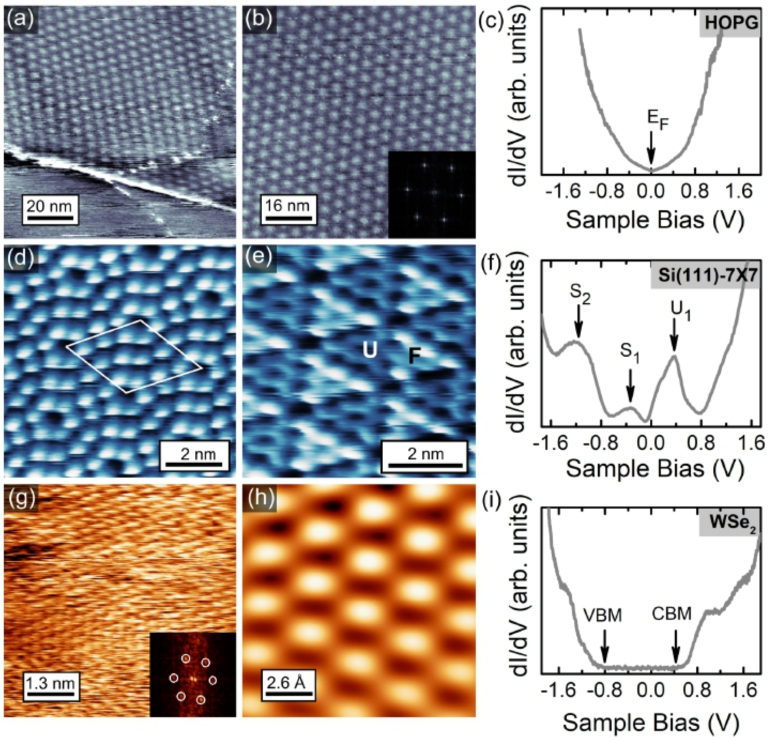

FIG. 8. STM images of Moiré pattern in HOPG measured at 12 K and with tunneling parameters of (a) 1.5 V, 300 pA and (b) 1.5 V, 500 pA. Inset: Fast Fourier Transform (FFT) pattern. (c) STS curve measured on HOPG (40 mV, 0.65 kHz). (d) STM image for the empty (0.7 V, 200 pA) and (e) filled (-1.8 V, 200 pA) states of the Si(111)-7x7 surface reconstruction at 80 K. (f) STS curve of Si(111)-7x7 (80 mV, 0.80 kHz). (g) STM image with atomic resolution of the WSe$_2$ surface at 80 K (-3.8 V, -500 pA). Insert: FFT image. (h) FFT filtered image. (i) STS curve obtained in WSe$_2$ (40 mV, 0.65 kHz). All the STS curves were taken at 80 K.

load-lock chamber. Fig. 8(a) shows the Moiré pattern usually found in the HOPG surfaces.[75–79] Moiré patterns are formed by the relative rotation between two graphene layers and its periodicity can be calculated by the equation $D = a/(2sin(\theta/2))$, where a=0.246 nm is the lattice parameter for graphene and θ is the rotation angle between graphene layers. For the structure in Fig. 8(b), the periodicity D was obtained by calculating the average distance between bright spots using different height profiles and also by superimposing a hexagonal lattice to the STM image. A periodicity of $D = 5.0$ nm has been determined which gives a rotation angle $\theta = 2.8^\circ$. Additionally, Fig. 8(c) displays an STS curve taken at 80 K. The result is the expected for graphite, this is, a V-shape LDOS symmetric with respect to the Fermi level[78–81].

The Si(111)-7x7 surface reconstruction was imaged with atomic resolution at 80 K and the results are shown in Fig. 8(d)-(f). The surface was prepared under UHV conditions by flash annealing of a p-type silicon (111) sample. STM images with atomic resolution for both empty and filled surface states[44,82,83] are presented in Fig. 8(d) and (e), respectively. In agreement with the well-known Dimer-Adatom-Stacking Fault model [84,85], in Fig. 8(d) the twelve adatoms inside the unit cell are resolved, while Fig. 8(e) shows the different heights of the faulted (F) and unfaulted (U) part of the unit cell. The LDOS of this sample is given by the STS curve shown in Fig. 8(f), where three electronic states are clearly resolved: one electronic state (U$_1$) at 0.4 V above the Fermi level and two electronic states at -0.3 V (S$_1$) and -1,2 V (S$_2$) below the Fermi level. U$_1$ and S$_1$ are states localized in the adatoms and the S$_2$ in the rest atoms. [44,82,83,85,86]

Finally, also at 80 K, we carried out STM/STS measurements on a thick micro flake of WSe$_2$ mechanically exfoliated and transferred on a p-doped silicon substrate. Fig. 8(g) shows an STM image with atomic resolution of the WSe$_2$ surface. In the inset on Fig. 8(g), an FFT pattern shows the hexagonal periodicity of the structure. Fig. 8(h) displays an FFT filtered image revealing the hexagonal atomic pattern clearly and in agreement with already reported images.[27,87] The STS curve in Fig. 8(i) is typical for a semiconducting sample, where the zero dI/dV region is associated to the electronic band gap of about 1.3 eV, as expected for this material[88,89], and the Fermi level position near the conduction band minimum indicates light n-type doping.

IV. LUMINESCENCE EXPERIMENTS INSIDE THE STM UNDER UHV

In the following, luminescence signals (STM-LE, STM-CL, *in situ* PL, and *in situ* Raman) observed from a metallic surface, from semiconducting systems (Core-shell QDots and WSe_2), and from HOPG and monolayer h-BN are shown as proof of principle of our implementation of the light collection/injection device discussed in Sec. II. The results display the functionality of the light injection and collection device and the potential for forthcoming applications in the study of semiconductor nanostructures. In this section, all the luminescence signals were recorded with the sample inside the RHK Technology PanScan STM and under UHV environment at RT and LT.

A. Plasmon emission on Gold(111) Surface

Metallic surfaces are commonly used to observe the plasmonic light emission in STM-LE experiments. The light emission is originated by the radiative decay of plasmon modes localized in the tunneling junction and excited by inelastic tunneling processes.[19,34,45] Plasmon confinement in the cavity formed by a sharp tip and a metallic surface has emerged as an excellent tool for exploring the light-matter interaction at the nanoscale, and has been employed to measure single-molecule Raman spectroscopy,[90] for instance.

Fig. 9 summarizes some topographic, spectroscopic and optical results obtained on a clean gold surface at LT. The sample consisted of a gold(111) thin film with large atomically flat areas.[91] Before measurements, the sample was heated at 470 K under UHV conditions for removing undesired contaminants. The STM image and the STS curve presented in Fig. 9(a) and (b), respectively, were acquired at 80 K, with the optical device retracted and thermal shields closed. The image shows a surface step with about 0.5 nm of height. The STS reveals the presence of a surface state between -0.5 V and the Fermi level, as expected for the gold surface.[92,93] When the thermal shields were opened and the mirror was inserted into the STM, the sample temperature increased up to 100 K and remained stable for several hours.

Fig. 9(c) shows three STM-LE spectra acquired at different sample biases and a constant tunneling current of 10 nA. The strong plasmonic emission was optimized after forming a gold tip by several indentations of a tungsten tip on the gold surface. The plasmonic spectra presented here are broad peaks whose final shape and maximum depend on the tip condition and geometry.[45,94,95] The inelastic tunneling process involved in the light emission mechanism is put in evidence by the quantum cut-off ($h\nu < eV_{bias}$) of the photons observed in the STM-LE spectra at low bias, from which it is shown that no photon can be emitted with an energy higher than the energy of tunneling electrons.[95] The luminescence spectra presented here were obtained using the setup illustrated in Fig. 2(b) in UHV and at a temperature of 100 K in the sample.

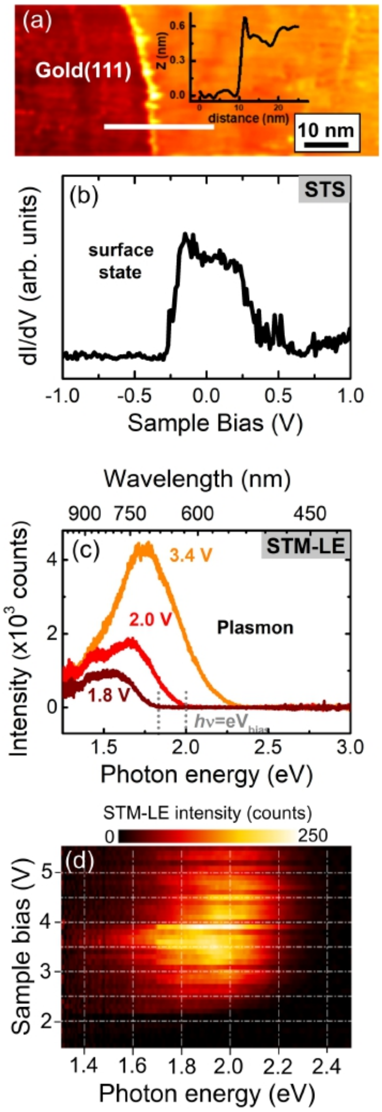

FIG. 9. (a) STM image of the gold(111) surface (-1.5 nA, -210 mV), the inset figure shows the height profile along the surface step. (b) STS curve (80 mV, 0.8 kHz).) (a) and (b) were obtained at 80 K. (c) STM-LE obtained at 3 different bias values with a tunneling current of 10 nA and 30 s acquisition time. (d) Series of spectra as a function of the applied sample bias for a tunneling current of 10 nA and 5 seconds of exposure time. (c) and (d) were measured at 100 K.

The dependence of the plasmonic light emission on the applied sample bias is better characterized by the voltage map shown in Fig 9(d). In this figure, each line represents a spectrum acquired at the samples bias indicated by the vertical axis. The color represents the light intensity recorded by the CCD. The highest count-rate is observed with about 3.5 V. The decrease in emission at higher bias voltages is attributed to the increasing distance between the tip and the surface that happens to keep a constant current at varying sample bias voltages.[34,45]

Changing the optical setup and sending all light into a PMT, as indicated in the setup of Fig. 2(d), we measured the quantum yield of the sample for some tip conditions. In this mode, only the viewport and one lens are between the mirror and the detector. Also, the quantum efficiency of PMTs is well documented allowing a straightforward calculation of the sample quantum yield. This is better than using the setup in 2(b) which has more elements (optical fiber, spectrometer mirrors, and grating and the CCD) that add uncertainty to the quantum yield calculation. For an unreconstructed gold(111) surface, we observed quantum yields between 1.4x10^{-4} to 1.4x10^{-5} photons per electron. This compares well with literature values for systems using lens or optical fibers.[42] This comparison is relevant as it, to a certain extent, validates the calculation of collection efficiency.

B. STS and optical spectroscopy on Quantum Dots

Fig. 10 shows some results obtained on spherical core/shell CdSe/ZnS QDots with a diameter of about 6 nm and deposited on HOPG substrate. Differently from previous STM/STS results, these measurements were carried out with the parabolic mirror inserted inside the STM head and placed between the sample surface and the tip holder, as shown in Fig. 5(c). The data were acquired at RT and under UHV. In general, the acquisition of STM images on QDs is always difficult because the capping ligands on the QDs surface produce instabilities in the tunneling current.[96] Therefore, to evaporate some ligands from the surface of the QDs and improve the STM imaging, before STM measurements the sample was annealed to 415 K for 4 hours in UHV. The inset in Fig. 10(a) shows a large area STM image where regions with one and two layers of QDots are observed. The darkest regions in the image correspond to the HOPG surface. The STS curve presented in the figure was taken fixing the STM tip position on a region with one layer of QDots. This STS curve presents a zero dI/dV region of about 2.7 V and some confined electronic states in the conduction band which are associated with the atomlike energy levels S, P, and D, in perfect agreement with reported STS studies on individual QDots.[97–100] Additionally, as explained above, the parabolic mirror can be used to inject light and measure the *in situ* PL response of the sample. Fig. 10(b) shows the PL spectrum obtained by injecting the laser light of 450 nm which shows an excitonic peak around 1.96 eV (632 nm).

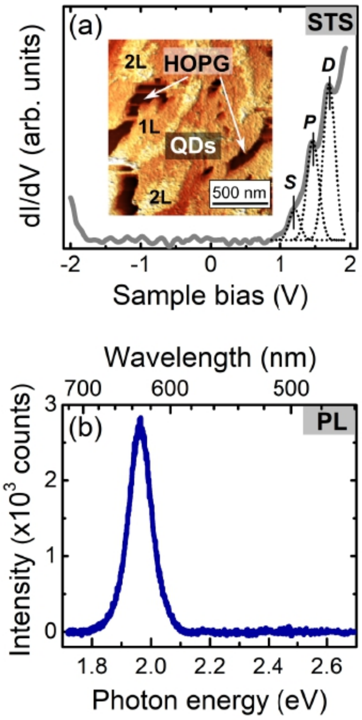

FIG. 10. (a) STS curve (80 mV, 0.80 kHz) of 6 nm CdSe/ZnS QDots on HOPG in UHV conditions and at RT. Inset: Constant-current STM image showing one (1L) and two (2L) layers of Qdots on HOPG (2.5 V, 1.8 nA). (b) PL spectrum on the same region as the inset in (a) obtained on the sample sequentially and with the same conditions as the sample inside the STM.

The possibility of combining STM/STS with *in situ* optical spectroscopy had been demonstrated to be an important approach to investigate the electronic structure and tunneling process in quantum-confined nanostructures.[101,102] On the one hand, STS can give us information about both conduction band (CB) and valence band (VB) confined states, and, on the other hand, optical spectra give access to the allowed optical transitions between the states in the CB and VB. In the case of the results presented in Fig. 10, we have that, in contrast to typical semiconducting surfaces like WSe_2, the electronic band gap of the QD is not given by the zero dI/dV gap region in the STS curve. The reason for that is that QDs are not in ohmic contact with the surface substrate, then a double barrier tunneling junction is formed between the STM tip, the QD, and the HOPG surface. This means that the bias applied to the substrate relative to the STM tip has to be distributed between two tunneling junctions.[96,100] Therefore, the measured gap $\Delta V = 2.7$ eV is always larger than the optical band gap (E_{opt}) of the QD by a factor $1/\eta$, where η corresponds to the ratio between the potential drop in the tip-QD junction and the sample bias. The relation between the zero dI/dV gap with the optical gap is given by the following equation: $\eta \Delta V = E_{\text{opt}} + J_{e-h}$, where J_{e-h} is the electron-hole Coulomb attraction energy.[100,103,104] Considering $J_{e-h} \approx 0.3$ eV as reported for Jdira, *et al* .[103], and taking into account that the maximum of the PL peak in Fig. 10(b) can be used as a measure of E_{opt},[105] it is possible to obtain that $\eta = 0.8$. This value is very close to the theoretical value of $\eta = 0.7$ calculated by Jdira, *et al* .[98] for one layer of CdSe/ZnS with 6 nm diameter QDs on HOPG substrate. The explanation given here illustrates how to use the data provided by the combination of tunneling and optical spectroscopies to test theoretical models of nanostructures. This also allows us to evaluate our setup and say that the mirror insertion around the tunneling junction does not affect the imaging and spectroscopic capability of the microscope.

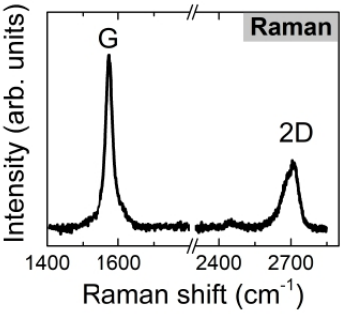

FIG. 11. Raman spectrum of HOPG measured without the STM tip near the sample surface. The spectrum was acquired using a 532 nm laser diode (60 mW of power) and 1800 gr/mm grating. The acquisition time was 10 s and 4 acquisitions were averaged.

C. *In situ* Raman Spectroscopy on HOPG

Raman spectroscopy is a powerful technique for material characterization. Performing Raman spectroscopy requires an efficient injection and collection system due to the relatively weak signal yield and the proximity between the signal and the excitation laser. Performing Raman spectroscopy inside an LT UHV STM can be challenging due to the lack of space for the optics close to the tunnel junction.[58] We performed Raman spectroscopy using a 532 nm laser diode and an 1800 gr/mm grating and keeping all other parameters identical to those used for usual STM-LE, that is, the same collecting optics and transmission into the spectrometer. The exception is the presence of a beam-splitter to inject the laser into the beam path, according to Figure 2(c).

Fig. 11 shows an *in situ* Raman spectrum measured in our setup. The result was obtained on a piece of HOPG, similar to the one used for Fig 8(a). The spectrum shows the characteristics G and 2D Raman bands at 1580 cm^{-1} and 2700 cm^{-1}, respectively.[106] This spectrum was acquired without the tungsten tip approached on the sample surface, being, hence, a regular (not tip-enhanced) Raman spectrum. For TERS experiments, gold or silver STM tips are required.[58,107,108]

D. STM-LE on exfoliated monolayer WSe$_2$

Observing micro-metric flakes of monolayers of 2D materials inside an STM requires the location of the object of interest under the STM tip and also, in our case, the alignment with the optical device. Fig. 12 illustrates this process for a typical mechanically transferred WSe$_2$ micro flake containing a monolayer (in this case, we used gold as substrate). First, as shown in Fig. 12(a) and (b) the sample is characterized outside the STM using optical microscopy and Atomic Force Microscopy (AFM). This allows the identification of the appropriate flake among those on the substrate. Fig. 12(c) shows the expected height profile in as transferred TMDs flakes.[29,110] Once inside the STM, a zoom-lens optical microscope helps finding the area of interest and approaching the tip accordingly, as shown in Fig. 12(d).

The light injection/collection device can be used to observe PL and the sample position can be adjusted according to the observed signal. Fig. 12(e) shows *in situ* PL spectra obtained at RT that display both the A exciton and an indirect transition, as expected in WSe$_2$ bilayers.[111] The band gap crossover is shown in Fig. 12(f) where a transition from bilayer to monolayer is observed for several spectra recorded at different sample positions. The most intense spectrum shows only the A exciton peak, indicating the laser spot is hitting a monolayer. The spectra in Fig. 12(e) and (f) were recorded with the STM tip retracted.

Turning off the laser light, and approaching the tip until observing tunneling current, STM-LE signals could be recorded. In Fig. 12(g) an *in situ* PL spectra is shown for comparison with two STM-LE spectra. In one position, both the WSe$_2$ exciton peak and a plasmon due to the substrate are observed. In another region, only the plasmon peak is recorded. Plasmon emission is expected when the TMD collapses and enters in contact with the metallic substrate.[29,112,113] In some cases, however, the presence of a thin water layer explains the decoupling of the TMD and the metallic substrate which could quench the excitonic emission. The presence and quenching of the excitonic and plasmonic emissions are discussed in detail in ref.[29]. Here, we would like just to point out that the STM-LE excitonic peak is aligned with the PL, while plasmon peaks shift in energy for different regions on the sample and tip conditions.

E. STM-CL and emission due to defects in epitaxial monolayer h-BN

h-BN is considered as a wide band gap semiconductor with many potential applications in deep ultraviolet sources and room temperature single photon emitters.[114–117] To unleash such applications, a better understanding of the fundamental electronic and optical properties of h-BN and the impact of structural defects is required. Fig. 13 summarizes some results obtained on monolayers h-BN epitaxially grown on HOPG.

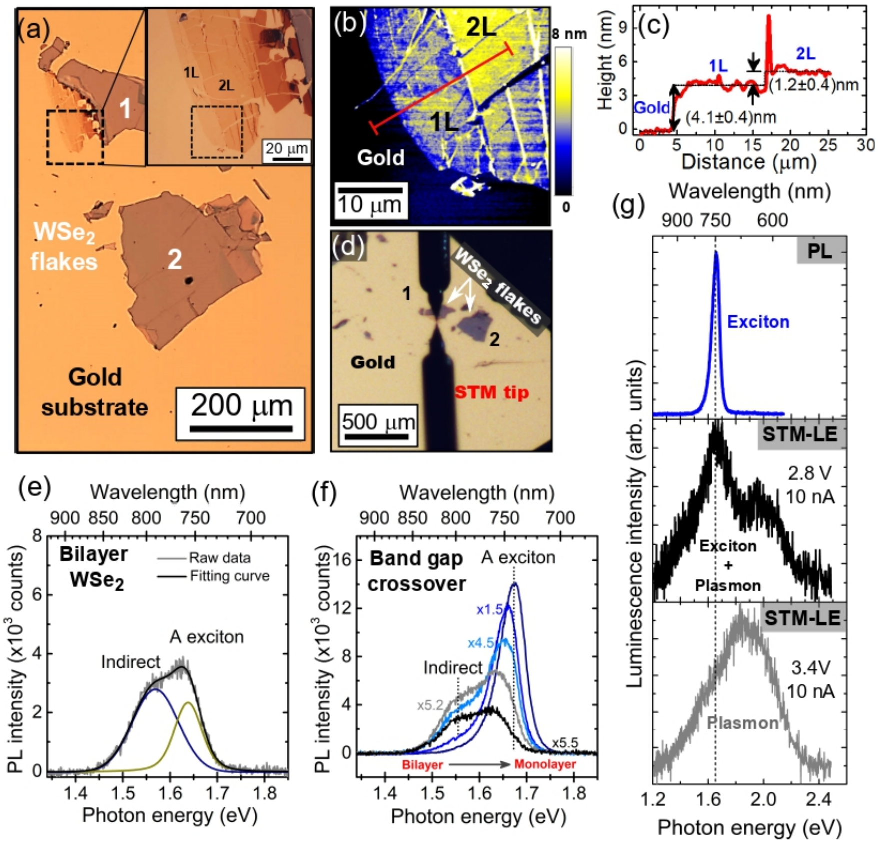

FIG. 12. (a) Optical microscopy image to locate the flake and the region of interest as shown in the inset image. (b) AFM image of the region with monolayer (1L) and bilayer (2L) of WSe$_2$ indicated in (a). (c) Average height profile measured along the red line in (b) confirming the ML height. (d) Location of the flake inside the STM, the tip is approached on the flake of interest. (e) *In situ* PL spectrum taken at room temperature on the bilayer, showing a decomposition in two peaks. (f) Band gap crossover observed in the transition from the bilayer to the monolayer region. (f) Comparison of the PL and STM-LE spectra acquired at RT and under UHV. The acquisition time for the STM-LE spectra was 10 s.

By using the experimental setup described in this work, h-BN monolayers were investigated by STM, STS, PL, Raman, and STM-CL measurements (see details in ref[109]). STM images together with Raman spectroscopy provide us information about the morphology of the sample surface and the atomic structure of the system. From STS, PL, and STM-CL, it is possible to describe the electronic structure and optical transitions of the sample. Fig. 13(a) shows an STM image of the sample surface free of defects. Since the h-BN and HOPG surfaces are morphological very similar, it is necessary to measure the STS curve of the scanned region to distinguish between them. The gray plot in Fig. 13(b) corresponds to a typical STS curve obtained in the region shown in Fig. 13(a). This dI/dV curve shows an electronic band gap of ∼6 eV, defined by the low differential conductance range from ∼-3 V to ∼+3 V confirming that the scanned region corresponds to an h-BN covered surface. In other regions with similar surface morphology, dI/dV curves with a zero band gap (like the blue curve in Fig. 13(b)) expected to graphite are measured. The h-BN electronic band gap can be obtained by in-depth analysis of ensembles of STS data, as shown in ref[109]. For a monolayer of h-BN on HOPG, an electronic band gap of (6.8 ± 0.2) eV was found. Regions with point defects were also identified in the sample. These defects appear as bright spots for positive sample bias, as can be seen in Fig. 13(c). They have from 1 to 2 nm of diameter, according to the full width at half maximum in the height profiles, shown in Fig. 13(d). STS measurements in regions with point defects, see Fig. 13(e), indicate an acceptor level around -2 eV.

For measuring *in situ* PL and Raman, the STM tip is retracted from the sample surface and the light of a green (532 nm) laser diode is injected into the STM in UHV. The

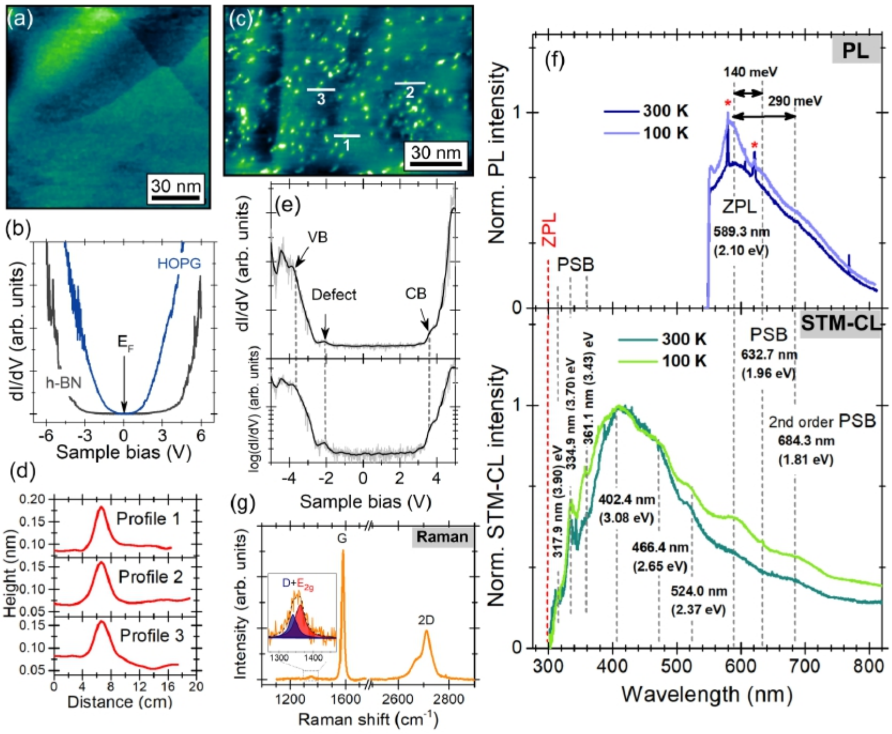

FIG. 13. (a) STM images of the monolayer h-BN/HOPG surface free of defects (0.8 nA, 0.2 V, 80 K). (b) STS curves obtained in the region free of defects. (c) h-BN/HOPG surface with point defects (0.8 nA, 0.8 V, 80 K). (d) Height profiles of some defects. (e) STS curves obtained in the region with point defects. (f) *In-situ* PL and STM-CL spectra in which Phonon Side-Bands (PSB) are observed near the Zero Phonon Line (ZPL) peaks. (g) *In-situ* Raman spectrum at room temperature. Thes STS curves were recorded at 80 K using a bias modulation of 80 mV of amplitude and 800 Hz of frequency. Reproduced with permission from 2D Mater. 8 044001 (2021)[109]. Copyright 2021 Institute of Physics.

in situ PL spectra measured at 100 K and 300 K are shown in Fig. 13(f). The PL spectra show a peak around 2.10 eV, which is clearly resolved at 100 K, and two shoulders around 1.96 and 1.81 eV. These emissions are typically associated with the zero-phonon line (ZPL) and two phonon replicas or phonon side bands (PSB) of carbon-related defects, respectively.[118] The sharp peaks present in the PL spectra at 300 K, indicated with the red stars, correspond to the Raman response of the sample. The full Raman spectra can be seen in Fig. 13(g), where the stronger peaks around 1580 and 2700 cm^{-1} are the G and 2D Raman bands of HOPG, respectively, and the weak peak at 1350 cm^{-1} coming from the D Raman mode of HOPG and the E_{2g} mode of monolayer h-BN.

For STM-CL measurements, the STM tip was retracted about 150 nm from the sample surface and a high voltage between 150 and 180 V was applied to the sample, obtaining FE currents of 5-10 μA.[109] It must be noted that usual CL experiments performed with fast electrons could only record CL signal for thicker h-BN samples with six or three monolayers of thickness.[119,120] Here, by using STM-CL, it is possible to measure the CL response of a single monolayer. From the STM-CL spectra in Fig. 13(f), it can be observed that the CL peaks are better resolved at 100 K than at 300 K. The peaks related to carbon defects are observed at ZPL at 2.10 eV and a PSB at 1.81 eV. At low wavelengths, the spectra show some transitions at 3.90, 3.70, and 3.43 eV, which have been reported as being phonon replicas of a carbon-related defect emitting at 4.1 eV. The most intense peaks in the STM-CL spectra are identified at 3.08, 2.65, and 2.37 eV. These transitions have been previously reported for bulk h-BN and are normally associated with carbon impurities or nitrogen vacancy type-centers.[121–123]

V. LUMINESCENCE EXPERIMENTS INSIDE THE STM IN AMBIENT CONDITIONS

Besides operating under UHV and at LT, the STM and light injection and collection device can be used in air (ambient conditions).[30,109] Here are presented some results obtained in WSe_2 monolayers excited with the tunneling current when the STM operated in ambient conditions.

A key point in STM-LE studies on semiconductors is the establishment of a partial coupling to a conductive support that allows the flow of the tunneling current but does not quench light emission due to all metallic states creating interface states inside the semiconductor band gap. This is particularly true for molecules and also holds for atomically thin 2D semiconductors.[19] Keeping the unintentional water layer that is present under mechanically transferred monolayers, it is possible to study monolayers of WSe_2 on top of metallic supports such as gold.[29] Using this strategy, it was possible to observe STM induced excitonic light emission from WSe_2, as shown in Fig. 14.

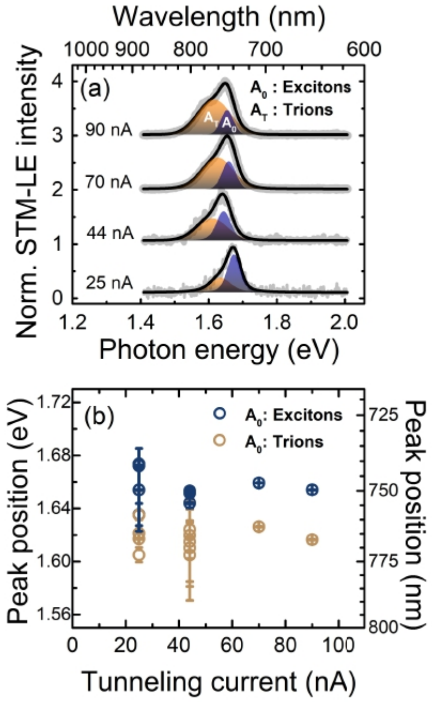

FIG. 14. (a) STM-LE spectra of the excitonic emission from WSe_2 recorded as a function of the tunneling current and for sample bias of 2.4 V. Neutral exciton and charged exciton (trions) contributions are indicated by the fit. (b) Emission energy as a function of the tunnel current for the charged and neutral exciton emission obtained from fitting emission spectra. For 25 and 44 nA, several measurements were made to gain some statistics. Reproduced with permission from Nanoscale, 12, 13460-13470(2020)[29]. Copyright 2020 Royal Chemical Society.

The light emission observed in Figure 14 has the same energy as recorded by PL, similarly as Figure 12(f), and is basically independent of the applied sample bias voltage (see ref. [29]), confirming its excitonic nature. TMDs such as WSe_2 are known to display charged exciton (trion) emission, a result of the high carrier density and strong Coulomb interaction. Using STM-LE, it was possible to, similarly as power dependent PL, observe the increase of the light emission associated with charged excitons with increasing tunnel current. Interestingly, the trion emission scales linearly with the tunnel current (see ref.[29]). Moreover, despite the considerable change in trion to neutral exciton ratio seen in Fig. 14(a), the emission energy of these two transitions remains fairly constant, as shown in Fig. 14(b). These energies are indeed in close agreement with those obtained from PL. This indicates that the intense electric field under the STM tip does not necessarily cause emission energy shifts in the TMD, as one could expect.

VI. CONCLUSIONS

Some design criteria, the implementation, and some illustrative results of a new light detection scheme and an STM employing such system are presented. The design criteria show how the use of a parabolic mirror associated with the Brightness/*Étendue* conservation theorems yields a high-performance light collection device that can be used in combination with an LT UHV STM to display 72% of collection efficiency, 50% of total transmission efficiency with a 0.5 nm spectral resolution. Moreover, the limits regarding efficiency and its relation to the available field of view and spectral resolution were discussed.

The results show that the performance of the STM was not affected by the presence of the light detection device or the modifications performed on the commercial STM system. Luminescence results including *in situ* PL, *In situ* Raman spectroscopy, STM-CL and STM-LE were shown for several systems, including h-BN, TMDs, QDots, metallic surfaces, and HOPG. This set of results demonstrates the potential of this light injection and collection device for studies of light emission and absorption in the context of an LT UHV STM.

We expect these design criteria and implementation represents a solid base for the development of light injection and collection devices for other LT UHV STMs and also other types of microscopes. Indeed, several experiments involving light injection and/or collection around a tunnel junction or focused electron beam are possible with the presented device and such setup could contribute to several areas of photonics and plasmonics.

ACKNOWLEDGMENTS

This work was supported by the Fundação de Amparo à Pesquisa do Estado de São Paulo (FAPESP) Projects 14/23399-9 and 18/08543-7. I.D.B. acknowledges the financial support from the Brazilian Nanocarbon Institute of Science and Technology (INCT/Nanocarbono) and Brazilian Synchrotron Light Laboratory (LNLS).

AUTHOR DECLARATIONS

Conflict of Interest

L.F.Z., R.J.F.R., and Y.A. have Patent No. BR102020015402-8 pending. L.F.Z., R.J.P.R., and Y.A. receive royalties in accordance with a technology transfer contract between Unicamp (represented by L.F.Z.) and RHK Technology, Inc.

DATA AVAILABILITY

The data that support the findings of this study are available from the corresponding author upon reasonable request.

REFERENCES

[1] D. F. Ogletree, P. J. Schuck, A. F. Weber-Bargioni, N. J. Borys, S. Aloni, W. Bao, S. Barja, J. Lee, M. Melli, K. Munechika, S. Whitelam, and S. Wickenburg, "Revealing optical properties of reduced-dimensionality materials at relevant length scales," Advanced Materials **27**, 5693–5719 (2015), https://onlinelibrary.wiley.com/doi/pdf/10.1002/adma.201500930.

[2] G. Jacopin, A. D. L. Bugallo, P. Lavenus, L. Rigutti, F. H. Julien, L. F. Zagonel, M. Kociak, C. Durand, D. Salomon, X. J. Chen, J. Eymery, and M. Tchernycheva, "Single-wire light-emitting diodes based on GaN wires containing both polar and nonpolar InGaN/GaN quantum wells," Applied Physics Express **5**, 014101 (2011).

[3] S. Rühle, M. Shalom, and A. Zaban, "Quantum-dot-sensitized solar cells," ChemPhysChem **11**, 2290–2304 (2010), https://chemistry-europe.onlinelibrary.wiley.com/doi/pdf/10.1002/cphc.201000069.

[4] R. Agarwal, "Heterointerfaces in semiconductor nanowires," Small **4**, 1872–1893 (2008), https://onlinelibrary.wiley.com/doi/pdf/10.1002/smll.200800556.

[5] Y. Zhang, J. Wu, M. Aagesen, and H. Liu, "III–v nanowires and nanowire optoelectronic devices," Journal of Physics D: Applied Physics **48**, 463001 (2015).

[6] K. F. Mak, C. Lee, J. Hone, J. Shan, and T. F. Heinz, "Atomically thin mos$_2$: A new direct-gap semiconductor," Phys. Rev. Lett. **105**, 136805 (2010).

[7] M. Xu, T. Liang, M. Shi, and H. Chen, "Graphene-like two-dimensional materials," Chemical Reviews **113**, 3766–3798 (2013), pMID: 23286380, https://doi.org/10.1021/cr300263a.

[8] W. Zheng, Y. Jiang, X. Hu, H. Li, Z. Zeng, X. Wang, and A. Pan, "Light emission properties of 2d transition metal dichalcogenides: Fundamentals and applications," Advanced Optical Materials **6**, 1800420 (2018), https://onlinelibrary.wiley.com/doi/pdf/10.1002/adom.201800420.

[9] M. Samadi, N. Sarikhani, M. Zirak, H. Zhang, H.-L. Zhang, and A. Z. Moshfegh, "Group 6 transition metal dichalcogenide nanomaterials: synthesis, applications and future perspectives," Nanoscale Horiz. **3**, 90–204 (2018).

[10] P. Tonndorf, R. Schmidt, R. Schneider, J. Kern, M. Buscema, G. A. Steele, A. Castellanos-Gomez, H. S. J. van der Zant, S. M. de Vasconcellos, and R. Bratschitsch, "Single-photon emission from localized excitons in an atomically thin semiconductor," Optica **2**, 347–352 (2015).

[11] X. Wei, Z. Yu, F. Hu, Y. Cheng, L. Yu, X. Wang, M. Xiao, J. Wang, X. Wang, and Y. Shi, "Mo-o bond doping and related-defect assisted enhancement of photoluminescence in monolayer mos2," AIP Advances **4**, 123004 (2014), https://doi.org/10.1063/1.4897522.

[12] S. Tongay, J. Suh, C. Ataca, W. Fan, A. Luce, J. S. Kang, J. Liu, C. Ko, R. Raghunathanan, J. Zhou, F. Ogletree, J. Li, J. C. Grossman, and J. Wu, "Defects activated photoluminescence in two-dimensional semiconductors: interplay between bound, charged and free excitons," Scientific Reports **3**, 2657 (2013), https://doi.org/10.1038/srep02657.

[13] Z. Wu, W. Zhao, J. Jiang, T. Zheng, Y. You, J. Lu, and Z. Ni, "Defect activated photoluminescence in wse2 monolayer," The Journal of Physical Chemistry C **121**, 12294–12299 (2017), https://doi.org/10.1021/acs.jpcc.7b03585.

[14] A. Gustafsson, M.-E. Pistol, L. Montelius, and L. Samuelson, "Local probe techniques for luminescence studies of low-dimensional semiconductor structures," Journal of Applied Physics **84**, 1715–1775 (1998), https://doi.org/10.1063/1.368613.

[15] M. Kociak, O. Stéphan, A. Gloter, L. F. Zagonel, L. H. Tizei, M. Tencé, K. March, J. D. Blazit, Z. Mahfoud, A. Losquin, S. Meuret, and C. Colliex, "Seeing and measuring in colours: Electron microscopy and spectroscopies applied to nano-optics," Comptes Rendus Physique **15**, 158 – 175 (2014), seeing and measuring with electrons: Transmission Electron Microscopy today and tomorrow.

[16] R. Wiesendanger, *Scanning Probe Microscopy and Spectroscopy: Methods and Applications* (Cambridge University Press, 1994).

[17] R. Plumadore, M. Baskurt, J. Boddison-Chouinard, G. Lopinski, M. Modarresi, P. Potasz, P. Hawrylak, H. Sahin, F. M. Peeters, and A. Luican-Mayer, "Prevalence of oxygen defects in an in-plane anisotropic transition metal dichalcogenide," Phys. Rev. B **102**, 205408 (2020).

[18] M. Kociak and L. Zagonel, "Cathodoluminescence in the scanning transmission electron microscope," Ultramicroscopy **176**, 112 – 131 (2017), 70th Birthday of Robert Sinclair and 65th Birthday of Nestor J. Zaluzec PICO 2017 – Fourth Conference on Frontiers of Aberration Corrected Electron Microscopy.

[19] K. Kuhnke, C. Große, P. Merino, and K. Kern, "Atomic-scale imaging and spectroscopy of electroluminescence at molecular interfaces," Chemical Reviews **117**, 5174–5222 (2017), pMID: 28294599, https://doi.org/10.1021/acs.chemrev.6b00645.

[20] T. Coenen and N. M. Haegel, "Cathodoluminescence for the 21st century learning more from light," Applied Physics Reviews **4**, 031103 (2017), https://doi.org/10.1063/1.4985767.

[21] F. Stavale, N. Nilius, and H.-J. Freund, "Stm luminescence spectroscopy of intrinsic defects in zno(0001) thin films," The Journal of Physical Chemistry Letters **4**, 3972–3976 (2013), https://doi.org/10.1021/jz401823c.

[22] F. Stavale, L. Pascua, N. Nilius, and H.-J. Freund, "Luminescence properties of nitrogen-doped zno," The Journal of Physical Chemistry C **118**, 13693–13696 (2014), https://doi.org/10.1021/jp5035536.

[23] E. Le Moal, S. Marguet, B. Rogez, S. Mukherjee, P. Dos Santos, E. Boer-Duchemin, G. Comtet, and G. Dujardin, "An electrically excited nanoscale light source with active angular control of the emitted light," Nano Letters **13**, 4198–4205 (2013), pMID: 23927672, https://doi.org/10.1021/nl401874m.

[24] T. Lutz, A. Kabakchiev, T. Dufaux, C. Wolpert, Z. Wang, M. Burghard, K. Kuhnke, and K. Kern, "Scanning tunneling luminescence of individual cdse nanowires," Small **7**, 2396–2400 (2011), https://onlinelibrary.wiley.com/doi/pdf/10.1002/smll.201100434.

[25] C. Chen, P. Chu, C. A. Bobisch, D. L. Mills, and W. Ho, "Viewing the interior of a single molecule: Vibronically resolved photon imaging at submolecular resolution," Phys. Rev. Lett. **105**, 217402 (2010).

[26] X. H. Qiu, G. V. Nazin, and W. Ho, "Vibrationally resolved fluorescence excited with submolecular precision," Science **299**, 542–546 (2003), https://science.sciencemag.org/content/299/5606/542.full.pdf.

[27] D. Pommier, R. Bretel, L. E. P. López, F. Fabre, A. Mayne, E. Boer-Duchemin, G. Dujardin, G. Schull, S. Berciaud, and E. Le Moal, "Scanning tunneling microscope-induced excitonic luminescence of a two-dimensional semiconductor," Phys. Rev. Lett. **123**, 027402 (2019).

[28] R. Péchou, S. Jia, J. Rigor, O. Guillermet, G. Seine, J. Lou, N. Large, A. Mlayah, and R. Coratger, "Plasmonic-induced luminescence of mose2 monolayers in a scanning tunneling microscope," ACS Photonics **0**, null (0), https://doi.org/10.1021/acsphotonics.0c01101.

[29] R. J. Peña Román, Y. Auad, L. Grasso, F. Alvarez, I. D. Barcelos, and L. F. Zagonel, "Tunneling-current-induced local excitonic luminescence in p-doped wse2 monolayers," Nanoscale **12**, 13460–13470 (2020).

[30] G. M. do Amaral, I. da Costa Tonon, R. J. Peña Román, H. de Oliveira Plath, T. M. Taniguchi, L. H. de Lima, L. F. Zagonel, R. Landers, and A. de Siervo, "Epitaxial growth, electronic hybridization and stability under oxidation of monolayer mos2 on ag(111)," Applied Surface Science **538**, 148138 (2021).

[31] M. Sakurai, C. Thirstrup, and M. Aono, "New aspects of light emission from stm," Applied Physics A **80**, 1153 (2005).

[32] L. F. Zagonel, L. H. G. Tizei, G. Z. Vitiello, G. Jacopin, L. Rigutti, M. Tchernycheva, F. H. Julien, R. Songmuang, T. Ostasevicius, F. de la Peña, C. Ducati, P. A. Midgley, and M. Kociak, "Nanometer-scale monitoring of quantum-confined stark effect and emission efficiency droop in multiple gan/aln quantum disks in nanowires," Phys. Rev. B **93**, 205410 (2016).

[33] R. Berndt, R. R. Schlittler, and J. K. Gimzewski, "Photon emission scanning tunneling microscope," Journal of Vacuum Science & Technology B: Microelectronics and Nanometer Structures Processing, Measurement, and Phenomena **9**, 573–577 (1991), https://avs.scitation.org/doi/pdf/10.1116/1.585571.

[34] K. Edelmann, L. Gerhard, M. Winkler, L. Wilmes, V. Rai, M. Schumann, C. Kern, M. Meyer, M. Wegener, and W. Wulfhekel, "Light collection from a low-temperature scanning tunneling microscope using integrated mirror tips fabricated by direct laser writing," Review of Scientific Instruments **89**, 123107 (2018), https://doi.org/10.1063/1.5053882.

[35] J. G. Keizer, J. K. Garleff, and P. M. Koenraad, "Simple and efficient scanning tunneling luminescence detection at low-temperature," Review of Scientific Instruments **80**, 123704 (2009), https://doi.org/10.1063/1.3274675.

[36] K. Kuhnke, A. Kabakchiev, W. Stiepany, F. Zinser, R. Vogelgesang, and K. Kern, "Versatile optical access to the tunnel gap in a low-temperature scanning tunneling microscope," Review of Scientific Instruments **81**, 113102 (2010), https://doi.org/10.1063/1.3480548.

[37] G. Hoffmann, J. Kröger, and R. Berndt, "Color imaging with a low temperature scanning tunneling microscope," Review of Scientific Instruments **73**, 305–309 (2002), https://doi.org/10.1063/1.1433946.

[38] L. G. Chen, C. Zhang, R. Zhang, X. L. Zhang, and Z. C. Dong, "Note: Optical optimization for ultrasensitive photon mapping with submolecular resolution by scanning tunneling microscope induced luminescence," Review of Scientific Instruments **84**, 066106 (2013), https://doi.org/10.1063/1.4811200.

[39] H.-J. Freund, N. Nilius, T. Risse, S. Schauermann, and T. Schmidt, "Innovative measurement techniques in surface science," ChemPhysChem **12**, 79–87 (2011), https://chemistry-europe.onlinelibrary.wiley.com/doi/pdf/10.1002/cphc.201000812.

[40] Y. Khang, Y. Park, M. Salmeron, and E. R. Weber, "Low temperature ultrahigh vacuum cross-sectional scanning tunneling microscope for luminescence measurements," Review of Scientific Instruments **70**, 4595–4599 (1999), https://doi.org/10.1063/1.1150118.

[41] Y. Suzuki, H. Minoda, and N. Yamamoto, "Stm light emission from ag/si(111)," Surface Science **438**, 297 – 304 (1999).

[42] N. J. Watkins, J. P. Long, Z. H. Kafafi, and A. J. Mäkinen, "Fiber optic light collection system for scanning-tunneling-microscope-induced light emission," Review of Scientific Instruments **78**, 053707 (2007), https://doi.org/10.1063/1.2740479.

[43] C. J. Chen, *Introduction to Scanning Tunneling Microscopy: Second Edition* (Oxford University Press, 2008).

[44] B. Voigtländer, *Scanning Probe Microscopy: Atomic Force Microscopy and Scanning Tunneling Microscopy. NanoScience and Technology* (Springer, Berlin, Heidelberg, 2015).

[45] F. Rossel, M. Pivetta, and W.-D. Schneider, "Luminescence experiments on supported molecules with the scanning tunneling microscope," Surface Science Reports **65**, 129 – 144 (2010).

[46] M. Bass, E. W. V. Stryland, D. R. Williams, and W. L. Wolfe, *Handbook of Optics Volume II Devices, Measurements, and Properties 2nd edition* (1995).

[47] M. Bass, E. W. V. Stryland, D. R. Williams, and W. L. Wolfe, *Handbook of Optics Volume III Classical Optics, Vision Optics, X-Ray Optics 2nd edition* (2001).

[48] M. Bass, E. W. V. Stryland, D. R. Williams, and W. L. Wolfe, *Handbook of Optics Volume I Fundamentals, Techniques, and Design 2nd edition* (1995).

[49] P. R. Edwards and R. W. Martin, "Cathodoluminescence nano-characterization of semiconductors," **26**, 064005 (2011).

[50] M. Kociak, L. F. Zagonel, M. Tence, and S. a. Mazzuco, "Flexible cathodoluminescence detection system and microscope employing such as system," (2011), wO/2011/148072.

[51] J. J. Sáenz and R. García, "Near field emission scanning tunneling microscopy," Applied Physics Letters **65**, 3022–3024 (1994), https://doi.org/10.1063/1.112496.

[52] K. Watanabe, Y. Nakamura, and M. Ichikawa, "Conductive optical-fiber stm probe for local excitation and collection of cathodoluminescence at semiconductor surfaces," Opt. Express **21**, 19261–19268 (2013).

[53] M. Rudolph, S. M. Carr, G. Subramania, G. Ten Eyck, J. Dominguez, T. Pluym, M. P. Lilly, M. S. Carroll, and E. Bussmann, "Probing the limits of si:p -doped devices patterned by a scanning tunneling microscope in a field-emission mode," Applied Physics Letters **105**, 163110 (2014), https://doi.org/10.1063/1.4899255.

[54] Y. Uehara, M. Kuwahara, and S. Katano, "Measurement of phonon energy of sb2te3 by scanning tunneling microscope light-emission spectroscopy," Solid State Communications **177**, 29 – 32 (2014).

[55] C. Chen, N. Hayazawa, and S. Kawata, "A 1.7 nm resolution chemical analysis of carbon nanotubes by tip-enhanced raman imaging in the ambient," Nature Communications **5**, 3312 (2006), https://doi.org/10.1038/ncomms4312.

[56] C. STANCIU, M. SACKROW, and A. MEIXNER, "High na particle- and tip-enhanced nanoscale raman spectroscopy with a parabolic-mirror microscope," Journal of Microscopy **229**, 247–253 (2008), https://onlinelibrary.wiley.com/doi/pdf/10.1111/j.1365-2818.2008.01894.x.

[57] A. Hartschuh, "Tip-enhanced near-field optical microscopy," Angewandte Chemie International Edition **47**, 8178–8191 (2008), https://onlinelibrary.wiley.com/doi/pdf/10.1002/anie.200801605.

[58] S. Sheng, W. Li, J. Gou, P. Cheng, L. Chen, and K. Wu, "Low-temperature, ultrahigh-vacuum tip-enhanced raman spectroscopy combined with molecular beam epitaxy for in situ two-dimensional materials' studies," Review of Scientific Instruments **89**, 053107 (2018), https://doi.org/10.1063/1.5019802.

[59] A. Drechsler, M. A. Lieb, C. Debus, A. J. Meixner, and G. Tarrach, "Confocal microscopy with a high numerical aperture parabolic mirror," Opt. Express **9**, 637–644 (2001).

[60] D. Zhang, X. Wang, K. Braun, H.-J. Egelhaaf, M. Fleischer, L. Hennemann, H. Hintz, C. Stanciu, C. J. Brabec, D. P. Kern, and A. J. Meixner, "Parabolic mirror-assisted tip-enhanced spectroscopic imaging for non-transparent materials," Journal of Raman Spectroscopy **40**, 1371–1376 (2009), https://onlinelibrary.wiley.com/doi/pdf/10.1002/jrs.2411.

[61] C. Debus, M. A. Lieb, A. Drechsler, and A. J. Meixner, "Probing highly confined optical fields in the focal region of a high na parabolic mirror with subwavelength spatial resolution," Journal of Microscopy **210**, 203–208 (2003), https://onlinelibrary.wiley.com/doi/pdf/10.1046/j.1365-2818.2003.01091.x.

[62] K. Sperlich and H. Stolz, "Quantum efficiency measurements of (EM)CCD cameras: high spectral resolution and temperature dependence," Measurement Science and Technology **25**, 015502 (2013).

[63] M. J. Romero, J. van de Lagemaat, I. Mora-Sero, G. Rumbles, and M. M. Al-Jassim, "Imaging of resonant quenching of surface plasmons by quantum dots," Nano Letters **6**, 2833–2837 (2006), pMID: 17163714, https://doi.org/10.1021/nl061997s.

[64] C. I. Osorio, T. Coenen, B. J. M. Brenny, A. Polman, and A. F. Koenderink, "Angle-resolved cathodoluminescence imaging polarimetry," ACS Photonics **3**, 147–154 (2016), https://doi.org/10.1021/acsphotonics.5b00596.

[65] T. Coenen, E. J. R. Vesseur, A. Polman, and A. F. Koenderink, "Directional emission from plasmonic yagi–uda antennas probed by angle-resolved cathodoluminescence spectroscopy," Nano Letters **11**, 3779–3784 (2011), pMID: 21780758, https://doi.org/10.1021/nl201839g.

[66] L. Zhang, Y.-J. Yu, L.-G. Chen, Y. Luo, B. Yang, F.-F. Kong, G. Chen, Y. Zhang, Q. Zhang, Y. Luo, J.-L. Yang, Z.-C. Dong, and J. G. Hou, "Electrically driven single-photon emission from an isolated single molecule," Nature Communications **8**, 580 (2017), https://doi.org/10.1038/s41467-017-00681-7.

[67] C. C. Leon, A. Rosławska, A. Grewal, O. Gunnarsson, K. Kuhnke, and K. Kern, "Photon superbunching from a generic tunnel junction," Science Advances **5** (2019), 10.1126/sciadv.aav4986, https://advances.sciencemag.org/content/5/5/eaav4986.full.pdf.

[68] P. Merino, C. Große, A. Rosławska, K. Kuhnke, and K. Kern, "Exciton dynamics of c60-based single-photon emitters explored by hanbury brown–twiss scanning tunnelling microscopy," Nature Communications **6**, 8461 (2015), https://doi.org/10.1038/ncomms9461.

[69] S. Meuret, T. Coenen, S. Y. Woo, Y.-H. Ra, Z. Mi, and A. Polman, "Nanoscale relative emission efficiency mapping using cathodoluminescence g(2) imaging," Nano Letters **18**, 2288–2293 (2018), pMID: 29546762, https://doi.org/10.1021/acs.nanolett.7b04891.

[70] M. Bass, C. DeCusatis, J. Enoch, V. Lakshminarayanan, G. Li, C. Macdonald, V. Mahajan, and E. Van Stryland, *Handbook of Optics, Third Edition Volume I: Geometrical and Physical Optics, Polarized Light, Components and Instruments(Set)*, 3rd ed. (McGraw-Hill, Inc., USA, 2009).

[71] L. F. Zagonel, L. Rigutti, M. Tchernycheva, G. Jacopin, R. Songmuang, and M. Kociak, "Visualizing highly localized luminescence in GaN/AlN heterostructures in nanowires," Nanotechnology **23**, 455205 (2012).

[72] F. Withers, O. Del Pozo-Zamudio, S. Schwarz, S. Dufferwiel, P. M. Walker, T. Godde, A. P. Rooney, A. Gholinia, C. R. Woods, P. Blake, S. J. Haigh, K. Watanabe, T. Taniguchi, I. L. Aleiner, A. K. Geim, V. I. Fal'ko, A. I. Tartakovskii, and K. S. Novoselov, "Wse2 light-emitting tunneling transistors with enhanced brightness at room temperature," Nano Letters **15**, 8223–8228 (2015), pMID: 26555037, https://doi.org/10.1021/acs.nanolett.5b03740.

[73] I. Horcas, R. Fernández, J. M. Gómez-Rodríguez, J. Colchero, J. Gómez-Herrero, and A. M. Baro, "Wsxm: A software for scanning probe microscopy and a tool for nanotechnology," Review of Scientific Instruments.

[74] D. Nečas and P. Klapetek, "Gwyddion: an open-source software for SPM data analysis," Central European Journal of Physics **10**, 181–188 (2012).

[75] H. S. Wong and C. Durkan, "Unraveling the rotational disorder of graphene layers in graphite," Phys. Rev. B **81**, 045403 (2010).

[76] S. Patil, S. Kolekar, and A. Deshpande, "Revisiting hopg superlattices: Structure and conductance properties," Surface Science **658**, 55 – 60 (2017).

[77] E. S. Morell, P. Vargas, P. Häberle, S. A. Hevia, and L. Chico, "Edge states of moiré structures in graphite," Phys. Rev. B **91**, 035441 (2015).

[78] L.-J. Yin, J.-B. Qiao, W.-X. Wang, Z.-D. Chu, K. F. Zhang, R.-F. Dou, C. L. Gao, J.-F. Jia, J.-C. Nie, and L. He, "Tuning structures and electronic spectra of graphene layers with tilt grain boundaries," Phys. Rev. B **89**, 205410 (2014).

[79] J. Červenka and C. F. J. Flipse, "Structural and electronic properties of grain boundaries in graphite: Planes of periodically distributed point defects," Phys. Rev. B **79**, 195429 (2009).

[80] P. Byszewski, Z. Klusek, S. Pierzgalski, S. Datta, E. Kowalska, and M. Popławska, "Stm/sts observation of ferrocene derivative adduct to c60 on hopg," Journal of Electron Spectroscopy and Related Phenomena **130**, 25 – 32 (2003).

[81] G. Teobaldi, E. Inami, J. Kanasaki, K. Tanimura, and A. L. Shluger, "Role of applied bias and tip electronic structure in the scanning tunneling microscopy imaging of highly oriented pyrolytic graphite," Phys. Rev. B **85**, 085433 (2012).

[82] K. Oura, M. Katayama, A. V. Zotov, V. G. Lifshits, and A. A. Saranin, "Electronic structure of surfaces," in *Surface Science: An Introduction* (Springer Berlin Heidelberg, Berlin, Heidelberg, 2003) pp. 261–293.

[83] J. Mysliveček, A. Stróżecka, J. Steffl, P. Sobotík, I. Ošťádal, and B. Voigtländer, "Structure of the adatom electron band of the Si(111)−7 × 7 surface," Phys. Rev. B **73**, 161302 (2006).

[84] K. Takayanagi, Y. Tanishiro, M. Takahashi, and S. Takahashi, "Structural analysis of si(111)-7×7 by uhv-transmission electron diffraction and microscopy," Journal of Vacuum Science & Technology A **3**, 1502–1506 (1985), https://doi.org/10.1116/1.573160.

[85] J. Wang, L. Jin, H. Zhou, H. Fu, C. Song, S. Meng, and J. Zhang, "Direct imaging of surface states hidden in the third layer of si (111)-7×7 surface by pz-wave tip," Applied Physics Letters **113**, 031604 (2018), https://doi.org/10.1063/1.5038954.

[86] A. B. Odobescu and S. V. Zaitsev-Zotov, "Energy gap revealed by low-temperature scanning–tunnelling spectroscopy of the si(111)-7×7 surface in illuminated slightly doped crystals," Journal of Physics: Condensed Matter **24**, 395003 (2012).

[87] E. Ponomarev, Pásztor, A. Waelchli, A. Scarfato, N. Ubrig, C. Renner, and A. F. Morpurgo, "Hole transport in exfoliated monolayer mos2," ACS Nano **12**, 2669–2676 (2018), pMID: 29481047, https://doi.org/10.1021/acsnano.7b08831.

[88] S. McDonnell, A. Azcatl, R. Addou, C. Gong, C. Battaglia, S. Chuang, K. Cho, A. Javey, and R. M. Wallace, "Hole contacts on transition metal dichalcogenides: Interface chemistry and band alignments," ACS Nano **8**, 6265–6272 (2014), pMID: 24797712, https://doi.org/10.1021/nn501728w.

[89] R. Addou and R. M. Wallace, "Surface analysis of wse2 crystals: Spatial and electronic variability," ACS Applied Materials & Interfaces **8**, 26400–26406 (2016), pMID: 27599557, https://doi.org/10.1021/acsami.6b08847.

[90] R. Zhang, Y. Zhang, Z. C. Dong, S. Jiang, C. Zhang, L. G. Chen, L. Zhang, Y. Liao, J. Aizpurua, Y. Luo, J. L. Yang, and J. G. Hou, "Chemical mapping of a single molecule by plasmon-enhanced Raman scattering," Nature **498**, 82–86 (2013).

[91] M. Hegner, P. Wagner, and G. Semenza, "Ultralarge atomically flat template-stripped au surfaces for scanning probe microscopy," Surface Science **291**, 39 – 46 (1993).

[92] R. Rösch and R. Schuster, "Tunneling spectroscopy of clean and adsorbate-covered gold surfaces in humid air, measured with fast bias voltage ramps," Surface Science **631**, 105 – 111 (2015), surface Science and Electrochemistry - 20 years later.

[93] T. Andreev, I. Barke, and H. Hövel, "Adsorbed rare-gas layers on au(111): Shift of the shockley surface state studied with ultraviolet photoelectron spectroscopy and scanning tunneling spectroscopy," Phys. Rev. B **70**, 205426 (2004).

[94] J. Aizpurua, S. P. Apell, and R. Berndt, "Role of tip shape in light emission from the scanning tunneling microscope," Phys. Rev. B **62**, 2065–2073 (2000).

[95] A. Martín-Jiménez, A. I. Fernández-Domínguez, K. Lauwaet, D. Granados, R. Miranda, F. J. García-Vidal, and R. Otero, en"Unveiling the radiative local density of optical states of a plasmonic nanocavity by STM," Nature Communications **11**, 1021 (2020).

[96] M. R. Hummon, A. J. Stollenwerk, V. Narayanamurti, P. O. Anikeeva, M. J. Panzer, V. Wood, and V. Bulović, "Measuring charge trap occupation and energy level in cdse/zns quantum dots using a scanning tunneling microscope," Phys. Rev. B **81**, 115439 (2010).

[97] B. Diaconescu, L. A. Padilha, P. Nagpal, B. S. Swartzentruber, and V. I. Klimov, "Measurement of electronic states of pbs nanocrystal quantum dots using scanning tunneling spectroscopy: The role of parity selection rules in optical absorption," Phys. Rev. Lett. **110**, 127406 (2013).

[98] L. Jdira, K. Overgaag, J. Gerritsen, D. Vanmaekelbergh, P. Liljeroth, and S. Speller, "Scanning tunnelling spectroscopy on arrays of cdse quantum dots: Response of wave functions to local electric fields," Nano Letters **8**, 4014–4019 (2008), pMID: 18844429, https://doi.org/10.1021/nl8026923.

[99] K. Overgaag, P. Liljeroth, B. Grandidier, and D. Vanmaekelbergh, "Scanning tunneling spectroscopy of individual pbse quantum dots and molecular aggregates stabilized in an inert nanocrystal matrix," ACS Nano **2**, 600–606 (2008), https://doi.org/10.1021/nn7003876.

[100] P. Liljeroth, L. Jdira, K. Overgaag, B. Grandidier, S. Speller, and D. Vanmaekelbergh, "Can scanning tunnelling spectroscopy measure the density of states of semiconductor quantum dots?" Phys. Chem. Chem. Phys. **8**, 3845–3850 (2006).

[101] D. Katz, T. Wizansky, O. Millo, E. Rothenberg, T. Mokari, and U. Banin, "Size-dependent tunneling and optical spectroscopy of cdse quantum rods," Phys. Rev. Lett. **89**, 086801 (2002).

[102] O. Millo, D. Katz, Y. Cao, and U. Banin, "Imaging and spectroscopy of artificial-atom states in core/shell nanocrystal quantum dots," Phys. Rev. Lett. **86**, 5751–5754 (2001).

[103] L. Jdira, P. Liljeroth, E. Stoffels, D. Vanmaekelbergh, and S. Speller, "Size-dependent single-particle energy levels and interparticle coulomb interactions in cdse quantum dots measured by scanning tunneling spectroscopy," Phys. Rev. B **73**, 115305 (2006).

[104] E. P. A. M. Bakkers, Z. Hens, A. Zunger, A. Franceschetti, L. P. Kouwenhoven, L. Gurevich, and D. Vanmaekelbergh, "Shell-tunneling spectroscopy of the single-particle energy levels of insulating quantum dots," Nano Letters **1**, 551–556 (2001), https://doi.org/10.1021/nl015572b.

[105] T. Lee, K. Noguchi, H. Nishimura, and D. Kim, "Absorption and photoluminescence properties of CdSe quantum dots prepared by hydrothermal method," Journal of Physics: Conference Series **1220**,

012028 (2019).

[106] V. Zólyomi, J. Koltai, and J. Kürti, en"Resonance Raman spectroscopy of graphite and graphene," physica status solidi (b) **248**, 2435–2444 (2011).

[107] A. Foti, F. Barreca, E. Fazio, C. D'Andrea, P. Matteini, O. M. Maragò, and P. G. Gucciardi, en"Low cost tips for tip-enhanced Raman spectroscopy fabricated by two-step electrochemical etching of 125 µm diameter gold wires," Beilstein Journal of Nanotechnology **9**, 2718–2729 (2018).

[108] Y. Fang, Z. Zhang, and M. Sun, "High vacuum tip-enhanced raman spectroscope based on a scanning tunneling microscope," Review of Scientific Instruments **87**, 033104 (2016), https://aip.scitation.org/doi/pdf/10.1063/1.4943291.

[109] R. J. P. Román, F. J. R. C. Costa, A. Zobelli, C. Elias, P. Valvin, G. Cassabois, B. Gil, A. Summerfield, T. S. Cheng, C. J. Mellor, P. H. Beton, S. V. Novikov, and L. F. Zagonel, "Band gap measurements of monolayer h-BN and insights into carbon-related point defects," **8**, 044001 (2021).

[110] S. Palleschi, G. D'Olimpio, P. Benassi, M. Nardone, R. Alfonsetti, G. Moccia, M. Renzelli, O. A. Cacioppo, A. Hichri, S. Jaziri, A. Politano, and L. Ottaviano, "On the role of nano-confined water at the 2D/SiO2 interface in layer number engineering of exfoliated MoS2 via thermal annealing," 2d Mater. **7**, 025001 (2020).

[111] V. S. Bagaev, S. N. Nikolaev, V. S. Krivobok, M. A. Chernopitsskii, A. A. Vasilchenko, and G. F. Kopytov, en"Exciton Luminescence of Wse2 Bilayers," Russian Physics Journal **62**, 1017–1022 (2019).

[112] F. Tumino, C. S. Casari, M. Passoni, V. Russo, and A. Li Bassi, "Pulsed laser deposition of single-layer mos2 on au(111): from nanosized crystals to large-area films," Nanoscale Adv. **1**, 643–655 (2019).

[113] U. Bhanu, M. R. Islam, L. Tetard, and S. I. Khondaker, "Photoluminescence quenching in gold - mos2 hybrid nanoflakes," Scientific Reports **4**, 5575 (2014).

[114] K. Watanabe and T. Taniguchi, "Hexagonal boron nitride as a new ultraviolet luminescent material and its application," International Journal of Applied Ceramic Technology **8**, 977–989 (2011), https://ceramics.onlinelibrary.wiley.com/doi/pdf/10.1111/j.1744-7402.2011.02626.x.

[115] H. X. Jiang and J. Y. Lin, "Hexagonal boron nitride for deep ultraviolet photonic devices," **29**, 084003 (2014).

[116] T. T. Tran, K. Bray, M. J. Ford, M. Toth, and I. Aharonovich, en"Quantum emission from hexagonal boron nitride monolayers," Nature Nanotechnology **11**, 37–41 (2016).

[117] T. T. Tran, C. Elbadawi, D. Totonjian, C. J. Lobo, G. Grosso, H. Moon, D. R. Englund, M. J. Ford, I. Aharonovich, and M. Toth, "Robust multicolor single photon emission from point defects in hexagonal boron nitride," ACS Nano **10**, 7331–7338 (2016), pMID: 27399936, https://doi.org/10.1021/acsnano.6b03602.

[118] N. Mendelson, D. Chugh, J. R. Reimers, T. S. Cheng, A. Gottscholl, H. Long, C. J. Mellor, A. Zettl, V. Dyakonov, P. H. Beton, S. V. Novikov, C. Jagadish, H. H. Tan, M. J. Ford, M. Toth, C. Bradac, and I. Aharonovich, en"Identifying carbon as the source of visible single-photon emission from hexagonal boron nitride," Nature Materials **20**, 321–328 (2021).

[119] L. Schué, B. Berini, A. C. Betz, B. Plaçais, F. Ducastelle, J. Barjon, and A. Loiseau, "Dimensionality effects on the luminescence properties of hbn," Nanoscale **8**, 6986–6993 (2016).

[120] A. Hernández-Mínguez, J. Lähnemann, S. Nakhaie, J. M. J. Lopes, and P. V. Santos, "Luminescent defects in a few-layer *h*-bn film grown by molecular beam epitaxy," Phys. Rev. Applied **10**, 044031 (2018).

[121] F. Hayee, L. Yu, J. L. Zhang, C. J. Ciccarino, M. Nguyen, A. F. Marshall, I. Aharonovich, J. Vučković, P. Narang, T. F. Heinz, and J. A. Dionne, en"Revealing multiple classes of stable quantum emitters in hexagonal boron nitride with correlated optical and electron microscopy," Nature Materials **19**, 534–539 (2020).

[122] B. Shevitski, S. M. Gilbert, C. T. Chen, C. Kastl, E. S. Barnard, E. Wong, D. F. Ogletree, K. Watanabe, T. Taniguchi, A. Zettl, and S. Aloni, "Blue-light-emitting color centers in high-quality hexagonal boron nitride," Phys. Rev. B **100**, 155419 (2019).

[123] B. Berzina, V. Korsaks, L. Trinkler, A. Sarakovskis, J. Grube, and S. Bellucci, "Defect-induced blue luminescence of hexagonal boron nitride," Diamond and Related Materials **68**, 131–137 (2016).

Chapter 5

Point defects, sample doping, and electrical generation of excitons in exfoliated WSe_2 monolayers on gold substrates

This chapter contains the publication:

Ricardo Javier Peña Román, Yves Auad, Lucas Grasso, Fernando Alvarez, Ingrid David Barcelos, and Luiz Fernando Zagonel

Tunneling-current-induced local excitonic luminescence in p-doped WSe_2 monolayers

Nanoscale, 2020,12, 13460-13470.

In this chapter, we present an STM study of the morphological, electronic, and optical properties of WSe_2. We investigated monolayers mechanically exfoliated from a p-doped WSe_2 single crystal and deposited on gold thin film substrates.

In order to identify intrinsic point defects and their role in the electronic properties of the sample, some monolayers were explored via STM imaging and STS measurements under UHV conditions at room temperature. Additionally, we combined Atomic Force Microscopy (AFM), Phothouminescence, and Raman measurements on as-transferred and thermally annealed monolayers to investigate the sample-substrate coupling and their impact on the electronic and optical properties of the sample. We identified that as-transferred monolayers are always optically active while the luminescence is quenched in annealed samples. We present a detailed study on the origin of the sample-substrate decoupling observed in as-transferred monolayers that allows the semiconductor to preserve its optical properties and makes it possible to carry out STM-LE measurements. Adittionally, we studied the conditions in which we can electrically and locally generate excitons in the 2D material via electroluminescence in STM-LE. The STM-LE measurements were performed in ambient conditions to preserve the optical activity of the sample. We combined the STM, STS, and STM-LE results to understand the role of point defects, sample doping, sample-substrate interaction, and the tunneling parameters on the electroluminescence of the sample and propose a possible excitation mechanism for the exciton emission involving electron tunneling processes.

In the following, we present the results published in **Nanoscale, 2020,12, 13460-13470**. We reported the first observation of the excitonic emission from a TMD on a metallic substrate using the tunneling current in an STM as a nanoscale excitation source. STM-LE and PL spectra present the typical spectroscopic characteristic associated with the radiative recombination of A-neutral excitons and A-trions (charged excitons). The charge injection rate, adjusted by setting the tunneling current setpoint, controls the ratio of light emission due to trions and to neutral excitons. STM images and STS evidenced the presence of intrinsic point defects and confirmed the p-type doping of the WSe_2 sample. The STM-LE excitation mechanism proposed is the injection of negative charges into the conduction band of the semiconductor. The injected negative charges form neutral and charged excitons by Coulomb interaction with the positive charges in the p-doped sample. We propose the presence of a thin water decoupling layer to explain the excitonic luminescence of the sample on the metallic support. The luminescence can be quenched on the whole flake by thermal annealing under ultra-high vacuum conditions or locally at the STM tip position by removing the interfacial water with the tunneling current. Our findings give a clearer understanding of the excitonic light emission in monolayers of TMDs employing STM-LE, and also of the quenching effect in 2D semiconducting materials supported by metallic substrates.

Nanoscale

ROYAL SOCIETY OF CHEMISTRY

PAPER

Cite this: *Nanoscale*, 2020, **12**, 13460

Tunneling-current-induced local excitonic luminescence in p-doped WSe_2 monolayers†

Ricardo Javier Peña Román, *[a] Yves Auad, [a] Lucas Grasso, [a] Fernando Alvarez, [a] Ingrid David Barcelos [b] and Luiz Fernando Zagonel *[a]

Received 1st May 2020, Accepted 8th June 2020

DOI: 10.1039/d0nr03400b

rsc.li/nanoscale

We have studied the excitonic properties of exfoliated tungsten diselenide (WSe_2) monolayers transferred to gold substrates using the tunneling current in a Scanning Tunneling Microscope (STM) operated in air to excite the light emission locally. In obtained spectra, emission energies are independent of the applied bias voltage and resemble photoluminescence (PL) results, indicating that, in both cases, the light emission is due to neutral and charged exciton recombination. Interestingly, the electron injection rate, that is, the tunneling current, can be used to control the ratio of charged to neutral exciton emission. The obtained quantum yield in the transition metal dichalcogenide (TMD) is ~5×10^{-7} photons per electron. The proposed excitation mechanism is the direct injection of carriers into the conduction band. The monolayer WSe_2 presents bright and dark defects spotted by STM images performed under UHV. STS confirms the sample as p-doped, possibly as a net result of the observed defects. The presence of an interfacial water layer decouples the monolayer from the gold support and allows excitonic emission from the WSe_2 monolayer. The creation of a water layer is an inherent feature of the sample transferring process due to the ubiquitous air moisture. Consequently, vacuum thermal annealing, which removes the water layer, quenches excitonic luminescence from the TMD. The tunneling current can locally displace water molecules leading to excitonic emission quenching and to plasmonic emission due to the gold substrate. The present findings extend the use and the understanding of STM induced light emission (STM-LE) on semiconducting TMDs to probe exciton emission and dynamics with high spatial resolution.

1. Introduction

Group-VI transition metal dichalcogenides (TMDCs or TMDs), like MoS_2 or WSe_2, are two dimensional (2D) semiconductors that display a transition from indirect band gap to direct band gap when thinned to a monolayer.[1] These materials have interesting properties like high quantum efficiency (QE), and high exciton binding energy and are flexible.[2–6] Moreover, some of their features can be engineered by defects which may, for instance, enhance their QE and act as single-photon emitters.[7–10] Such properties have triggered considerable interest for applications in several areas, including light-emitting devices and photovoltaic panels, among many others.[11–14] However, the exciton dynamics in the nanometer scale is far from been understood, despite the profound effect it has on the optical and electronic properties of such materials. The reports mentioned above lack nanometer-scale information on the exciton dynamics due to the resolution limit of widespread optical techniques, like photoluminescence (PL).

Recently, Pommier *et al.*[4] successfully applied Scanning Tunneling Microscopy Induced Light Emission (STM-LE, also referred to as STM induced Luminescence, STML) to study $MoSe_2$. They observed excitonic emission and confirm the diffusion of excitons at room temperature up to 2 micrometers. Their study was performed in $MoSe_2$ mechanically transferred to an ITO substrate. Previous STM-LE studies of gold or graphene supported TMDs could not observe excitonic emission even in quasi-freestanding MoS_2 (instead, reported light emission is due to radiative plasmonic modes).[15,16] Moreover, in the case of metallic supports, the Purcell effect could have even enhanced the light emission if it is possible to void quenching by fast charge transfer to the metal.[17,18] Indeed, for TMD monolayers, similarly to STM-LE performed on molecules, understanding the possibly quenching effect of the supporting substrate is crucial.[17,19–21] However, intriguingly, metallic substrates have been observed both to quench and to enhance luminescence from TMDs.[18,22–24] Also, recently both

---

[a] *Applied Physics Department, "Gleb Wataghin" Institute of Physics, University of Campinas – UNICAMP, 13083-859 Campinas, SP, Brazil. E-mail: rikrdopr@ifi.unicamp.br, zagonel@ifi.unicamp.br*

[b] *Brazilian Synchrotron Light Laboratory (LNLS), Brazilian Center for Research in Energy and Materials (CNPEM), 13083-970 Campinas, SP, Brazil*

† Electronic supplementary information (ESI) available. See DOI: 10.1039/d0nr03400b

tip-enhanced PL and subsequent PL quenching for short tip–sample distance were observed for WS_2 and WSe_2 monolayers, including on gold substrates.[25–27] Finally, very few results of STM-LE applied to study the TMDs have been reported so far, even if STM-LE is an undeniably powerful technique to investigate the exciton dynamics and the optoelectronic response of 2D semiconductors together with their electronic structure and morphology at the nanometer scale.[28] Furthermore, the enhancement or quenching effects in the light emission of TMDs due to metallic substrates are ambiguous in the literature.

Here, we report the first observation of excitonic emission from a TMD on a metallic substrate using electron tunneling current as a nanoscale excitation source. We studied exfoliated WSe_2 monolayers transferred to gold thin film substrates and locally excited them using the tunneling current in an STM. STM-LE and PL spectra present the typical spectroscopic characteristic associated with the radiative recombination of bright A-neutral excitons and A-trions (charged excitons). The charge injection rate, adjusted by setting the tunneling current setpoint, controls the ratio of light emission due to trions and to neutral excitons. STM images and Scanning Tunneling Spectroscopy (STS) evidenced the presence of intrinsic structural defects and confirmed the p-type doping of the WSe_2. The STM-LE excitation mechanism proposed is the injection of negative charges into the conduction band of the semiconductor. Injected negative charges form neutral and charged excitons by Coulomb interaction with the positive charges in the p-doped sample. We propose the presence of a thin water decoupling layer to explain the absence of (excitonic light emission) quenching (due to the metallic substrate). Without quenching, excitonic STM-LE and PL become possible. The luminescence can be quenched on the whole flake by thermal annealing under ultra-high vacuum conditions or very locally removing the interfacial water using the tunneling current at the STM tip position. The results presented here give a clearer understanding of the excitonic light emission in STM-LE applied to TMDs and the quenching effect in 2D semiconducting materials supported by metallic substrates.

2. Experimental details

The STM-LE experiments were performed using an STM (RHK Technology Inc.), where a light collector device has been installed. In the setup, both STM-LE and *in situ* PL can be performed, the latter using a 532 nm laser diode operated below 100 μW. Spectra are recorded using an imaging spectrometer coupled to a cooled CCD camera. *In situ* PL experiments were performed with the tip retracted but otherwise on the same sample location. STM-LE signal can also be recorded panchromatically using a photomultiplier tube (PMT). STM images were acquired in the constant current-mode using a virtually grounded tungsten tip and a bias voltage applied to the sample. Tungsten tips were prepared by electrochemical etching with a NaOH solution and using a circuit for quickly stop the etching process. Tips were replaced frequently (at least every three days) to avoid thick tungsten oxide layers. Differential conductance was measured by STS using the lock-in technique with a modulation voltage of 40 mV and a frequency of 650 Hz.[29]

Monolayers were obtained from the same WSe_2 crystal purchased from HQ Graphene (p-type, having typical charge carrier densities of $\sim 10^{15}$ cm^{-3} at room temperature and a hole density of $p \sim 8 \times 10^{12}$ cm^{-2}). Flakes of WSe_2 were exfoliated on commercial PDMS films (Gel-Film® PF-40-X4 sold by Gel-Pak) using blue tape. The PDMS stamp with WSe_2 was placed on a transparent quartz plate and upon slowly bringing WSe_2 in contact at room temperature with a gold thin film substrate (~100 nm), deposited by sputtering on silicon. The ensemble was heated to ~65 °C for two minutes using a Peltier module kept underneath the Si/Au substrate. After allowing the ensemble to cool down, the PDMS stamp was slowly detached, leaving behind the WSe_2 flake transferred on top. This transfer process was performed in a cleanroom at (23 ± 1) °C and a humidity of (55 ± 5)%. STM imaging and STS were performed under UHV (base pressure 5×10^{-8} Pa) in samples that undergone annealing also under UHV. STM-LE was performed in air in as transferred samples at room temperature, (23 ± 1) °C, and in a controlled humidity of (35 ± 5)%. In total, six large monolayers similar to Fig. 1(a) were prepared following this recipe and were studied. The presented results show a compilation that is entirely consistent with all acquired data. Raman spectroscopy and *ex situ* PL were performed out-side the STM in a Horiba MicroRaman system using a 532 nm laser at 10 μW.

3. Results and discussion

3.1. Monolayer WSe_2 on gold decoupled by a water layer

Fig. 1(a) and (b) show light optical and Atomic Force Microscopy (AFM) images of a typical WSe_2 flake, respectively. The gold substrate gives sufficient visual contrast to assist in identifying monolayers by optical microscopy. Raman and PL of the as transferred samples are similar to those observed in monolayers transferred to silicon dioxide substrates (see Fig. S1 in ESI†).[30–33] The height of the monolayer WSe_2 above the substrate is about 2.4 nm and, considering that the thickness of the monolayer is about 0.9 nm,[34] the height profile shown in Fig. 1(b) indicates the presence of the expected water layer under the 2D material transferred to a substrate in ambient conditions (see also Fig. S2†).[35–42] A detailed study of the presence of interfacial water and its effects on exfoliated MoS_2 was recently published by S. Palleschi *et al.*[43] In their study, a nano-confined water layer at the interface (TMD-substrate) has been probed by AFM in as transferred and annealed samples. Similarly, we have performed AFM measurements in as transferred and in annealed samples, and, as shown in Fig. S2 of the ESI,† the height profile of the annealed sample gives 0.9 nm, the expected thickness for a single WSe_2 monolayer, typically observed in as-grown monolayers.[34,44,45] For

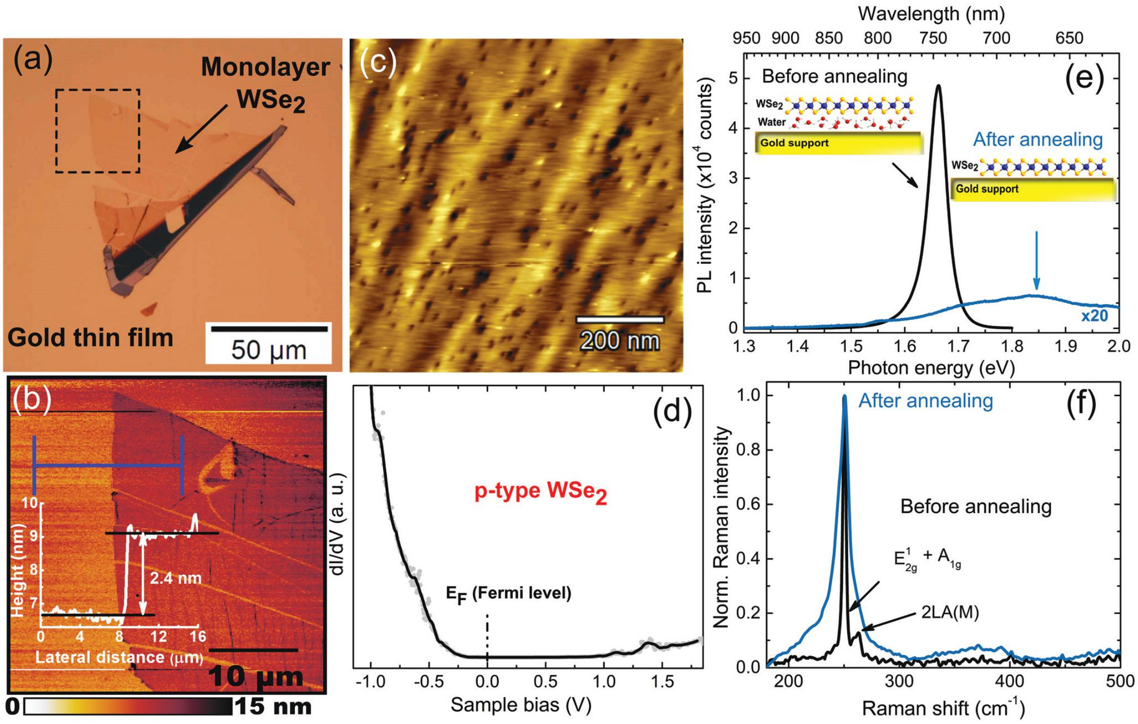

Fig. 1 (a) Light optical microscopy image of a typical WSe_2 flake. (b) AFM image of a region indicated in (a) by the dashed square. The average step height is 2.4 nm, as shown in the insert. (c) STM image obtained at room temperature and in UHV using a sample bias of 1.0 V and tunneling current of 65 pA. (d) dI/dV spectrum showing the p-doped nature of the WSe_2 sample. (e) PL and (f) Raman spectra before and after the UHV thermal annealing on the same monolayer WSe_2. The inserts in (e) illustrate the sample-substrate decoupling by the interfacial water layer.

WSe_2 flakes, water trapped between the exfoliated WSe_2 and the substrate can also lead to bottom flake surface oxidation.[46]

In ESI, Fig. S3† illustrates the STM tip approach process on the flake of interest for STM, STS, and STM-LE measurements. As prepared, the samples had atmospheric residues and transfer polymer residues on the surface. Such residues make them unsuitable for STM imaging or STS, both in air and under UHV. Samples are cleaned by mild thermal annealing at 400 K for 12 hours under UHV, as performed in other studies.[47] Annealing under these conditions should not modify the sample, and we consider it to be still the pristine WSe_2 monolayer only outgassed and cleaner after such process. After annealing, images as the one shown in Fig. 1(c) could be acquired, showing a surface undulation revealed as a height modulation. STM images recorded in TMDs samples frequently observe this type of surface morphology. It could be related to different sample substrate distances as proposed by I. Delač Marion *et al.*[47] or to the way the monolayer attaches to the (not atomically flat) gold substrate (see Fig. S4(a) in ESI†). Also, STM images show the presence of defects as bright and dark spots, similar to reported in the literature.[48–51] The apparent defect profile width and height/depth largely depend on the bias voltage,[50,51] and so does their visibility. As shown in Fig. S4,† the observed depth, ~0.5 nm, and width, ~5 nm, of the dark defects are roughly similar to (depth) or significantly larger (by a factor 2 to 3, width) than reported for MoS_2 and $MoSe_2$.[49,50] The defects observed here are intrinsic in the pristine sample,[48] since thermal annealing treatments at (or below) 400 K in TMDs should not induce defect creation but should only clean the surface from atmospheric contaminants.[43,52–54] The density of dark defects is about 4×10^{10} defects per cm^2, and of bright defects is 1×10^{10} defects per cm^2 (see Fig. S4 in ESI†). The order of magnitude of these intrinsic defects densities is consistent with reported results in exfoliated samples.[49,52,55] Previous STM/STS studies of point defects in TMD materials have shown that dark defects are related to transition metal defects (vacancies) inducing p-doping in the sample whereas bright defects are associated with chalcogen defects or adsorbate impurities with n-doping effect.[48–51,56,57] Therefore, since ~80% of the defects are of the dark type, the nominal p-doped character of the sample can be associated with dark defects. However, the difference between nominal p doping and the observed defect density could indicate other sources of doping or the existence of more defects than those observed in Fig. 1(c).[50]

We measured the density of states (DOS) using STS. In the STS curve, presented in Fig. 1(d), the Fermi level is closer to the valence band edge, indicating the hole-doped (p-type) nature of the sample. This result agrees with the expected (nominal) doping type and with reported for WSe_2 growth on highly oriented pyrolytic graphite (HOPG).[51] Additionally, in Fig. 1(d), the low DOS in the conduction band could indicate band bending, such as has been perceived in ref. 48, 49, 58 and 59. The reported band gap in the literature for exfoliated WSe_2 monolayers at room temperature lays between 1.9 and 2.0 eV.[60,61] However, the estimation or determination of a band gap value from the spectrum in Fig. 1(d) might be inaccurate since band edges are not observed clearly. The dI/dV curve may also be affected by the adhesion of the monolayer with the metallic substrate, such as found in systems such as MoS_2/Au(111),[15,62,63] WS_2/Ag(111) and WS_2/Au(111).[64] In such reports, samples are epitaxially grown on monocrystalline substrates and the interaction between the TMD and the metallic surface causes a hybridization of semiconductor states with substrate states leading to a band gap reduction. Also, it has been reported that this hybridization may produce other effects such as doping or metallization of the 2D semiconductor. However, these effects are expected only in epitaxial samples with high interfacial quality, and not in samples prepared by mechanical exfoliation methods.[64] The latter and the fact that the metallic substrates used in this work are not atomically flat could help explaining why, after all, to some extent, the STS data in Fig. 1(d) might be used as confirmation of the doping type. Finally, it is important to note that the STS in Fig. 1(d) refer to the monolayer WSe_2 absorbed on the gold substrate and it is a different scenario with respect to the water decoupled monolayer.

Fig. 1(e) and (f) show the (*ex situ*) PL and Raman spectra measured in a monolayer WSe_2 in air and at room temperature. These results were obtained before and after the UHV thermal annealing treatment. Before annealing, PL shows a sharp excitonic peak centered at 1.66 eV (747 nm), and the Raman spectrum shows the characteristic splitting of 12 cm^{-1} between the degenerate E^1_{2g} + A_{1g} and the 2LA(M) Raman modes around 250 cm^{-1}. One must note that PL experiments on TMDs are generally performed on samples grown on (or mechanically transferred to) isolating substrates like silicon dioxide.[9,38,60,65] Studies of TMDs on metallic substrates report luminescence enhancement or quenching, depending on the growth or transfer method.[15,18,22,66,67] However, it is known that mechanically transferred 2D material encapsulates thin airborne water (moisture) layers.[36,38,43,46] Such water layer could act as a spacer (also called barrier or buffer layer)[68] to decouple them and avoid the quenching by the metallic substrate, such as is illustrated in the inserts in Fig. 1(e). This decoupling layer is very similar to the needed spacer to observe STM luminescence of molecules in conducting substrates: a spacer that decouples to prevent quenching but allows electric contact within a reasonable compromise.[19–21] We consider the existence of a water layer beneath the monolayer WSe_2, as evidenced by AFM results in Fig. 1(b) and S2† after the mechanical transfer to the gold substrate. This layer acts as a dielectric insulating layer, and it is responsible for the effective semiconductor–metal (sample–substrate) decoupling and the observed PL and Raman spectra from Fig. 1(e) and (f).

After annealing, the step height, shown in Fig. 1(b) and S2(f),† reduces from 2.3 nm to 0.9 nm, as shown in Fig. S2(i),† indicating the removal of the water layer by the thermal annealing. That is, the step height after annealing is the monolayer thickness, suggesting the evaporation of the water that was under the monolayer. The drastic change in luminescence and Raman response after annealing also firms the vanished decoupling layer. After the annealing, the PL signal is severely quenched, and Raman peaks are broader (with respect to the Raman peaks in the as transferred samples) and the splitting between Raman peaks E^1_{2g} + A_{1g} and 2LA(M) is gone. These results suggest that the annealing produced a relevant electronic and mechanical contact between the monolayer and the gold substrate. This is consistent with the STS results which show that the sample–substrate interaction produces an electronic hybridization. The Raman peak widths could be related to stress gradients due to the monolayer adhesion on the gold thin film surface (see Fig. S4(a)†). Curiously, water intercalation enhanced the PL of sapphire supported WS_2, indicating its relevance even for insolating substrates.[37] However, water moisture trapped under TMDs was also reported to induced doping and be deleterious for the QE (as seen in PL) of MoS_2 and WS_2 but had a negligible effect on WSe_2.[38]

3.2. Excitonic light emission induced by the tunneling current

Being demonstrated above that there will be a sample–substrate decoupling that avoids the luminescence quenching, we performed STM-LE experiments in air on as transferred WSe_2 monolayers without previous annealing. The insert in Fig. 2(a) shows the STM tip approached on top of a monolayer WSe_2, as observed to find the sample. Fig. 2(a) shows STM-LE and *in situ* PL spectra obtained sequentially from the same monolayer WSe_2. In STM-LE, the sample bias was 4.0 V with a current setpoint of 44 nA in a fixed tip position. Panchromatic detection of the STM-LE signal using a PMT gave a Quantum Yield (QY) of $\sim 5 \times 10^{-7}$ photons per electron (see Fig. S5 in ESI†), a similar value to the reported for $MoSe_2$.[4] As shown in Fig. S5,† using a PMT, it is also possible to observe fluctuations of the light emission as expected in air.[69] Fig. 2(b) (see also Fig. S6†) shows STM-LE spectra acquired with different sample bias, each with a fixed STM tip position on the sample surface at different regions inside an area of 100 nm × 100 nm. No light could be detected for bias voltages of 1.9 eV or below, in agreement with the reported band gap, 2.0 eV.[61]

As pointed out in ref. 4 and 19, the close resemblance between the PL and STM-LE spectra (Fig. 2(a)) and the constant emission energies for different bias voltages in STM-LE spectra (Fig. 2(b)) are evidence that the emission mechanism is the same: radiative recombination of bright A excitons through the direct band gap of the semiconductor,[70] see also Fig. S7.† As shown in Fig. S8,† STM-LE spectra as a function of the sample bias voltage show no systematic peak energy shift, thus discarding any plasmon related emission from the tunneling cavity. Also, plasmon emission is distinctively different

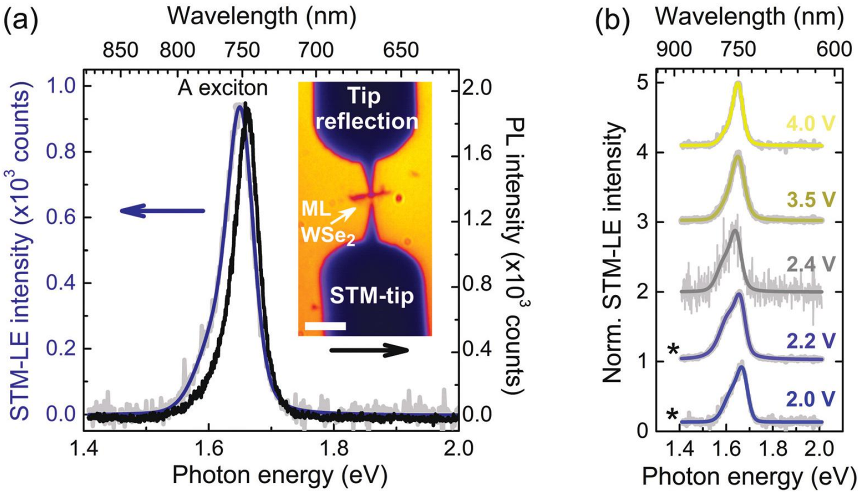

Fig. 2 (a) PL and STM-LE spectra of a monolayer of WSe$_2$. PL is excited with a laser (λ = 532 nm) when the tip is retracted. For STM-LE, the sample bias was 4.0 V, the current setpoint was 44 nA, and the integration time was 100 s. Insert: Zoom-lens optical micrograph showing the STM tip on top of the same flake shown in Fig. 1. The scale bar has 100 μm. (b) STM-LE for different sample bias voltages and different tunneling currents. The symbol * indicates those spectra taken using 25 nA as tunneling current, whereas the current was 44 nA for the others. In the spectra, the gray curves represent the raw data, and the solid colored lines are the result of curve fittings.

from WSe$_2$ excitonic emission, as discussed below and shown in Fig. S9.† The small peak position variations shown in Fig. S8† are due to the different acquisition positions for each spectrum. Indeed, each spectrum acquisition is performed in a new tip position to avoid changing the sample with the high tunneling current, as discussed in detail in ref. 4. Such peak energy variation happens because each different region of the WSe$_2$ layer is possibly subject to different stress due to the substrate roughness and possibly contains a slightly different density of defects.

In TMDs, the difference between the electronic band gap energy and the emitted photon energy is due to the exciton binding energy, 0.37 eV, that prevents the band-to-band radiative recombination and leads to excitonic light emission with smaller energy than the band gap even at room temperature.[61] Additionally, neutral excitons and charged excitons (trions) dominate the optical properties of TMDs.[60] STM-LE spectra in Fig. 2(a) is a convolution of the radiative recombination of bright A-neutral excitons at 1.65 eV (751 nm) and A-trion at 1.62 eV (765 nm). Fig. S7† shows fitted spectra in close agreement with recent literature.[71–73] In the PL spectra, the neutral exciton and trion emissions are observed at 1.66 eV (747 nm) and 1.63 eV (761 nm), respectively. The difference between the neutral exciton and trions peaks gives a trion binding energy of 30 meV. As mentioned previously, the neutral or charged exciton emission energies are independent of the bias voltage or tunneling current (see Fig. S8†). Fig. S8† indicates that the observed light emissions are related to what is happening inside the WSe$_2$ monolayer and do not depend on the proximity of the tip (tunneling cavity size) or the electric field under the tip.

3.3. Trion emission control using the tunneling current

The control and manipulation of neutral excitons and trions are crucial for improving and tuning the performance of TMDs based devices. Several approaches have been used with this propose in the last years, such as chemical doping,[74] gate doping,[75] photoexcitation,[76] and charges transfer in TMDs heterostructures.[77] More recently, He *et al.* have reported the nanoscale control of negative trions using a plasmonic picocavity in WS$_2$ monolayers.[25] In STM-LE, the charge carrier injection rate given by the tunneling current can control A trion emission. Fig. 3(a) shows STM-LE spectra acquired for different tunneling currents indicating this systematic change of the light emission related to trions for currents ranging from 25 nA to 90 nA. Below 25 nA, no exploitable spectrum could be acquired. As in other cases, each spectrum was acquired in a different (fresh) region to avoid any possible sample modification or cumulative effects. Also, optical microscopy before and after these measurements spotted no sign of STM related sample damage.

As shown in Fig. 3(b), which summarizes the data of Fig. 3(a) and other spectra not shown, the area of the trion peak, A_T, divided by the area of the neutral exciton, A_0, (area ratio A_T/A_0) scales linearly with the tunneling current. Interestingly, the low laser power PL spectrum in Fig. 2(a), also represented in Fig. 3(b) as the point at 0 nA, shows the ratio 0.5 when both electrons and holes are created with relatively low density (laser power below 100 μW in a spot with ~2 microns in diameter). In this case, trion formation relates to the sample doping. In STM-LE, with single carrier type (electron) injection, a 0.5 A_T/A_0 ratio would correspond roughly to a tunneling current of 20 nA (that is below our detection limit).

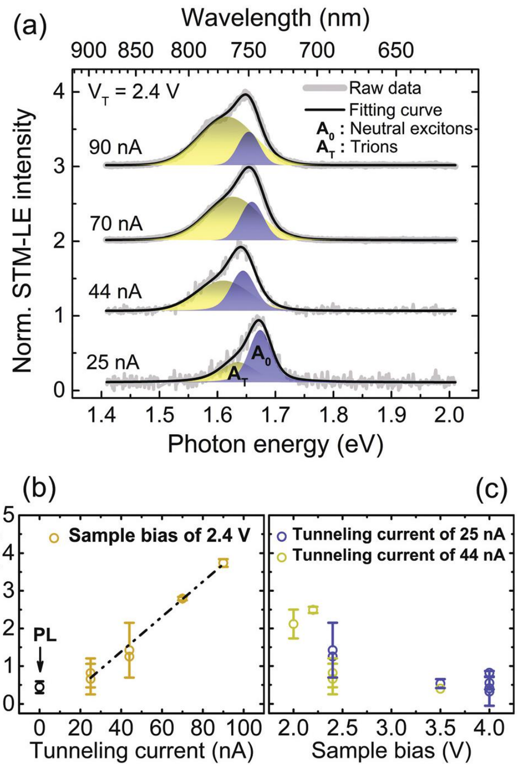

Fig. 3 (a) STM-LE spectra for 2.4 V (sample bias) shows the effect of different tunneling currents. Higher currents enhance trion emission. (b) and (c) show the dependence of the ratio of trion to neutral exciton emission as a function of the tunneling current and sample bias, respectively. In (b), the ratio for the PL spectrum is also indicated.

20 nA could be considered as the maximum charge injection rate that does not increase trion formation by an excess of injected electrons. On the other limit, at 90 nA, the trion emission is nearly four times greater than the emission of neutral excitons.

Considering the exciton lifetime that ranges from 0.4 ns to 4 ns in WSe_2 monolayers at room temperature[78,79] and the time interval between consecutive injected electrons, that is, for instance, 6.4 ps in average for a tunneling current of 25 nA, the tunneling current should affect the trion formation. That is, at low currents, each injected electron would have time to find a hole and form an exciton and latter possibly form a trion with another hole from the sample. At high currents, there would be an increased probability that an injected electron would find an already formed exciton before it had time do decay or to diffuse away. Using the diffusion coefficient of excitons measured by S. Mouri *et al.* in ref. 78, ~(2.2 ± 1.1) cm^2 s^{-1}, and the time interval between consecutive injecting electrons (supposing one electron arrives at a time in regular intervals), an exciton created under the tip could diffuse less than 10^2 nm before the next one arrives at 25 nA and half of this distance for 90 nA. Additionally, at least for high currents, one can consider that the observed trions are most likely negatively charged since the overwhelming electron injection forms them into the p-doped material. A more quantitative analysis, however, would require details that go beyond the scope of this work. In contrast to reported in ref. 25, where trions are controlled in a light excited picocavity, here we show that, in STM-LE, trions could be controlled by the tunneling current at the nanoscale. Dynamical effects due to the charge injection rate on light emission have also been explored in other semiconducting systems using STM-LE and Cathodoluminescence in Scanning Transmission Electron Microscope (STEM-CL).[80,81]

Whereas the effect of the tunneling current on the charged to neutral exciton ratio is about fivefold in the available tunneling current range and can be interpreted as an accumulation of injected negative charges, changing the sample bias also presents a similar effect, as shown in Fig. 3(c). Indeed, for constant current and increasing sample bias, the ratio changes from ~2.5 to ~0.5 (the ratio decreases for increasing bias). This effect is not expected in the simple view of charge injection. However, in STM, changing the sample bias changes more than the end state of elastically tunneled electrons. One could expect different ratios of elastic to inelastic tunneling, among other effects. In this sense, one must consider that the bias voltage has a broader impact on the experiment than the tunnel current, and a comparison between results obtained under different bias voltages requires care. It is worthy to note that the trion to neutral exciton ration increases for decreasing tip distance in both situations in Fig. 3(b) and (c). Nonetheless, as shown in Fig. S8,† the bias voltage and the tunneling current have no significant effect on the trion and neutral exciton emission energies, indicating the absence of energy shifts due to the tip electric field.

3.4. Local excitonic emission quenching

We also observed that the excitonic light emission quenching due to the gold substrate could be produced locally by the tunneling current. Fig. 4 shows STM-LE spectra measured sequentially in the same point of the monolayer just after moving the STM tip to a new region and keeping the tip position fixed during the spectra integration time (100 s per spectrum). The sample bias was 4.0 V and the tunneling current setpoint 44 nA. We note that the excitonic emission at 1.65 eV progressively vanishes, and a broad plasmonic emission appears. This plasmon emission is interpreted as a cavity mode between the tip and the gold substrate surface with the TMD in the middle, similarly as previously observed for MoS_2.[15] Other tunneling parameters can also lead to plasmon emission after the excitonic light emission from the WSe_2 is quenched (see Fig. S9†). Particularly, approaching the tip to create a brief contact between sample and tip (a tip reconstruction process called 'tip pulse') quickly quenches excitonic emissions and triggers plasmonic emission. The tip and the tunneling current causes the progressive change from excitonic to plasmonic emission by the local removal of water molecules that move away from the tip position, as already observed in graphene transferred on mica[39] and MoS_2/HOPG samples.[40] The direct sample–sub-

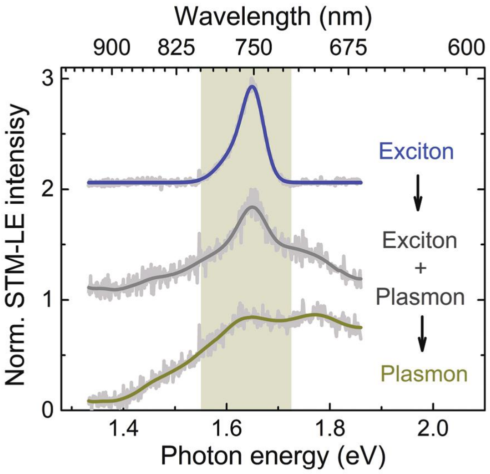

Fig. 4 STM-LE spectra taken sequentially in the same sample region with the tip position fixed (44 nA, 4.0 V, and 100 s). The highlighted region shows the position of excitonic emissions.

strate contact when the water under the monolayer is removed quenches exciton emission locally by creating fast non-radiative recombination paths. A transition from excitonic to plasmonic emission has also been systematically obtained in STM-LE studies on molecular systems by varying the effectiveness of the decoupling between the optically active molecule and the conducting substrate.[19,28] It is interesting to note also that plasmon emission could be readily obtained using the parameter given in Fig. 4 in some regions. However, in other regions, pure excitonic emission would persist for longer times, possibly due to the gold support topography. Also, using lower sample bias voltages, excitonic emission is observed for longer times with no significant plasmon emission. Finally, sample damage (defect creation) can be ruled out due to the absence of luminescence changes when using high current or high bias (see Fig. 2 and 3) and since plasmon emission appears when excitonic emission vanishes which indicate the collapse of the monolayer into the substrate (following water removal).

3.5. Excitation mechanism due to the tunneling current

In Fig. 5, we summarize a proposition of the light emission and excitation mechanisms in STM-LE in monolayer WSe_2 together with a scheme of the experiment and band diagrams. First, the emission mechanism, as discussed previously, is the neutral exciton and trion recombination, as observed in PL. The sample–substrate decoupling due to the substrate–borne water moisture is fundamental to avoid luminescence quenching by the gold substrate. Fig. 5(a) illustrates the experiment and the emission mechanism.

Unlike PL, however, the excitation in STM-LE happens in the nanoscale, and the excitation mechanism is not the creation of electron–hole pairs. In this work, we propose the direct electron injection in the conduction band by the STM tip as the excitation mechanism. Subsequently, injected electrons form excitons and trions with the holes already present in the monolayer. The following results support this excitation mechanism: (i) the STM/STS results evidenced the presence of defects and p-type doping (in agreement with the nominal sample doping), which imply that positively charged carriers (holes) are present in the sample and, by injecting electrons, exciton formation is possible; (ii) no STM-LE signal was observed with negative biases, in connection to the p-doped nature of the sample, which also rules out the possibility of

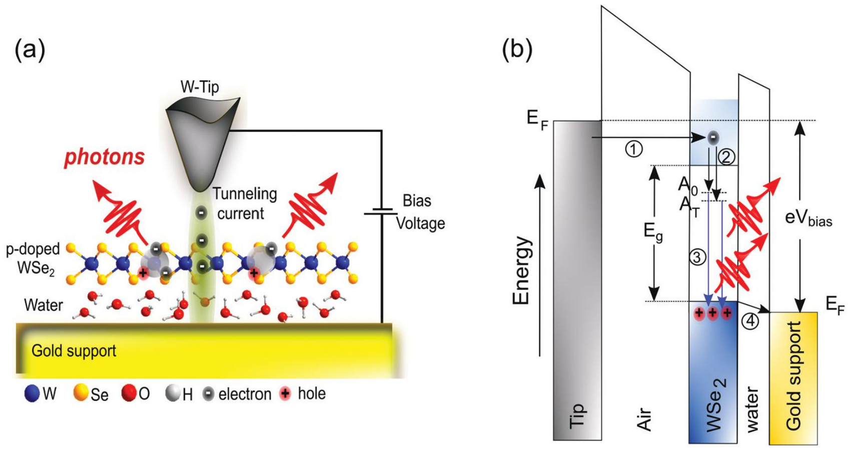

Fig. 5 (a) Scheme of the experiment showing the presence of the decoupling water layer. (b) Proposed STM-LE excitation mechanism. Elastically tunneling electrons are injected as hot carriers in the WSe_2 conduction band (1), after thermalization, the injected carrier binds into an excitonic state (2) then photons are emitted by exciton recombination (3), and, finally, electrons tunnel from the monolayer to the gold to keep the monolayer neutral (4). The sample bias voltage is larger than the electronic band gap.

plasmon mediated emission;[82–84] (iii) excitonic light emission was only observed with positive bias voltages at or above 2.0 V, which is expected for electron injection luminescence mechanisms, where biases higher than the electronic band gap are necessary to excite the light emission.[19,85,86]

In Fig. 5(b), a band diagram summarizes such excitation mechanism. First, the electrons tunnel elastically into the conduction band of the 2D semiconductor. Then, they bound with existing holes into excitonic states. The substrate–borne water moisture acts as a dielectric barrier to decouple the monolayer and the gold substrate (support), preventing non-radiative recombinations due to substrate effect (quenching). Next, the recombination of neutral excitons and trions gives rise to the light emission. The possible band banding in the monolayer, if present, does not affect excitonic emission energies, as shown in Fig. 2(b) and S8.† Finally, an electron tunnels from the monolayer to the substrate to neutralize the monolayer. Regarding the role of the water layer, one might consider its effects go beyond that of mere decoupling the monolayer WSe_2 and making it behave as if it were free-standing. Additionally, TMDs on top of trapped water layers have much smaller PL efficiency than truly suspended ones.[38] Indeed, the water layer might change the TMD quantum efficiency and light emission by chemical doping,[38] similarly as observed for aromatic solvent.[87]

Generally speaking, one must also note that, in STM-LE, only one carrier polarity is created (injected). Hence, exciton formation depends on the sample doping for the other carrier, while, in PL, both carriers are created inside the sample. Another striking contrast between these techniques is that, in STM-LE, the excitation is exceptionally local, certainly in the sub-nanometer range. While, in PL, the excitation region spams over at least nearly one squared micrometer. Also, it is important to note that the light detection region in STM is different from that in PL or in a Scanning Near-Field Optical Microscope (SNOM) in which both excitation and detection are local and similar.[28] In STM-LE, similarly to CL-STEM, the excitation is local (local excitation, possibly below one squared nanometre), but the region from which emitted light is detected is much larger (global detection).[88,89] This means that one knows where the excitation was performed (tip or electron probe position) but does not know the location of the emitted light. In the context of the local quenching due to the point contact between the monolayer WSe_2 and the gold substrate, global light detection means that all injected carriers are lost into the gold substrate before any diffusion in the TMD could take place. This is expected since the electrons in the WSe_2 conduction band should recombine non-radiatively through the metal very quickly (quench effect), and the vast majority of the injected carrier would follow this recombination path since the contact is precisely at the tip position.

4. Conclusions

We observed excitonic light emission from WSe_2 monolayers excited by the tunneling current within an STM in ambient conditions, using a non-plasmonic (tungsten) tip and on a metallic support. The luminescence excited by the tunneling current resembles that excited by light (PL) and is attributed to radiative recombination of bright A-neutral excitons and A-trions. The ratio of trions to neutral excitons emission can be controlled and manipulated using the tunneling current, but the emission energies remain unaffected by tunneling parameters. The gold support where the monolayers were transferred to did not quench the excitonic light emission from the monolayer due to an inherent interfacial water layer that effectively decouples them. Quenching could be triggered either by thermal annealing under vacuum, as confirmed by PL and Raman, or locally using the tip and tunneling current, as observed by STM-LE. Both processes remove the underneath interfacial water layer, either globally or locally, respectively. Without the water layer, plasmonic emission could be observed by STM-LE due to the gold substrate. These results contribute to the understanding of the STM-LE use in the investigations of light emission from TMDs and of the quenching effect due to metallic supports.

Conflicts of interest

The authors have no conflicts of interest to declare.

Acknowledgements

This work was supported by the Fundação de Amparo à Pesquisa do Estado de São Paulo (FAPESP) Projects 14/23399-9 and 18/08543-7. I. D. B. acknowledges the financial support from the Brazilian Nanocarbon Institute of Science and Technology (INCT/Nanocarbono) and Brazilian Synchrotron Light Laboratory (LNLS). L. F. Z. thanks Dr. Eric Le Moal (ISMO) and Dr. Mathieu Kociak (LPS) for valuable and insightful discussions which were exceedingly helpful to this research.

References

1 K. F. Mak, C. Lee, J. Hone, J. Shan and T. F. Heinz, Atomically thin MoS_2: A new direct-gap semiconductor, *Phys. Rev. Lett.*, 2010, **105**, 136805.
2 F. Xia, H. Wang, D. Xiao, M. Dubey and A. Ramasubramaniam, Two-dimensional material nanophotonics, *Nat. Photonics*, 2014, **8**, 899–907.
3 M. Amani, *et al.*, Near-unity photoluminescence quantum yield in MoS_2, *Science*, 2015, **350**, 1065–1068.
4 D. Pommier, *et al.*, Scanning Tunneling Microscope-Induced Excitonic Luminescence of a Two-Dimensional Semiconductor, *Phys. Rev. Lett.*, 2019, **123**, 1–7.
5 M. Bernardi, C. Ataca, M. Palummo and J. C. Grossman, Optical and Electronic Properties of Two-Dimensional Layered Materials, *Nanophotonics*, 2017, **6**, 479–493.

6 T. Mueller and E. Malic, Exciton physics and device application of two-dimensional transition metal dichalcogenide semiconductors, *npj 2D Mater. Appl.*, 2018, **2**, 29.

7 S. Tongay, *et al.*, Defects activated photoluminescence in two-dimensional semiconductors: interplay between bound, charged and free excitons, *Sci. Rep.*, 2013, **3**, 2657.

8 H. Nan, *et al.*, Strong photoluminescence enhancement of MoS_2 through defect engineering and oxygen bonding, *ACS Nano*, 2014, **8**, 5738–5745.

9 P. Tonndorf, *et al.*, Single-photon emission from localized excitons in an atomically thin semiconductor, *Optica*, 2015, **2**, 347.

10 Q. Qian, *et al.*, Defect creation in WSe_2 with a microsecond photoluminescence lifetime by focused ion beam irradiation, *Nanoscale*, 2020, **12**, 2047–2056.

11 F. Withers, *et al.*, Light-emitting diodes by band-structure engineering in van der Waals heterostructures, *Nat. Mater.*, 2015, **14**, 301–306.

12 C. Li, *et al.*, Engineering graphene and TMDs based van der Waals heterostructures for photovoltaic and photoelectrochemical solar energy conversion, *Chem. Soc. Rev.*, 2018, **47**, 4981–5037.

13 T. Akama, *et al.*, Schottky solar cell using few-layered transition metal dichalcogenides toward large-scale fabrication of semitransparent and flexible power generator, *Sci. Rep.*, 2017, **7**, 1–10.

14 J. Wong, *et al.*, High Photovoltaic Quantum Efficiency in Ultrathin van der Waals Heterostructures, *ACS Nano*, 2017, **11**, 7230–7240.

15 N. Krane, C. Lotze, J. M. Läger, G. Reecht and K. J. Franke, Electronic Structure and Luminescence of Quasi-Freestanding MoS_2 Nanopatches on Au(111), *Nano Lett.*, 2016, **16**, 5163–5168.

16 B. Schuler, *et al.*, Electrically driven photon emission from individual atomic defects in monolayer WS_2, 2019, arXiv:1910.04612v1.

17 J. Kröger, B. Doppagne, F. Scheurer and G. Schull, Fano Description of Single-Hydrocarbon Fluorescence Excited by a Scanning Tunneling Microscope, *Nano Lett.*, 2018, **18**, 3407–3413.

18 Z. Wang, *et al.*, Giant photoluminescence enhancement in tungsten-diselenide-gold plasmonic hybrid structures, *Nat. Commun.*, 2016, **7**, 1–8.

19 X. H. Qiu, G. V. Nazin and W. Hot, Vibrationally resolved fluorescence excited with submolecular precision, *Science*, 2003, **299**, 542–546.

20 H. Imada, *et al.*, Real-space investigation of energy transfer in heterogeneous molecular dimers, *Nature*, 2016, **538**, 364–367.

21 Y. Zhang, *et al.*, Visualizing coherent intermolecular dipole–dipole coupling in real space, *Nature*, 2016, **531**, 623–627.

22 U. Bhanu, M. R. Islam, L. Tetard and S. I. Khondaker, Photoluminescence quenching in gold-MoS_2 hybrid nanoflakes, *Sci. Rep.*, 2014, **4**, 1–5.

23 K. C. J. Lee, *et al.*, Plasmonic gold nanorods coverage influence on enhancement of the photoluminescence of two-dimensional MoS_2 monolayer, *Sci. Rep.*, 2015, **5**, 1–9.

24 A. Arora, *et al.*, Plasmon induced brightening of dark exciton in monolayer WSe_2 for quantum optoelectronics, *Appl. Phys. Lett.*, 2019, **114**, 201101.

25 Z. He, *et al.*, Quantum plasmonic control of trions in a picocavity with monolayer WS_2, *Sci. Adv.*, 2019, **5**, 1–9.

26 K. D. Park, *et al.*, Hybrid Tip-Enhanced Nanospectroscopy and Nanoimaging of Monolayer WSe_2 with Local Strain Control, *Nano Lett.*, 2016, **16**, 2621–2627.

27 K.-D. Park, T. Jiang, G. Clark, X. Xu and M. B. Raschke, Radiative control of dark excitons at room temperature by nano-optical antenna-tip Purcell effect, *Nat. Nanotechnol.*, 2018, **13**, 59–64.

28 K. Kuhnke, C. Große, P. Merino and K. Kern, Atomic-scale imaging and spectroscopy of electroluminescence at molecular interfaces, *Chem. Rev.*, 2017, **117**, 5174–5222.

29 H. J. Liu, *et al.*, Molecular-beam epitaxy of monolayer and bilayer WSe_2: a scanning tunneling microscopy/spectroscopy study and deduction of exciton binding energy, *2D Mater.*, 2015, **2**, 034004.

30 P. Tonndorf, *et al.*, Photoluminescence emission and Raman response of monolayer MoS_2, $MoSe_2$, and WSe_2, *Opt. Express*, 2013, **21**, 4908.

31 H. Zeng, *et al.*, Optical signature of symmetry variations and spin-valley coupling in atomically thin tungsten dichalcogenides, *Sci. Rep.*, 2013, **3**, 2–6.

32 H. Terrones, *et al.*, New First Order Raman-active Modes in Few Layered Transition Metal Dichalcogenides, *Sci. Rep.*, 2014, **4**, 1–9.

33 W. Zhao, *et al.*, Lattice dynamics in mono- and few-layer sheets of WS_2 and WSe_2, *Nanoscale*, 2013, **5**, 9677.

34 B. Liu, *et al.*, Chemical Vapor Deposition Growth of Monolayer WSe_2 with Tunable Device Characteristics and Growth Mechanism Study, *ACS Nano*, 2015, **9**, 6119–6127.

35 R. Nelz, *et al.*, Near-Field Energy Transfer between a Luminescent 2D Material and Color Centers in Diamond, *Adv. Quantum Technol.*, 2020, **3**, 1900088.

36 Q. Li, J. Song, F. Besenbacher and M. Dong, Two-dimensional material confined water published as part of the accounts of chemical research special issue ‘2d nanomaterials beyond Graphene’, *Acc. Chem. Res.*, 2015, **48**, 119–127.

37 Q. Zhang, *et al.*, Reliable Synthesis of Large-Area Monolayer WS_2 Single Crystals, Films, and Heterostructures with Extraordinary Photoluminescence Induced by Water Intercalation, *Adv. Opt. Mater.*, 2018, **6**, 1–9.

38 Y. Yu, *et al.*, Engineering Substrate Interactions for High Luminescence Efficiency of Transition-Metal Dichalcogenide Monolayers, *Adv. Funct. Mater.*, 2016, **26**, 4733–4739.

39 K. T. He, J. D. Wood, G. P. Doidge, E. Pop and J. W. Lyding, Scanning tunneling microscopy study and nanomanipulation of graphene-coated water on mica, *Nano Lett.*, 2012, **12**, 2665–2672.

40 M. Hong, *et al.*, Decoupling the Interaction between Wet-Transferred MoS_2 and Graphite Substrate by an Interfacial Water Layer, *Adv. Mater. Interfaces*, 2018, **5**, 1–8.

41 J. Song, *et al.*, Evidence of Stranski-Krastanov growth at the initial stage of atmospheric water condensation, *Nat. Commun.*, 2014, **5**, 1–8.

42 D. A. Sanchez, *et al.*, Mechanics of spontaneously formed nanoblisters trapped by transferred 2D crystals, *Proc. Natl. Acad. Sci. U. S. A.*, 2018, **115**, 7884–7889.

43 S. Palleschi, *et al.*, On the role of nano-confined water at the 2D/SiO_2 interface in layer number engineering of exfoliated MoS_2 via thermal annealing, *2D Mater.*, 2020, 7, 025001.

44 L. Fang, *et al.*, Quick Optical Identification of the Defect Formation in Monolayer WSe_2 for Growth Optimization, *Nanoscale Res. Lett.*, 2019, **14**, 274.

45 M. S. Diware, *et al.*, Characterization of wafer-scale MoS_2 and WSe_2 2D films by spectroscopic ellipsometry, *Curr. Appl. Phys.*, 2017, **17**, 1329–1334.

46 Y. Liu, *et al.*, Thermal Oxidation of WSe_2 Nanosheets Adhered on SiO_2/Si Substrates, *Nano Lett.*, 2015, **15**, 4979–4984.

47 I. Delač Marion, *et al.*, Atomic-scale defects and electronic properties of a transferred synthesized MoS_2 monolayer, *Nanotechnology*, 2018, **29**, 305703.

48 R. Addou and R. M. Wallace, Surface Analysis of WSe_2 Crystals: Spatial and Electronic Variability, *ACS Appl. Mater. Interfaces*, 2016, **8**, 26400–26406.

49 D. Edelberg, *et al.*, Approaching the Intrinsic Limit in Transition Metal Diselenides via Point Defect Control, *Nano Lett.*, 2019, **19**, 4371–4379.

50 R. Addou, L. Colombo and R. M. Wallace, Surface Defects on Natural MoS_2, *ACS Appl. Mater. Interfaces*, 2015, **7**, 11921–11929.

51 S. Zhang, *et al.*, Defect Structure of Localized Excitons in a WSe_2 Monolayer, *Phys. Rev. Lett.*, 2017, **119**, 1–6.

52 M. Liu, *et al.*, Temperature-Triggered Sulfur Vacancy Evolution in Monolayer MoS_2/Graphene Heterostructures, *Small*, 2017, **13**, 1602967.

53 S. McDonnell, *et al.*, Hole contacts on transition metal dichalcogenides: Interface chemistry and band alignments, *ACS Nano*, 2014, **8**, 6265–6272.

54 S. McDonnell, R. Addou, C. Hinkle and R. Wallace, Physico-Chemical Characterisation of MoS_2/Metal and MoS_2/Oxide Interfaces, in *2D Materials for Nanoelectronics*, 2016, pp. 163–206. DOI: 10.1201/b19623-10.

55 C. P. Lu, G. Li, J. Mao, L. M. Wang and E. Y. Andrei, Bandgap, mid-gap states, and gating effects in MoS_2, *Nano Lett.*, 2014, **14**, 4628–4633.

56 S. N. Magonov, H. J. Cantow and M. H. Whangbo, On the nature of nanometer-scale ring structures in the scanning tunneling microscopy images of tungsten diselenide WSe2, *Surf. Sci.*, 1994, **318**, L1175–L1180.

57 T. W. Matthes, *et al.*, Imaging of dopants in surface and sub-surface layers of the transitionmetal dichalcogenides WS_2 and WSe_2 by scanning tunneling microscopy, *Appl. Phys. A: Mater. Sci. Process.*, 1998, **66**, S1007–S1011.

58 T. Le Quang, *et al.*, Band-bending induced by charged defects and edges of atomically thin transition metal dichalcogenide films, *2D Mater.*, 2018, **5**, 035034.

59 F. Zhang, *et al.*, Atomically Resolved Observation of Continuous Interfaces between an As-Grown MoS_2 Monolayer and a WS_2/MoS_2 Heterobilayer on SiO_2, *ACS Appl. Nano Mater.*, 2018, **1**, 2041–2048.

60 G. Wang, *et al.*, Colloquium : Excitons in atomically thin transition metal dichalcogenides, *Rev. Mod. Phys.*, 2018, **90**, 021001.

61 K. He, *et al.*, Tightly bound excitons in monolayer WSe_2, *Phys. Rev. Lett.*, 2014, **113**, 1–5.

62 A. Bruix, *et al.*, Single-layer MoS_2 on Au(111): Band gap renormalization and substrate interaction, *Phys. Rev. B*, 2016, **93**, 1–10.

63 N. Krane, C. Lotze and K. J. Franke, Moiré structure of MoS_2 on Au(111): Local structural and electronic properties, *Surf. Sci.*, 2018, **678**, 136–142.

64 M. Dendzik, *et al.*, Substrate-induced semiconductor-to-metal transition in monolayer WS_2, *Phys. Rev. B*, 2017, **96**, 1–6.

65 S. Lippert, *et al.*, Influence of the substrate material on the optical properties of tungsten diselenide monolayers, *2D Mater.*, 2017, **4**, 025045.

66 W. Zhao, *et al.*, Exciton-Plasmon Coupling and Electromagnetically Induced Transparency in Monolayer Semiconductors Hybridized with Ag Nanoparticles, *Adv. Mater.*, 2016, **28**, 2709–2715.

67 P. Garg, R. Laishram, R. Raman and R. K. Soni, Photoluminescence Quenching and SERS in Tri-layer MoS_2 Flakes, *J. Electron. Mater.*, 2019, **48**, 5883–5890.

68 K. Kuhnke, A. Kabakchiev, T. Lutz and K. Kern, Electroluminescence properties of organic nanostructures studied by scanning tunnelling microscopy, *Phys. Status Solidi B*, 2012, **249**, 644–652.

69 B. Rogez, *et al.*, The mechanism of light emission from a scanning tunnelling microscope operating in air, *Nanotechnology*, 2016, **27**, 465201.

70 M. Koperski, *et al.*, Optical properties of atomically thin transition metal dichalcogenides: Observations and puzzles, *Nanophotonics*, 2017, **6**, 1289–1308.

71 J. Jadczak, *et al.*, Probing of free and localized excitons and trions in atomically thin WSe_2, WS_2, $MoSe_2$ and MoS_2 in photoluminescence and reflectivity experiments, *Nanotechnology*, 2017, **28**, 395702.

72 S. Lippert, *et al.*, Influence of the substrate material on the optical properties of tungsten diselenide monolayers, *2D Mater.*, 2017, **4**, 025045.

73 J. Huang, T. B. Hoang and M. H. Mikkelsen, Probing the origin of excitonic states in monolayer WSe_2, *Sci. Rep.*, 2016, **6**, 1–7.

74 N. Peimyoo, *et al.*, Chemically driven tunable light emission of charged and neutral excitons in monolayer WS2, *ACS Nano*, 2014, **8**, 11320–11329.

75 J. S. Ross, *et al.*, Electrical control of neutral and charged excitons in a monolayer semiconductor, *Nat. Commun.*, 2013, **4**, 1–6.

76 A. A. Mitioglu, *et al.*, Optical manipulation of the exciton charge state in single-layer tungsten disulfide, *Phys. Rev. B: Condens. Matter Mater. Phys.*, 2013, **88**, 1–5.
77 M. Z. Bellus, F. Ceballos, H. Y. Chiu and H. Zhao, Tightly Bound Trions in Transition Metal Dichalcogenide Heterostructures, *ACS Nano*, 2015, **9**, 6459–6464.
78 S. Mouri, *et al.*, Nonlinear photoluminescence in atomically thin layered WSe_2 arising from diffusion-assisted exciton-exciton annihilation, *Phys. Rev. B: Condens. Matter Mater. Phys.*, 2014, **90**, 155449.
79 N. B. Mohamed, *et al.*, Long radiative lifetimes of excitons in monolayer transition-metal dichalcogenides MX_2 (M = Mo, W; X = S, Se), *Appl. Phys. Express*, 2018, **11**, 015201.
80 L. F. Zagonel, *et al.*, Nanometer-scale monitoring of quantum-confined Stark effect and emission efficiency droop in multiple GaN/AlN quantum disks in nanowires, *Phys. Rev. B*, 2016, **93**, 205410.
81 P. Merino, *et al.*, Bimodal exciton-plasmon light sources controlled by local charge carrier injection, *Sci. Adv.*, 2018, **4**, 1–8.
82 G. Tian, J. C. Liu and Y. Luo, Density-matrix approach for the electroluminescence of molecules in a scanning tunneling microscope, *Phys. Rev. Lett.*, 2011, **106**, 1–4.
83 G. Tian and Y. Luo, Electroluminescence of molecules in a scanning tunneling microscope: Role of tunneling electrons and surface plasmons, *Phys. Rev. B: Condens. Matter Mater. Phys.*, 2011, **84**, 1–9.
84 N. L. Schneider and R. Berndt, Plasmonic exciation of light emission and absorption by porphyrine molecules in a scanning tunneling microscope, *Phys. Rev. B: Condens. Matter Mater. Phys.*, 2012, **86**, 2–5.
85 G. Reecht, *et al.*, Electroluminescence of a polythiophene molecular wire suspended between a metallic surface and the tip of a scanning tunneling microscope, *Phys. Rev. Lett.*, 2014, **112**, 1–5.
86 E. Ćavar, *et al.*, Fluorescence and phosphorescence from individual C_{60} molecules excited by local electron tunneling, *Phys. Rev. Lett.*, 2005, **95**, 5–8.
87 Y. Wang, *et al.*, Doping of Monolayer Transition-Metal Dichalcogenides via Physisorption of Aromatic Solvent Molecules, *J. Phys. Chem. Lett.*, 2019, **10**, 540–547.
88 L. F. Zagonel, *et al.*, Visualizing highly localized luminescence in GaN/AlN heterostructures in nanowires, *Nanotechnology*, 2012, **23**, 455205.
89 M. Kociak and L. F. Zagonel, Cathodoluminescence in the scanning transmission electron microscope, *Ultramicroscopy*, 2017, **176**, 112–131.

Electronic Supplementary Information

Tunneling-current-induced local excitonic luminescence in p-doped WSe_2 monolayers

Ricardo Javier Peña Román,*[a] Yves Auad, [a] Lucas Grasso,[a] Fernando Alvarez,[a] Ingrid David Barcelos [b] and Luiz Fernando Zagonel **[a]

* rikrdopr@ifi.unicamp.br

** zagonel@ifi.unicamp.br

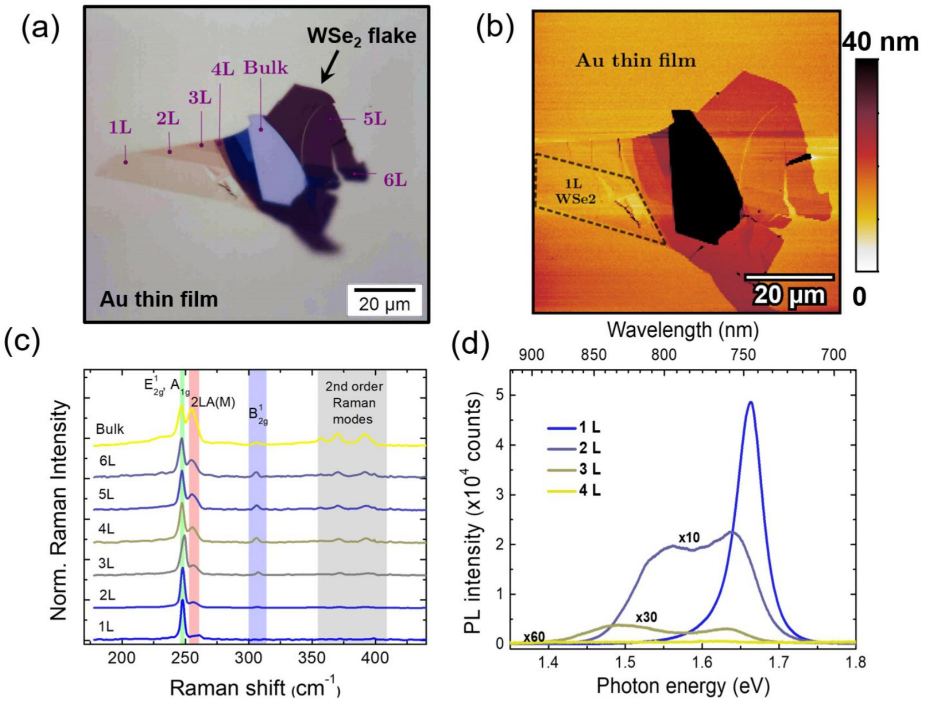

Figure S1: Pre-characterization of an exfoliated WSe$_2$ flake transferred to 100 nm Au thin film on Si substrate. (a) Optical microscopy image. The optical contrast in the gold substrate helps to identify regions with a different number of layers. (b) Atomic Force Microscopy (AFM) image showing regions with different heights and imperfections created in the flake during the transferring process. (c) Raman and (d) photoluminescence spectra at room temperature. The monolayer WSe$_2$ has been confirmed by the absence of the interlayer Raman mode (B_{2g}^{1}) around 300 cm^{-1}, as well as, by the strong PL peak at 1.65 eV. The Raman and PL spectra have the same characteristic of those observed in samples deposited on silicon dioxide substrates [1–4], indicating that in as-transferred samples there is no coupling between the TMD and the metallic substrate (quenching effects are not observed).

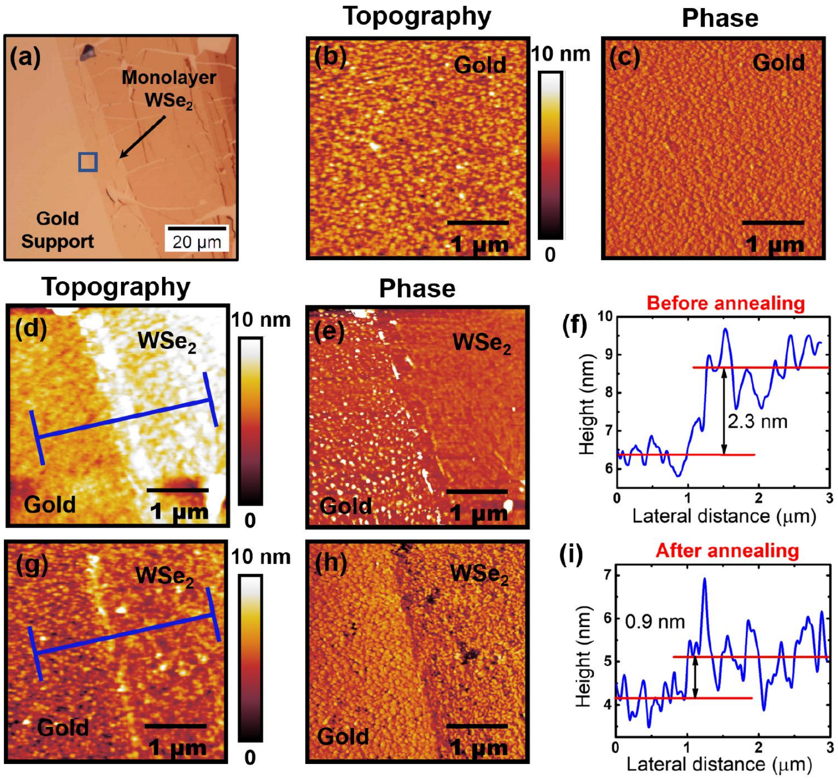

Figure S2: (a) Optical microscope image showing the Monolayer WSe$_2$ on top of the gold substrate. (b) Topography and (c) Phase AFM images of the gold substrate. (d) Topography and (e) Phase AFM images of the interface between the gold substrate and the monolayer WSe$_2$ before the 400 K thermal annealing in UHV for 12 hours. (f) AFM line profile obtained from (d) averaging a 3 μm long and 1 μm large area indicating a step height of 2.3 nm. (g) Topography and (h) Phase AFM images of the interface between the gold substrate and the monolayer WSe$_2$ after the 400 K thermal annealing in UHV for 12 hours. (i) The AFM line profile obtained from (g), averaging a 3 microns long and 1 μm large area, indicates ~0.9 nm of step height. Since the expected thickness of the monolayer WSe$_2$ is about 1 nm, we consider that before the thermal annealing in UHV there was a water layer under the TMD.

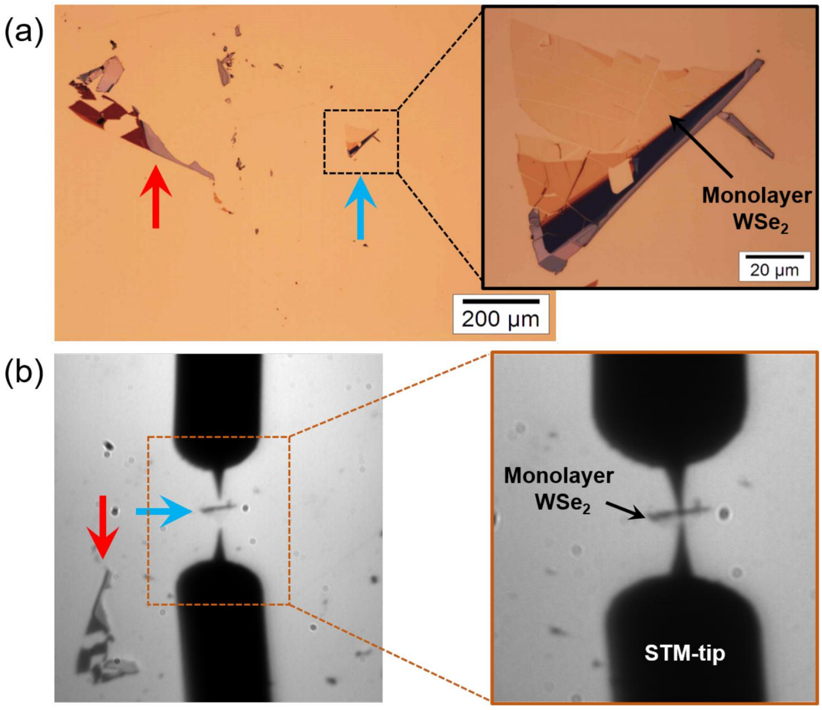

Figure S3: Localization of the flake of interest inside the STM microscope for the tip approach. (a) Optical microscopy image. The flake indicated by the red arrow is used as a reference point to localize the flake of interest with monolayer WSe_2 as indicated by the blue arrow. (b) By using a zoom lens, the monolayer WSe_2 is localized inside the STM, and the tip is approached. In the image, the STM tip and its reflection on the metallic substrate are observed. The tip wire diameter is 250 µm. This procedure is the same for STM measurements in UHV, and STM-LE in air.

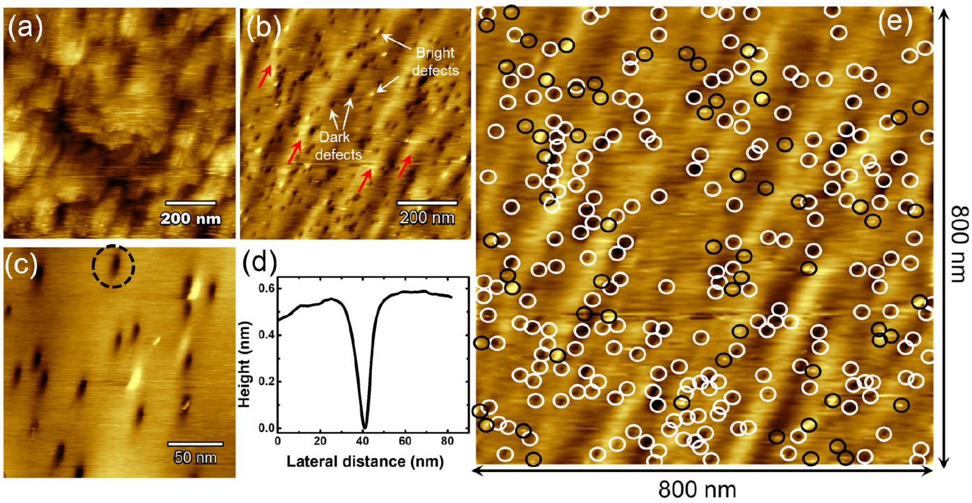

Figure S4: STM images obtained in UHV at room temperature in monolayer WSe_2/Au/Si annealed at 400 K. (a) STM-image of 1.0 μm × 1.0 μm of the Au thin film surface (3.5 V, 300 pA). (b) STM-image of 0.8 μm × 0.8 μm of the WSe_2 surface (1.0 V, 65 pA). A surface height undulation (red arrows) is observed in addition to some dark and bright point defects. (c) STM-image of 226 nm × 226 nm of the WSe_2 surface (1.0 V, 65 pA) showing dark defects and (d) the depth profile of one of them. (e) Quantification of the defects density in the image shown in (b). Dark and bright defects are indicated in white and black circles, respectively.

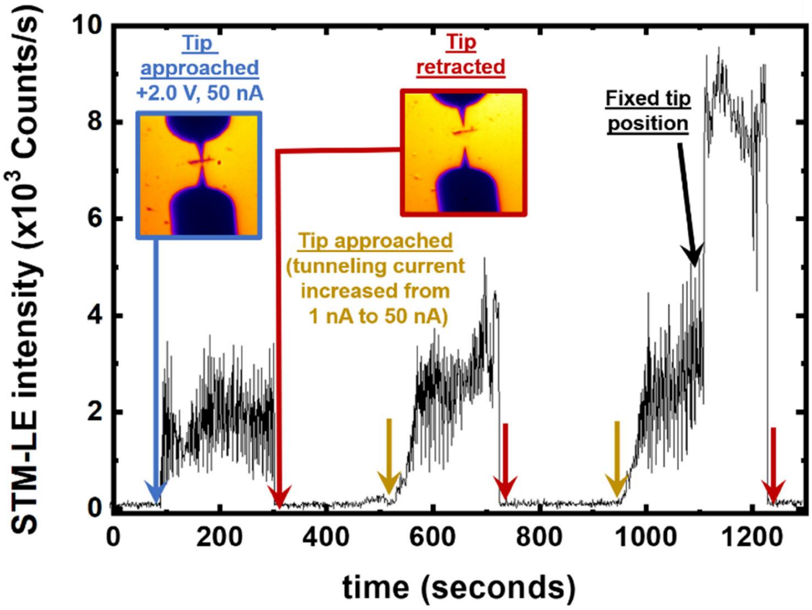

Figure S5: The STM-LE signal was recorded panchromatically as a function of time using a PMT to evaluate the quantum yield and temporal stability. Three cycles of tip approach and retraction are shown. Sample bias is set to 2.0V, and the tunneling current increased up to 50 nA. The results indicate the variation of the observed signal as well as the ease of getting the signal back after establishing a tunneling current. The signal variations are also observed due to the short PMT integration time: 0.3 seconds. Similar variations are typically observed in the tunnel current, as one could expect in air [5]. In the first 1100 s (~18 minutes) the signal was acquired scanning the tip on a surface area of 130 nm × 130 nm, after that the STM tip position was fixed, and signal of about 9×10^3 counts per second was obtained with 50 nA. This gives a Quantum Yield (QY) of ~5×10^{-7} photons per electron, similar to observed in $MoSe_2$ mechanically transferred on ITO [6].

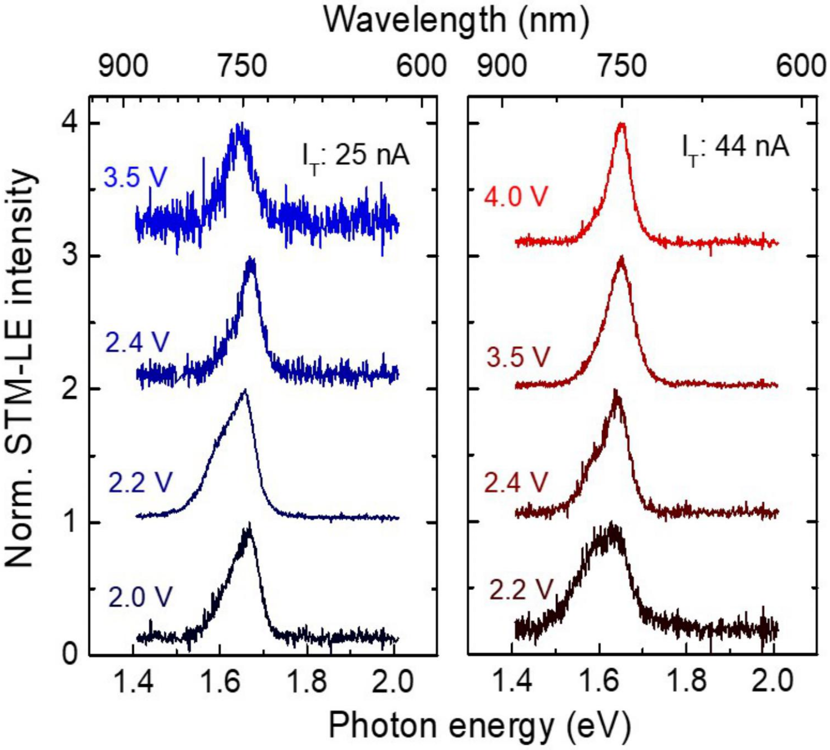

Figure S6: STM-LE spectra measured with different sample bias and tunneling currents of 25 nA (black to blue curves) and 44 nA (black to red curves), the integration time per spectrum was of 100 s. Some different peak shapes are observed due to the different intensities of the charged exciton (trion) and of the neutral excitons. See the decomposed spectra in Figure S7 and the ratio as a function of sample bias in Figure 3(c). The center of each emission remains roughly at the same energy, as shown in Figure S8. That is, no systematic energy shift is observed in the STM-LE peak as a function of the sample bias. The same spectral features are observed both at 25 nA and at 44 nA.

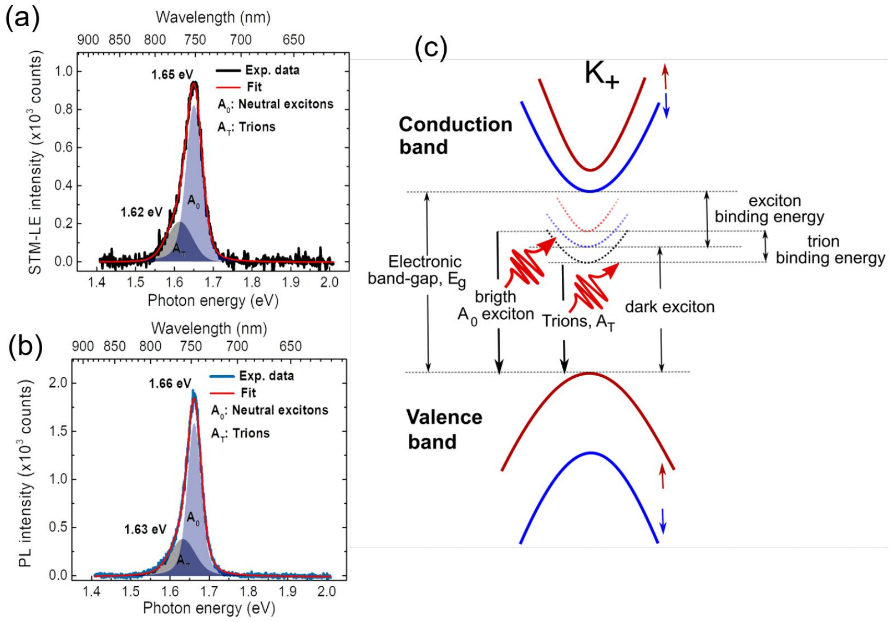

Figure S7: (a) STM-LE (4.0 V, 44 nA) and (b) PL spectra of monolayer WSe_2 fitted with two Voight peaks associated with the emission due to bright A neutral excitons (A_0) recombination and trions (A_T) recombination. (c) The schematic diagram for the energy levels in monolayer WSe_2 at the K_+ point of the Brillouin zone showing the direct electronic band-gap, binding energy for excitons and trions, and the recombination A_0 and A_T. According to reference [7], the electronic band gap is 2.0 eV, and the exciton binding energy is 0.37 eV. Hence, the neutral exciton emission from single-layer WSe_2 is expected at 1.65 eV, as observed here.

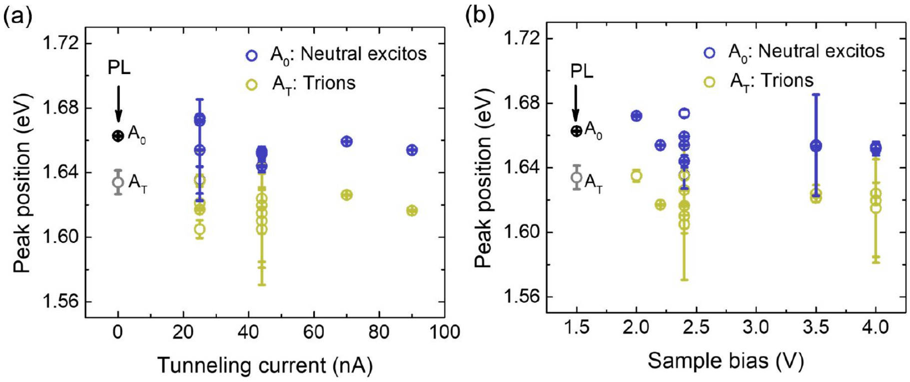

Figure S8: Position of the charged exciton (trion) and neutral exciton obtained from decomposing of STM-LE spectra. The spectra considered included those in Figure 2(c), 3(a), S6, and S7. In these cases, no plasmon contribution is observed, and all spectra can be decomposed as (and adjusted with) 2 peaks related to trion and neutral exciton emission. In (a) the position of the peaks is shown as a function of the tunneling current and in (b) as a function of the sample bias. In both cases, no systematic shift is observed. The small energy variation shown in these graphs is possibly related to the difference between each region on the monolayer WSe_2 that can be subjection to different stress states or have slightly different defect concentration. In (a) and in (b), the energy of both trion and neutral exciton obtained from low power PL (spectrum in Figure S7) is indicated for comparison. For the PL acquisition, there was no tunneling current or sample bias voltage.

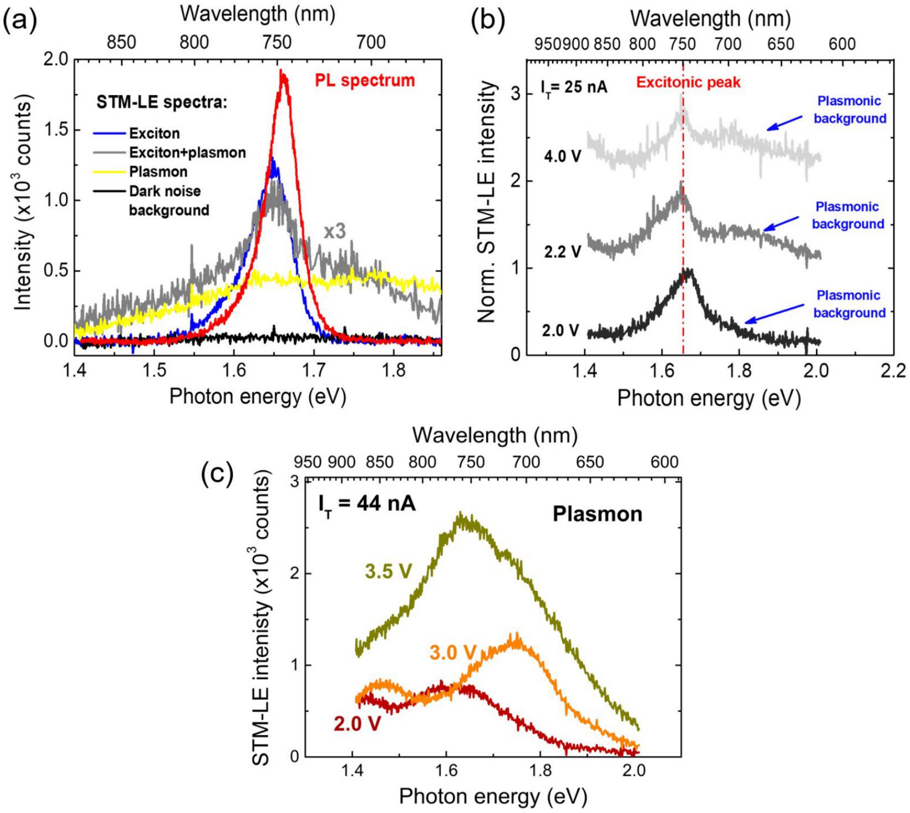

Figure S9: In (a), for comparison, the raw data of different spectra are shown, including the CCD dark noise, one PL spectrum, one STM-LE excitonic spectrum, one STM-LE with both plasmonic and excitonic emission and one STM-LE purely plasmonic. The STM-LE excitonic spectrum closely resembles the PL spectrum. In contrast, spectra with plasmonic contributions are readily spotted as much broader spectrally, covering the whole spectral range (as observed comparing them with the dark noise background). (b) STM-LE spectra of the simultaneous excitonic and plasmonic emission obtained with different tunneling parameters. (c) Pure plasmonic emission due to the gold metallic support for different sample bias voltage. The spectra obtained in (b) and (c) were recorded in the same sample region were high sample bias and high tunneling current was applied or in the same region were 'tip pulse' procedures were performed. A 'tip pulse' is a procedure in which the tip is put in contact with the sample (short circuit) for a brief moment to induce tip reconstruction.

References

1. Tonndorf, P. *et al.* Photoluminescence emission and Raman response of monolayer MoS_2, $MoSe_2$, and WSe_2. *Opt. Express* **21**, 4908 (2013).

2. Zeng, H. *et al.* Optical signature of symmetry variations and spin-valley coupling in atomically thin tungsten dichalcogenides. *Sci. Rep.* **3**, 4908–4916 (2013).

3. Terrones, H. *et al.* New First Order Raman-active Modes in Few Layered Transition Metal Dichalcogenides. *Sci. Rep.* **4**, 1–9 (2014).

4. Zhao, W. *et al.* Lattice dynamics in mono- and few-layer sheets of WS_2 and WSe_2. *Nanoscale* **5**, 9677 (2013).

5. Rogez, B. *et al.* The mechanism of light emission from a scanning tunnelling microscope operating in air. *Nanotechnology* **27**, (2016).

6. Pommier, D. *et al.* Scanning Tunneling Microscope-Induced Excitonic Luminescence of a Two-Dimensional Semiconductor. *Phys. Rev. Lett.* **123**, 1–7 (2019).

7. He, K. *et al.* Tightly bound excitons in monolayer WSe_2. *Phys. Rev. Lett.* **113**, 1–5 (2014).

Chapter 6

Electronic band gap, exciton binding energy, and properties of point defects in epitaxial monolayers h-BN on graphite

This chapter contains the publication:

Ricardo Javier Peña Román, Fábio J R Costa Costa, Alberto Zobelli, Christine Elias, Pierre Valvin, Guillaume Cassabois, Bernard Gil, Alex Summerfield, Tin S Cheng, Christopher J Mellor, Peter H Beton, Sergei V Novikov and Luiz F Zagonel

Band gap measurements of monolayer h-BN and insights into carbon-related point defects

2D Materials, 2021, 8,044001 (**arXiv:2107.07950v1**)

This chapter presents our study on monolayer h-BN employing STM and STM-luminescence spectroscopy. Monolayer h-BN was grown on HOPG substrate by the high-temperature plasma-assisted molecular beam epitaxy technique. This sample preparation method allows producing monolayer and few-layer h-BN with atomically flat surfaces and monolayer control of the sample thickness.

We used STM imaging to explore the local sample surface morphology and identify the presence of point defects. We performed STS measurements at 80 K to investigate the sample's electronic properties of defect-free monolayers and point defects. Here we present a detailed STS study of monolayer h-BN for the experimental determination of the electronic band gap. We combined the STS results with *ex-situ* deep ultraviolet PL (DUV PL) measurements to obtain the exciton binding energy. The values for the electronic band gap and exciton binding energy are compared with the predicted in a free-standing monolayer to understand the effect of the substrate on the electronic and optical properties of the sample. In addition, we used STM, STS, STM-CL, and *in-situ* PL to investigate the impacts of point defects in monolayer h-BN.

In the following, we present the results published in **2D Materials, 2021, 8,044001** (**arXiv:2107.07950v1**) . In this work, we demonstrated that monolayer h-BN epitaxially grown on HOPG is a model system for the study of the morphological, electronic, and optical properties of h-BN monolayers. The weak sample-substrate interaction enables, for the first time, the determination of the electronic band gap value through STS measurements at low temperature. Correlation between STS and DUV PL enables a value for the exciton binding energy in monolayer h-BN to be estimated. These results indicate that monolayer h-BN does not form significant interface states with HOPG, so that h-BN exhibits its fundamental electronic and optical properties. However, the measured values for the electronic band gap and the exciton biding energy are about 1 eV lower than the velues predicted for free-standing monolayer due to substrate screening. The energy of the excitonic emission is not affected by the presence of the substrate. Additionally, point defects are observed in STM images and insights into the electronic and optical signatures of carbon-related point defects are obtained from STS, *in situ* PL and CL measurements. Luminescence due to defects in a broad emission range is observed for the first time using CL in monolayer h-BN.

Band gap measurements of monolayer h-BN and insights into carbon-related point defects

Ricardo Javier Peña Román,*,† Fábio J. R. Costa ,† Alberto Zobelli,‡ Christine Elias,¶ Pierre Valvin,¶ Guillaume Cassabois,¶ Bernard Gil,¶ Alex Summerfield,§ Tin S. Cheng,§ Christopher J. Mellor,§ Peter H. Beton,§ Sergei V. Novikov,§ and Luiz F. Zagonel*,†

†*Institute of Physics "Gleb Wataghin", Department of Applied Physics, State University of Campinas-UNICAMP, 13083-859, Campinas, Brazil*

‡*Université Paris-Saclay, CNRS, Laboratoire de Physiques des Solides, 91405, Orsay, France*

¶*Laboratoire Charles Coulomb, UMR5221 CNRS-Université de Montpellier, 34095 Montpellier, France*

§ *School of Physics and Astronomy, University of Nottingham, Nottingham, NG7 2RD, UK*

E-mail: rikrdopr@ifi.unicamp.br; zagonel@unicamp.br

This is the version of the article before peer review or editing, as submitted by an author to IOP 2D Materials.

Find the published version at: https://doi.org/10.1088/2053-1583/ac0d9c

Cite as: Ricardo Javier Peña Román et al 2021 2D Mater. 8 044001

Pena Roman et al 2021 2D Material 8 044001 doi:10.1088/2053-1583/ac0d9c

Abstract

Being a flexible wide band gap semiconductor, hexagonal boron nitride (h-BN) has great potential for technological applications like efficient deep ultraviolet (DUV) light sources, building block for two-dimensional heterostructures and room temperature single photon emitters in the UV and visible spectral range. To enable such applications, it is mandatory to reach a better understanding of the electronic and optical properties of h-BN and the impact of various structural defects. Despite the large efforts in the last years, aspects such as the electronic band gap value, the exciton binding energy and the effect of point defects remained elusive, particularly when considering a single monolayer.

Here, we directly measured the density of states of a single monolayer of h-BN epitaxially grown on highly oriented pyrolytic graphite, by performing low temperature scanning tunneling microscopy (LT-STM) and spectroscopy (STS). The observed h-BN electronic band gap on defect-free regions is (6.8 ± 0.2) eV. Using optical spectroscopy to obtain the h-BN optical band gap, the exciton binding energy is determined as being of (0.7 ± 0.2) eV. In addition, the locally excited cathodoluminescence and photoluminescence show complex spectra that are typically associated to intragap states related to carbon defects. Moreover, in some regions of the monolayer h-BN we identify, using STM, point defects which have intragap electronic levels around 2.0 eV below the Fermi level.

Introduction

Hexagonal boron nitride (h-BN) is a layered compound that is isomorphous with graphite. In its bulk form, h-BN is formed from monolayers composed of boron and nitrogen atoms in a hexagonal sp^2 covalent lattice that are organized vertically by van der Waals (vdW) interactions.[1–3] With an optical band gap of about 6 eV, and an indirect-to-direct band gap crossover in the transition from bulk to monolayer,[4–6] h-BN shows very bright deep ultraviolet (DUV) emission[7–9] and defect mediated emission from the DUV all the way to the near-infrared.[10–14] In particular, point defects have been observed to act as single-photon sources.[15–23] Such properties place bulk h-BN and its monolayer form in the spotlight for many potential applications, including DUV light emitting devices,[24–26] dielectric layers for two-dimensional (2D) heterostructures[27–29] and room temperature (RT) single photon emitters (SPEs) for quantum technologies.[30–34] Similarly to other technologically-relevant semiconductors, the successful application of h-BN depends on the understanding and control of its electronic and optical properties. However, partially due to its wide band gap and challenging large area synthesis, many fundamental electronic and optical properties of h-BN remain elusive. Moreover, the morphology, the electronic properties and the optical emission of structural point defects are complex and are currently poorly understood.

Given the wide band gap of h-BN and its insulating character, studying its morphological, electronic and optical properties can be tricky, particularly for the case of a single monolayer. The band structure of bulk and monolayer h-BN have been reported by Angle Resolved Photoemission Spectroscopy (ARPES).[35,36] However, ARPES cannot resolve the conduction band structure. Electron Energy Loss spectroscopy (EELS) has already been applied to measure the band gap on h-BN nanotubes and h-BN monolayers, but EELS measures the optical band gap, similarly to optical absorption.[37,38] Therefore, scanning tunneling spectroscopy (STS) becomes an appropriate approach to probe both the valence band and conduction band edges as well as for the determination of the electronic band gap.[39,40] Still, so far, STS has not provided a clear measurement of the electronic band gap for monolayer h-BN or intra-gap states related to defects. The structure of individual defects in h-BN has been explored in previous works by means of scanning tunneling microscopy (STM)[41] and high resolution transmission electron microscopy,[42] but, despite these efforts, a clear correlation between electronic levels and light emission related to defects has not been established yet. Optically, the properties of few-layer h-BN samples have recently been investigated by cathodoluminescence (CL) measurements. However, the thinnest h-BN samples for which a CL signal could be collected were six[43] and three[44] monolayers flakes. Consequently, the electronic band gap value and the exciton binding energy are unaddressed experimentally even now, alongside the CL emission in the monolayer and electronic signatures of defect states. Finally, the direct character of the band gap and optical transitions in the DUV in monolayer h-BN have been recently reported,[6] but the optical transition in the near UV and visible spectral range have not yet been extensively explored.

Here, we show that monolayer h-BN epitaxially grown on highly oriented pyrolytic graphite (HOPG) is a model system for the study of the morphological, electronic, and optical properties of h-BN monolayers. The weak sample-substrate interaction enables, for the first time, the determination of the electronic band gap value by means of STS measurements. Correlation between tunneling spectroscopy with DUV optical spectroscopy enables a value for the exciton binding energy in monolayer h-BN to be estimated. Additionally, structural point defects are observed by STM images. Luminescence due to defects in a broad emission range is observed for the first time using CL in monolayer h-BN. Moreover, insights on the optical signatures of defects are obtained from the interesting contrast between *in situ* photoluminescence (PL) and CL. These results indicate that monolayer h-BN does not form significant interface states with HOPG, so that h-BN exhibits its fundamental electronic and optical properties.

Results and discussion

Sample and methods descriptions

In Figure 1, a general description of the h-BN sample investigated in this work is displayed. As shown in Figure 1(a), h-BN and HOPG have an in-plane hexagonal structure with similar lattice parameters. The small lattice mismatch makes them highly compatible and appropriate for the epitaxial growth of vertical heterostructures. Additionally, the surfaces of these kinds of materials are naturally passivated without any dangling bonds. Therefore, in vdW epitaxial heterostructures, an atomically sharp interface is obtained, where chemical bonds are absent and only vdW interactions are present between the sample and the substrate.[45–49] The region at the interface is usually referred to as vdW gap, such as illustrated in Figure 1(a). Since the vdW interaction is weak, it is expected that each material in the heterostructure preserves most of its electronic properties. This was revealed in recent works by ARPES measurements. Sediri *et al.*[50] proved that when a monolayer h-BN is epitaxially grown on graphene (Gr), the electronic structure of Gr remains unaffected under the presence of h-BN. In the same way, Pierucci *et al.*[36] demonstrated in monolayer h-BN/HOPG that the electronic properties of h-BN are not perturbed significantly by the substrate. This means that in vdW heterostructures, the sample and the substrate are electronically decoupled, and there are no doping effects or charge transfer. All these effects make the vdW heterostructure of monolayer h-BN on HOPG an important model system for the study of the fundamental properties of h-BN, and for applications when conductivity is relevant as in STM/STS and light emitting diodes.

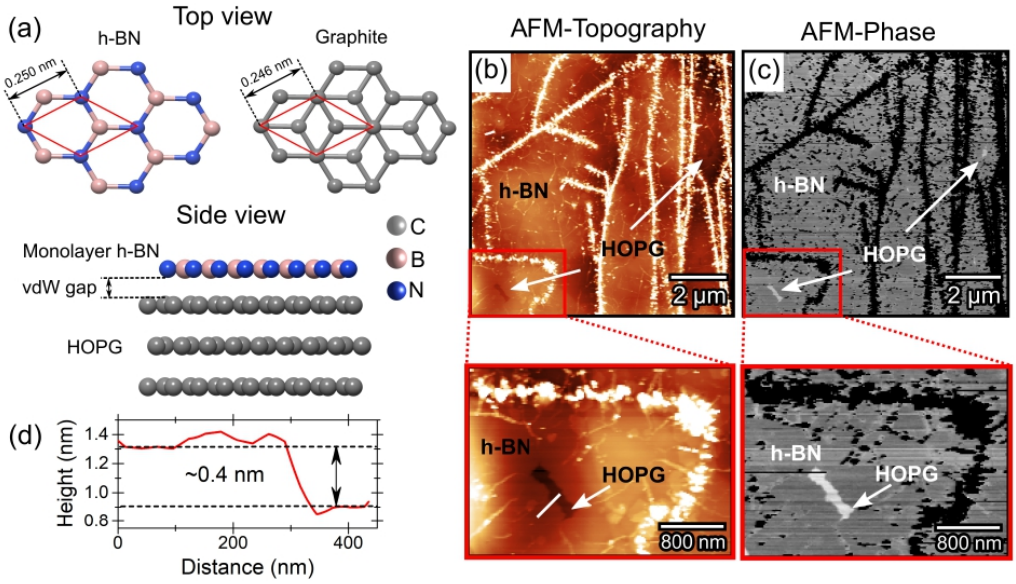

Figure 1: (a) Top view of the in-plane atomic structure of h-BN and HOPG. Side view of the monolayer h-BN/HOPG van der Waals heterostructure. AFM (b) topographic and (c) phase images of the epitaxial monolayer h-BN/HOPG. (d) Height profile of a single monolayer h-BN.

The h-BN layers were grown on HOPG substrates by high-temperature plasma-assisted molecular beam epitaxy (PA-MBE).[6,51–53] Figures 1(b) and (c) show large area topographic and phase atomic force microscopy (AFM) images, respectively, of the h-BN layer on the HOPG substrate, acquired with the amplitude-modulated tapping mode in ambient conditions. As observed, the HOPG surface is almost totally covered by h-BN, where the white regions in the phase image correspond to uncovered HOPG surface areas. The AFM topographic image in Figure 1(b) shows that the sample is predominantly composed by large terraces of monolayer h-BN with some small bilayer regions and some thick regions around the HOPG grain boundaries and surface steps, which appear as bright (dark) features in the topography (phase) zoomed image (see also Figure S1). The height profile in Figure 1(d), taken along the white line on the h-BN/HOPG surface of Figure 1(b), shows that the step height is approximately 0.4 nm, in agreement with the expected thickness of a single monolayer h-BN. This morphology is consistent with previous reported results on similar samples.[6,51–53]

The surface morphology and electronic properties of the monolayer h-BN were investigated locally by means of STM and STS measurements performed under ultra-high vacuum (UHV) conditions at cryogenic temperatures using a modified RHK PanScan FlowCryo microscope. An STM image revealing the smooth sample surface is shown in Figure 2(a), as observed previously by AFM (Figure S1). Considering only the STM image, it is difficult to know if the imaged area corresponds to the h-BN or to the HOPG surface because they are morphologically very similar. Despite being isomorphic, h-BN and HOPG have striking different electronic structures (wide band gap semiconductor and zero-gap conductor, respectively) and therefore very different local density of states (LDOS) to be measured by STS. The gray curve in Figure 2(b) is a typical STS spectrum obtained in the region of Figure 2(a). This dI/dV curve shows an electronic band gap of ∼6 eV, defined by the low differential conductance range from ∼-3 V to ∼+3V, confirming that the scanned region corresponds to a h-BN covered surface. Considering the general morphology of the h-BN

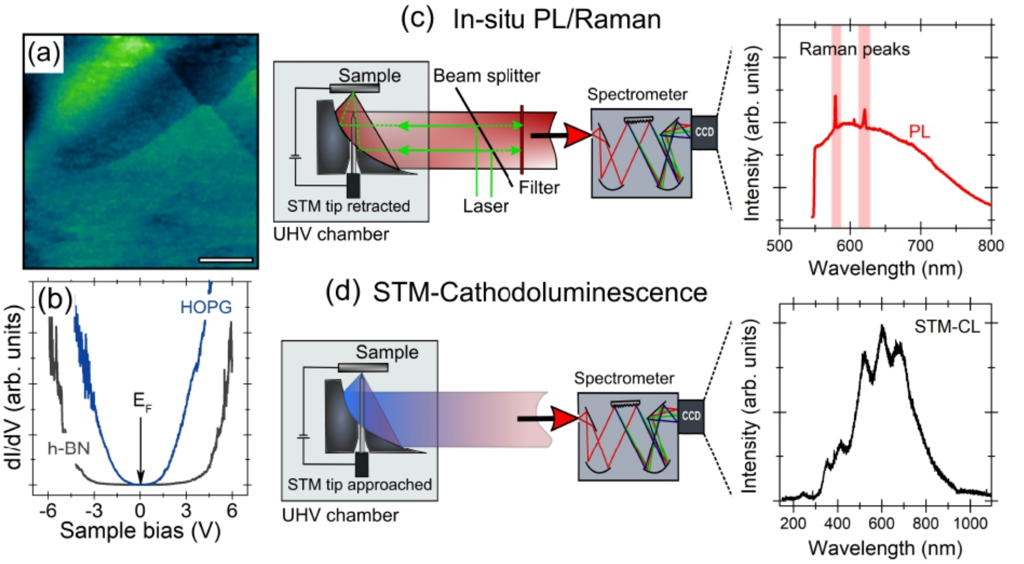

Figure 2: (a) STM image of the monolayer h-BN/HOPG surface (0.8 nA, 0.2 V, 80 K). Scale bar of 30 nm. (b) STS curves at 80 K (The feedback loop was disabled at -6.2 V, -150 pA.). Schematic illustration of the experimental setup for (c) *in-situ* PL/Raman and (d) STM-CL measurements in the STM configuration. The spectra shown here are uncorrected raw data.

grown on HOPG observed by AFM and the fact the the majority of the sample is covered by monolayers, the h-BN thickness in smooth regions as that one in Figure 2(a) is a considered to be a monolayer. In other regions with similar surface morphology, the STS curves exhibit the characteristic parabolic shape around the Fermi level of the LDOS of graphite,[54,55] as in the blue plot in Figure 2(b).

The STM was adapted to include a high numerical aperture light collection and injection system with optimized transmission. This system uses an off-axis parabolic mirror inserted around the tunneling junction and *in situ* PL and Raman spectroscopies can be performed using the light injection and collection system as illustrated in Figure 2(c). In this experimental configuration, the STM tip is retracted from the sample surface and the light of a green (532 nm) laser diode is injected into the STM junction under UHV conditions. Additionally, STM-induced light emission or the CL response of the sample can be investigated using the setup, see Figure 2(d). For recording the CL signal, the STM is operated in field emission mode using an external voltage source of (0-500) V for the local excitation of the sample by electron bombardment (STM-CL). The PL/Raman and CL spectra, shown in Figure 2(c) and (d), correspond to the spectroscopic raw data that need to be corrected for the proper interpretation, as explained in the Supplementary materials (SM). This setup has also been previously used to investigate WSe_2 and MoS_2 monolayers.[56,57]

Electronic band gap, optical band gap and exciton binding energy

Since monolayer h-BN is an atomically thin and a wide band gap material, access to its electronic structure is always a highly challenging experimental and theoretical task. Within the last twenty years, the h-BN electronic band gap has been calculated a number of times within the GW approximation, while the optical response has been calculated using the Bethe-Salpeter equation.[58–61] In this approximation, the Green's function for the quasi-particles are evaluated within the screened Coulomb potential in a way to consider many-body problems of the interacting electrons.[62] However, non self-consistent GW calculations (G_0W_0), which start from DFT orbitals and perform the calculation only once, typically provide underevaluated values for the electronic band gap and, in the case of h-BN, a rigid shift of the optical spectra is required for a direct comparison with experiments. Only very recently, self-consistent GW calculations, which update interactively both the wave functions and the eigenvalues, managed a good agreement with synchrotron ellipsometry experiments for bulk h-BN.[63] In the case of free-standing monolayer h-BN and using the GW_0 approach, which updates interactively the eigenvalues only in the Green's function, the electronic band gap has been evaluated as 8.2 eV and the related optical gap at 6.1 eV.[60,64] Slightly higher values might be expected within the full self-consistent GW approach. On the other hand, at the moment, there is no experimental evidence with effective measurements of the electronic band gap in both bulk or monolayer h-BN. A particular reason for the lack of such results is the technical challenge regarding the accomplishment of experiments for

DUV wavelengths. The electronic properties and band structure of epitaxial monolayer h-BN on graphite have been studied recently by ARPES measurements.[36] This study reported important information about band alignment, Fermi level and Valence Band (VB) positions. However, it is noteworthy that ARPES measurements only resolve filled states,[35,36,65,66] and therefore the description of the whole band structure and electronic band gap of monolayer h-BN are still open questions.

One technique able to probe both filled and empty states, with a complete information about the LDOS, doping effects and charge transfer is scanning tunneling spectroscopy or STS.[40,67–71] Previous STM/STS measurements on h-BN have not given a clear answer for the electronic band gap. The main reason for that is because most of the STM/STS studies have been carried out on h-BN samples grown directly on metallic substrates.[72] Nowadays, it is well documented that the growth of a 2D material on a metallic substrate leads to a band gap renormalization due to strong interactions with the substrate, which is related to the dielectric screening by the metal and/or the formation of additional interface electronic states, including hybridization among others.[57,73–76] These effects reduce the electronic band gap value to about 3 eV for h-BN on Ru(0001)[75] and on Re(0001)[77] surfaces, to ∼4 eV for h-BN on Au(001),[78] and to ∼5 eV for the case of h-BN on Rh(111),[79,80] Ir(111),[81] and Cu(111)[82] substrates. In addition, performing scanning tunneling experiments on h-BN can be complex due to its expected insulating character. For instance, Wong, *et al* used Gr as conducting layer on top of bulk h-BN.[41] Using the Gr as conducting electrode affects considerably STM images and make STS spectra difficult to interpret, particularly with respect to the h-BN band gap. Interestingly, when h-BN is grown on Gr/Cu(111), electronic states of the metallic substrate are observed on the Gr and also on the h-BN layer.[76] In this case, intragap states due to the copper support are measured by STS and the h-BN band gap is not observed. For vdW epitaxial heterostructures, the sample-substrate interaction is not an issue because, as mentioned above, there is a sharp interface between the monolayer h-BN and the HOPG substrate governed by weak vdW bonds (vdW gap). Therefore, h-BN on HOPG can be considered as being electronically decoupled from the substrate, and is not expected to demonstrate intragap states coming from graphite, but only effect of the dielectric environment surrounding the monolayer.

Figure 3(a) and (b) shows STM and STS results acquired at 80 K in the monolayer h-BN/HOPG. A STM image of a smooth and defect-free region of the sample surface together with an insert showing a moiré structure with with a periodicity of approximately 2.4 nm are displayed in Figure 3(a). This moiré pattern corresponds to a local rotation of approximately 5.8° between the monolayer h-BN and the HOPG surface in a particular region, as recently observed on similar samples.[51] The apparent height profile of the moiré is presented in Figure 3(b). Detailed studies of the moiré structure in this system were reported in recent works.[51,83]

The LDOS of the monolayer h-BN has been investigated by performing STS measurements on the defect-free region at different tip positions. The tunneling processes that probe both empty and filled states by STS in the monolayer h-BN are illustrated in Figure 3(c) and (d), respectively. The alignment between the Fermi level in h-BN and HOPG at 0 V was demonstrated in the results depicted in Figure 2(b). Thus, when a positive sample bias ranging from 0 V to +6 V is applied, the Fermi level in the tip is shifted with respect to the Fermi level in h-BN/HOPG, and, as a consequence, electrons tunnel from the tip to empty states of the sample, such as shown in Figure 3(c). The red curve in the figure represents the measured dI/dV for positive biases, which is a direct measurement of the local empty DOS. It can be observed that the LDOS increases from biases above ∼3.0 V, which means that electrons are tunneling only for states in the Conduction Band (CB) of h-BN. Below ∼3.0 V the curve is flat (the tunneling current is equal to ∼0 pA), because there are no available electronic states inside the h-BN electronic band gap for electrons to tunnel to. The same process happens when the polarity of the bias is changed to negative values in order to probe filled states, as illustrated in Figure 3(d). It is worthwhile to note that, during typical STS measurements, the voltage ramps while the current is measured but the tip-sample dis-

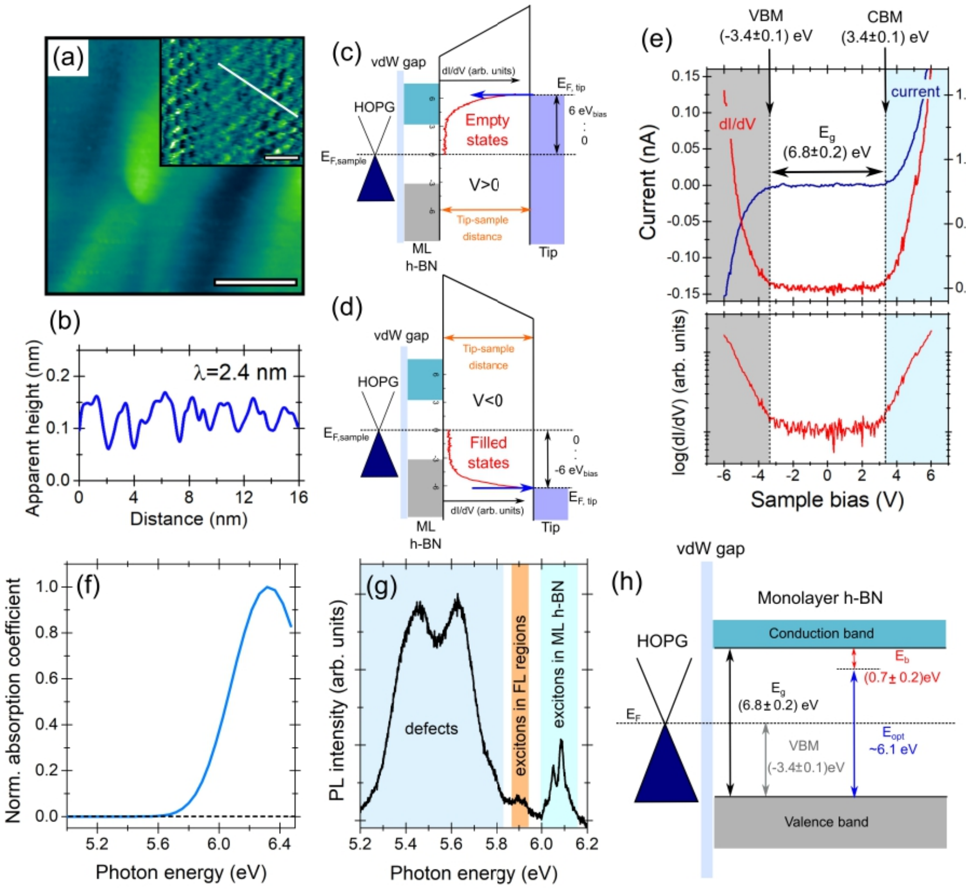

Figure 3: (a) STM image of a smooth and defect-free monolayer h-BN region (0.66 nA, 3.8 V, 80 K). Scale bar of 30 nm. Inset: moiré structure (-0.3 nA, -1.0 V, 16 K). Scale bar of 5 nm. (b) Height profile associated to the moiré. Schematic illustration of the tunneling process for (c) positive and (d) negative biases. The red curve corresponds to the LDOS measured by STS as dI/dV. The blue arrow indicates the tunneling direction. (e) I-V and dI/dV typical curves obtained on a smooth and defect-free monolayer h-BN region and at 80 K (The feedback loop was disabled at -6.2 V, -150 pA). The electronic band gap and band edges are indicated with the values obtained of a statistical analysis of 480 individual curves. Global measurements of the (f) optical absorption at RT and (g) PL at 10 K. (h) Energy levels diagram proposed for defect-free monolayer h-BN. In the figure VBM, E_g, E_{opt} and E_b correspond to the valence band maximum, the electronic band gap, the optical band gap and the exciton binding energy, respectively.

tance is not adjusted. Therefore, the tip-sample distance is set by the tunneling current and sample bias prior to disabling the tip-sample distance feedback loop and starting the STS measurement (stable tunneling parameters). Here, we used typically -150 pA at -6.2 V (see Methods section for more details) as the stable condition prior to starting the acquisition of the scanning tunneling spectra in order to ensure reproducible and reliable spectra. If the tunneling current is set to slightly higher or lower values (from -50 to -300 pA) before disabling the feedback loop, the obtained spectra are compatible to those measured using -150 pA, see Figure S2.

It is relevant to mention that direct tunneling from or to the HOPG is possible even through the monolayer h-BN. In fact, this effect can be observed when STS curves were recorded stabilizing the tunneling junction at high tunneling currents ($\geq$ 600 pA) with -6.2 V of sample bias, as discussed in the SM, see Figure S2. A possible explanation for this observation is that for a fixed sample bias and higher stabilization currents, the tip-sample distance becomes shorter, which means that the tunneling barrier is narrower, and then the probability of the direct tunneling from or to the substrate is not negligible. This leads to the measurement of an apparent reduced band gap, because states of the HOPG near the band edges of h-BN are observed in the STS curve for h-BN, as can be seen in Figure S2(b). The direct tunneling from/to the HOPG substrate for short tip-sample distance in STS measurements on vdW epitaxy MoS_2/HOPG and WSe_2/HOPG samples have been demonstrated by Chiu *et al.*[84] In that work, it was also demonstrated that the LDOS of HOPG can be measured by tunneling electrons through the TMD layer if the stabilizing bias for the STS acquisition lays inside the band gap region of the TMD. For wide band gap materials such as h-BN, using appropriate tunnel junction conditions before starting the STS is therefore crucial.

Figure 3(e) shows typical STS results obtained from a smooth and defect-free h-BN sample surface region. The top panel of the figure shows the I-V curve plotted together with the dI/dV tunneling spectrum. The electronic band gap of the h-BN sample is defined by the bias range at which the current and dI/dV are close to their background values. The band edges and band gap values were extracted from the dI/dV curve in logarithmic scale,[68,85] as represented in the bottom panel of Figure 3(e). The values shown in the figure were obtained following the method and the statistical analysis explained in the SM, Figures S3 and S4, which considers a total number of 480 individual dI/dV curves similar to Figure 3(e) taken at different tip positions. The final results are a Valence Band Maximum (VBM) and a Conduction Band Minimum (CBM) positioned at (-3.4 ± 0.1) eV and (3.4 ± 0.1) eV, respectively, for monolayer h-BN on HOPG. This results in an electronic band gap of (6.8 ± 0.2) eV. Also, the Fermi level is in the middle of the band gap, indicating that the defect-free monolayer h-BN regions, as shown in Figure 3(a), are undoped and therefore there is no charge transfer with the HOPG. ARPES found the VBM position close to the $\sim$ -2.8 eV on a similar h-BN sample.[36] This ARPES result for the VBM is slightly different than the value measured by STS (-3.4 eV). This difference is possibly caused by some degree of p-type doping on the sample and/or some level of hole excess coming from a insufficient compensation of the photo-emitted electrons. On 3-monolayer thick h-BN samples, ARPES determined the VBM at -3.2 eV, which, considering the band structure for 3-monolayer thick h-BN and the expected electronic band gap opening for a monolayer h-BN, agrees well with the results presented here.[86] From the experimental point of view, STS is not sensitive to the direct or indirect nature of the electronic band gap. Nonetheless, recently, it was confirmed the recombination of direct excitons in monolayer h-BN,[6] which suggests that this is a direct band gap material.

The electronic band gap value found here for monolayer h-BN is larger, as expected from simulations,[61] than values for bulk single crystal and thin films of h-BN, as obtained indirectly by photocurrent spectroscopy, which results in an electronic band gap of about 6.45 eV.[87,88] Regarding theoretical predictions for free-standing monolayer h-BN, GW_0 calculations indicate a band gap of 8.2 eV at the K point of the Brillouin zone with an exciton binding energy of 2.1 eV, giving an optical band gap of 6.1 eV.[60,64] This value is close to the optical onset of 6.3 eV measured by EELS on a free-standing monolayer.[38] Simulations for monolayer h-BN on top of graphene have shown a strong renormalization of the electronic band gap, of the order of 1 eV, due to strong screening effects of the substrate.[89,90] The simulations also show that the electronic band gap renormalization of monolayer h-BN is basically the same on top of graphene and on top of graphite.[89] This last scenario is the perfect model for our system of monolayer h-BN on HOPG and gives a strong support for the band gap value measured here by STS.

Optical absorption and PL were performed in the DUV to determine the optical (excitonic) band gap of monolayer h-BN on HOPG (see details in SM). Figure 3(f) and (g) show measurements of the optical absorption and PL (spot-size of 200 μm and 50 μm, respectively) obtained at RT and at 10 K, respectively. The optical absorption spectrum was calculated from spectroscopic ellipsometry data. The PL in the DUV employs a 6.4 eV laser obtained from the fourth harmonic of a Ti:Sa oscillator. A systematic study on the complex DUV absorption and emission of high-temperature PA-MBE h-BN on HOPG can be found in recent reports.[6,52] The spectrum in Figure 3(f) shows an abrupt change in the absorption coefficient that suggests an optical band gap of above 5.7 eV. Furthermore, the PL in Figure 3(g) shows the direct fundamental exciton transition at 6.1 eV (optical band gap) in monolayer h-BN, besides other emission lines associated with transitions in few-layer and defective regions around 5.9 eV and 5.6 eV, respectively. These results are in excellent agreement with previous experiments by Elias *et al.*[6] Moreover, this value for the optical band gap is consistent with recent simulation and indicate, as expected, an invariance of the exciton emission.[60,64,68,90]

The knowledge of both the electronic band gap and the optical band gap is essential to the design of applications in optoelectronics and light emitting devices employing large exciton binding energy materials, like the monolayer h-BN. Considering the h-BN electronic band gap found by STS and the energy observed for the exciton recombination, the obtained exciton binding energy is (0.7±0.2) eV. The comparison between this experimental evaluation and the theoretical predicted value of 2.1 eV for the free-standing monolayer, suggest a strong renormalization, of about 1.4 eV, of the exciton binding energy due to substrate screening effects.[64] Moreover, the observed renormalization of the exciton binding energy is expected to be the same on the electronic band gap, which nearly leads to an invariance of the optical onset.[68,90] This renormalization is in close agreement with simulations for monolayer h-BN on top of graphite.[89] The similar shift on the electronic band gap and on the exciton biding energy agrees well with simulations for monolayer h-BN and with experiments and simulations for monolayer $MoSe_2$.[68,90] Based on all the spectroscopic data, Figure 3(h) summarizes the energy levels determined here for a defect-free region of monolayer h-BN on HOPG. In Figure 3(h), the h-BN electronic band gap is indicated as (6.8 ± 0.2) eV, while the h-BN optical band gap is 6.1 eV. This leads to a Frenkel exciton with a binding energy estimated as (0.7 ± 0.2) eV.

Electronic Structure and Light Emission related to point defects

The wide electronic band gap in h-BN allows the observation of several optical transitions involving different intragap states associated with defects.[10,12,13,91] Therefore, light emission in h-BN may be dominated by structural defects. Point defects have a particular interest due to their characteristic quantum emission at RT in a broad range of wavelengths.[16–18,20] Different types of point defects have been proposed as being the sources of the single photon emission observed in h-BN.[14,91,92] However, their morphological and electronic signatures have not been measured directly. Furthermore, a direct correlation with the optical emission is missing. Even though STM is a tool able to identify atomic defects in 2D materials,[56,93–96] STM/STS measurements of point defects in monolayer h-BN have not been reported yet. The properties of individual point defects have been investigated only by simulated STM images in recent theoretical works.[97–100] Here some results obtained on defective regions of the sample are presented in order to help acquiring a better understanding of the impact of point defects in the properties of monolayer h-BN.

Figure 4(a) shows a STM image of the monolayer h-BN/HOPG surface, where point defects are revealed. These defects are bright spots of about 1 to 2 nm of diameter, according

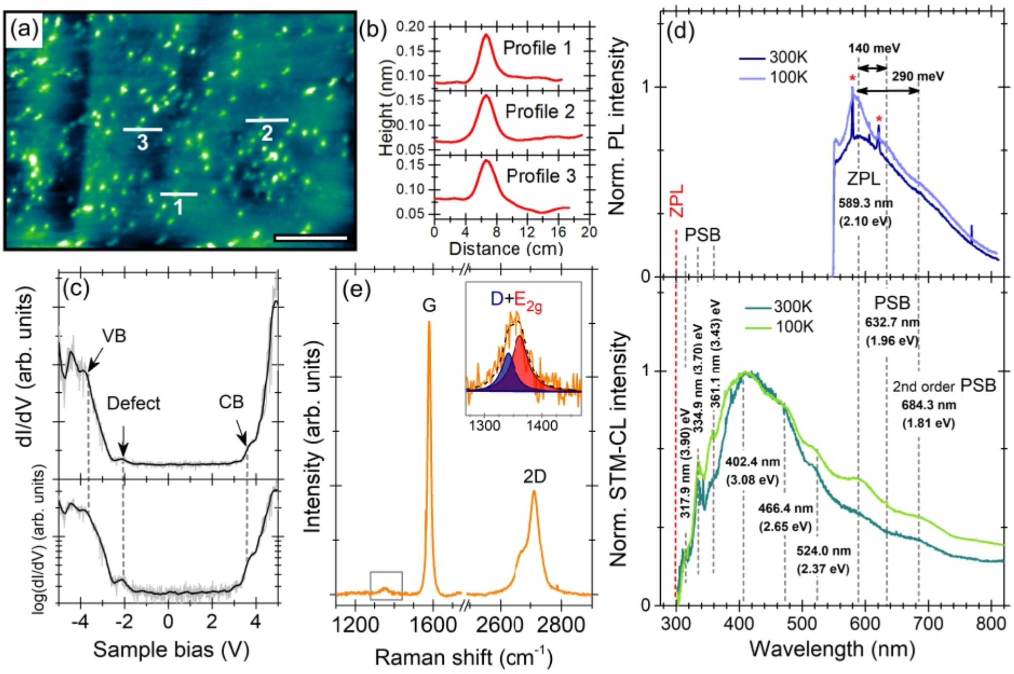

Figure 4: (a) STM image of bright point defects in monolayer h-BN (0.8 nA, 0.8 V, 80 K). Scale bar of 30 nm. (b) Heigth profile of some individual defects. (c) Typical STS curve obtained on the defective region at 80 K (The feedback loop was disabled at -6.2 V, -150 pA). (d) *In-situ* PL and STM-CL spectra in which Phonon Side-Bands (PSB) are observed near Zero Phonon Loss (ZPL) peaks. (e) *In-situ* Raman spectrum at RT. Inset: Lorenztian fitting of the peak at 1350 cm^{-1}.

to the full width at half maximum in the height profiles of Figure 4(b), see also Figure S5. Defects in h-BN on HOPG were already observed by Summerfield *et al.*[51] using conductive AFM and STM measurements, and were attributed to defects in the HOPG substrate, created by the active nitrogen plasma irradiation damage during the sample growth process. In another study, bright point defects relating to possible carbon impurities were imaged by STM in Gr capped bulk h-BN.[41] In order to inspect the electronic signature of the point defects found here, STS curves were acquired. Figure 4(c) displays a typical tunneling spectrum recorded when the STM tip is paced close to such a defect. By plotting the STS curve in logarithmic scale, it can be noted that the bands onset are not linear, in contrast to the ones observed in defect-free regions (see Figure 3(e) and Figure S3(c)). The curve in Figure 4(c) presents three main resonances at ~ -3.5 V, ~ -2.0 V and $\sim +3.5$ V. By comparing with the results for defect-free regions, the resonances at ± 3.5 V are located on top of the CB and VB edges, respectively, indicating that such defects have energy levels close to the band edges. Besides the spectra on Figure 4(c), the electronic level near -2.0 V was observed in several other tunneling spectra obtained on regions with point defects, see Figure S5. Therefore, this energy level is attributed to the observed defects. The fact that the STS curves show roughly the expected band gap for h-BN even on defective regions suggests that the scanned regions corresponds to a h-BN covered area and the observed point defects are in the monolayer h-BN.

A good starting point to interpret the imaged defects and the STS results is to consider that in the system of monolayer h-BN on HOPG, the atoms of Boron (B), Nitrogen (N) and Carbon (C) are present. Thus, substitutional defects such as C_B and C_N, carbon dimer defects like C_BC_N, or carbon anti-sites vacancies of the types V_BC_N, and V_NC_B are possible, and also are the main point defect candidates to be considered. Indeed, the random distribution of C atoms in the h-BN lattice is energetically possible,[101] and on the other hand, the high temperature and plasma assisted growth process can create vacancies during the sample preparation.[19,51] From the electronic point of view, band structure calculations show that for the LDOS in monolayer h-BN the states near the VBM are concentrated in the N sites, while the states near the CBM are in the B sites.[101,102] Impurities occupying N or B sites could act as acceptor-like or donor-like impurities, respectively. There are several theoretical reports exploring the doping effects of C impurities in single layers of h-BN. In those works, it is demonstrated that C_B and C_N defects induce n-doping and p-doping, respectively.[97,99,103,104] In particular, C_N defects introduce an acceptor state localized at 2.0 eV below the Fermi level and between 1-2 eV above the VBM.[97,103,105] The density of this defect state depends on the C concentration,[101] and the energy position can be shifted due to local strain effects,[97,106,107] and also by band bending effects.[93] More recently, it also has been predicted that the C_BC_N dimer introduces a stable and neutral intragap state localized at ∼0.8 eV above the VBM.[108,109]

It is important to point out that our STM results are consistent with the predictions made by Fujimoto *et al.*[97] and by Haga *et al.*[99,100] in their works on simulated STM images of individual point defects in h-BN and Gr vertical heterostructures. In those reports, the bright appearance of C_N point defects were simulated for negative tunneling biases. The calculated STM images of C-doped monolayer h-BN show that C atoms produce a redistribution of the local electron density around the defects, being the electron density in C_N higher than in C_B, which results in STM images where C_N defects look as bright spots when compared with the image of C_B.[97,99] Moreover, the local electron density, and as a consequence, the size of the bright spots related to C_N defects can be affected by the stacking and moiré pattern between the h-BN and Gr.[99,100] Defects imaged with negative bias can be observed in Figure S5. These theoretical considerations indicate that the defects identified by STM are consistent with defects involving C on N sites, i. e. C_N, C_BC_N and V_BC_N, even if other kinds of defect can not be excluded. Nonetheless, it is noteworthy that a detailed study of the morphological and electric structure of individual point defects in h-BN is required, which can be achieved by performing STM/AFM imaging and STS measurements at cryogenic temperatures, such as what has been done in the case of point defects in single layers of transition metal dichalcogenides.[110–113]

In order to obtain more insights on the observed defects, *in situ* PL and STM-CL experiments were carried out at 100 K and 300 K, using the experimental setup described in Figure 2. The raw luminescence data were presented in Figure 2(c) and (d), but for the proper interpretation, the spectra were corrected following the procedure explained in SM and the results are presented in Figure 4(d). The PL spectra show a main peak at 2.10 eV, which is best resolved at 100 K, and two shoulders around 1.96 eV and 1.81 eV. These transitions are related to the zero-phonon line (ZPL) and two phonon replicas or phonon side bands (PSB) of carbon-related defects, which behave as single photon sources.[22] Simulations suggest V_BC_N or C_BV_N as defects at the origin of this emission.[22,106] The width of the PL peaks is larger than that typically observed in thick h-BN flakes, but in agreement with reports on monolayers.[15] Also in the PL spectra, two sharp peaks are observed and labeled with a red star symbol. These peaks correspond to the Raman response depicted fully in Figure 4(e), where the stronger peaks around 1580 cm^{-1} and 2700 cm^{-1} are the G and 2D Raman bands of HOPG, respectively.[114] In addition, an asymmetric and weak peak is observed at 1350 cm^{-1}, and as shown in the inset figure, this peak has two contributions. One contribution at 1341 cm^{-1} associated to the D Raman mode of HOPG and another one at 1362 cm^{-1} corresponding to the E_{2g} Raman mode of monolayer h-BN, in agreement with recent reported results.[53]

The CL spectra in the bottom panel of Figure 4(d) show a broad luminescence that ranges from the near infrared to the UV. As in PL, the peaks are better resolved at 100 K than at 300 K. Again, the optical transitions associated to carbon-related defects are observed with the ZPL at 2.10 eV and the PSB at 1.81 eV, respectively, as seen in PL. At higher energies, the CL spectra present a series of peaks at 3.90 eV, 3.70 eV and 3.43 eV, which have been reported as being phonon replicas of a deep well-known carbon-related defect level at 4.1 eV.[105,115] Unfortunately, the emission at 4.1 eV has not been resolved here due to the transmission function of the setup. The spectra only could be corrected for the instrument response function up to 300 nm (4.1 eV). However, the PSB were observed, which means that the transitions at 4.1 eV were also present in the emitted spectra. Interestingly, the light emission at 4.1 eV has been reported as being an optical transition related to the single photon emission.[16] Recent literature suggests that this emission is associated with C_BC_N defects, carbon dimers, but other defects like C_N are also considered in some cases.[108,109,116,117] The most intense features observed in the CL spectra of Figure 4(d) are the peaks at 3.08, 2.65 and 2.37 eV, with shifts of 430 meV and 280 meV between them. Such peaks possibly have distinct origins related to the several possible defects, particularly in the presence of carbon.[116] Emissions in this energy range have been observed in bulk h-BN by performing CL and PL experiments, and are associated to carbon[21,105] impurities or nitrogen vacancy type-centers.[118,119]

Conclusions

We used low temperature UHV STM together with an optimized light collection and injection device to study the morphological, electronic, and optical properties of a monolayer h-BN epitaxially grown on HOPG. The STM images reveal h-BN regions free of defects and regions with point defects. An electronic band gap of (6.8 ± 0.2) eV was determined by performing STS measurements on defect-free monolayer h-BN. This result, combined with the h-BN optical band gap of 6.1 eV from the exciton transition, leads to a binding energy for the Frenkel exciton of (0.7 ± 0.2) eV. Additionally, bright point defects were observed in h-BN by STM imaging. The STS indicates an acceptor level around -2 eV related to the presence of the observed defects. PL and CL have shown the emission typically associated to carbon-related defects at 2.1 eV. Besides that, emissions at 3.08 eV and photon side band possibly associated to an emission at 4.1 eV were observed by CL on monolayer h-BN. These results indicate the simultaneous presence of more than one kind of carbon-related defect. We consider that the findings presented in this work could help in the understanding of the fundamental properties of monolayer h-BN, as well as in the identification at the atomic level of sources responsible for the SPEs in h-BN samples. Moreover, h-BN on HOPG represents an excellent platform to study individual defects with respect to their morphology, electronic and optical properties.

Methods

Sample preparations

Monolayer h-BN was grown on HOPG substrate by the high-temperature plasma-assisted molecular beam epitaxy (PA-MBE) method.[6,51–53] This sample preparation method allows to produce monolayer and few-layer h-BN with atomically flat surfaces and monolayer control of the sample thickness. The h-BN thickness and coverage can be controlled by substrate temperature, boron:nitrogen flux ratio and growth time. In particular, the sample investigated here was grown at a substrate temperature of about 1390 °C with a high-temperature effusion Knudsen cell for boron and a standard Veeco radio-frequency plasma source for active nitrogen. More details about the sample growth conditions and the MBE system can be found elsewhere.[53,120–122]

STM/STS

STM and STS measurements were performed under ultra-high vacuum (UHV) conditions at low-temperatures using a modified RHK PanScan FlowCryo microscope. This STM was adapted to receive a high numerical aperture light collection and injection system with optimized transmission. In this setup, imaging can be associated to electronic and optical spectroscopies as illustrated in Figure 2.

Prior to STM/STS measurements, the h-BN sample was annealed at 773 K under a base pressure of $1.9\text{x}10^{-10}$ mbar for about six hours, in order to eliminate surface impurities and contaminants. STM images were acquired in the constant-current mode using a grounded tungsten tip and a bias voltage applied to the h-BN sample. Tungsten tips were prepared by electrochemical etching with a NaOH solution. After preparation, the tips were inserted in the UHV chamber to be subjected to thermal annealing and argon sputtering. This procedure allows the removal tungsten oxide layers. For the acquisition of STS curves, differential conductance (dI/dV) measurements at 80 K were carried out using the lock-in technique, with a bias modulation of 80 mV of amplitude and 800 Hz of frequency.

To perform STS measurements, the tunnel junction was stabilized at a sample bias outside the electronic band gap of the monolayer h-BN. In most measurements, we stabilized the tip at -150 pA and -6.2 V on a specific tip position before disabling the tip-sample distance feedback loop. Using these parameters, the tunnel current is effectively related to states on the h-BN. Each tunneling spectrum was recorded by turning off the tip distance feedback loop and ramping the bias from -6.0 V to 6.0 V in steps of 50 mV and a dwell time of 50 ms. This dwell time is needed to avoid overestimating the electronic band gap due to low signal to noise ratio near the band edges. A detailed description of the STS analysis is presented in the SM, Figures S3 and S4.

***In situ* PL, Raman and CL**

PL and Raman were excited with a laser diode of 532 nm. The spot size of the light focused by the mirror on the sample surface is ~ 2 μm. The PL/Raman signal emitted by the sample is collected by the mirror and sent as parallel rays towards an optical setup outside the UHV STM chamber.

CL, also called STM-CL, was performed by operation of the STM in field emission mode. In this case, the STM tip was retracted by approximately 150 nm from the h-BN sample surface. A high bias voltage, between 150-180 V, was applied to the sample, which caused a field emission currents of 5-10 μA. In this STM operation mode, the spatial (lateral) resolution is roughly similar to the tip-to-sample distance.[45] Therefore, the obtained CL spectra refer to a region of about one hundred nanometers wide of the monolayer h-BN.

Acknowledgement

This work was supported by the Fundação de Amparo à Pesquisa do Estado de São Paulo (FAPESP) Projects 14/23399-9 and 18/08543-7. This work at Nottingham was supported by the Engineering and Physical Sciences Research Council UK (Grant Numbers EP/K040243/1 and EP/P019080/1). We also thank the University of Nottingham Propulsion Futures Beacon for funding towards this research. PHB thanks the Leverhulme Trust for the award of a Research Fellowship (RF-2019-460). This work was financially supported by the network GaNeX (ANR-11-LABX-0014), the ZEOLIGHT project (ANR-19-CE08-0016), and the BONASPES project (ANR-19-CE30-0007).

Supplementary materials available

AFM measurements and sample surface morphology. Tunneling parameters and STS. Electronic band gap determination and statistical analysis. Optical absorption. STM/STS of points defects. Correction in the luminescence spectra.

References

(1) Adachi, S. *Optical Constants of Crystalline and Amorphous Semiconductors: Numerical Data and Graphical Information*; Springer US: Boston, MA, 1999; pp 127–136.

(2) Alem, N.; Erni, R.; Kisielowski, C.; Rossell, M. D.; Gannett, W.; Zettl, A. Atomically thin hexagonal boron nitride probed by ultrahigh-resolution transmission electron microscopy. *Phys. Rev. B* **2009**, *80*, 155425.

(3) Bhimanapati, G.; Glavin, N.; Robinson, J. In *2D Materials*; Iacopi, F., Boeckl, J. J., Jagadish, C., Eds.; Semiconductors and Semimetals; Elsevier, 2016; Vol. 95; pp 101 – 147.

(4) Watanabe, K.; Taniguchi, T.; Kanda, H. Direct-bandgap properties and evidence for ultraviolet lasing of hexagonal boron nitride single crystal. *Nature Materials* **2004**, *3*, 404–409.

(5) Cassabois, G.; Valvin, P.; Gil, B. Hexagonal boron nitride is an indirect bandgap semiconductor. *Nature Photonics* **2016**, *10*, 262–266.

(6) Elias, C.; Valvin, P.; Pelini, T.; Summerfield, A.; Mellor, C. J.; Cheng, T. S.; Eaves, L.; Foxon, C. T.; Beton, P. H.; Novikov, S. V.; Gil, B.; Cassabois, G. Direct band-gap crossover in epitaxial monolayer boron nitride. *Nature Communications* **2019**, *10*, 2639.

(7) Watanabe, K.; Taniguchi, T.; Miya, K.; Sato, Y.; Nakamura, K.; Niiyama, T.; Taniguchi, M. Hexagonal boron nitride as a new ultraviolet luminescent material and its application—Fluorescence properties of hBN single-crystal powder. *Diamond and Related Materials* **2011**, *20*, 849–852.

(8) Kubota, Y.; Watanabe, K.; Tsuda, O.; Taniguchi, T. Deep Ultraviolet Light-Emitting Hexagonal Boron Nitride Synthesized at Atmospheric Pressure. *Science* **2007**, *317*, 932–934.

(9) Valvin, P.; Pelini, T.; Cassabois, G.; Zobelli, A.; Li, J.; Edgar, J. H.; Gil, B. Deep ultraviolet hyperspectral cryomicroscopy in boron nitride: Photoluminescence in crystals with an ultra-low defect density. *AIP Advances* **2020**, *10*, 075025.

(10) Museur, L.; Feldbach, E.; Kanaev, A. Defect-related photoluminescence of hexagonal boron nitride. *Phys. Rev. B* **2008**, *78*, 155204.

(11) Bourrellier, R.; Amato, M.; Galvão Tizei, L. H.; Giorgetti, C.; Gloter, A.; Heggie, M. I.; March, K.; Stéphan, O.; Reining, L.; Kociak, M.; Zobelli, A. Nanometric Resolved Luminescence in h-BN Flakes: Excitons and Stacking Order. *ACS Photonics* **2014**, *1*, 857–862.

(12) Schué, L.; Stenger, I.; Fossard, F.; Loiseau, A.; Barjon, J. Characterization methods dedicated to nanometer-thick hBN layers. *2D Materials* **2016**, *4*, 015028.

(13) Vuong, T. Q. P.; Cassabois, G.; Valvin, P.; Ouerghi, A.; Chassagneux, Y.; Voisin, C.; Gil, B. Phonon-Photon Mapping in a Color Center in Hexagonal Boron Nitride. *Phys. Rev. Lett.* **2016**, *117*, 097402.

(14) Gil, B.; Cassabois, G.; Cusco, R.; Fugallo, G.; Artus, L. Boron nitride for excitonics, nano photonics, and quantum technologies. *Nanophotonics* **2020**, *9*, 3483–3504.

(15) Tran, T. T.; Bray, K.; Ford, M. J.; Toth, M.; Aharonovich, I. Quantum emission from hexagonal boron nitride monolayers. *Nature Nanotechnology* **2016**, *11*, 37–41.

(16) Bourrellier, R.; Meuret, S.; Tararan, A.; Stéphan, O.; Kociak, M.; Tizei, L. H. G.; Zobelli, A. Bright UV Single Photon Emission at Point Defects in h-BN. *Nano Letters* **2016**, *16*, 4317–4321, PMID: 27299915.

(17) Tran, T. T.; Elbadawi, C.; Totonjian, D.; Lobo, C. J.; Grosso, G.; Moon, H.; Englund, D. R.; Ford, M. J.; Aharonovich, I.; Toth, M. Robust Multicolor Single Photon Emission from Point Defects in Hexagonal Boron Nitride. *ACS Nano* **2016**, *10*, 7331–7338, PMID: 27399936.

(18) Tran, T. T.; Zachreson, C.; Berhane, A. M.; Bray, K.; Sandstrom, R. G.; Li, L. H.; Taniguchi, T.; Watanabe, K.; Aharonovich, I.; Toth, M. Quantum Emission from Defects in Single-Crystalline Hexagonal Boron Nitride. *Phys. Rev. Applied* **2016**, *5*, 034005.

(19) Xu, Z.-Q. et al. Single photon emission from plasma treated 2D hexagonal boron nitride. *Nanoscale* **2018**, *10*, 7957–7965.

(20) Tan, Q.-H.; Xu, K.-X.; Liu, X.-L.; Guo, D.; Xue, Y.-Z.; Ren, S.-L.; Gao, Y.-F.; Dou, X.-M.; Sun, B.-Q.; Deng, H.-X.; Tan, P.-H.; Zhang, J. Ultraviolet to Near-infrared Single Photon Emitters in hBN. *arXiv:1908.06578 [cond-mat, physics:physics]* **2019**, arXiv: 1908.06578.

(21) Hayee, F.; Yu, L.; Zhang, J. L.; Ciccarino, C. J.; Nguyen, M.; Marshall, A. F.; Aharonovich, I.; Vučković, J.; Narang, P.; Heinz, T. F.; Dionne, J. A. Revealing multiple classes of stable quantum emitters in hexagonal boron nitride with correlated optical and electron microscopy. *Nature Materials* **2020**, *19*, 534–539.

(22) Mendelson, N. et al. Identifying carbon as the source of visible single-photon emission from hexagonal boron nitride. *Nature Materials* **2020**, *20*, 321–328.

(23) Martínez, L. J.; Pelini, T.; Waselowski, V.; Maze, J. R.; Gil, B.; Cassabois, G.; Jacques, V. Efficient single photon emission from a high-purity hexagonal boron nitride crystal. *Phys. Rev. B* **2016**, *94*, 121405.

(24) Watanabe, K.; Taniguchi, T.; Niiyama, T.; Miya, K.; Taniguchi, M. Far-ultraviolet plane-emission handheld device based on hexagonal boron nitride. *Nature Photonics* **2009**, *3*, 591–594.

(25) Watanabe, K.; Taniguchi, T. Hexagonal Boron Nitride as a New Ultraviolet Luminescent Material and Its Application. *International Journal of Applied Ceramic Technology* **2011**, *8*, 977–989.

(26) Jiang, H. X.; Lin, J. Y. Hexagonal boron nitride for deep ultraviolet photonic devices. *Semiconductor Science and Technology* **2014**, *29*, 084003.

(27) Hui, F.; Pan, C.; Shi, Y.; Ji, Y.; Grustan-Gutierrez, E.; Lanza, M. On the use of two dimensional hexagonal boron nitride as dielectric. *Microelectronic Engineering* **2016**, *163*, 119–133.

(28) Wang, J.; Ma, F.; Sun, M. Graphene, hexagonal boron nitride, and their heterostructures: properties and applications. *RSC Adv.* **2017**, *7*, 16801–16822.

(29) Wu, L. et al. InSe/hBN/graphite heterostructure for high-performance 2D electronics and flexible electronics. *Nano Research* **2020**, *13*, 1127–1132.

(30) Wrachtrup, J. Single photons at room temperature. *Nature Nanotechnology* **2016**, *11*, 7–8.

(31) Aharonovich, I.; Englund, D.; Toth, M. Solid-state single-photon emitters. *Nature Photonics* **2016**, *10*, 631–641.

(32) Aharonovich, I.; Toth, M. Quantum emitters in two dimensions. *Science* **2017**, *358*, 170–171.

(33) Kim, S.; Duong, N. M. H.; Nguyen, M.; Lu, T.-J.; Kianinia, M.; Mendelson, N.; Solntsev, A.; Bradac, C.; Englund, D. R.; Aharonovich, I. Integrated on Chip Platform with Quantum Emitters in Layered Materials. *Advanced Optical Materials* **2019**, *7*, 1901132.

(34) Lukishova, S. G. Room-Temperature Single-Photon Sources: State of the Art. OSA Quantum 2.0 Conference. 2020; p QW6B.3.

(35) Henck, H.; Pierucci, D.; Fugallo, G.; Avila, J.; Cassabois, G.; Dappe, Y. J.; Silly, M. G.; Chen, C.; Gil, B.; Gatti, M.; Sottile, F.; Sirotti, F.; Asensio, M. C.; Ouerghi, A. Direct observation of the band structure in bulk hexagonal boron nitride. *Phys. Rev. B* **2017**, *95*, 085410.

(36) Pierucci, D.; Zribi, J.; Henck, H.; Chaste, J.; Silly, M. G.; Bertran, F.; Le Fevre, P.; Gil, B.; Summerfield, A.; Beton, P. H.; Novikov, S. V.; Cassabois, G.; Rault, J. E.; Ouerghi, A. Van der Waals epitaxy of two-dimensional single-layer h-BN on graphite by molecular beam epitaxy: Electronic properties and band structure. *Applied Physics Letters* **2018**, *112*, 253102.

(37) Arenal, R.; Stéphan, O.; Kociak, M.; Taverna, D.; Loiseau, A.; Colliex, C. Electron Energy Loss Spectroscopy Measurement of the Optical Gaps on Individual Boron Nitride Single-Walled and Multiwalled Nanotubes. *Phys. Rev. Lett.* **2005**, *95*, 127601.

(38) Liu, Z.; Tizei, L. H. G.; Sato, Y.; Lin, Y.-C.; Yeh, C.-H.; Chiu, P.-W.; Terauchi, M.; Iijima, S.; Suenaga, K. Postsynthesis of h-BN/Graphene Heterostructures Inside a STEM. *Small* **2015**, *12*, 252–259.

(39) Feenstra, R. M. Scanning tunneling spectroscopy. *Surface Science* **1994**, *299-300*, 965–979.

(40) Feenstra, R. M. Tunneling spectroscopy of the (110) surface of direct-gap III-V semiconductors. *Phys. Rev. B* **1994**, *50*, 4561–4570.

(41) Wong, D.; Velasco, J.; Ju, L.; Lee, J.; Kahn, S.; Tsai, H.-Z.; Germany, C.; Taniguchi, T.; Watanabe, K.; Zettl, A.; Wang, F.; Crommie, M. F. Characterization and manipulation of individual defects in insulating hexagonal boron nitride using scanning tunnelling microscopy. *Nature Nanotechnology* **2015**, *10*, 949–953.

(42) Jin, C.; Lin, F.; Suenaga, K.; Iijima, S. Fabrication of a Freestanding Boron Nitride Single Layer and Its Defect Assignments. *Phys. Rev. Lett.* **2009**, *102*, 195505.

(43) Schué, L.; Berini, B.; Betz, A. C.; Plaçais, B.; Ducastelle, F.; Barjon, J.; Loiseau, A. Dimensionality effects on the luminescence properties of hBN. *Nanoscale* **2016**, *8*, 6986–6993.

(44) Hernández-Mínguez, A.; Lähnemann, J.; Nakhaie, S.; Lopes, J. M. J.; Santos, P. V. Luminescent Defects in a Few-Layer *h*-BN Film Grown by Molecular Beam Epitaxy. *Phys. Rev. Applied* **2018**, *10*, 044031.

(45) Sáenz, J. J.; García, R. Near field emission scanning tunneling microscopy. *Applied Physics Letters* **1994**, *65*, 3022–3024.

(46) Koma, A. Van der Waals epitaxy for highly lattice-mismatched systems. *Journal of Crystal Growth* **1999**, *201-202*, 236–241.

(47) Novoselov, K. S.; Mishchenko, A.; Carvalho, A.; Castro Neto, A. H. 2D materials and van der Waals heterostructures. *Science* **2016**, *353*.

(48) Walsh, L. A.; Hinkle, C. L. van der Waals epitaxy: 2D materials and topological insulators. *Applied Materials Today* **2017**, *9*, 504–515.

(49) Choi, J.-H.; Cui, P.; Chen, W.; Cho, J.-H.; Zhang, Z. Atomistic mechanisms of van der Waals epitaxy and property optimization of layered materials. *WIREs Computational Molecular Science* **2017**, *7*, e1300.

(50) Sediri, H.; Pierucci, D.; Hajlaoui, M.; Henck, H.; Patriarche, G.; Dappe, Y. J.; Yuan, S.; Toury, B.; Belkhou, R.; Silly, M. G.; Sirotti, F.; Boutchich, M.; Ouerghi, A. Atomically Sharp Interface in an h-BN-epitaxial graphene van der Waals Heterostructure. *Scientific Reports* **2015**, *5*, 16465.

(51) Summerfield, A.; Kozikov, A.; Cheng, T. S.; Davies, A.; Cho, Y.-J.; Khlobystov, A. N.; Mellor, C. J.; Foxon, C. T.; Watanabe, K.; Taniguchi, T.; Eaves, L.; Novoselov, K. S.; Novikov, S. V.; Beton, P. H. Moiré-Modulated Conductance of Hexagonal Boron Nitride Tunnel Barriers. *Nano Letters* **2018**, *18*, 4241–4246, PMID: 29913062.

(52) Vuong, T. Q. P.; Cassabois, G.; Valvin, P.; Rousseau, E.; Summerfield, A.; Mellor, C. J.; Cho, Y.; Cheng, T. S.; Albar, J. D.; Eaves, L.; Foxon, C. T.; Beton, P. H.; Novikov, S. V.; Gil, B. Deep ultraviolet emission in hexagonal boron nitride grown by high-temperature molecular beam epitaxy. *2D Materials* **2017**, *4*, 021023.

(53) Cho, Y.-J.; Summerfield, A.; Davies, A.; Cheng, T. S.; Smith, E. F.; Mellor, C. J.; Khlobystov, A. N.; Foxon, C. T.; Eaves, L.; Beton, P. H.; Novikov, S. V. Hexagonal Boron Nitride Tunnel Barriers Grown on Graphite by High Temperature Molecular Beam Epitaxy. *Scientific Reports* **2016**, *6*, 34474.

(54) Zhou, S. Y.; Gweon, G.-H.; Graf, J.; Fedorov, A. V.; Spataru, C. D.; Diehl, R. D.;

Kopelevich, Y.; Lee, D.-H.; Louie, S. G.; Lanzara, A. First direct observation of Dirac fermions in graphite. *Nature Physics* **2006**, *2*, 595–599.

(55) Castellanos-Gomez, A.; Wojtaszek, M.; Arramel,; Tombros, N.; van Wees, B. J. Reversible Hydrogenation and Bandgap Opening of Graphene and Graphite Surfaces Probed by Scanning Tunneling Spectroscopy. *Small* **2012**, *8*, 1607–1613.

(56) Peña Román, R. J.; Auad, Y.; Grasso, L.; Alvarez, F.; Barcelos, I. D.; Zagonel, L. F. Tunneling-current-induced local excitonic luminescence in p-doped WSe2 monolayers. *Nanoscale* **2020**, *12*, 13460–13470.

(57) do Amaral, G. M.; da Costa Tonon, I.; Peña Román, R. J.; de Oliveira Plath, H.; Taniguchi, T. M.; de Lima, L. H.; Zagonel, L. F.; Landers, R.; de Siervo, A. Epitaxial growth, electronic hybridization and stability under oxidation of monolayer MoS2 on Ag(111). *Applied Surface Science* **2021**, *538*, 148138.

(58) Blase, X.; Rubio, A.; Louie, S. G.; Cohen, M. L. Quasiparticle band structure of bulk hexagonal boron nitride and related systems. *Physical Review B* **1995**, *51*, 6868–6875.

(59) Arnaud, B.; Lebègue, S.; Rabiller, P.; Alouani, M. Huge Excitonic Effects in Layered Hexagonal Boron Nitride. *Physical Review Letters* **2006**, *96*.

(60) Wirtz, L.; Marini, A.; Rubio, A. Excitons in Boron Nitride Nanotubes: Dimensionality Effects. *Physical Review Letters* **2006**, *96*.

(61) Paleari, F.; Galvani, T.; Amara, H.; Ducastelle, F.; Molina-Sánchez, A.; Wirtz, L. Excitons in few-layer hexagonal boron nitride: Davydov splitting and surface localization. *2D Materials* **2018**, *5*, 045017.

(62) Aryasetiawan, F.; Gunnarsson, O. TheGWmethod. *Reports on Progress in Physics* **1998**, *61*, 237–312.

(63) Artús, L.; Feneberg, M.; Attaccalite, C.; Edgar, J. H.; Li, J.; Goldhahn, R.; Cuscó, R. Ellipsometry Study of Hexagonal Boron Nitride Using Synchrotron Radiation: Transparency Window in the Far-UVC. *Advanced Photonics Research* **2021**, *2*, 2000101.

(64) Hunt, R. J.; Monserrat, B.; Zólyomi, V.; Drummond, N. D. Diffusion quantum Monte Carlo and *GW* study of the electronic properties of monolayer and bulk hexagonal boron nitride. *Phys. Rev. B* **2020**, *101*, 205115.

(65) Yang, H.; Liang, A.; Chen, C.; Zhang, C.; Schroeter, N. B. M.; Chen, Y. Visualizing electronic structures of quantum materials by angle-resolved photoemission spectroscopy. *Nature Reviews Materials* **2018**, *3*, 341–353.

(66) Zhang, Y. et al. Direct observation of the transition from indirect to direct bandgap in atomically thin epitaxial MoSe 2. *Nature Nanotechnology* **2014**, *9*, 111–115.

(67) Zhang, C.; Johnson, A.; Hsu, C.-L.; Li, L.-J.; Shih, C.-K. Direct Imaging of Band Profile in Single Layer MoS2 on Graphite: Quasiparticle Energy Gap, Metallic Edge States, and Edge Band Bending. *Nano Letters* **2014**, *14*, 2443–2447, PMID: 24783945.

(68) Ugeda, M. M.; Bradley, A. J.; Shi, S.-F.; da Jornada, F. H.; Zhang, Y.; Qiu, D. Y.; Ruan, W.; Mo, S.-K.; Hussain, Z.; Shen, Z.-X.; Wang, F.; Louie, S. G.; Crommie, M. F. Giant bandgap renormalization and excitonic effects in a monolayer transition metal dichalcogenide semiconductor. *Nature Materials* **2014**, *13*, 1091–1095.

(69) Huang, Y. L.; Chen, Y.; Zhang, W.; Quek, S. Y.; Chen, C.-H.; Li, L.-J.; Hsu, W.-T.; Chang, W.-H.; Zheng, Y. J.; Chen, W.; Wee, A. T. S. Bandgap tunability at single-layer molybdenum disulphide grain boundaries. *Nature Communications* **2015**, *6*, 6298.

(70) Zhang, C.; Chen, Y.; Johnson, A.; Li, M.-Y.; Li, L.-J.; Mende, P. C.; Feenstra, R. M.; Shih, C.-K. Probing Critical Point Energies of Transition Metal Dichalcogenides: Sur-

prising Indirect Gap of Single Layer WSe2. *Nano Letters* **2015**, *15*, 6494–6500, PMID: 26389585.

(71) Krane, N.; Lotze, C.; Franke, K. J. Moiré structure of MoS2 on Au(111): Local structural and electronic properties. *Surface Science* **2018**, *678*, 136–142, Surface Structure and Dynamics – in Honor of Karl-Heinz Rieder.

(72) Auwärter, W. Hexagonal boron nitride monolayers on metal supports: Versatile templates for atoms, molecules and nanostructures. *Surface Science Reports* **2019**, *74*, 1–95.

(73) Bruix, A.; Miwa, J. A.; Hauptmann, N.; Wegner, D.; Ulstrup, S.; Grønborg, S. S.; Sanders, C. E.; Dendzik, M.; Grubišić Čabo, A.; Bianchi, M.; Lauritsen, J. V.; Khajetoorians, A. A.; Hammer, B.; Hofmann, P. Single-layer MoS_2 on Au(111): Band gap renormalization and substrate interaction. *Phys. Rev. B* **2016**, *93*, 165422.

(74) Dendzik, M.; Bruix, A.; Michiardi, M.; Ngankeu, A. S.; Bianchi, M.; Miwa, J. A.; Hammer, B.; Hofmann, P.; Sanders, C. E. Substrate-induced semiconductor-to-metal transition in monolayer WS_2. *Phys. Rev. B* **2017**, *96*, 235440.

(75) Zhang, Q.; Chen, Y.; Zhang, C.; Pan, C.-R.; Chou, M.-Y.; Zeng, C.; Shih, C.-K. Bandgap renormalization and work function tuning in MoSe2/hBN/Ru(0001) heterostructures. *Nature Communications* **2016**, *7*, 13843.

(76) Pan, M.; Liang, L.; Lin, W.; Kim, S. M.; Li, Q.; Kong, J.; Dresselhaus, M. S.; Meunier, V. Modification of the electronic properties of hexagonal boron-nitride in BN/graphene vertical heterostructures. *2D Materials* **2016**, *3*, 045002.

(77) Qi, Y.; Han, N.; Li, Y.; Zhang, Z.; Zhou, X.; Deng, B.; Li, Q.; Liu, M.; Zhao, J.; Liu, Z.; Zhang, Y. Strong Adlayer–Substrate Interactions “Break” the Patching Growth of h-BN onto Graphene on Re(0001). *ACS Nano* **2017**, *11*, 1807–1815, PMID: 28110522.

(78) Zhang, Z. et al. Direct Chemical Vapor Deposition Growth and Band-Gap Characterization of MoS2/h-BN van der Waals Heterostructures on Au Foils. *ACS Nano* **2017**, *11*, 4328–4336, PMID: 28333441.

(79) Brihuega, I.; Michaelis, C. H.; Zhang, J.; Bose, S.; Sessi, V.; Honolka, J.; Alexander Schneider, M.; Enders, A.; Kern, K. Electronic decoupling and templating of Co nanocluster arrays on the boron nitride nanomesh. *Surface Science* **2008**, *602*, L95–L99.

(80) Herrera-Reinoza, N.; dos Santos, A. C.; de Lima, L. H.; Landers, R.; de Siervo, A. Atomically Precise Bottom-Up Synthesis of h-BNC: Graphene Doped with h-BN Nanoclusters. *Chemistry of Materials* **2021**, *33*, 2871–2882.

(81) Liu, M.; Li, Y.; Chen, P.; Sun, J.; Ma, D.; Li, Q.; Gao, T.; Gao, Y.; Cheng, Z.; Qiu, X.; Fang, Y.; Zhang, Y.; Liu, Z. Quasi-Freestanding Monolayer Heterostructure of Graphene and Hexagonal Boron Nitride on Ir(111) with a Zigzag Boundary. *Nano Letters* **2014**, *14*, 6342–6347, PMID: 25268563.

(82) Li, Q.; Zou, X.; Liu, M.; Sun, J.; Gao, Y.; Qi, Y.; Zhou, X.; Yakobson, B. I.; Zhang, Y.; Liu, Z. Grain Boundary Structures and Electronic Properties of Hexagonal Boron Nitride on Cu(111). *Nano Letters* **2015**, *15*, 5804–5810.

(83) Thomas, J.; Bradford, J.; Cheng, T. S.; Summerfield, A.; Wrigley, J.; Mellor, C. J.; Khlobystov, A. N.; Foxon, C. T.; Eaves, L.; Novikov, S. V.; Beton, P. H. Step-flow growth of graphene-boron nitride lateral heterostructures by molecular beam epitaxy. *2D Materials* **2020**, *7*, 035014.

(84) Chiu, M.-H.; Zhang, C.; Shiu, H.-W.; Chuu, C.-P.; Chen, C.-H.; Chang, C.-Y. S.; Chen, C.-H.; Chou, M.-Y.; Shih, C.-K.; Li, L.-J. Determination of band alignment in the single-layer MoS 2 /WSe 2 heterojunction. *Nature Communications* **2015**, *6*, 7666.

(85) Bradley, A. J.; M. Ugeda, M.; da Jornada, F. H.; Qiu, D. Y.; Ruan, W.; Zhang, Y.; Wickenburg, S.; Riss, A.; Lu, J.; Mo, S.-K.; Hussain, Z.; Shen, Z.-X.; Louie, S. G.; Crommie, M. F. Probing the Role of Interlayer Coupling and Coulomb Interactions on Electronic Structure in Few-Layer MoSe2 Nanostructures. *Nano Letters* **2015**, *15*, 2594–2599, PMID: 25775022.

(86) Zribi, J.; Khalil, L.; Avila, J.; Chaste, J.; Henck, H.; Oehler, F.; Gil, B.; Liu, S.; Edgar, J. H.; Giorgetti, C.; Dappe, Y. J.; Lhuillier, E.; Cassabois, G.; Ouerghi, A.; Pierucci, D. Structural and electronic transitions in few layers of isotopically pure hexagonal boron nitride. *Physical Review B* **2020**, *102*.

(87) Museur, L.; Brasse, G.; Pierret, A.; Maine, S.; Attal-Tretout, B.; Ducastelle, F.; Loiseau, A.; Barjon, J.; Watanabe, K.; Taniguchi, T.; Kanaev, A. Exciton optical transitions in a hexagonal boron nitride single crystal. *physica status solidi (RRL) – Rapid Research Letters* **2011**, *5*, 214–216.

(88) Uddin, M. R.; Li, J.; Lin, J. Y.; Jiang, H. X. Probing carbon impurities in hexagonal boron nitride epilayers. *Applied Physics Letters* **2017**, *110*, 182107.

(89) Hüser, F.; Olsen, T.; Thygesen, K. S. Quasiparticle GW calculations for solids, molecules, and two-dimensional materials. *Phys. Rev. B* **2013**, *87*, 235132.

(90) Guo, C.; Xu, J.; Ping, Y. Substrate effect on excitonic shift and radiative lifetime of two-dimensional materials. *Journal of Physics: Condensed Matter* **2021**, *33*, 234001.

(91) Sajid, A.; Ford, M. J.; Reimers, J. R. Single-photon emitters in hexagonal boron nitride: a review of progress. *Reports on Progress in Physics* **2020**, *83*, 044501.

(92) Zhang, J.; Sun, R.; Ruan, D.; Zhang, M.; Li, Y.; Zhang, K.; Cheng, F.; Wang, Z.; Wang, Z.-M. Point defects in two-dimensional hexagonal boron nitride: A perspective. *Journal of Applied Physics* **2020**, *128*, 100902.

(93) Edelberg, D. et al. Approaching the Intrinsic Limit in Transition Metal Diselenides via Point Defect Control. *Nano Letters* **2019**, *19*, 4371–4379, PMID: 31180688.

(94) Addou, R.; Colombo, L.; Wallace, R. M. Surface Defects on Natural MoS2. *ACS Applied Materials & Interfaces* **2015**, *7*, 11921–11929, PMID: 25980312.

(95) Ziatdinov, M.; Dyck, O.; Li, X.; Sumpter, B. G.; Jesse, S.; Vasudevan, R. K.; Kalinin, S. V. Building and exploring libraries of atomic defects in graphene: Scanning transmission electron and scanning tunneling microscopy study. *Science Advances* **2019**, *5*.

(96) Zhussupbekov, K.; Ansari, L.; McManus, J. B.; Zhussupbekova, A.; Shvets, I. V.; Duesberg, G. S.; Hurley, P. K.; Gity, F.; Ó Coileáin, C.; McEvoy, N. Imaging and identification of point defects in PtTe2. *npj 2D Materials and Applications* **2021**, *5*, 14.

(97) Fujimoto, Y.; Saito, S. Effects of strain on carbon donors and acceptors in hexagonal boron nitride monolayers. *Phys. Rev. B* **2016**, *93*, 045402.

(98) Fujimoto, Y. Formation and Physical Properties of *h* -BN Atomic Layers: A First-Principles Density-Functional Study. *Advances in Materials Science and Engineering* **2017**, *2017*, 1–6.

(99) Haga, T.; Fujimoto, Y.; Saito, S. STM visualization of carbon impurities in sandwich structures consisting of hexagonal boron nitride and graphene. *Japanese Journal of Applied Physics* **2019**, *58*, SIIB03.

(100) Haga, T.; Fujimoto, Y.; Saito, S. Electronic structure and scanning tunneling microscopy images of heterostructures consisting of graphene and carbon-doped hexagonal boron nitride layers. *Phys. Rev. B* **2019**, *100*, 125403.

(101) Jamróz, A.; Majewski, J. A. Morphology, Ordering, Stability, and Electronic Structure of Carbon-Doped Hexagonal Boron Nitride. *physica status solidi (b)* **2019**, *256*, 1800554.

(102) Galvani, T.; Paleari, F.; Miranda, H. P. C.; Molina-Sánchez, A.; Wirtz, L.; Latil, S.; Amara, H.; Ducastelle, F. m. c. Excitons in boron nitride single layer. *Phys. Rev. B* **2016**, *94*, 125303.

(103) Berseneva, N.; Gulans, A.; Krasheninnikov, A. V.; Nieminen, R. M. Electronic structure of boron nitride sheets doped with carbon from first-principles calculations. *Phys. Rev. B* **2013**, *87*, 035404.

(104) Attaccalite, C.; Bockstedte, M.; Marini, A.; Rubio, A.; Wirtz, L. Coupling of excitons and defect states in boron-nitride nanostructures. *Phys. Rev. B* **2011**, *83*, 144115.

(105) Katzir, A.; Suss, J. T.; Zunger, A.; Halperin, A. Point defects in hexagonal boron nitride. I. EPR, thermoluminescence, and thermally-stimulated-current measurements. *Phys. Rev. B* **1975**, *11*, 2370–2377.

(106) Sajid, A.; Thygesen, K. S. VNCB defect as source of single photon emission from hexagonal boron nitride. *2D Materials* **2020**, *7*, 031007.

(107) Grosso, G.; Moon, H.; Lienhard, B.; Ali, S.; Efetov, D. K.; Furchi, M. M.; Jarillo-Herrero, P.; Ford, M. J.; Aharonovich, I.; Englund, D. Tunable and high-purity room temperature single-photon emission from atomic defects in hexagonal boron nitride. *Nature Communications* **2017**, *8*, 705.

(108) Mackoit-Sinkevičienė, M.; Maciaszek, M.; Van de Walle, C. G.; Alkauskas, A. Carbon dimer defect as a source of the 4.1 eV luminescence in hexagonal boron nitride. *Applied Physics Letters* **2019**, *115*, 212101.

(85) Bradley, A. J.; M. Ugeda, M.; da Jornada, F. H.; Qiu, D. Y.; Ruan, W.; Zhang, Y.; Wickenburg, S.; Riss, A.; Lu, J.; Mo, S.-K.; Hussain, Z.; Shen, Z.-X.; Louie, S. G.; Crommie, M. F. Probing the Role of Interlayer Coupling and Coulomb Interactions on Electronic Structure in Few-Layer MoSe2 Nanostructures. *Nano Letters* **2015**, *15*, 2594–2599, PMID: 25775022.

(86) Zribi, J.; Khalil, L.; Avila, J.; Chaste, J.; Henck, H.; Oehler, F.; Gil, B.; Liu, S.; Edgar, J. H.; Giorgetti, C.; Dappe, Y. J.; Lhuillier, E.; Cassabois, G.; Ouerghi, A.; Pierucci, D. Structural and electronic transitions in few layers of isotopically pure hexagonal boron nitride. *Physical Review B* **2020**, *102*.

(87) Museur, L.; Brasse, G.; Pierret, A.; Maine, S.; Attal-Tretout, B.; Ducastelle, F.; Loiseau, A.; Barjon, J.; Watanabe, K.; Taniguchi, T.; Kanaev, A. Exciton optical transitions in a hexagonal boron nitride single crystal. *physica status solidi (RRL) – Rapid Research Letters* **2011**, *5*, 214–216.

(88) Uddin, M. R.; Li, J.; Lin, J. Y.; Jiang, H. X. Probing carbon impurities in hexagonal boron nitride epilayers. *Applied Physics Letters* **2017**, *110*, 182107.

(89) Hüser, F.; Olsen, T.; Thygesen, K. S. Quasiparticle GW calculations for solids, molecules, and two-dimensional materials. *Phys. Rev. B* **2013**, *87*, 235132.

(90) Guo, C.; Xu, J.; Ping, Y. Substrate effect on excitonic shift and radiative lifetime of two-dimensional materials. *Journal of Physics: Condensed Matter* **2021**, *33*, 234001.

(91) Sajid, A.; Ford, M. J.; Reimers, J. R. Single-photon emitters in hexagonal boron nitride: a review of progress. *Reports on Progress in Physics* **2020**, *83*, 044501.

(92) Zhang, J.; Sun, R.; Ruan, D.; Zhang, M.; Li, Y.; Zhang, K.; Cheng, F.; Wang, Z.; Wang, Z.-M. Point defects in two-dimensional hexagonal boron nitride: A perspective. *Journal of Applied Physics* **2020**, *128*, 100902.

(109) Jara, C.; Rauch, T.; Botti, S.; Marques, M. A. L.; Norambuena, A.; Coto, R.; Castellanos-Águila, J. E.; Maze, J. R.; Munoz, F. First-Principles Identification of Single Photon Emitters Based on Carbon Clusters in Hexagonal Boron Nitride. *The Journal of Physical Chemistry A* **2021**, *125*, 1325–1335, PMID: 33554602.

(110) Zheng, Y. J.; Chen, Y.; Huang, Y. L.; Gogoi, P. K.; Li, M.-Y.; Li, L.-J.; Trevisanutto, P. E.; Wang, Q.; Pennycook, S. J.; Wee, A. T. S.; Quek, S. Y. Point Defects and Localized Excitons in 2D WSe2. *ACS Nano* **2019**, *13*, 6050–6059, PMID: 31074961.

(111) Schuler, B. et al. How Substitutional Point Defects in Two-Dimensional WS2 Induce Charge Localization, Spin–Orbit Splitting, and Strain. *ACS Nano* **2019**, *13*, 10520–10534, PMID: 31393700.

(112) Barja, S. et al. Identifying substitutional oxygen as a prolific point defect in monolayer transition metal dichalcogenides. *Nature Communications* **2019**, *10*, 3382.

(113) Schuler, B.; Cochrane, K. A.; Kastl, C.; Barnard, E. S.; Wong, E.; Borys, N. J.; Schwartzberg, A. M.; Ogletree, D. F.; de Abajo, F. J. G.; Weber-Bargioni, A. Electrically driven photon emission from individual atomic defects in monolayer WS2. *Science Advances* **2020**, *6*.

(114) Zólyomi, V.; Koltai, J.; Kürti, J. Resonance Raman spectroscopy of graphite and graphene. *physica status solidi (b)* **2011**, *248*, 2435–2444.

(115) Pelini, T.; Elias, C.; Page, R.; Xue, L.; Liu, S.; Li, J.; Edgar, J. H.; Dréau, A.; Jacques, V.; Valvin, P.; Gil, B.; Cassabois, G. Shallow and deep levels in carbon-doped hexagonal boron nitride crystals. *Phys. Rev. Materials* **2019**, *3*, 094001.

(116) Weston, L.; Wickramaratne, D.; Mackoit, M.; Alkauskas, A.; Van de Walle, C. G. Native point defects and impurities in hexagonal boron nitride. *Phys. Rev. B* **2018**, *97*, 214104.

(117) Linderälv, C.; Wieczorek, W.; Erhart, P. Vibrational signatures for the identification of single-photon emitters in hexagonal boron nitride. *Phys. Rev. B* **2021**, *103*, 115421.

(118) Shevitski, B.; Gilbert, S. M.; Chen, C. T.; Kastl, C.; Barnard, E. S.; Wong, E.; Ogletree, D. F.; Watanabe, K.; Taniguchi, T.; Zettl, A.; Aloni, S. Blue-light-emitting color centers in high-quality hexagonal boron nitride. *Phys. Rev. B* **2019**, *100*, 155419.

(119) Berzina, B.; Korsaks, V.; Trinkler, L.; Sarakovskis, A.; Grube, J.; Bellucci, S. Defect-induced blue luminescence of hexagonal boron nitride. *Diamond and Related Materials* **2016**, *68*, 131–137.

(120) Cheng, T.; Summerfield, A.; Mellor, C.; Khlobystov, A.; Eaves, L.; Foxon, C.; Beton, P.; Novikov, S. High-Temperature Molecular Beam Epitaxy of Hexagonal Boron Nitride with High Active Nitrogen Fluxes. *Materials* **2018**, *11*, 1119.

(121) Cheng, T. S.; Summerfield, A.; Mellor, C. J.; Davies, A.; Khlobystov, A. N.; Eaves, L.; Foxon, C. T.; Beton, P. H.; Novikov, S. V. High-temperature molecular beam epitaxy of hexagonal boron nitride layers. *Journal of Vacuum Science & Technology B* **2018**, *36*, 02D103.

(122) Wrigley, J.; Bradford, J.; James, T.; Cheng, T. S.; Thomas, J.; Mellor, C. J.; Khlobystov, A. N.; Eaves, L.; Foxon, C. T.; Novikov, S. V.; Beton, P. H. Epitaxy of boron nitride monolayers for graphene-based lateral heterostructures. *2D Materials* **2021**, *8*, 034001.

Supplementary materials: Band gap measurements of monolayer h-BN and insights into carbon-related point defects

Ricardo Javier Peña Román,*,† Fábio J. R. Costa ,† Alberto Zobelli,‡ Christine Elias,¶ Pierre Valvin,¶ Guillaume Cassabois,¶ Bernard Gil,¶ Alex Summerfield,§ Tin S. Cheng,§ Christopher J. Mellor,§ Peter H. Beton,§ Sergei V. Novikov,§ and Luiz F. Zagonel*,†

†*Institute of Physics "Gleb Wataghin", Department of Applied Physics, State University of Campinas-UNICAMP, 13083-859, Campinas, Brazil.*

‡*Université Paris-Saclay, CNRS, Laboratoire de Physiques des Solides, 91405, Orsay, France*

¶*Laboratoire Charles Coulomb, UMR5221 CNRS-Université de Montpellier, 34095 Montpellier, France*

§ *School of Physics and Astronomy, University of Nottingham, Nottingham, NG7 2RD, UK*

E-mail: rikrdopr@ifi.unicamp.br; zagonel@unicamp.br

AFM and sample surface morphology

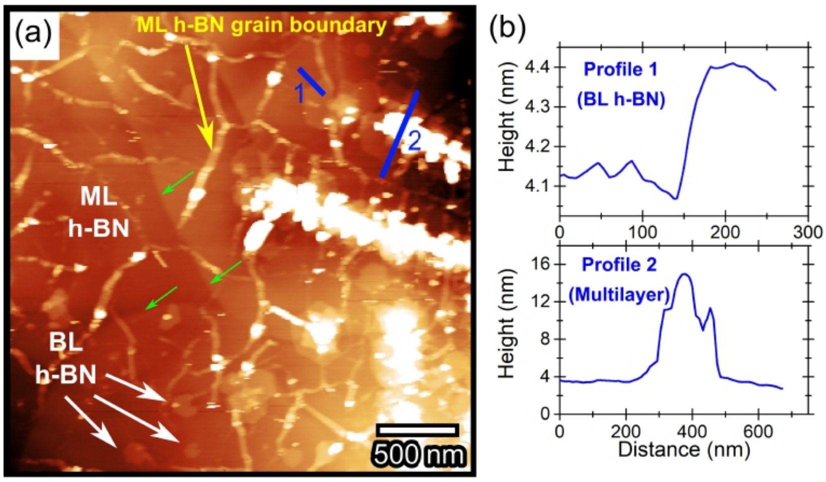

Figure S1: (a) AFM topography image of the h-BN/HOPG sample surface. The image shows an area totally covered by monolayer h-BN. Some thick regions corresponding to monolayer h-BN grain bondaries, hexagonal bilayer (BL) nano-islands, and multilayer regions are indicated in the figure. The green arrows indicate some characteristic features of the HOPG surface morphology under the h-BN. (b) Height profiles taken along an hexagonal BL h-BN and a multilayer region.

Tunneling current and the electronic band gap

For the correct determination of the electronic band gap by means of STS, we analyzed the impact of the stabilization tunneling current that is set before turning off the tip-sample distance feedback loop prior to the STS measurements. During the acquisition of the STS curves, the tip-sample distance is fixed on a specific tip position, and the sample bias is ramped with simultaneous measurement of the tunneling current and the differential conductance, dI/dV, by using a lock-in. The tip-sample distance in which the STS curves were measured is defined by the stabilization parameters (tunneling current and sample bias) set before disabling the feedback loop and starting with the acquisition of the STS.

In order to determine if the tip to sample distance plays a role in the STS results, different tunneling spectra were acquired varying the stabilization tunneling current for a fixed stabilization sample bias. Figure S2 shows some STS results as a function of the tunneling current set point of the stable tunneling condition before disabling the tip-sample distance feedback loop. Figure S2(a) contains a set of STS curves acquired after stabilizing the junction at -6.2 V and at different tunneling currents, on specific tip positions. Most of the curves in the figure present a zero dI/dV region between ∼-3 V and ∼3 V. However, by plotting the curves in logarithmic scale, such as shown in Figure S2(b), an apparent shift of the band edges is observed when the value of the tunneling current of the stable condition prior to the STS is increased. This behavior can be understood by analyzing the tunneling process and the transmission/tunneling probability.

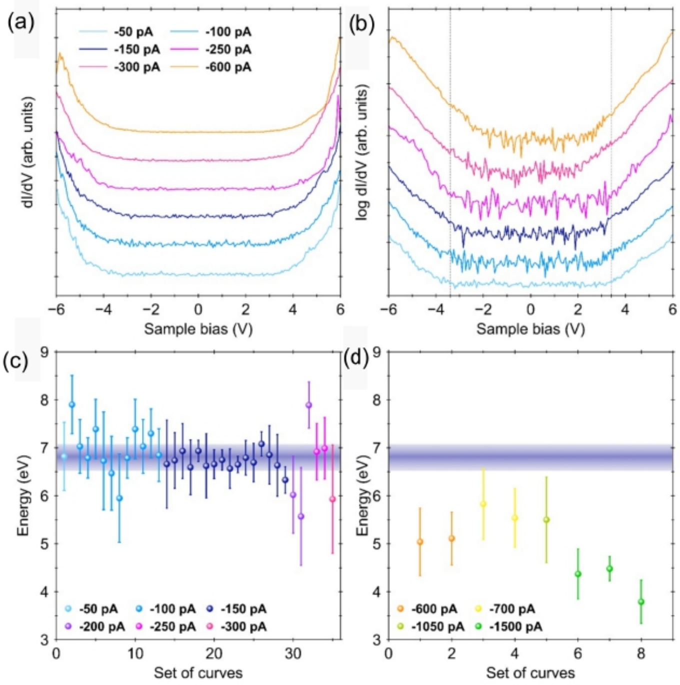

Figure S2: dI/dV spectra at (a) linear and (b) logarithmic scale, taken with different stabilizing tunneling currents before the feedback loop was disabled, with a sample bias of -6.2 V at 80 K, and using the lock-in technique with 80 mV and 800 Hz for the bias modulation. (c) and (d) Band gap values for the set of curves shown in (a), with tunneling currents before the feedback loop was disabled ranging from -50 to -300 pA (d) and from -600 to -1500 pA (e).

In order to understand the effect shown in Figure S2(b), we turn our attention to the fundamental theory of STM. The tunneling current can be described by the following expression:[1]

$$I = \frac{4\pi e}{\hbar} \int_0^{eV} \rho_t(\epsilon - eV)\rho_s(\epsilon)T(\epsilon, V_{bias}, d)\, d\epsilon \tag{1}$$

where the ρ_t and ρ_s are the density of states of the tip and the sample, respectively. With their energy variables referred relative to the respective Fermi level. $T(\epsilon, V_{bias}, d)$ is the transmission factor given by:

$$T(\epsilon, V_{bias}, d) \propto \exp\Bigg[-2d\sqrt{\frac{2m}{\hbar^2}\left(\frac{\phi_t + \phi_s}{2} + \frac{eV_{bias}}{2} - \epsilon\right)}\Bigg] \tag{2}$$

where d, ϕ_t,ϕ_s, and V_{bias} are the tip-sample distance, and the work functions of the tip and the sample, and the sample bias, respectively. The transmission factor gives the probability of electron tunneling between the tip and the sample states. From Equations (1) and (2), it can be noted that the tunneling probability decreases exponentially for lower electron energies, i. e, small ϵ. On the other hand, the tunneling probability, and consequently, the tunneling current increase exponentially for smaller tip-sample distance.

Considering ρ_t as being constant around the Fermi level, the differential conductance can be written as:

$$\frac{dI}{dV} \approx \frac{4\pi e^2}{\hbar}\rho_t(0)\rho_s(eV_{bias})T(eV_{bias}, V_{bias}, d) \tag{3}$$

This equation can be used to describe the set of curves in Figure S2(a) and (b), for which the same sample bias of -6.2 V was used to stabilize the tunneling junction before the STS measurement. In this case, the transmittance factor depends only on the tip-sample distance d, which is held fixed during the STS measurement and is set before starting by the stable tunnel conditions. When the value of tunneling current set point is increased, the tip-sample distance becomes smaller, and the transmission factor increases. This means that at higher currents the direct tunneling from or to the substrate becomes more significant and hence possibly not negligible, which leads to the measurement of an apparent reduced band gap, because states of the HOPG near the band edges of h-BN are reflected in the STS curve for h-BN, due to the electron tunneling trough the band gap of h-BN.

Figure S2(c) shows that using from -50 pA and up to -300 pA as tunneling current for stabilizing the tunneling junction, the obtained electronic band gap for monolayer h-BN is between ∼6-7 eV and is consistent to the average valued discussed in the next section. For tunneling processes with stabilization currents above 600 pA, the band gap is reduced to ∼5 or ∼4 eV, as shown in Figure S2(d). It is important to know that this apparent band gap reduction is not a band gap renormalization due to the sample substrate interaction or inhomogeneities on the sample surface. The results in Figure S2 show that it is an effect of the dependence on the transmission factor with the tunneling parameters.

Band gap determination from STS curves and statistical analysis

The STS data for the determination of the electronic band gap in monolayer h-BN were acquired after stabilizing the tip at -150 pA and -6.2 V on a specific tip position of a defect-free region. At each tip position a set of 30 tunneling spectra was recorded by sweeping the bias from -6.0 V to 6.0 V with 50 ms of time per step of 50 mV. These parameters ensure that each curve is acquired with sufficient statistics in order avoid overestimating the electronic band gap due to electronic noise in the current measurement. Figure S3(a) and (b) show a set of 30 I-V curves with the corresponding dI/dV spectra, respectively. The band edges and band gap values were determined analyzing individual differential conductance curves in logarithmic scale and following a method similar to the reported by Ugeda.[2] First, each curve was vertically displaced by a factor of 2 times its minimum value. This is to avoid negative data points. After that, the logarithm of the data was taken, such as shown in Figure S3(c). The mean value of the in-gap signal was calculated, $\mathsf{C}_{\mathsf{g,av}}$, to determine the noise background of the tunneling spectrum. The standard deviation, σ, of the signal fluctuation around $C_{g,av}$ was also calculated. Considering the linearities of the band onsets, the conduction band minimum (CBM) and valence band maximum (VBM) were determined by the intersection points between the line for 2σ and the linear fitting of the bands. The obtained values for the 30 curves were represented in the histograms shown in Figure S3(d). The uncertainty was determined by the standard deviation of the Gaussian distribution, and whose origin could be due to band bending effects.[2,3]

The values for the band edges and the electronic band gap obtained from different sets of tunneling spectra acquired on a defect-free region at different tip positions are plotted in Figure S4. Each point represents the results for a set of 30 individual curves, which were analyzed following the procedure described above. The total number of analyzed curves is 480. The final values for the electronic band gap and the band edges are indicated in the figures. The uncertainty is taken as the standard deviation for the mean value between the points.

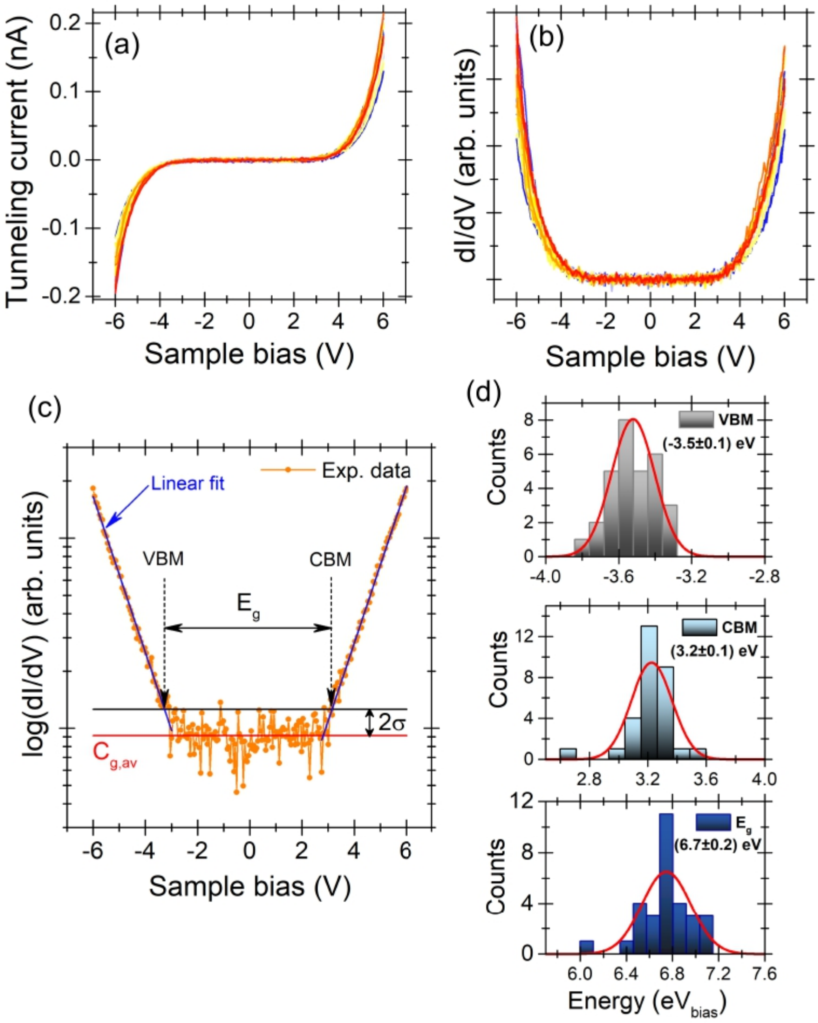

Figure S3: Sets of 30 (a) I-V curves and (b) dI/dV curves obtained in a specific tip position of a defect-free region. The data were acquired at 80 K using the lock-in technique. The feedback loop was disabled at -6.2 V, -150 pA. For measuring each curve, the sample bias was swept from -6.0 V to 6.0 V. (c) Band edges and band gap determination. (d) Statistical analysis for the set of 30 dI/dV curves presented in (b).

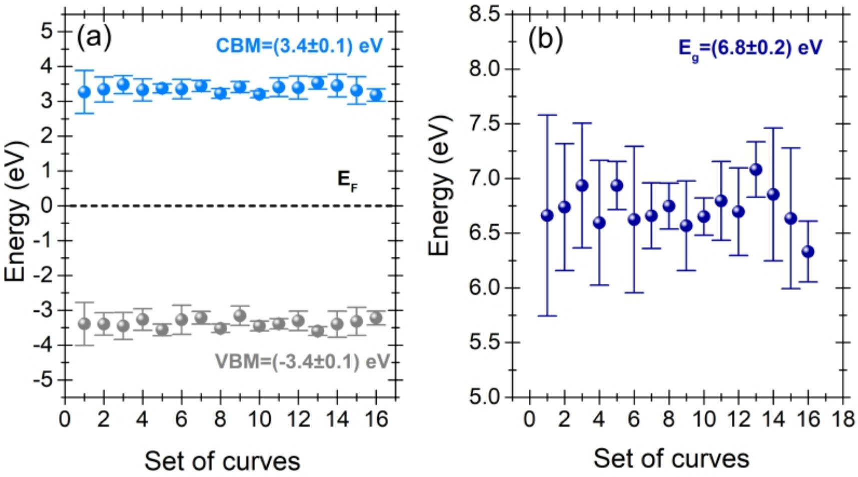

Figure S4: (a) Band edges and (b) band gap values obtained from different sets of curves using the method explained in figure S2. Each set of 30 individual curves was measured in different tip positions in a defect-free region. The error bar corresponds to the width of the Gaussian fit of each histogram.

Optical absorption spectrum

Variable angle spectroscopic ellipsometry was carried out using a M2000-DI instrument made by J.A. Woollam Inc. The results were obtained over a wavelength range from 1690 to 192 nm using focusing probes, resulting in an elliptical spot with a minor axis of 200 μm; the major axis of the ellipse depends on the angles of incidence, which were 55°, 60°and 65°. Analysis was carried out using CompleteEase version 5.19. The mosaic spread of the HOPG substrate means that we need to allow for a small angular offset (<1°) in the ellipsometric models. A Gaussian oscillator and UV pole were used to model the optical response of the boron nitride layer. A Tauc-Lorentz oscillator was also tried but did not significantly improve the fit and so the results presented here use the Gaussian oscillator as the model has fewer parameters. When measuring thin layers (<10 nm) correlations occur between the fitting parameters making it hard to estimate the layer thickness. To ensure that the thicknesses were physically reasonable, the refractive index at 632.8 nm was constrained to be close to

2.0.

DUV PL spectroscopy

In DUV PL spectroscopy, the excitation beam was provided by the fourth harmonic of a cw mode-locked Ti:Sa oscillator with a repetition of 82 MHz. The spot diameter is of the order of 50 μm, with a power of 30 μW. An achromatic optical system couples the emitted signal to our detection system, composed of a f=300 mm Czerny-Turner monochromator, equipped with a 1800 grooves.mm^{-1} grating blazed at 250 nm, and with a back-illuminated CCD camera (Andor Newton 920), with a quantum efficiency of 50% at 210 nm, operated over integration times of 5 min.

Bright point defects and STS

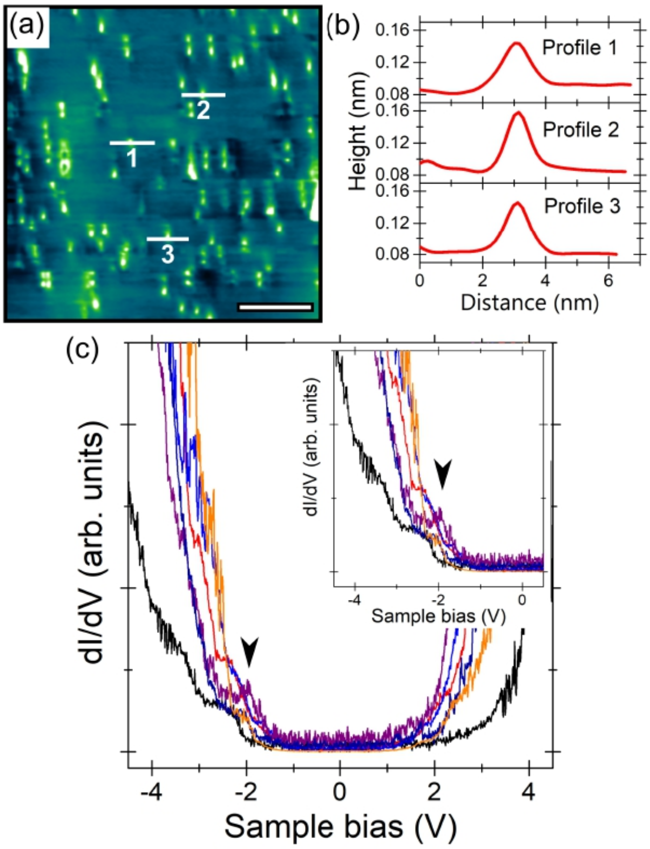

Figure S5: STM/STS resuts in point defect regions.(a) STM image of point defects in the monolayer h-BN/HOPG (-90 pA, -6.2 V, 80 K) (b) Profiles of some individual defects with about 1 nm of size. (c) STS curves acquired at different tip positions and with different tunneling parameters (80 mV, 800 Hz, 80 K). In most spectra a peak around -2V is observed, likely to the observed defects.

Correction of the luminescence spectra

To properly analyze the measured CL spectra, a few treatments were applied to the raw data, leading to the corrected data presented in the main text. A comparison between as measured and treated curves can be viewed in Figure S6. At first, dark reference spectra is removed from the acquired data and any spikes (liked due to cosmic rays) are removed. Then, an instrument response correction[4] was applied to compensate for variations of the system light transmission function that otherwise affect the registered data. This was achieved through the comparison between the acquired spectra from a tungsten halogen calibration lamp (LS-1-CAL by Ocean Optics) and its standard irradiance data. The ratio between these two curves is known as the instrument response curve, which is presented in the insert of Figure S6. This function offers a description of how the optical components affect the intensity measured at each wavelength. The correction is performed by multiplying it to the measured spectra, attenuating instrumental effects present in the data. After this procedure, a wavelength calibration was also applied, following the methods described in.[5] To perform this step, spectral lines from a Hg calibration lamp were acquired, within the 400-900 nm range, leading to an estimation of the shift between the measured and known wavelengths. By considering that these two sets share a linear dependency, a wavelength calibration fitting can be obtained, which was utilized in the correction of the acquired data.

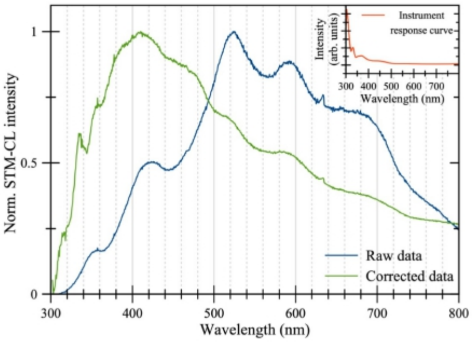

Figure S6: Normalized STM-CL emission for the monolayer h-BN sample. Both normalized raw data and data after correction by the instrument transmission function are shown. In the insert, the shape of the instrument transmission function is shown. The instrument transmission function is dominated by variation of the quantum efficiency of the CCD detector and of the diffraction grating used.

References

(1) Voigtländer, B. *Scanning Probe Microscopy: Atomic Force Microscopy and Scanning Tunneling Microscopy*; Springer Berlin Heidelberg: Berlin, Heidelberg, 2015; pp 309–334.

(2) Ugeda, M. M.; Bradley, A. J.; Shi, S.-F.; da Jornada, F. H.; Zhang, Y.; Qiu, D. Y.; Ruan, W.; Mo, S.-K.; Hussain, Z.; Shen, Z.-X.; Wang, F.; Louie, S. G.; Crommie, M. F. Giant bandgap renormalization and excitonic effects in a monolayer transition metal dichalcogenide semiconductor. *Nature Materials* **2014**, *13*, 1091–1095.

(3) Bradley, A. J.; M. Ugeda, M.; da Jornada, F. H.; Qiu, D. Y.; Ruan, W.; Zhang, Y.; Wickenburg, S.; Riss, A.; Lu, J.; Mo, S.-K.; Hussain, Z.; Shen, Z.-X.; Louie, S. G.; Crommie, M. F. Probing the Role of Interlayer Coupling and Coulomb Interactions on Electronic Structure in Few-Layer MoSe2 Nanostructures. *Nano Letters* **2015**, *15*, 2594–2599, PMID: 25775022.

(4) Horiba Jobin Yvon technical notes. `https://www.horiba.com/fileadmin/uploads/Scientific/Documents/OSD/203_Instrument_Response_Corrections.pdf`, Accessed: 2021-03-12.

(5) Gaigalas, A. K.; Wang, L.; He, H.-J.; DeRose, P. Procedures for Wavelength Calibration and Spectral Response Correction of CCD Array Spectrometers. *Journal of Research of the National Institute of Standards and Technology* **2009**, *114*, 215.

Chapter 7

General conclusions and perspectives

In this thesis, we presented a new approach for light detection in experiments of STM luminescence spectroscopy, where electrons in the STM tunneling junction are used as a nanoscale excitation source for investigating the electroluminescence or cathodoluminescence response of the sample. We developed an optical device based on a high solid angle off-axis parabolic mirror with 72% of collection efficiency and 50% overall efficiency, including collection, transmission, and detection with the spectral resolution of 0.5 nm. The device can be coupled as an optical accessory to an adapted commercial LT-UHV STM. The developed device can also be employed for light injection inside the STM, allowing other in-situ complementary optical measurements like PL and Raman. In this way, it is possible to correlate the local morphological, electronic, and optical properties of the sample under investigation with global optical measurements in the same sample region. The acquisition of atomically resolved images and STS curves on standard surfaces, like HOPG and Si (111)-7x7 reconstruction, demonstrated that the performance of the STM is not affected by the installation of the optical accessory. The capability of our approach for optical measurements in the context of STM has been tested by performing different luminescence experiments (STM-LE, STM-CL, in-situ PL/Raman) on several systems such as metallic surfaces, 2D materials, and semiconducting quantum dots.

In our study of 2D materials, we identified intrinsic point defects by acquiring STM images in both a monolayer WSe_2 mechanically transferred on gold support and a single layer h-BN epitaxially grown on graphite. The results demonstrated that point defects in the monolayer of TMDs induce sample doping. The dark point defects observed in WSe_2 monolayers correspond likely to vacancies in the transition metal sites and are considered responsible for the p-type sample doping, as evidenced by STS measurements. In monolayer h-BN, we observed bright point defects in the STM images, and the STS results indicated an electronic defect level at -2.0 eV below the Fermi level.

In WSe_2 monolayers, we observed that the monolayers are optically active in as-transferred samples on gold substrates. We attributed the optical activity of the sample to the fact that as-transferred monolayers are decoupled from the metallic support by a nanoconfined interfacial water layer. The water layer between the monolayer and the metallic substrate comes from the air moisture, and it is an inherent feature of the sample preparation method (mechanical exfoliation). The interfacial water layer works as an additional tunneling barrier between the 2D semiconductor and the metallic substrate that acts as a tunneling electrode. This system configuration enables the local electrical generation and control of excitons in WSe_2 monolayers on a metallic substrate employing tunneling electrons in ambient conditions (the environment compatible with optoelectronic device performance). The sample doping induced by the intrinsic point defects (as observed by STM/STS) also plays an important role in the electrical generation of excitons. The STM-LE spectra obtained in p-doped WSe_2 monolayers correspond to the excitation and recombination of spin-allowed excitons and trions. The excitonic emission via STM-LE was possible only at positive sample bias above the electronic band gap of monolayer WSe_2, meaning the excitation mechanism is the injection of charge; this is, electrons tunnel from tip states to sample states in the conduction band of the semiconductor. The tunneling electrons interact electrostatically with the opposite charge already present in the doped sample to form excitons and trions. The trions to neutral excitons ratio can be controlled by changing the tunneling current set point. The electrical generation of excitons via STM-LE can be lost after exciting the sample for a long time at the same STM tip position. The STM-LE signal, initially excitonic, changes progressively to a bimodal emission (exciton plus a plasmonic background) and then to a total plasmonic emission. The plasmonic emission indicated that we could induce a quenching of the intrinsic luminescence of the TMD. This quenching is local at the STM tip position. It is produced due to direct contact between the monolayer and the metallic substrate, likely due to heating effects or remotion of water molecules at the sample-substrate interface with the tunneling electrons. The quenching can also be global in the whole sample when it is thermally annealed. The interfacial water layer is totally removed in annealed samples, and the monolayer completely adheres to the substrate surface. STM/AFM images showed that the substrate surface morphology is transferred to the monolayer in this case. In addition, PL/Raman results confirmed that thermal annealing produces an electronic and mechanical contact/coupling between the monolayer and the metallic substrate.

In contrast to WSe_2 samples, we found that monolayer h-BN grown on graphite is always optically active, even after the thermal annealing necessary for sample cleaning prior to STM measurements. It is a consequence of the weak character of the van der Waals interaction at the interface between the sample and the substrate. The van der Waals gap at the interface between h-BN and graphite allows the sample to preserve its electronic and optical properties. We used this fact to explore the morphological, electronic, and optical properties of a single layer h-BN. We measured the electronic band gap and the exciton binding energy by combining low-temperature STM and STS results with ex-situ DUV PL measurements. Using STM imaging and STS, we found an electronic band gap value of $E_g = 6.8 \pm 0.2$ eV in a defect-free monolayer. This value, combined with the optical band gap of $E_{opt} = 6.1$ eV obtained by PL, allowed us to determine an exciton binding energy of $E_b = 0.7 \pm 0.2$ eV. Both E_g and E_b are about 1 eV lower than the values predicted for free-standing monolayers. Therefore, even if the interfacial sample-substrate interaction is weak, the presence of the substrate produces a renormalization of the electronic band gap and the exciton binding energy due to screening effects. The energy for the excitonic emission remains unaffected.

We also measured the CL emission of monolayer h-BN by operating the STM in field emission mode. The CL spectra and the in-situ PL showed emission peaks related to point defects. In particular, we observed the emission at 2.1 eV, usually associated with the zero-phonon line (ZPL) emission in spectra for point defect responsible for the single-photon emission in h-BN. Moreover, the CL spectra showed additional peaks in the UV range; some are considered phonon replicas of the ZPL at 4.1 eV, typically attributed to the single-photon emission of carbon-related point defects in h-BN samples.

The findings presented in this thesis on the investigation of atomically thin materials employing STM and luminescence spectroscopy in STM contributes to understanding the fundamental electronic and optical properties of 2D materials at the nanometer or atomical scale. In particular, we probed in which conditions expect the electrical generation and control of light emission from the sample when electrons in a tunneling junction are used as an excitation source. We described the role of point defects in sample doping and the effect of the sample-substrate coupling on the electronic and optical properties.

Perspectives

We propose to continue investigating the point defects properties in 2D materials.

Combining LT STM measurements with simulated STM images might help identify the defect observed in the acquired STM images. The developed optical device could be implemented in single-photon detection experiments, such as time-correlation in Hanbury Brown and Twiss (HBT) interferometry, to demonstrate single-photon emission involving point defects states or defect-bound excitons. These measurements represent an opportunity to address the identification at the atomic level of the specific point defects with quantum emission in both TMDs and h- BN monolayers.

Recently it has been demonstrated that excitons can be trapped in Moiré potentials of twisted monolayers, giving rise to a new variety of excitonic phenomena controlled via the twist angle. Moiré excitons in TMDs and h-BN have been investigated by far-field optical spectroscopy like micro-photoluminescence, whose spatial resolution is limited to about 1 μm [21, 23, 148]. Understanding the properties of Moiré excitons, with a direct correlation between the periodicity of the moiré potential (below 50 nm) [22] and the optical properties, requires investigations with a high spatial resolution, for instance, less than 10 nm. STM/STS and STM-LE measurements can be employed to investigate Moiré potentials and excitons in vdW heterostructures with nanometric or atomic resolution.

Bibliography

[1] K. S. Novoselov et al. “Electric Field Effect in Atomically Thin Carbon Films”. In: *Science* 306.5696 (2004), pp. 666–669. DOI: 10.1126/science.1102896. eprint: https://www.science.org/doi/pdf/10.1126/science.1102896.

[2] A. K. Geim and K. S. Novoselov. “The rise of graphene”. In: *Nature Materials* 6.3 (Mar. 2007), pp. 183–191. DOI: 10.1038/nmat1849.

[3] C. Lee et al. “Measurement of the Elastic Properties and Intrinsic Strength of Monolayer Graphene”. In: *Science* 321.5887 (2008), pp. 385–388. DOI: 10.1126/science.1157996. eprint: https://www.science.org/doi/pdf/10.1126/science.1157996.

[4] M. Xu et al. “Graphene-Like Two-Dimensional Materials”. In: *Chemical Reviews* 113.5 (2013). PMID: 23286380, pp. 3766–3798. DOI: 10.1021/cr300263a. eprint: https://doi.org/10.1021/cr300263a.

[5] K. F. Mak et al. “Atomically Thin MoS_2: A New Direct-Gap Semiconductor”. In: *Phys. Rev. Lett.* 105 (13 Sept. 2010), p. 136805. DOI: 10.1103/PhysRevLett.105.136805.

[6] M. Chhowalla et al. “The chemistry of two-dimensional layered transition metal dichalcogenide nanosheets”. en. In: *Nature Chemistry* 5.4 (Apr. 2013), pp. 263–275. DOI: 10.1038/nchem.1589.

[7] K. F. Mak et al. “Control of valley polarization in monolayer MoS2 by optical helicity”. en. In: *Nature Nanotechnology* 7.8 (Aug. 2012), pp. 494–498. DOI: 10.1038/nnano.2012.96.

[8] G. Wang et al. “Colloquium: Excitons in atomically thin transition metal dichalcogenides”. In: *Rev. Mod. Phys.* 90 (2 Apr. 2018), p. 021001. DOI: 10.1103/RevModPhys.90.021001.

[9] T. Mueller and E. Malic. “Exciton physics and device application of two-dimensional transition metal dichalcogenide semiconductors”. In: *npj 2D Materials and Applications* 2.1 (Sept. 2018). DOI: 10.1038/s41699-018-0074-2.

[10] K. F. Mak and J. Shan. “Photonics and optoelectronics of 2D semiconductor transition metal dichalcogenides”. In: *Nature Photonics* 10.4 (Mar. 2016), pp. 216–226. DOI: 10.1038/nphoton.2015.282.

[11] A. Krasnok, S. Lepeshov, and A. Alú. “Nanophotonics with 2D transition metal dichalcogenides. *Invited*”. In: *Opt. Express* 26.12 (June 2018), pp. 15972–15994. DOI: 10.1364/OE.26.015972.

[12] K. Watanabe and T. Taniguchi. “Hexagonal Boron Nitride as a New Ultraviolet Luminescent Material and Its Application”. In: *International Journal of Applied Ceramic Technology* 8.5 (2011), pp. 977–989. DOI: https://doi.org/10.1111/j.1744-7402.2011.02626.x.

[13] G. M. do Amaral et al. “Epitaxial growth, electronic hybridization and stability under oxidation of monolayer MoS2 on Ag(111)”. In: *Applied Surface Science* 538 (2021), p. 148138. DOI: https://doi.org/10.1016/j.apsusc.2020.148138.

[14] A. Raja et al. “Dielectric disorder in two-dimensional materials”. In: *Nature Nanotechnology* 14.9 (Aug. 2019), pp. 832–837. DOI: 10.1038/s41565-019-0520-0.

[15] M. Grzeszczyk et al. “The effect of metallic substrates on the optical properties of monolayer MoSe2”. In: *Scientific Reports* 10.1 (Mar. 2020). DOI: 10.1038/s41598-020-61673-0.

[16] C. Guo, J. Xu, and Y. Ping. “Substrate effect on excitonic shift and radiative lifetime of two-dimensional materials”. In: *Journal of Physics: Condensed Matter* 33.23 (May 2021), p. 234001. DOI: 10.1088/1361-648x/abeacf.

[17] G. Grosso et al. “Tunable and high-purity room temperature single-photon emission from atomic defects in hexagonal boron nitride”. In: *Nature Communications* 8.1 (Sept. 2017). DOI: 10.1038/s41467-017-00810-2.

[18] N. V. Proscia et al. “Near-deterministic activation of room-temperature quantum emitters in hexagonal boron nitride”. In: *Optica* 5.9 (Sept. 2018), pp. 1128–1134. DOI: 10.1364/OPTICA.5.001128.

[19] M. G. Harats et al. “Dynamics and efficient conversion of excitons to trions in non-uniformly strained monolayer WS2”. In: *Nature Photonics* 14.5 (Feb. 2020), pp. 324–329. DOI: 10.1038/s41566-019-0581-5.

[20] A. Branny et al. “Deterministic strain-induced arrays of quantum emitters in a two-dimensional semiconductor”. In: *Nature Communications* 8.1 (May 2017). DOI: 10.1038/ncomms15053.

[21] K. Tran et al. “Evidence for moiré excitons in van der Waals heterostructures”. In: *Nature* 567.7746 (Feb. 2019), pp. 71–75. DOI: 10.1038/s41586-019-0975-z.

[22] D. Huang et al. “Excitons in semiconductor moiré superlattices”. In: *Nature Nanotechnology* 17.3 (Mar. 2022), pp. 227–238. DOI: 10.1038/s41565-021-01068-y.

[23] Y. Li et al. “Giant moiré trapping of excitons in twisted hBN”. In: *Opt. Express* 30.7 (Mar. 2022), pp. 10596–10604. DOI: 10.1364/OE.450409.

[24] N. Krane et al. “Electronic Structure and Luminescence of Quasi-Freestanding MoS2 Nanopatches on Au(111)”. In: *Nano Letters* 16.8 (2016). PMID: 27459588, pp. 5163–5168. DOI: 10.1021/acs.nanolett.6b02101.

[25] U. Bhanu et al. “Photoluminescence quenching in gold - MoS2 hybrid nanoflakes”. In: *Scientific Reports* 4.1 (July 2014). DOI: 10.1038/srep05575.

[26] R. S. Sundaram et al. “Electroluminescence in Single Layer MoS2”. In: *Nano Letters* 13.4 (2013). PMID: 23514373, pp. 1416–1421. DOI: 10.1021/nl400516a. eprint: https://doi.org/10.1021/nl400516a.

[27] H. Henck et al. “Direct observation of the band structure in bulk hexagonal boron nitride”. In: *Phys. Rev. B* 95 (8 Feb. 2017), p. 085410. DOI: 10.1103/PhysRevB.95.085410.

[28] D. Pierucci et al. “Van der Waals epitaxy of two-dimensional single-layer h-BN on graphite by molecular beam epitaxy: Electronic properties and band structure”. In: *Applied Physics Letters* 112.25 (2018), p. 253102. DOI: 10.1063/1.5029220.

[29] Q. Zhang et al. “Bandgap renormalization and work function tuning in MoSe2/hBN/Ru(0001) heterostructures”. In: *Nature Communications* 7.1 (Dec. 2016). DOI: 10.1038/ncomms13843.

[30] N. Herrera-Reinoza et al. “Atomically Precise Bottom-Up Synthesis of h-BNC: Graphene Doped with h-BN Nanoclusters”. In: *Chemistry of Materials* 33.8

(2021), pp. 2871–2882. DOI: 10.1021/acs.chemmater.1c00081. eprint: https://doi.org/10.1021/acs.chemmater.1c00081.

[31] A. Koma. “Van der Waals epitaxy for highly lattice-mismatched systems”. In: *Journal of Crystal Growth* 201-202 (1999), pp. 236–241. DOI: https://doi.org/10.1016/S0022-0248(98)01329-3.

[32] A. K. Geim and I. V. Grigorieva. “Van der Waals heterostructures”. In: *Nature* 499.7459 (July 2013), pp. 419–425. DOI: 10.1038/nature12385.

[33] P. Nagler et al. “Interlayer exciton dynamics in a dichalcogenide monolayer heterostructure”. In: *2D Materials* 4.2 (June 2017), p. 025112. DOI: 10.1088/2053-1583/aa7352.

[34] Y. Jiang et al. “Interlayer exciton formation, relaxation, and transport in TMD van der Waals heterostructures”. In: *Light: Science & Applications* 10.1 (Apr. 2021). DOI: 10.1038/s41377-021-00500-1.

[35] C. Elias et al. “Direct band-gap crossover in epitaxial monolayer boron nitride”. en. In: *Nature Communications* 10.1 (June 2019), p. 2639. DOI: 10.1038/s41467-019-10610-5.

[36] L. Loh et al. “Impurity-Induced Emission in Re-Doped WS2 Monolayers”. In: *Nano Letters* 21.12 (2021). PMID: 34115939, pp. 5293–5300. DOI: 10.1021/acs.nanolett.1c01439. eprint: https://doi.org/10.1021/acs.nanolett.1c01439.

[37] N. Peimyoo et al. “Chemically Driven Tunable Light Emission of Charged and Neutral Excitons in Monolayer WS2”. In: *ACS Nano* 8.11 (2014). PMID: 25317839, pp. 11320–11329. DOI: 10.1021/nn504196n. eprint: https://doi.org/10.1021/nn504196n.

[38] Z. Lin et al. “Defect engineering of two-dimensional transition metal dichalcogenides”. In: *2D Materials* 3.2 (Apr. 2016), p. 022002. DOI: 10.1088/2053-1583/3/2/022002.

[39] R. Bourrellier et al. “Bright UV Single Photon Emission at Point Defects in h-BN”. In: *Nano Letters* 16.7 (2016). PMID: 27299915, pp. 4317–4321. DOI: 10.1021/acs.nanolett.6b01368.

[40] R. Bourrellier et al. “Nanometric Resolved Luminescence in h-BN Flakes: Excitons and Stacking Order”. In: *ACS Photonics* 1.9 (2014), pp. 857–862. DOI: 10.1021/ph500141j. eprint: https://doi.org/10.1021/ph500141j.

[41] K. Wu et al. “Controllable defects implantation in MoS2 grown by chemical vapor deposition for photoluminescence enhancement”. In: *Nano Research* 11.8 (Feb. 2018), pp. 4123–4132. DOI: 10.1007/s12274-018-1999-7.

[42] M. Zhou et al. “How defects influence the photoluminescence of TMDCs”. In: *Nano Research* 14.1 (Sept. 2020), pp. 29–39. DOI: 10.1007/s12274-020-3037-9.

[43] Y.-M. He et al. “Single quantum emitters in monolayer semiconductors”. In: *Nature Nanotechnology* 10.6 (May 2015), pp. 497–502. DOI: 10.1038/nnano.2015.75.

[44] P. Tonndorf et al. “Single-photon emission from localized excitons in an atomically thin semiconductor”. In: *Optica* 2.4 (Apr. 2015), pp. 347–352. DOI: 10.1364/OPTICA.2.000347.

[45] T. T. Tran et al. “Quantum emission from hexagonal boron nitride monolayers”. In: *Nature Nanotechnology* 11.1 (Oct. 2015), pp. 37–41. DOI: 10.1038/nnano.2015.242.

[46] T. T. Tran et al. “Robust Multicolor Single Photon Emission from Point Defects in Hexagonal Boron Nitride”. In: *ACS Nano* 10.8 (2016). PMID: 27399936, pp. 7331–

7338. DOI: 10.1021/acsnano.6b03602. eprint: https://doi.org/10.1021/acsnano.6b03602.

[47] X. Liu and M. C. Hersam. “2D materials for quantum information science”. In: *Nature Reviews Materials* 4.10 (Aug. 2019), pp. 669–684. DOI: 10.1038/s41578-019-0136-x.

[48] K. Kuhnke et al. “Atomic-Scale Imaging and Spectroscopy of Electroluminescence at Molecular Interfaces”. In: *Chemical Reviews* 117.7 (2017). PMID: 28294599, pp. 5174–5222. DOI: 10.1021/acs.chemrev.6b00645.

[49] D. Pommier et al. “Scanning Tunneling Microscope-Induced Excitonic Luminescence of a Two-Dimensional Semiconductor”. In: *Phys. Rev. Lett.* 123 (2 July 2019), p. 027402. DOI: 10.1103/PhysRevLett.123.027402.

[50] D. Wong et al. “Characterization and manipulation of individual defects in insulating hexagonal boron nitride using scanning tunnelling microscopy”. In: *Nature Nanotechnology* 10.11 (Aug. 2015), pp. 949–953. DOI: 10.1038/nnano.2015.188.

[51] C. Jin et al. “Fabrication of a Freestanding Boron Nitride Single Layer and Its Defect Assignments”. In: *Phys. Rev. Lett.* 102 (19 May 2009), p. 195505. DOI: 10.1103/PhysRevLett.102.195505.

[52] L. Schué et al. “Dimensionality effects on the luminescence properties of hBN”. In: *Nanoscale* 8 (13 2016), pp. 6986–6993. DOI: 10.1039/C6NR01253A.

[53] A. Splendiani et al. “Emerging Photoluminescence in Monolayer MoS2”. In: *Nano Letters* 10.4 (2010). PMID: 20229981, pp. 1271–1275. DOI: 10.1021/nl903868w. eprint: https://doi.org/10.1021/nl903868w.

[54] W. Zhao et al. “Evolution of Electronic Structure in Atomically Thin Sheets of WS2 and WSe2”. In: *ACS Nano* 7.1 (2013). PMID: 23256505, pp. 791–797. DOI: 10.1021/nn305275h. eprint: https://doi.org/10.1021/nn305275h.

[55] S. Manzeli et al. “2D transition metal dichalcogenides”. In: *Nature Reviews Materials* 2.8 (June 2017). DOI: 10.1038/natrevmats.2017.33.

[56] M. Samadi et al. “Group 6 transition metal dichalcogenide nanomaterials: synthesis, applications and future perspectives”. In: *Nanoscale Horiz.* 3 (2 2018), pp. 90–204. DOI: 10.1039/C7NH00137A.

[57] A. Kormányos et al. “Spin-Orbit Coupling, Quantum Dots, and Qubits in Monolayer Transition Metal Dichalcogenides”. In: *Phys. Rev. X* 4 (1 Mar. 2014), p. 011034. DOI: 10.1103/PhysRevX.4.011034.

[58] Y. Sun, D. Wang, and Z. Shuai. “Indirect-to-Direct Band Gap Crossover in Few-Layer Transition Metal Dichalcogenides: A Theoretical Prediction”. In: *The Journal of Physical Chemistry C* 120.38 (2016), pp. 21866–21870. DOI: 10.1021/acs.jpcc.6b08748. eprint: https://doi.org/10.1021/acs.jpcc.6b08748.

[59] M. Samadi et al. “Group 6 transition metal dichalcogenide nanomaterials: synthesis, applications and future perspectives”. In: *Nanoscale Horiz.* 3 (2 2018), pp. 90–204. DOI: 10.1039/C7NH00137A.

[60] P. Y. Yu and M. Cardona. *Fundamentals of Semiconductors.* Springer Berlin Heidelberg, 2010. DOI: 10.1007/978-3-642-00710-1.

[61] M. Fox. *Optical properties of solids.* Oxford University Press, 2010.

[62] A. Chernikov et al. “Exciton Binding Energy and Nonhydrogenic Rydberg Series in Monolayer WS_2”. In: *Phys. Rev. Lett.* 113 (7 Aug. 2014), p. 076802. DOI: 10.1103/PhysRevLett.113.076802.

[63] Y. Li et al. “Measurement of the optical dielectric function of monolayer transition-metal dichalcogenides: MoS_2, $MoSe_2$, WS_2, and WSe_2”. In: *Phys. Rev. B* 90 (20 Nov. 2014), p. 205422. DOI: 10.1103/PhysRevB.90.205422.

[64] F. Cadiz et al. “Excitonic Linewidth Approaching the Homogeneous Limit in MoS_2-Based van der Waals Heterostructures”. In: *Phys. Rev. X* 7 (2 May 2017), p. 021026. DOI: 10.1103/PhysRevX.7.021026.

[65] M. Koperski et al. “Optical properties of atomically thin transition metal dichalcogenides: observations and puzzles”. In: *Nanophotonics* 6.6 (2017), pp. 1289–1308. DOI: doi:10.1515/nanoph-2016-0165.

[66] M. M. Ugeda et al. “Giant bandgap renormalization and excitonic effects in a monolayer transition metal dichalcogenide semiconductor”. In: *Nature Materials* 13.12 (Aug. 2014), pp. 1091–1095. DOI: 10.1038/nmat4061.

[67] G. Wang et al. “In-Plane Propagation of Light in Transition Metal Dichalcogenide Monolayers: Optical Selection Rules”. In: *Phys. Rev. Lett.* 119 (4 July 2017), p. 047401. DOI: 10.1103/PhysRevLett.119.047401.

[68] M. Zinkiewicz et al. “Neutral and charged dark excitons in monolayer WS2”. In: *Nanoscale* 12 (35 2020), pp. 18153–18159. DOI: 10.1039/D0NR04243A.

[69] M. Paur et al. “Electroluminescence from multi-particle exciton complexes in transition metal dichalcogenide semiconductors”. en. In: *Nature Communications* 10.1 (Apr. 2019), p. 1709. DOI: 10.1038/s41467-019-09781-y.

[70] E. Lorchat et al. “Filtering the photoluminescence spectra of atomically thin semiconductors with graphene”. In: *Nature Nanotechnology* 15.4 (Mar. 2020), pp. 283–288. DOI: 10.1038/s41565-020-0644-2.

[71] J. Jadczak et al. “Probing of free and localized excitons and trions in atomically thin WSesub2/sub, WSsub2/sub, MoSesub2/sub and MoSsub2/sub in photoluminescence and reflectivity experiments”. In: *Nanotechnology* 28.39 (Sept. 2017), p. 395702. DOI: 10.1088/1361-6528/aa87d0.

[72] R. Addou, L. Colombo, and R. M. Wallace. “Surface Defects on Natural MoS2”. In: *ACS Applied Materials & Interfaces* 7.22 (2015). PMID: 25980312, pp. 11921–11929. DOI: 10.1021/acsami.5b01778. eprint: https://doi.org/10.1021/acsami.5b01778.

[73] S. McDonnell et al. “Hole Contacts on Transition Metal Dichalcogenides: Interface Chemistry and Band Alignments”. In: *ACS Nano* 8.6 (2014). PMID: 24797712, pp. 6265–6272. DOI: 10.1021/nn501728w. eprint: https://doi.org/10.1021/nn501728w.

[74] S. Zhang et al. “Defect Structure of Localized Excitons in a WSe_2 Monolayer”. In: *Phys. Rev. Lett.* 119 (4 July 2017), p. 046101. DOI: 10.1103/PhysRevLett.119.046101.

[75] P. Rivera et al. “Intrinsic donor-bound excitons in ultraclean monolayer semiconductors”. In: *Nature Communications* 12.1 (Feb. 2021). DOI: 10.1038/s41467-021-21158-8.

[76] D. Edelberg et al. “Approaching the Intrinsic Limit in Transition Metal Diselenides via Point Defect Control”. In: *Nano Letters* 19.7 (2019). PMID: 31180688, pp. 4371–4379. DOI: 10.1021/acs.nanolett.9b00985. eprint: https://doi.org/10.1021/acs.nanolett.9b00985.

[77] L. Wirtz et al. *Excitonic effects in optical absorption and electron-energy loss spectra of hexagonal boron nitride.* 2005. DOI: 10.48550/ARXIV.COND-MAT/0508421.

[78] K. Watanabe, T. Taniguchi, and H. Kanda. "Direct-bandgap properties and evidence for ultraviolet lasing of hexagonal boron nitride single crystal". In: *Nature Materials* 3.6 (May 2004), pp. 404–409. DOI: 10.1038/nmat1134.

[79] R. Bourrellier. "Luminescence at Defects in h-BN : Excitons at Stacking Faults and Single Photon Emitters". Theses. Université Paris Sud - Paris XI, Oct. 2014.

[80] F. Paleari et al. "Excitons in few-layer hexagonal boron nitride: Davydov splitting and surface localization". In: *2D Materials* 5.4 (Aug. 2018), p. 045017. DOI: 10.1088/2053-1583/aad586.

[81] L. Schué et al. "Characterization methods dedicated to nanometer-thick hBN layers". In: *2D Materials* 4.1 (Nov. 2016), p. 015028. DOI: 10.1088/2053-1583/4/1/015028.

[82] R. J. Hunt et al. "Diffusion quantum Monte Carlo and *GW* study of the electronic properties of monolayer and bulk hexagonal boron nitride". In: *Phys. Rev. B* 101 (20 May 2020), p. 205115. DOI: 10.1103/PhysRevB.101.205115.

[83] L. Wirtz, A. Marini, and A. Rubio. "Excitons in Boron Nitride Nanotubes: Dimensionality Effects". In: *Phys. Rev. Lett.* 96 (12 Mar. 2006), p. 126104. DOI: 10.1103/PhysRevLett.96.126104.

[84] K. S. Thygesen. "Calculating excitons, plasmons, and quasiparticles in 2D materials and van der Waals heterostructures". In: *2D Materials* 4.2 (June 2017), p. 022004. DOI: 10.1088/2053-1583/aa6432.

[85] F. Hüser, T. Olsen, and K. S. Thygesen. "Quasiparticle GW calculations for solids, molecules, and two-dimensional materials". In: *Phys. Rev. B* 87 (23 June 2013), p. 235132. DOI: 10.1103/PhysRevB.87.235132.

[86] A. Bruix et al. "Single-layer MoS_2 on Au(111): Band gap renormalization and substrate interaction". In: *Phys. Rev. B* 93 (16 Apr. 2016), p. 165422. DOI: 10.1103/PhysRevB.93.165422.

[87] M. Dendzik et al. "Substrate-induced semiconductor-to-metal transition in monolayer WS_2". In: *Phys. Rev. B* 96 (23 Dec. 2017), p. 235440. DOI: 10.1103/PhysRevB.96.235440.

[88] M. Pan et al. "Modification of the electronic properties of hexagonal boron-nitride in BN/graphene vertical heterostructures". In: *2D Materials* 3.4 (Sept. 2016), p. 045002. DOI: 10.1088/2053-1583/3/4/045002.

[89] A. Summerfield et al. "Moiré-Modulated Conductance of Hexagonal Boron Nitride Tunnel Barriers". In: *Nano Letters* 18.7 (2018). PMID: 29913062, pp. 4241–4246. DOI: 10.1021/acs.nanolett.8b01223. eprint: https://doi.org/10.1021/acs.nanolett.8b01223.

[90] G. Binnig et al. "Surface Studies by Scanning Tunneling Microscopy". In: *Phys. Rev. Lett.* 49 (1 July 1982), pp. 57–61. DOI: 10.1103/PhysRevLett.49.57.

[91] G. Binnig et al. "7 × 7 Reconstruction on Si(111) Resolved in Real Space". In: *Phys. Rev. Lett.* 50 (2 Jan. 1983), pp. 120–123. DOI: 10.1103/PhysRevLett.50.120.

[92] C. J. Chen. *Introduction to Scanning Tunneling Microscopy*. Oxford University Press, Sept. 2007. DOI: 10.1093/acprof:oso/9780199211500.001.0001.

[93] R. Wiesendanger. *Scanning Probe Microscopy and Spectroscopy: Methods and Applications*. Cambridge University Press, 1994. DOI: 10.1017/CBO9780511524356.

[94] B. Voigtländer. *Scanning Probe Microscopy*. Springer Berlin Heidelberg, 2015. DOI: 10.1007/978-3-662-45240-0.

[95] J. K. Gimzewski et al. “Photon emission with the scanning tunneling microscope”. In: *Zeitschrift für Physik B Condensed Matter* 72.4 (Dec. 1988), pp. 497–501. DOI: 10.1007/bf01314531.

[96] R. Berndt, J. K. Gimzewski, and P. Johansson. “Inelastic tunneling excitation of tip-induced plasmon modes on noble-metal surfaces”. In: *Phys. Rev. Lett.* 67 (27 Dec. 1991), pp. 3796–3799. DOI: 10.1103/PhysRevLett.67.3796.

[97] R. Berndt and J. K. Gimzewski. “Injection luminescence from CdS(112¯0) studied with scanning tunneling microscopy”. In: *Phys. Rev. B* 45 (24 June 1992), pp. 14095–14099. DOI: 10.1103/PhysRevB.45.14095.

[98] F. Rossel, M. Pivetta, and W.-D. Schneider. “Luminescence experiments on supported molecules with the scanning tunneling microscope”. In: *Surface Science Reports* 65.5 (2010), pp. 129–144. DOI: https://doi.org/10.1016/j.surfrep.2010.06.001.

[99] L. Novotny and B. Hecht. *Principles of Nano-Optics*. 2nd ed. Cambridge University Press, 2012. DOI: 10.1017/CBO9780511794193.

[100] K. Kuhnke et al. “Versatile optical access to the tunnel gap in a low-temperature scanning tunneling microscope”. In: *Review of Scientific Instruments* 81.11 (2010), p. 113102. DOI: 10.1063/1.3480548. eprint: https://doi.org/10.1063/1.3480548.

[101] R. W. Rendell and D. J. Scalapino. “Surface plasmons confined by microstructures on tunnel junctions”. In: *Phys. Rev. B* 24 (6 Sept. 1981), pp. 3276–3294. DOI: 10.1103/PhysRevB.24.3276.

[102] J. K. Gimzewski et al. “Enhanced Photon Emission in Scanning Tunnelling Microscopy”. In: *Europhysics Letters (EPL)* 8.5 (Mar. 1989), pp. 435–440. DOI: 10.1209/0295-5075/8/5/007.

[103] B. N. J. Persson and A. Baratoff. “Theory of photon emission in electron tunneling to metallic particles”. In: *Phys. Rev. Lett.* 68 (21 May 1992), pp. 3224–3227. DOI: 10.1103/PhysRevLett.68.3224.

[104] K. Meguro et al. “Origin of multiple peaks in the light emission spectra of a Au(111) surface induced by the scanning tunneling microscope”. In: *Phys. Rev. B* 65 (16 Apr. 2002), p. 165405. DOI: 10.1103/PhysRevB.65.165405.

[105] M. Sakurai, C. Thirstrup, and M. Aono. “New aspects of light emission from STM”. In: *Applied Physics A* 80 (6 July 2005), p. 1153. DOI: 10.1007/s00339-004-3180-2.

[106] M. Reinhardt et al. “Atomic resolution in tunneling induced light emission from GaAs(110)”. In: *Applied Physics Letters* 96.15 (2010), p. 152107. DOI: 10.1063/1.3360203. eprint: https://doi.org/10.1063/1.3360203.

[107] H. Imada et al. “Atomic-scale luminescence measurement and theoretical analysis unveiling electron energy dissipation at aip/i-type GaAs(110) surface”. In: *Nanotechnology* 26.36 (Aug. 2015), p. 365402. DOI: 10.1088/0957-4484/26/36/365402.

[108] H. Carstensen et al. “Direct determination of III-V semiconductor surface band gaps”. In: *Phys. Rev. B* 41 (14 May 1990), pp. 9880–9885. DOI: 10.1103/PhysRevB.41.9880.

[109] P. Avouris and B. N. J. Persson. “Excited states at metal surfaces and their non-radiative relaxation”. In: *The Journal of Physical Chemistry* 88.5 (1984), pp. 837–848. DOI: 10.1021/j150649a004. eprint: https://doi.org/10.1021/j150649a004.

[110] K. Sakamoto et al. “Light emission spectra of the monolayer-island of C60 molecules on Au(111) induced by scanning tunneling microscope”. In: *Surface*

Science 502-503 (2002), pp. 149–155. DOI: https://doi.org/10.1016/S0039-6028(01)01924-0.

[111] D. Fujita et al. “STM induced photon emission from adsorbed porphyrin molecules on a Cu(100) surface in ultrahigh vacuum”. In: *Surface Science* 454-456 (2000), pp. 1021–1025. DOI: https://doi.org/10.1016/S0039-6028(00)00274-0.

[112] F. Geng et al. “Modulation of nanocavity plasmonic emission by local molecular states of C60 on Au(111)”. In: *Opt. Express* 20.24 (Nov. 2012), pp. 26725–26735. DOI: 10.1364/OE.20.026725.

[113] Z.-C. Dong et al. “Tunneling electron induced luminescence from monolayered Cu-TBP porphyrin molecules adsorbed on Cu(100)”. In: *Thin Solid Films* 438-439 (2003). The 5th International Conference on Nano-Molecular Electronics, pp. 262–267. DOI: https://doi.org/10.1016/S0040-6090(03)00797-1.

[114] A. Yu et al. “Visualization of Nanoplasmonic Coupling to Molecular Orbital in Light Emission Induced by Tunneling Electrons”. In: *Nano Letters* 18.5 (2018). PMID: 29660286, pp. 3076–3080. DOI: 10.1021/acs.nanolett.8b00613. eprint: https://doi.org/10.1021/acs.nanolett.8b00613.

[115] X. H. Qiu, G. V. Nazin, and W. Ho. “Vibrationally Resolved Fluorescence Excited with Submolecular Precision”. In: *Science* 299.5606 (2003), pp. 542–546. DOI: 10.1126/science.1078675. eprint: https://www.science.org/doi/pdf/10.1126/science.1078675.

[116] Y. Zhang et al. “Sub-nanometre control of the coherent interaction between a single molecule and a plasmonic nanocavity”. In: *Nature Communications* 8 (2017). Cited by: 116; All Open Access, Gold Open Access, Green Open Access. DOI: 10.1038/ncomms15225.

[117] J. Kröger et al. “Fano Description of Single-Hydrocarbon Fluorescence Excited by a Scanning Tunneling Microscope”. In: *Nano Letters* 18.6 (2018). PMID: 29719154, pp. 3407–3413. DOI: 10.1021/acs.nanolett.8b00304. eprint: https://doi.org/10.1021/acs.nanolett.8b00304.

[118] Y. Zhang et al. “Visualizing coherent intermolecular dipole–dipole coupling in real space”. In: *Nature* 531.7596 (Mar. 2016), pp. 623–627. DOI: 10.1038/nature17428.

[119] M. C. Chong et al. “Narrow-Line Single-Molecule Transducer between Electronic Circuits and Surface Plasmons”. In: *Phys. Rev. Lett.* 116 (3 Jan. 2016), p. 036802. DOI: 10.1103/PhysRevLett.116.036802.

[120] Z. C. Dong et al. “Generation of molecular hot electroluminescence by resonant nanocavity plasmons”. In: *Nature Photonics* 4.1 (Dec. 2009), pp. 50–54. DOI: 10.1038/nphoton.2009.257.

[121] C. Große et al. “Nanoscale Imaging of Charge Carrier and Exciton Trapping at Structural Defects in Organic Semiconductors”. In: *Nano Letters* 16.3 (2016). PMID: 26871739, pp. 2084–2089. DOI: 10.1021/acs.nanolett.6b00190. eprint: https://doi.org/10.1021/acs.nanolett.6b00190.

[122] P. Merino et al. “Exciton dynamics of C60-based single-photon emitters explored by Hanbury Brown–Twiss scanning tunnelling microscopy”. In: *Nature Communications* 6.1 (Sept. 2015). DOI: 10.1038/ncomms9461.

[123] E. Ćavar et al. “Fluorescence and Phosphorescence from Individual C_{60} Molecules Excited by Local Electron Tunneling”. In: *Phys. Rev. Lett.* 95 (19 Nov. 2005), p. 196102. DOI: 10.1103/PhysRevLett.95.196102.

[124] L. Zhang et al. “Electrically driven single-photon emission from an isolated single molecule”. English. In: *NATURE COMMUNICATIONS* 8 (Sept. 2017). DOI: 10.1038/s41467-017-00681-7.

[125] C. Chen et al. “Viewing the Interior of a Single Molecule: Vibronically Resolved Photon Imaging at Submolecular Resolution”. In: *Phys. Rev. Lett.* 105 (21 Nov. 2010), p. 217402. DOI: 10.1103/PhysRevLett.105.217402.

[126] M. C. Chong et al. “Ordinary and Hot Electroluminescence from Single-Molecule Devices: Controlling the Emission Color by Chemical Engineering”. In: *Nano Letters* 16.10 (2016). PMID: 27652517, pp. 6480–6484. DOI: 10.1021/acs.nanolett.6b02997. eprint: https://doi.org/10.1021/acs.nanolett.6b02997.

[127] D. Pommier et al. “Inelastic tunneling-induced luminescence of excitons in monolayer MoSe2 and WS2”. In: *Nanophotonics of 2D Materials, N2D 2020*. Donostia-San Sebastián, Spain, July 2020. eprint: https://hal.archives-ouvertes.fr/hal-03334474.

[128] B. Schuler et al. “Electrically driven photon emission from individual atomic defects in monolayer WS₂”. In: *Science Advances* 6.38 (2020), eabb5988. DOI: 10.1126/sciadv.abb5988.

[129] D. D. D. Ma et al. “Scanning Tunneling Microscope Excited Cathodoluminescence from ZnS Nanowires”. In: *Nano Letters* 6.5 (2006). PMID: 16683827, pp. 926–929. DOI: 10.1021/nl052507j. eprint: https://doi.org/10.1021/nl052507j.

[130] K. Watanabe, Y. Nakamura, and M. Ichikawa. “Measurements of local optical properties of Si-doped GaAs (110) surfaces using modulation scanning tunneling microscope cathodoluminescence spectroscopy”. In: *Journal of Vacuum Science & Technology B: Microelectronics and Nanometer Structures Processing, Measurement, and Phenomena* 26.1 (2008), pp. 195–200. DOI: 10.1116/1.2830640. eprint: https://avs.scitation.org/doi/pdf/10.1116/1.2830640.

[131] K. Watanabe et al. “Development of Novel System Combining Scanning Tunneling Microscope-Based Cathodoluminescence and Electroluminescence Nanospectroscopies”. In: *Japanese Journal of Applied Physics* 50.8 (Aug. 2011), 08LB18. DOI: 10.1143/jjap.50.08lb18.

[132] K. Watanabe, Y. Nakamura, and M. Ichikawa. “Conductive optical-fiber STM probe for local excitation and collection of cathodoluminescence at semiconductor surfaces”. In: *Opt. Express* 21.16 (Aug. 2013), pp. 19261–19268. DOI: 10.1364/OE.21.019261.

[133] W. A. de Heer, A. Châtelain, and D. Ugarte. “A Carbon Nanotube Field-Emission Electron Source”. In: *Science* 270.5239 (1995), pp. 1179–1180. DOI: 10.1126/science.270.5239.1179. eprint: https://www.science.org/doi/pdf/10.1126/science.270.5239.1179.

[134] F. Stavale, N. Nilius, and H.-J. Freund. “Cathodoluminescence of near-surface centres in Cr-doped MgO(001) thin films probed by scanning tunnelling microscopy”. In: *New Journal of Physics* 14.3 (Mar. 2012), p. 033006. DOI: 10.1088/1367-2630/14/3/033006.

[135] F. Stavale et al. “Morphology and Luminescence of ZnO Films Grown on a Au(111) Support”. In: *The Journal of Physical Chemistry C* 117.20 (2013), pp. 10552–10557. DOI: 10.1021/jp401939x. eprint: https://doi.org/10.1021/jp401939x.

[136] F. Stavale, N. Nilius, and H.-J. Freund. “STM Luminescence Spectroscopy of Intrinsic Defects in ZnO(0001) Thin Films”. In: *The Journal of Physical Chemistry Letters* 4.22 (2013), pp. 3972–3976. DOI: 10.1021/jz401823c. eprint: https://doi.org/10.1021/jz401823c.

[137] Y.-J. Cho et al. "Hexagonal Boron Nitride Tunnel Barriers Grown on Graphite by High Temperature Molecular Beam Epitaxy". In: *Scientific Reports* 6.1 (Sept. 2016). DOI: 10.1038/srep34474.

[138] R. Berndt, R. R. Schlittler, and J. K. Gimzewski. "Photon emission scanning tunneling microscope". In: *Journal of Vacuum Science & Technology B: Microelectronics and Nanometer Structures Processing, Measurement, and Phenomena* 9.2 (1991), pp. 573–577. DOI: 10.1116/1.585571. eprint: https://avs.scitation.org/doi/pdf/10.1116/1.585571.

[139] K. Edelmann et al. "Light collection from a low-temperature scanning tunneling microscope using integrated mirror tips fabricated by direct laser writing". In: *Review of Scientific Instruments* 89.12 (2018), p. 123107. DOI: 10.1063/1.5053882. eprint: https://doi.org/10.1063/1.5053882.

[140] E. Le Moal et al. "An Electrically Excited Nanoscale Light Source with Active Angular Control of the Emitted Light". In: *Nano Letters* 13.9 (2013). PMID: 23927672, pp. 4198–4205. DOI: 10.1021/nl401874m. eprint: https://doi.org/10.1021/nl401874m.

[141] J. G. Keizer, J. K. Garleff, and P. M. Koenraad. "Simple and efficient scanning tunneling luminescence detection at low-temperature". In: *Review of Scientific Instruments* 80.12 (2009), p. 123704. DOI: 10.1063/1.3274675. eprint: https://doi.org/10.1063/1.3274675.

[142] G. Hoffmann, J. Kröger, and R. Berndt. "Color imaging with a low temperature scanning tunneling microscope". In: *Review of Scientific Instruments* 73.2 (2002), pp. 305–309. DOI: 10.1063/1.1433946. eprint: https://doi.org/10.1063/1.1433946.

[143] L. G. Chen et al. "Note: Optical optimization for ultrasensitive photon mapping with submolecular resolution by scanning tunneling microscope induced luminescence". In: *Review of Scientific Instruments* 84.6 (2013), p. 066106. DOI: 10.1063/1.4811200. eprint: https://doi.org/10.1063/1.4811200.

[144] H.-J. Freund et al. "Innovative Measurement Techniques in Surface Science". In: *ChemPhysChem* 12.1 (2011), pp. 79–87. DOI: 10.1002/cphc.201000812. eprint: https://chemistry-europe.onlinelibrary.wiley.com/doi/pdf/10.1002/cphc.201000812.

[145] Y. Khang et al. "Low temperature ultrahigh vacuum cross-sectional scanning tunneling microscope for luminescence measurements". In: *Review of Scientific Instruments* 70.12 (1999), pp. 4595–4599. DOI: 10.1063/1.1150118. eprint: https://doi.org/10.1063/1.1150118.

[146] Y. Suzuki, H. Minoda, and N. Yamamoto. "STM light emission from Ag/Si(111)". In: *Surface Science* 438.1 (1999), pp. 297–304. DOI: https://doi.org/10.1016/S0039-6028(99)00594-4.

[147] N. J. Watkins et al. "Fiber optic light collection system for scanning-tunneling-microscope-induced light emission". In: *Review of Scientific Instruments* 78.5 (2007), p. 053707. DOI: 10.1063/1.2740479. eprint: https://doi.org/10.1063/1.2740479.

[148] K. L. Seyler et al. "Signatures of moiré-trapped valley excitons in MoSe2/WSe2 heterobilayers". In: *Nature* 567.7746 (Feb. 2019), pp. 66–70. DOI: 10.1038/s41586-019-0957-1.

[149] R. E. Prange. "Tunneling from a Many-Particle Point of View". In: *Phys. Rev.* 131 (3 Aug. 1963), pp. 1083–1086. DOI: 10.1103/PhysRev.131.1083.

[150] J. J. Sakurai and J. Napolitano. *Modern Quantum Mechanics*. 2nd ed. Cambridge University Press, 2017. DOI: 10.1017/9781108499996.

[151] J. Tersoff and D. R. Hamann. “Theory and Application for the Scanning Tunneling Microscope”. In: *Phys. Rev. Lett.* 50 (25 June 1983), pp. 1998–2001. DOI: 10.1103/PhysRevLett.50.1998.

[152] G. K. Pang, K. Baba-Kishi, and A. Patel. “Topographic and phase-contrast imaging in atomic force microscopy”. In: *Ultramicroscopy* 81.2 (2000), pp. 35–40. DOI: https://doi.org/10.1016/S0304-3991(99)00164-3.

[153] G. Pettinari, A. Polimeni, and M. Capizzi. “Photoluminescence: A Tool for Investigating Optical, Electronic, and Structural Properties of Semiconductors”. In: *Semiconductor Research: Experimental Techniques*. Ed. by A. Patane and N. Balkan. Berlin, Heidelberg: Springer Berlin Heidelberg, 2012, pp. 125–170. DOI: 10.1007/978-3-642-23351-7_5.

[154] “Raman Spectroscopy: From Graphite to sp2 Nanocarbons”. In: *Raman Spectroscopy in Graphene Related Systems*. John Wiley Sons, Ltd, 2011. Chap. 4, pp. 73–101. DOI: https://doi.org/10.1002/9783527632695.ch4. eprint: https://onlinelibrary.wiley.com/doi/pdf/10.1002/9783527632695.ch4.

Appendices

Appendix A

Quantum tunneling and Bardeen's theory in the context of STM

A.1 Quantum tunneling and transmission coefficient

Let us discuss the solution to the Schrödinger equation for an electron traveling towards a rectangular potential barrier $V(z)$:

$$V(z) = \begin{cases} V_0 \text{ if } 0 \leq z \leq d \\ 0 \text{ if } z < 0 \text{ and } z > d, \end{cases} \tag{A.1}$$

The wavefunction of the electron must satisfy the time-independent Schrödinger equation:

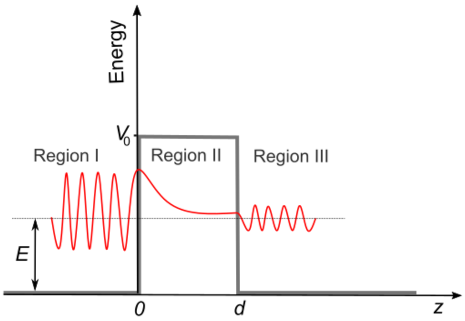

Figure A.1: One-dimensional model of quantum tunneling through a rectangular potential barrier.

$$\left[-\frac{\hbar^2}{2m_e}\frac{d^2}{dz^2} + V(z) \right] \psi(z) = E\psi(z), \ \forall \ z, \tag{A.2}$$

Where m_e is the mass of the electron, $\hbar$ is the Plank's constant, and E is the particle's energy.

- **Region ① and ③ ($z < 0$ and $z > d$):** outside the barrier the electron is free since $V(z) = 0$, then we expect solutions like $\psi(z) \propto e^{\pm ikz}$, where $k = k_1 = k_3 = \sqrt{2m_e E/\hbar^2}$. The ± sing indicates the direction of propagation of the wavefunction, towards $+z$ or $-z$, respectively,
- **Region ② ($0 \leq z \leq d$):** in this case, if $E < V_0$, equation A.2 can be written as:

$$\left[\frac{d^2}{dz^2} - \kappa^2\right]\psi(z) = E\psi(z), \text{ where } \kappa^2 = \frac{2m_e}{\hbar^2}(V_0 - E), \tag{A.3}$$

which leads to real wavefunctions $\psi(z) \propto e^{\pm\kappa z}$ inside the barrier.

Now, considering the initial wavefunction traveling from region ① to ③, we expect to have partial reflections of $\psi(z)$ on the walls of the barrier ($z = 0$ and $z = d$). Thus, we need to take into account components of the wavefunction traveling towards the $-z$ direction for $z < d$, then the general solutions for the wavefunctions are:

$$\begin{cases} \text{Region ①: } \psi_1(z) = Ae^{ikz} + Be^{-ikz} \ \forall \ z < 0 \\ \text{Region ②: } \psi_2(z) = Ce^{-\kappa z} + De^{\kappa z} \ \forall \ 0 \leq z \leq d \\ \text{Region ③: } \psi_3(z) = Fe^{ikz} \ \forall \ z > d, \end{cases} \tag{A.4}$$

The following boundary conditions are necessary to guarantee the continuity of the wavefunction at $z = 0$ and $z = d$:

$$\begin{cases} \psi_1(0) = \psi_2(0) \text{ and } \frac{d}{dz}\psi_1(z)\big|_{\bar{z}=0} = \frac{d}{dz}\psi_2(z)\big|_{\bar{z}=0} \\ \\ \psi_2(d) = \psi_3(d) \text{ and } \frac{d}{dz}\psi_2(z)\big|_{\bar{z}=d} = \frac{d}{dz}\psi_3(z)\big|_{\bar{z}=d}, \end{cases} \tag{A.5}$$

which applied on the wavefunctions in equations. A.4 result in:

$$\begin{cases} A + B = C + D \\ ik(A - B) = \kappa(D - C) \\ Ce^{-\kappa d} + De^{\kappa d} = Fe^{ikd} \\ \kappa(De^{\kappa d} - Ce^{-\kappa d}) = ikFe^{ikd} \end{cases} \Rightarrow \begin{cases} 2ikA = (ik - \kappa)C + (ik + \kappa)D \\ 2ikB = (ik + \kappa)C + (ik - \kappa)D \\ 2D\kappa e^{\kappa d} = (\kappa + ik)Fe^{ikd} \\ 2C\kappa e^{-\kappa d} = (\kappa - ik)Fe^{ikd}, \end{cases} \tag{A.6}$$

from these equations, we can find the constants A, B, C, and F.

We are interested in obtaining the probability of finding the electron at the end of the barrier, i. e., in region ③. The transmission coefficient, T, gives this probability. For calculating T we need to know what is the flux density of particles, that in quantum mechanics is described as a *probability current density*, $\mathbf{j}(\mathbf{r}, t)$:

$$\mathbf{j}(\mathbf{r}, t) = -\frac{i\hbar}{2m_e}[\Psi^*(\mathbf{r}, t)\nabla\Psi(\mathbf{r}, t) - \Psi(\mathbf{r}, t)\nabla\Psi^*(\mathbf{r}, t)], \tag{A.7}$$

the ratio between the transmitted current density and the incident current density defines the transmission coefficient of the barrier. Taking, in our 1D problem, the incident and transmitted components of the wavefunction as being $\psi_{\text{inc}}(z) = Ae^{ikz}$ and $\psi_{\text{trans}}(z) = Fe^{ikz}$, respectively, we have:

$$T = \frac{j_{\text{trans}}}{j_{\text{inc}}} = \frac{\psi^*_{\text{trans}}\frac{d}{dz}\psi_{\text{trans}} - \psi_{\text{trans}}\frac{d}{dz}\psi^*_{\text{trans}}}{\psi^*_{\text{inc}}\frac{d}{dz}\psi_{\text{inc}} - \psi_{\text{inc}}\frac{d}{dz}\psi^*_{\text{inc}}} = \frac{|F|^2}{|A|^2}, \tag{A.8}$$

if we know the constants A and F, the coefficient T is determined. Equations in A.6 can be used to solve F in relation to A:

$$\begin{aligned} 4ik\kappa A &= [-(ik-\kappa)^2 e^{\kappa d} + (ik+\kappa)^2 e^{-\kappa d}]Fe^{ikd} \\ &= [2ik\kappa(e^{\kappa d} + e^{\kappa d}) + (k^2-\kappa^2)(e^{\kappa d} - e^{\kappa d})]Fe^{ikd} \\ &= [4ik\kappa\cosh{(\kappa d)} + 2(k^2-\kappa^2)\sinh{(\kappa d)}]Fe^{ikd}, \end{aligned} \tag{A.9}$$

Therefore, we have found that:

$$T = \frac{4k^2\kappa^2}{(k^2-\kappa^2)^2\sinh^2{(\kappa d)} + 4k^2\kappa^2\cosh^2{(\kappa d)}} = \frac{4k^2\kappa^2}{(k^2+\kappa^2)^2\sinh^2{(\kappa d)} + 4k^2\kappa^2}, \tag{A.10}$$

For a strong attenuation barrier, $\kappa d \gg 1$, in this case, $\sinh^2{(\kappa d)} \approx e^{2\kappa d}/4$ and the transmission factor is:

$$T \approx \frac{16k^2\kappa^2}{((k^2+\kappa^2)^2)}e^{-2\kappa d} = \frac{16E(V_0-E)}{V_0^2}e^{-2d\sqrt{2m_e(V_0-E)/\hbar^2}}, \tag{A.11}$$

This expression shows an exponential dependence of T on the barrier width d, which is characteristic of quantum tunneling for any shape of the tunneling barrier.

A.2 Bardeen's theory applied to tunneling in STM

Here we will follow the Bardeen theory for tunneling to find an expression that describes the tunneling current in STM. In Bardeen's formalism, instead of solving the Schrodinger equation for the combined tip+sample system, we first determine the electronic states for electrons in the tip and the sample by solving the Schrodinger equation of each isolated sub-system (tip and sample) separately. After that, the transition rate of electrons from one electrode to another is calculated using first-order time-dependent perturbation theory [92, 149]. [1]

Let us consider that the STM tip is initially far away from the sample surface. We can treat the tip and the sample as individual systems in this case. Therefore, the wavefunctions $\Psi^T_\alpha(\mathbf{r},t)$ and $\Phi^S_\beta(\mathbf{r},t)$, that describe the electrons in the states α and β of the tip and the sample, respectively; satisfy the corresponding Schrodinger equation:

$$\begin{cases} H_T\Psi^T_\alpha(\mathbf{r},t) = \big[-\frac{\hbar^2}{2m_e}\frac{\partial^2}{\partial z^2} + U_T(z)\big]\Psi^T_\alpha(\mathbf{r},t) = i\hbar\frac{\partial}{\partial t}\Psi^T_\alpha(\mathbf{r},t) \ \forall \ \mathbf{r} \in \text{tip} \\ \\ H_s\Phi^T_\alpha(\mathbf{r},t) = \big[-\frac{\hbar^2}{2m_e}\frac{\partial^2}{\partial z^2} + U_S(z)\big]\Phi^T_\alpha(\mathbf{r},t) = i\hbar\frac{\partial}{\partial t}\Phi^T_\alpha(\mathbf{r},t) \ \forall \ \mathbf{r} \in \text{sample}, \end{cases} \tag{A.12}$$

---

[1] We will see that the perturbative theory of Bardeen is different from the typical perturbation theory that we can find in quantum mechanics textbook [150]

where U_T and U_S and the tip and sample potentials, respectively. Since H_T and H_S are time-independent, we can express the wavefunction as:

$$\begin{cases} \Psi^T_\alpha(\mathbf{r},t) = \psi_\alpha(\mathbf{r})e^{-iE_\alpha t/\hbar} \\ \\ \Phi^S_\alpha(\mathbf{r},t) = \phi_\beta(\mathbf{r})e^{-iE_\beta t/\hbar}, \end{cases} \tag{A.13}$$

where $\psi_\alpha(\mathbf{r})$, $\phi_\beta(\mathbf{r})$, and $E_{\alpha,\beta}$ are solutions of the time-independent Schrödinger equation:

$$\begin{cases} H_T\psi_\alpha(\mathbf{r}) = \big[-\frac{\hbar^2}{2m_e}\frac{\partial^2}{\partial z^2} + U_T(z)\big]\psi_\alpha(\mathbf{r}) = E_\alpha\psi_\alpha(\mathbf{r}) \ \ \forall \ \ \mathbf{r} \in \text{tip} \\ \\ H_S\phi_\beta(\mathbf{r}) = \big[-\frac{\hbar^2}{2m_e}\frac{\partial^2}{\partial z^2} + U_S(z)\big]\phi_\beta(\mathbf{r}) = E_\beta\phi_\beta(\mathbf{r}) \ \ \forall \ \ \mathbf{r} \in \text{tip}, \end{cases} \tag{A.14}$$

For example, if we consider for the tip equation in A.14 that $V_T(z) = V_0\Theta(z)$, being V_0 constant and $\Theta(z)$ the Heaviside function, we will find wavefunctions[2] with $\psi_\alpha(z) \propto e^{ik_\alpha z}$ for $z < 0$ and $\psi_\alpha(z) \propto e^{-\kappa_\alpha z}$ for $z > 0$. The same is expected for ϕ_β if a similar potential shape is considered in the sample.

Once the electrodes (tip and sample surface) are approached one another until coupled in a combined system tip+sample, we have the wavefunction $\Psi(z,t)$ that describes electrons in this new system must satisfy the following Schrödinger equation:

$$H\Psi(z,t) = \left[-\frac{\hbar^2}{2m_e}\frac{\partial^2}{\partial z^2} + U_T(z) + U_S(z)\right]\Psi(z),t) = i\hbar\frac{\partial}{\partial t}\Psi(z,t) \ \ \forall \ \ z \in \text{tip-sample gap}, \tag{A.15}$$

Note that $\psi_\alpha(z) = \langle z|\psi_\alpha\rangle$ and $\phi_\beta(z) = \langle z|\phi_\beta\rangle$ are eigenfunctions of H_T and H_s, respectively; but these are not eigenfunctions of H for the coupled system. An important point of the Bardeen's theory for tunneling is to assume the sets $\{\psi_\alpha(z)\}$ and $\{\phi_\beta(z)\}$ as being approximately orthonormal:

$$\langle\psi_\alpha|\phi_\beta\rangle = \langle\psi_\alpha|\Big(\int dz|z\rangle\langle z|\Big)|\phi_\beta\rangle = \int dz\psi^*_\alpha(z)\phi_\beta(z) \approx 0, \tag{A.16}$$

additionally, Bardeen saw that $\psi_\alpha(z)$ and $\phi_\beta(z)$ seem to be good solutions for the wavefunctions inside the barrier ($\propto e^{\mp\kappa z}$ for $0 \le z \le d$), its drops to zero. Therefore, considering the tunneling as a single-electron process, what Bardeen proposed was to take the time-depended solutions in equation A.15 as a linear combination of the tip and sample states. Meaning the wavefunction that describes the transfer process of an electron from an initial tip state ψ_α (at $t = 0$) with energy E_α to one of the possible final states ϕ_β (at $t > 0$) in the sample with energy E_β can be expressed as:

$$\Psi(\mathbf{r},t) = \Psi^T_\alpha(\mathbf{r},t) + \sum_\beta c_\beta(t)\Phi^S_\beta(\mathbf{r},t) = \psi_\alpha(\mathbf{r})e^{-iE_\alpha t/\hbar} + \sum_\beta c_\beta(t)\phi_\beta(\mathbf{r})e^{-iE_\beta t/\hbar}, \tag{A.17}$$

---

[2] remember that $\psi_\alpha(\mathbf{r}) = \psi_\alpha(x)\psi_\alpha(y)\psi_\alpha(z)$

it's easy to see that if $\Psi(\mathbf{r}, t=0) = \psi_\alpha(\mathbf{r})$, $c_\beta(0) = 0 \ \forall \ \beta$.

Equation A.17 tells us that the tunneling process corresponds to a small perturbation of the initial state. This is valid only for weak coupling (tip-sample distance $\approx$4Å), where the final state will almost be the same that the initial state plus a sum over the stationary states in the sample with $c_\beta(t)$ representing a probability amplitude and, of course, $|c_\beta(t)|^2$ gives us the probability of the electron tunnels or be transferred to the sample state $\Phi^S_\beta(\mathbf{r}, t)$. By evaluating equation A.17 in A.15, we have:

$$\left[-\tfrac{\hbar^2}{2m_e}\tfrac{\partial^2}{\partial z^2} + U_T + U_S\right]\left[\psi_\alpha(\mathbf{r})e^{-iE_\alpha t/\hbar} + \textstyle\sum_\beta c_\beta(t)\phi_\beta(\mathbf{r})e^{-iE_\beta t/\hbar}\right] = E_\alpha\psi_\alpha(\mathbf{r})e^{-iE_\alpha t/\hbar}$$

$$+U_S\psi_\alpha(\mathbf{r})e^{-iE_\alpha t/\hbar} + \textstyle\sum_\beta c_\beta(t)E_\beta\phi_\beta(\mathbf{r})e^{-iE_\beta t/\hbar} + U_T\sum_\beta c_\beta(t)(\mathbf{r})e^{-iE_\beta t/\hbar} = i\hbar\tfrac{\partial}{\partial t}\Psi(\mathbf{r}, t)$$

$$= E_\alpha\psi_\alpha(\mathbf{r})e^{-iE_\alpha t/\hbar} + i\hbar\textstyle\sum_\beta(\tfrac{d}{dt}c_\beta(t))\phi_\beta(\mathbf{r})e^{-iE_\beta t/\hbar} + \sum_\beta c_\beta(t)E_\beta\phi_\beta(\mathbf{r})e^{-iE_\beta t/\hbar},$$

which is reduced to:

$$i\hbar\sum_\beta\left(\frac{d}{dt}c_\beta(t)\right)\langle z|\phi_\beta\rangle e^{-iE_\beta t/\hbar} = U_S\langle z|\psi_\alpha\rangle e^{-iE_\alpha t/\hbar} + U_T\sum_\beta c_\beta(t)\langle z|\phi_\beta\rangle e^{-iE_\beta t/\hbar}, \quad \text{(A.18)}$$

multiplying equation A.18 by $\Phi^{*S}_{\beta'}(z, t) = \langle\phi_{\beta'}|z\rangle e^{iE_{\beta'}t/\hbar}$ and manipulating a little bit the equation we will find:

$$i\hbar\frac{d}{dt}c_\beta(t) = \langle\phi_\beta|U_S|\psi_\alpha\rangle e^{-i(E_\alpha - E_\beta)t/\hbar} + \sum_{\beta'} c_{\beta'}(t)\langle\phi_\beta|U_T|\phi_{\beta'}\rangle e^{-i(E_{\beta'} - E_\beta)t/\hbar}, \qquad \text{(A.19)}$$

Considering U_s as a perturbation of the initial state in the tip, we can treat the first term on the RHS of equation A.19 as the first-order preservative term, and the second ones can be neglected. Then:

$$i\hbar\frac{d}{dt}c_\beta(t) = \langle\phi_\beta|U_S|\psi_\alpha\rangle e^{-i(E_\alpha - E_\beta)t/\hbar} \Rightarrow c_\beta(t) = M_{\beta\alpha}\frac{e^{-i(E_\alpha - E_\beta)t/\hbar} - 1}{E_\alpha - E_\beta}, \qquad \text{(A.20)}$$

where $M_{\beta\alpha} \equiv \langle\phi_\beta|U_S|\psi_\alpha\rangle$ is known as the *tunneling matrix element*. From equation A.20 we obtain:

$$|c_\beta(t)|^2 = |M_{\beta\alpha}|^2\frac{4\sin^2(\Delta E_{\alpha\beta}t/2\hbar)}{\Delta E^2_{\alpha\beta}}, \qquad \text{(A.21)}$$

with $\Delta E_{\alpha\beta} = E_\alpha - E_\beta$. If $\Delta t = t - 0$ is the time interval for the electron transition from the tip to the sample, we have that any transition in the tunneling process must follow the uncertainty principle $\Delta E_{\alpha\beta} \sim \hbar/\Delta t$. Furthermore, by plotting the function $g(\Delta E_{\alpha\beta}) = \sin^2(\Delta E_{\alpha\beta}t/2\hbar)/\Delta E^2_{\alpha\beta}$, it is possible to find out that $g(\Delta E_{\alpha\beta})$ has a maximum and dominant contribution at $\Delta E_{\alpha\beta} = 0$ (*elastic tunneling*) which leads to large tunneling time. Hence, $t \gg 2\hbar/\Delta E_{\alpha\beta}$ in $g(\Delta E_{\alpha\beta})$ defines a Dirac delta function[3] and the transition probability with energy conservation from a single tip state with energy E_α to a single sample state with energy E_β can be written as:

$$P_{\alpha\rightarrow\beta} = \frac{2\pi}{\hbar}|M_{\beta\alpha}|^2\delta(E_\alpha - E_\beta)t, \tag{A.22}$$

and the transition rate is given by:

$$W_{\alpha\rightarrow\beta=} = \frac{P_{\alpha\rightarrow\beta}}{t} = \frac{2\pi}{\hbar}|M_{\beta\alpha}|^2\delta(E_\alpha - E_\beta), \tag{A.23}$$

This expression is analogous to Fermi's golden rule obtained from first-order perturbation theory for a constant perturbative potential [150].

Now it is possible to write an expression for the tunneling current from equation A.23. For that, we need to consider: i) the current should be proportional to the elementary charge of the electron, e. ii) There are two possible spin states for the tunneling electron. iii) Electrons tunnel from occupied states in one electrode to unoccupied states in the other ones. The occupation probability is described by the Fermi-Dirac distribution $f(\epsilon) = [1 + \exp(-\epsilon/k_BT)]^{-1}$, where $\epsilon = E - E_F$ is the energy measured with respect to the Fermi energy E_F and k_B is the Boltzmann constant. Hence, $f(\epsilon)$ gives the occupation probability of the state with energy E, while $[1 - f(\epsilon)]$ is the probability that the state is unoccupied. Considering all these elements, we can express the total current for electrons tunneling in thermal equilibrium from the tip to the sample as:

$$I_{T\rightarrow S} = \frac{4\pi e}{\hbar}\sum_{\alpha,\beta}|M_{\beta\alpha}|^2 f(E_\alpha - E_F^T)[1 - f(E_\beta - E_F^S)]\delta(E_\alpha - E_\beta), \tag{A.24}$$

there is also a fraction of electron tunneling in the opposite direction; hence we can procedure analogously and write:

$$I_{S\rightarrow T} = \frac{4\pi e}{\hbar}\sum_{\alpha,\beta}|M_{\alpha\beta}|^2 f(E_\beta - E_F^S)[1 - f(E_\alpha - E_F^T)]\delta(E_\alpha - E_\beta), \tag{A.25}$$

The difference between equation A.24 and A.25 results in the total net current:

$$I_t = \frac{4\pi e}{\hbar}\sum_{\alpha,\beta}|M_{\alpha\beta}|^2[f(E_\alpha - E_F^T) - f(E_\beta - E_F^S)]\delta(E_\alpha - E_\beta), \tag{A.26}$$

To introduce the sample bias voltage, V, applied in the STM junction, we can define the Fermi's levels as $E_F^S = E_F$ and $E_F^T = E_F + eV$:

$$I_t = \frac{4\pi e}{\hbar}\sum_{\alpha,\beta}|M_{\alpha\beta}|^2[f(E_\alpha - E_F - eV) - f(E_\beta - E_F)]\delta(E_\alpha - E_\beta), \tag{A.27}$$

---

[3] Defined as: $\delta(x) = \lim_{\eta\rightarrow\infty}\frac{1}{\pi}\frac{\sin^2(\eta x)}{\eta x^2}$

this is the general expression that describes the tunneling current in STM. In practice, some approximations are made in equation A.27

A.2.1 Tunneling matrix element and the Tersoff-Hamann approach

The complete determination of the tunneling current requires to know what is the tunneling matrix element, which was defined above as:

$$M_{\beta\alpha} = \langle\phi_\beta|U_S|\psi_\alpha\rangle = \langle\phi_\beta|U_S\bigg(\int dr^3|\mathbf{r}\rangle\langle\mathbf{r}|\bigg)|\psi_\alpha\rangle = \int_{\text{sample}} dr^3\phi_\beta(\mathbf{r})^*U_S\psi_\alpha(\mathbf{r}), \quad \text{(A.28)}$$

where, according to A.14, $U_S = [E_\beta + (\hbar^2/2m_e)\nabla^2]$. Using the condition for elastic tunneling that we have found and the fact that in the sample side $U_T = 0$, equation A.28 shows that:

$$M_{\beta\alpha} = -\frac{\hbar^2}{2m_e}\int_{\text{sample}} dr^3\bigg[\phi_\beta^*\nabla^2\psi_\alpha - \psi_\alpha\nabla^2\phi_\beta^*\bigg], \quad \text{(A.29)}$$

which can be written as an integral over any surface in the barrier separating the two electrodes:

$$M_{\beta\alpha} = -\frac{\hbar^2}{2m_e}\int d\mathbf{S}\cdot\bigg[\phi_\beta^*\nabla\psi_\alpha - \psi_\alpha\nabla\phi_\beta^*\bigg], \quad \text{(A.30)}$$

this expression shows the connection between $M_{\beta\alpha}$ and the probability current density in equation A.7. Both quantities are related to the same thing, i.e. the transmission or tunneling probability between two electronic states with equal energies in separated systems.

Now, equation A.30 indicates that we can obtain $M_{\beta\alpha}$ from the tip and sample wavefunctions of the unperturbed systems, which are solutions to the equations in A.14. Here is where the approach adopted by Tersoff and Hamann takes place [151]. Since it is hard to know what is the atomic structure of the STM tip, they considered the simplest model for the tip probe, which is a tip with locally spherical symmetry, meaning that the tunneling matrix element in equation A.30 can be evaluated with s-type tip wavefunctions [92]. In the following, we will use the *Green's functions method* for evaluating the tunneling matrix elements with $s-$wave tip states. The final results will be similar to those obtained by Tersoff and Hamann in the original paper.

The Schrödinger equation for the tip wavefunctions can be written as:

$$(\nabla^2 - \kappa^2)\psi_s(\mathbf{r}) = 0, \quad \text{(A.31)}$$

with $\kappa = \sqrt{2m_e\phi/\hbar^2}$ the decay constant and ϕ the work function. Of course, we have a similar equation for the sample states, and for simplicity, we will assume similar work functions for the tip and the sample. equation A.31 is a *Poisson*-like equation, very common in many physical systems, its solution can be given in terms of the Green's function $G(\mathbf{r}-\mathbf{r_0})$, which is a solution of:

$$(\nabla^2-\kappa^2)G(\mathbf{r}-\mathbf{r_0})=-\delta(\mathbf{r}-\mathbf{r_0})\Rightarrow G(\mathbf{r}-\mathbf{r_0})=\frac{1}{4\pi}\frac{e^{-\kappa|\mathbf{r}-\mathbf{r_0}|}}{|\mathbf{r}-\mathbf{r_0}|}, \tag{A.32}$$

On the other hand, the wavefunctions of the atomic orbitals are formed by radial and angular components. The radial part can be written in terms of the spherical modified Bessel functions, while the angular part by spherical-harmonic functions.[4] In particular, for s-wave tip wavefunction, the Green's function can be expressed in terms of the spherical modified Bessel function of the second kind, $k_0=k(\kappa\rho)=e^{-\kappa\rho}/\kappa\rho$:

$$G(\mathbf{r}-\mathbf{r_0})=\frac{1}{4\pi}\frac{e^{-\kappa|\mathbf{r}-\mathbf{r_0}|}}{|\mathbf{r}-\mathbf{r_0}|}=\frac{\kappa}{4\pi}k_0 \tag{A.33}$$

where we denote $\rho=|\mathbf{r}-\mathbf{r_0}|$. Then, the s-type wavefunction for the tip is:

$$\psi_s(\mathbf{r})=C'G(\mathbf{r}-\mathbf{r_0}), \tag{A.34}$$

being C' a constant, and the center of the apex atom is described by $\mathbf{r}_0$. We can use this wavefunction for evaluating the tunneling matrix elements:

$$\begin{aligned} M_{\beta\alpha} &= -\tfrac{\hbar^2C'}{2m_e}\int dr^3\left[\phi_\beta^*\nabla^2G(\mathbf{r}-\mathbf{r_0})-G(\mathbf{r}-\mathbf{r_0})\nabla^2\phi_\beta^*\right] \\ &= -\tfrac{\hbar^2C'}{2m_e}\int dr^3\left\{\phi_\beta^*[\kappa^2G(\mathbf{r}-\mathbf{r_0})-\delta(\mathbf{r}-\mathbf{r_0})]-G(\mathbf{r}-\mathbf{r_0})\kappa^2\phi_\beta^*\right\} \\ &= \tfrac{\hbar^2C'}{2m_e}\int dr^3\phi_\beta^*(\mathbf{r})\delta(\mathbf{r}-\mathbf{r_0})=\tfrac{\hbar^2C'}{2m_e}\phi_\beta^*(\mathbf{r}_0), \end{aligned} \tag{A.35}$$

the tunneling matrix element depends on the sample wavefunction at the position where the apex atom of the STM tip is centered. Then we have found that:

$$|M_{\beta\alpha}|^2=|M_{\alpha\beta}|^2\propto|\phi_\beta(\mathbf{r}_0)|^2, \tag{A.36}$$

Before introducing this result in the equation for the tunneling current, it is convenient to consider some approximations in equation A.27, which can be rewritten as[5]:

$$\begin{aligned} I_t &= \tfrac{4\pi e}{\hbar}\textstyle\sum_{\alpha,\beta}\int_{-\infty}^{\infty}d\epsilon\int_{-\infty}^{\infty}d\epsilon'|M|^2[f(\epsilon'-E_F-eV)-f(\epsilon-E_F)]\delta(\epsilon'-\epsilon)\delta(\epsilon'-E_\alpha)\delta(\epsilon-E_\beta) \\ &= \tfrac{4\pi e}{\hbar}\textstyle\sum_{\alpha,\beta}\int_{-\infty}^{\infty}d\epsilon|M(\epsilon)|^2[f(\epsilon-E_F-eV)-f(\epsilon-E_F)]\delta(\epsilon-E_\alpha)\delta(\epsilon-E_\beta), \end{aligned} \tag{A.37}$$

Since most of the STM experiments are performed at room temperature or cryogenic temperatures, the Fermi-Dirac distributions become in Heaviside functions and:

---

[4] See Appendix C, Julian Chen textbook [92].

[5] Using the following property for the Dirac's delta function: $\int_{-\infty}^{\infty}dx\Lambda(x)\delta(x-x_0)=\Lambda(x_0)$

$$f(\epsilon - E_F - eV) - f(\epsilon - E_F) \approx \Theta[(E_F + eV) - \epsilon] - \Theta(E_F - \epsilon) = 1 \ \forall \ E_F \leq \epsilon \leq E_F + eV,$$

which allows us to write:

$$I_t = \frac{4\pi e}{\hbar} \sum_{\alpha,\beta} \int_{E_F}^{E_F+eV} d\epsilon |M(\epsilon)|^2 \delta(\epsilon - E_\alpha)\delta(\epsilon - E_\beta) \propto \sum_{\alpha,\beta} \int_0^{eV} d\epsilon |M(\epsilon)|^2 \delta(\epsilon - E_\alpha)\delta(\epsilon - E_\beta), \tag{A.38}$$

where $E_F = 0$ has been taken as a reference point for energies.

In the Tersoff-Hamman approach, we found that the tunneling matrix element is constant (this is true only for small bias), then from equation A.38 we have:

$$I_t \propto \sum_{\alpha,\beta} \int_0^{eV} d\epsilon \delta(\epsilon - E_\alpha) |\phi_\beta(\mathbf{r}_0)|^2 \delta(\epsilon - E_\beta) = \int_0^{eV} d\epsilon \rho^{\text{tip}}(\epsilon - eV) \rho^{\text{sample}}(\epsilon, \mathbf{r}_0), \tag{A.39}$$

where $\rho^{\text{tip}}(\epsilon) \equiv \sum_\alpha \delta(\epsilon - E_\alpha)$ is the density of states (DOS) of the tip and the local density of states (LDOS) of the sample is defined as $\rho^{\text{sample}}(\epsilon, \mathbf{r}_0) \equiv \sum_\beta |\phi_\beta(\mathbf{r}_0)|^2 \delta(\epsilon - E_\beta)$. Moreover, the variable for the energy in the DOS of the tip has been rewritten relative to the Fermi's energy of the tip by changing ϵ by $\epsilon - eV$. It is worthwhile to note that equation A.39 is significant for the interpretation of STM images. The DOS of the tip is usually considered a constant. Therefore, we can see that an STM image represents the LDOS of the sample evaluated at the STM tip position and the energy ϵ around the Fermi's level.

Moreover, the behavior of the wavefunction of the sample inside the tunneling barrier is given by $\phi_\beta(\mathbf{r}_0) \propto \phi_\beta(z_0) = Ae^{-\kappa z}$, meaning that:

$$I_t \propto |\phi_\beta(z_0)|^2 \propto e^{-2\kappa(R+d)} \propto e^{-2\kappa d}, \tag{A.40}$$

which shows the exponential dependence on the tip-sample distance d expected for the tunneling current and responsible for the high spatial resolution in STM.

A.2.2 Semiclassical approximation

The Tersoff-Hamann approach is useful for understanding the meaning of the tunneling current and what we are measuring in an STM image. However, the approach has some limitations. On the one hand, the work functions of the tip and the sample are not necessarily equal, and on the other hand, the tunneling matrix element can depend on the energy. Therefore, we need a more general expression for the tunneling current. Going back to equation A.38, we have that [92, 94]:

$$I_t = \frac{4\pi e}{\hbar} \int_0^{eV} d\epsilon |M(\epsilon)|^2 \rho^{\text{tip}}(\epsilon - eV) \rho^{\text{sample}}(\epsilon), \tag{A.41}$$

in practice, the low-temperature approximation is still valid.

We can consider the semiclassical Wentzel, Kramers, and Brillouin (WKB) approximation of the solutions of the Schrödinger equation for a trapezoidal potential barrier and make the substitution of the tunneling matrix element for the corresponding transmission coefficient. i.e.:

$$I_t = \frac{4\pi e}{\hbar} \int_0^{eV} d\epsilon \, T(z, \epsilon, V) \rho^{\mathrm{tip}}(\epsilon - eV) \rho^{\mathrm{sample}}(\epsilon), \tag{A.42}$$

where:

$$|M|^2 \to T(z, \epsilon, V) = \exp\bigg(- 2 \int_0^z dz' \kappa \bigg) \cong \exp\bigg\{ - 2z \sqrt{\frac{2m_e}{\hbar^2} \bigg(\frac{\phi_\mathrm{t} + \phi_\mathrm{s}}{2} + \frac{eV}{2} - \epsilon \bigg)} \bigg\}, \tag{A.43}$$

with z the tip-sample distance, ϕ_t, and ϕ_s the work function for the tip and the sample, respectively.

Appendix B

Atomic force microscopy, photoluminescence, and Raman spectroscopy

B.1 Atomic force microscopy

In atomic force microscopy (AFM), the interaction force between a sharp tip (probe) and the sample surface is measured to obtain an image. The AFM images give us morphological and chemical information about the surface under investigation. The technique uses as a force sensor a flexible cantilever with a sharp tip at its end. Depending on the distance between the AFM tip and the sample surface, the tip-surface interaction can be attractive or repulsive, leading to deflections of the cantilever. As illustrated in Figure B.1(a), this deflection is measured with an optical system that employs a laser beam incident on the cantilever and reflected toward a photodiode. Thereby, the photodiode signals are transmitted to a feedback system to acquire images [94].

The force curve shown in Figure B.1(b), describe the interaction between the AFM tip and the sample surface. Depending on the tip-surface distance, there are different regimes to be considered. (i) When the tip is far away from the sample surface, the interaction is negligible, and the cantilever will not suffer deflections. (ii) For closer tip-surface distances, the cantilever will feel an attractive force that deflects it toward the sample surface but without mechanical contact. (iii) For short distances, the cantilever will deflect due to repulsive forces, and the AFM tip is in contact with the sample surface. Based on these regimes, two AFM operation modes for imaging acquisition are possible:

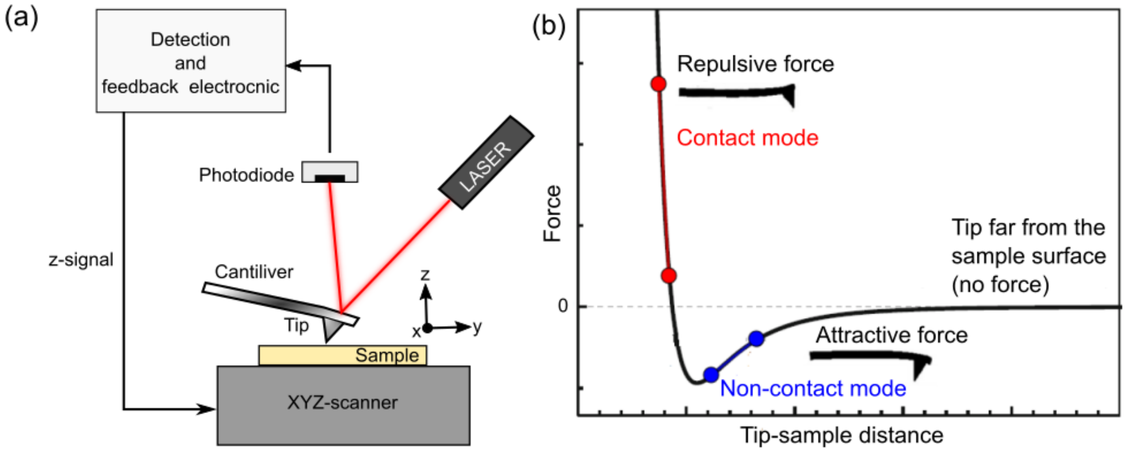

Figure B.1: (a) Schematic diagram of the AFM working principle. (b) Qualitative behavior of tip-sample force. Adapted from [94].

Contact mode: the cantilever works like a spring, and its deflection in the z-direction is proportional to the tip-sample force. The AFM tip is scanned over the surface to record an image of the sample surface. The feedback system controls the tip-sample distance through the piezoelectric scanner to keep the cantilever deflection constant. In this way, topographic images of the sample surface are obtained by monitoring the z-movement of the scanner. The main issue of this mode is that it operates in a repulsive regime and the AFM tip is in contact with the sample. Therefore, the sample can be damaged by the tip.

Non-contact mode: this mode operates in the attractive regimen. The cantilever is set to oscillate with a frequency close to its resonance frequency at a selected amplitude (free amplitude). When the tip is approached to the sample surface, attractive forces modify the frequency, phase, and amplitude of the oscillating cantilever. There are two methods for recording AFM images in non-contact mode. These are the amplitude modulation (AM-AFM) and the frequency modulation (FM-AFM) methods. In AM-AFM, the cantilever's oscillation frequency is fixed, and changes in the amplitude are measured and used as feedback signals for the acquisition of images. Variations of the surface topography modify the oscillation amplitude, then images with topographic contrast are recorded by monitoring the z-movement of the piezo-scanner, which is adjusted by the feedback system to keep the amplitude constant. In FM-AFM, the oscillation amplitude is fixed, and the cantilever always oscillates on resonance. In this case, the imaging signal is the variation in the cantilever's resonance frequency.

The AM-AFM mode can be employed in the so-called tapping mode. In this case, the cantilever oscillates with a high amplitude at a fixed frequency near its resonance. Due to the high oscillation amplitude, the AFM tip is in intermittent contact with the sample surface. Topographic-contrast image can be acquired as described above, i.e., using the oscillation amplitude as the feedback signal. However, the amplitude of the cantilever can be characterized by its phase relative to the driving oscillator. Thereby, phase-contrast images can be recorded simultaneously with de topography data by monitoring the Phase difference between the cantilever's oscillations and the drive signal. Phase-contrast images are useful for the chemical mapping of the sample. Besides that, phase-contrast images are sensitive to surface properties such as friction and adhesion [152].

We used a Nanosurf EasyScan2 Flex and a BRUKER / VEECO INNOVA AFM for this thesis. These microscopes operate in ambient conditions. We employed AFM measurements to explore the sample surface morphology and investigate the sample-substrate coupling.

B.2 Photoluminescence and Raman spectroscopy

In photoluminescence (PL), the sample is excited by monochromatic light. Then the light emitted by the sample after excitation is analyzed to obtain optical and electronic information about the material. In semiconductors, an electron in the valence band is excited to the condition band by absorbing the energy of the incident photon. The subsequent radiative recombination of electron-hole pairs gives a luminescence spectrum that provides information about the electronic band gap, excitons, or defect states [60, 61, 153]. Figure B.2 summarizes the main recombination processes observe in PL measurements.

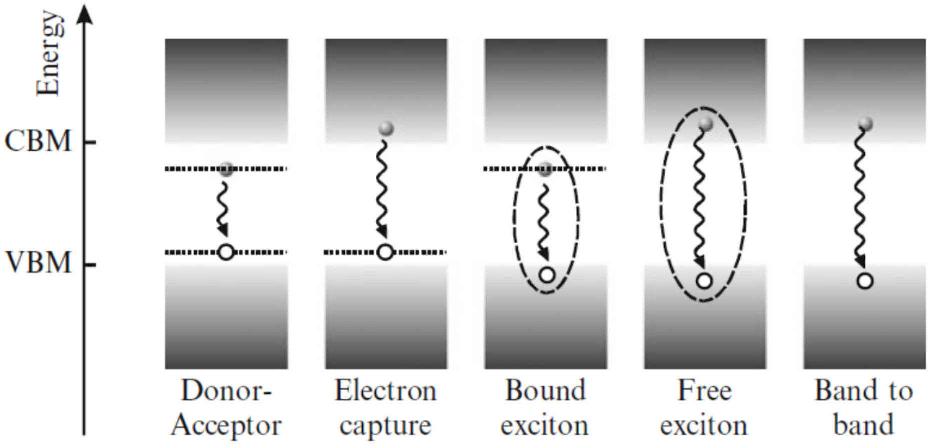

Figure B.2: Recombination processes observed in PL. The shaded areas represent the conduction and valence bands. The conduction band minimum (CBM) and valence band maximum (VBM) are indicated in the energy axis. Horizontal dotted lines represent the energy position of impurity states. Electrons (holes) are indicated by dark-shaded (hollow) dots. Undulated arrows indicate radiative recombination. Dashed curves highlight the Coulomb interaction in excitons.. Taken from [153].

In Raman spectroscopy, the monochromatic incident light is inelastically scattered. The difference in frequency between the incident and the scattered photon is related to the excitation of vibrational modes (phonons) in the sample. The phonons excited by Raman scattering are associated with the chemical and structural properties of the material. Therefore, a Raman spectrum is a chemical fingerprint of a material and provides information about the chemical nature, strain, among other sample properties.

In a Raman scattering, a photon with energy $E_{\mathrm{Laser}} = \hbar\omega_{\mathrm{Laser}}$ and momentum $\hbar k_{\mathrm{Laser}}$ reaches the sample and suffers an inelastic scattering. Therefore, a photon with a different energy $E_{\mathrm{s}} = \hbar\omega_{\mathrm{s}}$ and momentum $\hbar k_{\mathrm{s}}$ is emitted. From the energy and momentum conservation, we have that:

$$\omega_{\mathrm{s}} = \omega_{\mathrm{Laser}} \pm \Omega \quad \text{and} \quad k_{\mathrm{s}} = k_{\mathrm{Laser}} \pm q, \tag{B.1}$$

where $E_q = \hbar\Omega_q$ and $\hbar k_q$ are the energy and momentum, respectively; of the phonon that is created (Stokes scattering) or annihilated (anti-Stokes scattering) in the Raman process [60, 154].

A Raman spectrum is a plot of the scattered intensity as a function of the difference frequency [$\Omega_q = \pm(\omega_{\text{Laser}} - \omega_{\text{s}})$] or momentum [$q = \pm(k_{\text{Laser}} - k_{\text{s}})$], commonly known as *Raman shift*. The + and − correspond to the stokes and anti-stokes processes, respectively. In practice, the Raman shift is obtained using the relation [$(1/\lambda_{\text{Laser}})$-$(1/\lambda_{\text{emission}})$] and has unit of cm^{-1}. A Raman spectrum will show stokes and anti-stokes peaks, as shown in Figure B.3. The anti-stokes peaks appear in the opposite position relative to the stokes peaks with respect to the central peak at 0 cm^{-1}. The central peak is due to the elastic scattering of photons (Rayleigh scattering) and corresponds to the laser beam.

In this thesis, we employed PL and Raman to explore the samples' optical activity and the identification of monolayers.

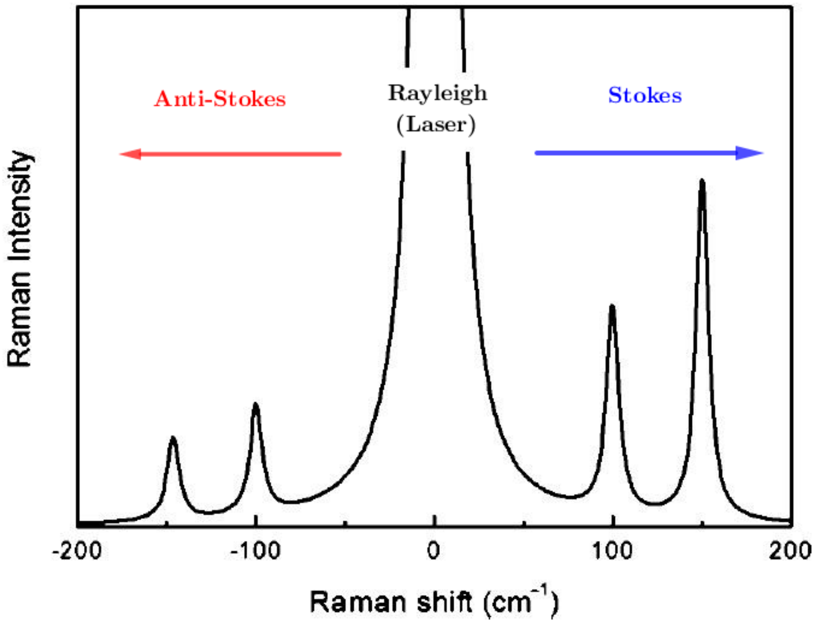

Figure B.3: Representation of a Raman spectrum. Adapted from [154].